Real-time Quantum Control of Qubits

UNIVERSITY OF COPENHAGEN
FACULTY OF SCIENCE
NIELS BOHR INSTITUTE

Real-time Quantum Control of Qubits

Fabrizio Berritta

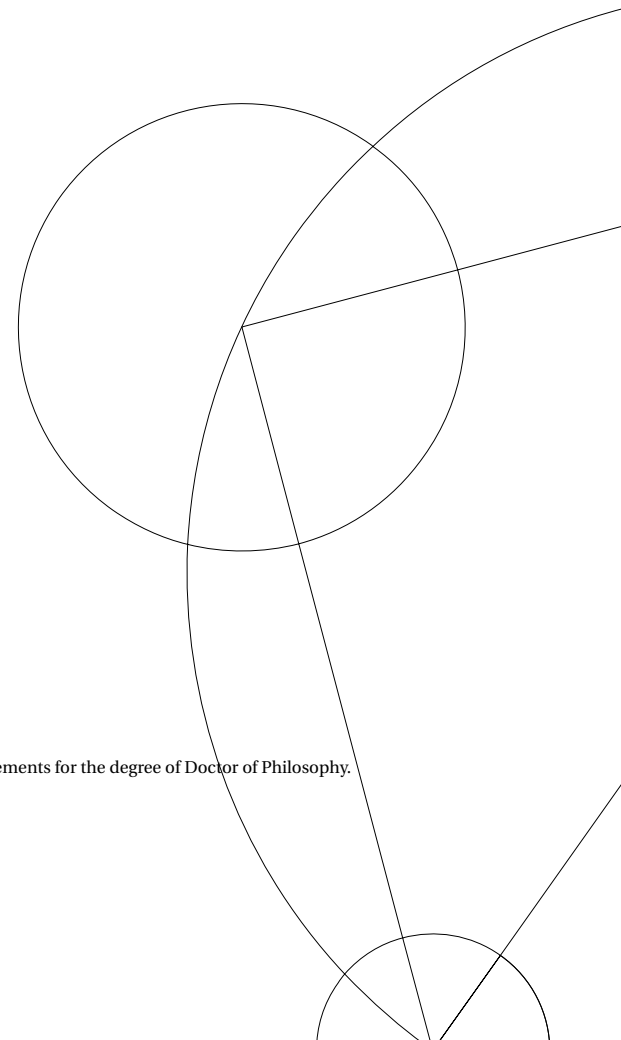

Academic advisor:
Prof. Dr. Ferdinand Kuemmeth

Academic co-advisor:
Assoc. Prof. Dr. Anasua Chatterjee

Assessment committee:
Prof. Dr. Cristian Bonato
Prof. Dr. Karsten Flensberg
Prof. Dr. Lieven M. K. Vandersypen

Thesis submitted in partial fulfillment of the requirements for the degree of Doctor of Philosophy.

Real-time Quantum Control of Qubits
Fabrizio Berritta
Copenhagen, June 2024.

Citation (APA):
Berritta, F. (2024). *Real-time Quantum Control of Qubits.* [Doctoral dissertation, Niels Bohr Institute, Faculty of Science, University of Copenhagen].

Revised: June 15, 2024

Abstract

Quantum computing relies on developing quantum devices that are robust against small and uncontrolled parameter variations in the Hamiltonian. One can apply feedback by estimating such uncontrolled variations in real time to stabilize quantum devices and improve their coherence. This task is important for many quantum platforms such as spins, superconducting circuits, trapped atoms, and others towards error suppression or correction. Semiconductor spin qubits are attractive due to their long coherence times, compact size, and potential large-scale integration with existing semiconductor technology. Until now however, spin qubits shine with high-fidelity operations of selected devices. Further scalability and reproducibility may require actively compensating for environmental fluctuations.

In this Thesis, we focus on real-time closed-loop feedback protocols to estimate uncontrolled fluctuations of the qubit Hamiltonian parameters, followed by enhancing the quality of qubit rotations. First, we coherently control a spin qubit with a low-latency quantum controller. The protocol uses a singlet-triplet spin qubit implemented in a gallium arsenide double quantum dot. We establish real-time feedback on both control axes and enhance the resulting quality factor of coherent spin rotations. Even with some components of the Hamiltonian purely governed by noise, we demonstrate noise-driven coherent control. As an application, we implement Hadamard rotations in the presence of two fluctuating control axes.

Next, we present a protocol for a physics-informed real-time Hamiltonian estimation. We estimate the fluctuating nuclear field gradient within the double dot on-the-fly by updating its probability distribution according to the Fokker-Planck equation. We further improve the physics-informed protocol by adaptively choosing the free evolution time of the electrons singlet pair, based on the previous measurement outcomes. The protocol results in a ten-fold improvement of the estimation speed compared to former schemes.

Finally, we present an adaptive frequency binary search scheme for efficiently tracking low-frequency fluctuations in a resonantly-driven qubit. In real time, we implement the Bayesian algorithm to estimate low-frequency magnetic flux noise in a flux-tunable transmon qubit, whose coherence and fidelity are improved. Furthermore, we show by gate set tomography that our frequency tracking protocol minimizes the amount of drift in the system.

Our approaches introduce closed-loop feedback schemes aimed at mitigating the effects of decoherence and extending the lifetime of quantum systems. This Thesis pushes the field towards integrating qubit hardware and control hardware, and implementing Bayesian estimation and optimization methods from computer science.

Resumé

Kvantecomputere er afhængige af at udvikle kvantebits eller qubits, der er robuste over for små og ukontrollerede parametervariationer i deres Hamiltonian. Man kan anvende feedback ved at estimere sådanne ukontrollerede variationer i realtid for at stabilisere kvantebits og forbedre deres kohærens. Denne opgave er vigtig for mange kvanteplatforme som f.eks. spins, superledende kredsløb, fangede atomer og andre med henblik på fejlundertrykkelse eller -korrektion. Halvleder-spin-qubits er attraktive på grund af deres lange kohærenstider, kompakte størrelse og potentielle integration i storskalaproduktion med eksisterende halvlederteknologi. Indtil nu har spin-qubits brilleret med high-fidelity-operationer af udvalgte enheder. Yderligere opskalering og reproducerbarhed kan kræve, at man aktivt kompenserer for miljøudsving.

I denne afhandling fokuserer vi på feedbackprotokoller med lukket kredsløb i realtid for at estimere ukontrollerede udsving i qubit-hamiltonparametrene og derefter forbedre kvaliteten af qubit-rotationer. Først kontrollerer vi kohærent en spin-qubit med en kvantecontroller med lav latenstid. Protokollen bruger en singlet-triplet spin-qubit, der er implementeret i et dobbelt kvantepunkt af galliumarsenid. Vi etablerer feedback i realtid på begge kontrolakser og forbedrer den resulterende kvalitetsfaktor for sammenhængende spinrotationer. Selv med komponenter i Hamiltonianen, der udelukkende styres af støj, demonstrerer vi støjdrevet kohærent kontrol. Som en applikation implementerer vi Hadamard-rotationer ved brug af to fluktuerende kontrolakser.

Dernæst præsenterer vi en protokol for en fysikinformeret realtids-hamiltonian-estimering. Vi estimerer den fluktuerende kernefeltgradient inden for dobbeltpunktet on-the-fly ved at opdatere dens sandsynlighedsfordeling i henhold til Fokker-Planck-ligningen. Vi forbedrer yderligere den fysikinformerede protokol ved adaptivt at vælge den frie udviklingstid for elektronernes singlet-par baseret på de tidligere måleresultater. Protokollen resulterer i en tifoldig forbedring af estimeringshastigheden sammenlignet med tidligere ordninger.

Endelig præsenterer vi et adaptivt frekvensbinært søgeprogram til effektiv sporing af lavfrekvente udsving i en resonansdrevet qubit. I realtid implementerer vi den bayesianske algoritme til at estimere lavfrekvent magnetisk fluxstøj i en flux-tunable transmon-qubit, hvis kohærens og troværdighed er forbedret. Desuden viser vi ved hjælp af gate-set tomografi, at vores frekvenssporingsprotokol minimerer mængden af frekvensstøj i systemet.

Vores tilgange introducerer feedback-ordninger med lukket kredsløb, der har til formål at afbøde virkningerne af dekohærens og forlænge kvantesystemers levetid. Denne afhandling skubber feltet i retning af at integrere qubit-hardware og kontrolhardware og implementere Bayesianske estimerings- og optimeringsmetoder fra datalogi.

List of Abbreviations, Constants and Symbols

Abbreviations

2DEG	Two-dimensional electron gas
BPE	Bayesian parameter estimation
DQD	Double quantum dot
DUT	Device under test
EMA	Effective mass approximation
FBS	Frequency binary search
FID	Free induction decay
HF	High-frequency
LD	Loss-DiVincenzo
LF	Low-frequency
MC	Mixing chamber
PCB	Printed circuit board
PSB	Pauli spin blockade
QD	Quantum dot
QPU	Quantum processing unit
QSA	Quasi-static approximation
QW	Quantum well
RAP	Rapid adiabatic passage
RF	Radio-frequency
r.m.s.	Root-mean-square
RT	Room temperature
SAP	Slow adiabatic passage
SD	Sensor dot
SET	Single-electron transistor
SMD	Surface mounted devices
T4	Triton 4 dilution refrigerator setup
T7	Triton 7 dilution refrigerator setup
VNA	Vector network analyzer

Constants and symbols

$m_0 \approx 9.31 \times 10^{-31}\,\mathrm{kg}$	Bare electron mass
$k_\mathrm{B} \approx 86.2\,\mu\mathrm{eV K}^{-1}$	Boltzmann constant
$\mu_\mathrm{B} \approx 57.9\,\mu\mathrm{eV T}^{-1}$	Bohr magneton
J	Exchange coupling
GaAs	Gallium arsenide
Ω	Larmor frequency
ΔB_z	Overhauser field gradient
Si	Silicon

Contents

List of Figures

Introduction

More than 40 years after the first proposal for a quantum computer, we can now implement limited control over various quantum systems in pursuing this goal [1]. The fundamental component of a quantum computer is a quantum bit (qubit), a physical system with two quantum mechanical basis states ($|0\rangle$ and $|1\rangle$) which can be controlled and measured reliably, and sufficiently protected from decoherence. Unlike a classical bit, a qubit can also occupy a superposition of both states at the same time and be entangled with other qubits to form exponentially large computational spaces. However, a quantum bit cannot be completely isolated from its environment, as it must respond to control signals to perform computations and measurements.

Fluctuations of the qubit's environment (such as magnetic or electrical noise) lead to undesired dynamics known as decoherence. Decoherence explains why the control signals must be sufficiently fast compared to the qubit decoherence timescale. Two common strategies are to improve the computations' quality and reduce the noise in the qubit's environment; another is to reduce the noise coupling strength to the qubit. Quantum error correction [2] can detect and correct errors at the expense of an increased number of physical qubits. An alternative route is feedback or feedforward control to mitigate or correct noise in the qubit's environment [3].

In this introduction, we introduce feedback control and explain why it could be useful for a quantum processing unit. We conclude with a summary of the Spin Qubit Group research at the Center for Quantum Devices (QDev) and the content of this Thesis.

Closed-loop control In a closed-loop control (or feedback) protocol, there are fundamentally two entities: the controller and the system [3]. The controller receives information about the system's state to manipulate its trajectory in real time, even in the presence of noise or errors. Thus, the information that the controller receives is fed back to the system. This can be seen as a "closed-loop scheme" that reduces the system's entropy and allows it to be controlled. Indeed, noise contributes to uncertainty in the system dynamics, which can be reduced by transferring it to another system. More specifically, when we measure a system, it reduces our uncertainty. Therefore, it allows us to adjust the motion while reducing the spread in the system's state, i.e. randomness. The system is measured by a device that records the necessarily random result of the measurement. The result is as random as the quantity being measured [3]. Thus, the quantum controller transfers randomness from the system to its memory through the measurement. As randomness is entropy and all physical laws are reversible, entropy must be transferred in a different system, such as the environment. That is why a feedback process, according to quantum feedback control, is any process that transfers entropy from the system to the controller.

Historically, Ctesibios's water clock, dating back to the 3rd century BC, is considered the first example of feedback control [4]. The ancient Greeks measured time by dividing the daylight hours into twelve. However, this method caused the known water clock to fall out of sync between seasons. Presumably, Ctesibios added a waterwheel and cogs to the already-known water clock. The waterwheel and cogs would then rotate a cylinder every day by some amount and trace the hour lines on a pole based on the time of the year. In this example, the variability introduced by the different seasons contributes to the randomness. The randomness is transferred to the feedback mechanical components, which adjust the water clock.

A more modern example is Watt's centrifugal governor, from the second half of the 17th century, whose mathematical model was studied for the first time by Maxwell [5]. By adding feedback to control the flow of steam into the cylinder by a throttle valve, it is possible to speed up transients, set the stationary regime, and improve stability. The steam engine's speed can fluctuate, introducing randomness into the system. The feedback mechanism then acts to correct deviations from the desired speed, thus reducing the spread of its fluctuations.

Feedback control first joined the field of quantum dynamics in the early 1980s [3], but it became more popular later in the 1990s. A mathematical theory on feedback control in quantum systems was introduced by Belavkin [7, 6] by extending the theory of classical continuous measurements to the quantum field. In the same decade, Wiseman and Milburn [8] described how continuous feedback in quantum systems can be derived from a Markovian master equation. A few years later, in 1998, Yanigasawa and Kimura [9], as well as Doherty and Jacobs [10], introduced the concept of feedback by exploiting estimates from the stochastic master equation. In the context of quantum control, Bayesian feedback refers to the use of estimates obtained from the stochastic master equation, differently from Markovian feedback [3]. While in the Bayesian approach measurement results are used to obtain an estimate of the current state properties, in the case of Markovian feedback the measurements are directly fed back to the state.

From *classical* to *quantum* bits The quest to realize a useful quantum computer resembles the effort from the 1940s to engineer the fundamental hardware unit that would lead to the first solid-state computers. The basic unit of classical computing is the transistor functioning as a switch, depending on an applied voltage that turns it "on" or "off". The binary information can be encoded in the flow of current. Ideally, if current flows, the transistor is "on," and it encodes, e.g., the "1" logical state. If the current does not flow, the transistor is "off," encoding the "0" state. The transistor may then hold a bit of information. A number N of available transistors form an N-dimensional space since a binary vector of dimension N can represent any possible state.

If we consider a single qubit, it spans a two-dimensional space to describe the direction of its spin, e.g. spin-up or spin-down. If we increase the number of electrons to N, the dimensional space becomes 2^N because of the possible presence of entangled states between different electrons. Unlike the classical case where N bits can describe an N-dimensional space, representing a quantum state with N particles requires a complex vector with 2^N components. This originates from the possibility of creating a superposition of the basis states, which eventually leads to quantum entanglement.

The (classical) exponential scaling to represent quantum states was already known almost one hundred years ago. Indeed, in 1929, Paul Dirac explicitly stated that if we tried to solve the Schrödinger equation for many particles, it would be an intractable problem [11]. At the time, there was a relatively good understanding of the underlying physical laws for the branch of chemistry

and material science. Nevertheless, solving these laws exactly for many particles is too complicated to be done in practice. This intractability was already understood by researchers interested in solid-state physics in the 1930s.

We highlight a few events to trace the origin behind the idea of a quantum computer [1]. In the 1980s, Yuri Manin mentioned the idea of a quantum automaton that used superposition and entanglement [12]. Paul Benioff was also interested in quantum computing [13] around that time. But he was not particularly interested in what we now call quantum advantage or quantum complexity, but rather in understanding whether we could compute a time-independent Hamiltonian without dissipation.

Other physicists were discussing similar topics at the time, including Richard Feynman. He was interested in quantum chromodynamics (QCD), with theories of strong interaction [1]. At the time, the interest in computing the predictions of QCD for the properties had grown. Though the theory was known, it was unclear how to do computations for many processes in QCD or other strongly coupled quantum field theories. That problem was part of the background that inspired Feynman to propose the idea of a quantum computer [14]. Feynman proposed storing and manipulating information encoded in the state of a quantum system. This would then make it possible to simulate a system of many particles by keeping track of the required number of amplitudes, which is exponential in the particle number (as mentioned above).

Some years later, it was shown that quantum computers can, in principle, beat classical computers in several tasks [15, 16, 17]. To perform quantum computation, the information has to be represented in an appropriate physical platform [18], such as quantum dots, nitrogen-vacancy centers, solid-state superconducting circuits, atomic and molecular systems, e.g. Rydberg atoms and trapped ions, photons, and others.

Nowadays, quantum processors have on the order of a hundred qubits with about 20-30 gate operations [19]. In the past years, academic interest has been accompanied by industrial efforts, leading to an increased number of physical qubits every year. These devices are categorized as noisy intermediate-scale quantum (NISQ) [20], where "intermediate scale" refers to the number of qubits, and "noisy" emphasizes the imperfect control over them. Indeed, while a classical bit is digital and insensitive to small variations of the control signals, small errors can lead to significant errors in qubits when long algorithms are performed.

In classical devices errors are corrected, for instance, by having many copies of the information, as a majority vote across the classical bits can correct errors. Nevertheless, the no-cloning theorem forbids copying quantum information. Therefore, quantum information is encoded in the non-local degrees of freedom of many physical qubits [21]. Fault-tolerant quantum computers using quantum error correction [2] are expected to rely on integrating millions of qubits.

The early 2020s have witnessed the first demonstrations of experimental quantum error correction [21], marked first by trapped ions qubits [22, 23]. A 17-transmon-qubit Kitaev's surface code has been demonstrated in superconducting qubits within academia [24]. Again, in superconducting qubits, the suppression of logical error with increasing code size has been shown by industry [25]. Fault-tolerant logic over hundreds of physical qubits has been shown in reconfigurable atom arrays [26]. Regarding spin qubits, in Ref. [27] a three-qubit phase-correcting code has been recently demonstrated in silicon.

Overall, the advantage (supremacy) of quantum computing over classical computing has been shown by NISQ devices, although on problems with limited usefulness. Efforts are in play to demonstrate a quantum advantage in practical problems such as optimization and chemistry [16, 28].

The Spin Qubit Group at the Niels Bohr Institute

The work described in this Thesis has been realized at QDev, at the Niels Bohr Institute (NBI), under the supervision of Prof. Ferdinand Kuemmeth and Assoc. Prof. Anasua Chatterjee. The Spin Qubit Group at QDev focuses on different semiconductor material platforms to investigate new directions for qubit networks with optimal control, while still addressing condensed matter physics-related research questions [29].

The group and its collaborators have studied gallium-arsenide (GaAs) heterostructures to study nuclear spins dynamics [30, 31], as well as electron-electron correlations [32, 33]. Further research has been done on the use of symmetry points that prolong qubit coherence [34], elongated quantum dots as quantum mediators [35], and two-dimensional spin qubit arrays [36].

Moreover, academic and industrially fabricated spin qubit devices in silicon have been studied [37, 38, 39], as isotopically-purified silicon-28 (^{28}Si) has longer coherence times and it holds promising compatibility with industrial fabrication.

Experiments have also implemented computer science-related techniques for optimization, automation, and machine learning [41, 40] for a deeper understanding of spin phenomena while increasing control complexity in larger quantum-dot circuits.

Thesis outline

This Thesis deals with implementing real-time quantum control techniques in gate-defined spin qubits and superconducting qubits for quantum information processing. By coherently controlling electron spins with a low-latency FPGA-powered quantum controller, we establish a real-time feedback protocol to enable noise-driven coherent qubit rotations. Moreover, we show the first experimental implementation of a physics-informed tracking of the qubit fluctuations, and of a Bayesian approach for real-time Hamiltonian tracking and stabilization of a superconducting qubit. In the following, we summarize the Chapters content:

- In Chapter 1, we introduce semiconductor spin qubits and provide an overview of the state-of-the-art before going more in-depth on the singlet-triplet qubit encoding used in this work. Ultimately, we illustrate the basics of feedback control by comparing different qubit platforms, and we describe an introductory example.

- In Chapter 2 we describe the experimental setup “T4" at QDev, and we provide an introduction to radio-frequency (RF) reflectometry based-readout of spin qubits.

- Chapter 3 is based on Ref. [42]. We implement a feedback protocol for real-time control of a singlet-triplet qubit with fluctuating Hamiltonian parameters in a quantum controller. The protocol involves two main steps: leveraging a new control axis based on estimating one of the fluctuating parameters and using this control axis to probe the qubit frequency in real time across different operating points. The quality of coherent qubit rotation is significantly improved by counteracting fluctuations along both axes. Some of the results are extended to two qubits simultaneously, and they are not contained in Ref. [42].

- Chapter 4 is based on Ref. [43]. We show a physics-informed and real-time Hamiltonian estimation protocol. The scheme estimates the fluctuating environment of a spin qubit (a nuclear spin bath) on-the-fly on a quantum controller. The controller updates the probability distribution of the fluctuating parameter according to a model describing the nuclear spins

(by the Fokker-Planck equation). The protocol is further improved by adaptively choosing the probing time of the qubit, based on the previous measurement outcomes, to maximize the information gathered per measurement.

- In Chapter 5 we present an adaptive frequency binary search algorithm to estimate and stabilize in real time the frequency of a flux-tunable transmon qubit affected by flux noise. The protocol adaptively updates the frequency of the qubit drive pulses and the duration of the probing evolution times after each measurement. We evaluate the algorithm by randomized benchmarking and gate set tomography, which show improved fidelity and reduction of drift in the system, respectively. This Chapter's measurements have been performed at the Engineering Quantum System group (EQuS) at the Massachusetts Institute of Technology, under the supervision of Dr. Jeffrey A. Grover and Prof. Dr. William D. Oliver.
- Chapter 6 provides a comprehensive summary and an outlook of possible future developments in the field of quantum control.

Publications

1. **Berritta, F.**, Krzywda, J. A., Benestad, J., van der Heijden, J., Fedele, F., Fallahi, S., Gardner, G. C., Manfra, M. J., van Nieuwenburg, E., Danon, J., Chatterjee, A., and Kuemmeth, F. Physics-informed tracking of qubit fluctuations. arXiv:2404.09212 (2024). Accepted for publication in *Physical Review Applied*.
   I led the measurements and data analysis, and wrote the manuscript with input from all authors.

2. **Berritta, F.**, Rasmussen, T., Krzywda, J. A., van der Heijden, J., Fedele, F., Fallahi, S., Gardner, G. C., Manfra, M. J., van Nieuwenburg, E., Danon, J., Chatterjee, A. & Kuemmeth, F. Real-time two-axis control of a spin qubit. *Nature Communications* **15**, 1676 (2024).
   I led the measurements and data analysis, and wrote the manuscript with input from all authors.

3. Patomäki, S. M., Williams, J., **Berritta, F.**, Laine, C., Fogarty, M. A., Leon, R. C. C., Jussot, J., Kubicek, S., Chatterjee, A., Govoreanu, B., Kuemmeth, F., Morton, J. J. L., and Gonzalez-Zalba, M. F. An elongated quantum dot as a distributed charge sensor. *Physical Review Applied* **21**, 054042 (2024).
   I contributed to the experimental setup, measurements, and writing the manuscript.

4. Ansaloni, F., Bohuslavskyi, H., Fedele, F., Rasmussen, T., Brovang, B., **Berritta, F.**, Heskes, A., Li, J., Hutin, L., Venitucci, B., Bertrand, B., Vinet, M., Niquet, Y.-M., Chatterjee, A., Kuemmeth, F. Gate reflectometry in dense quantum dot arrays. *New Journal of Physics* **25** 033023 (2023).
   I contributed to the experimental setup, measurements, and writing the manuscript.

5. Murphy, T., **Berritta, F.**, et al. Radiofrequency Electron Cascade in Quantum Dots. *Manuscript in preparation*.
   I contributed to the experimental setup, measurements, and writing the manuscript.

1

Semiconductor Spin qubits and Real-time Quantum Control

The spin degree of freedom of one electron, spin-up or spin-down, can define a qubit [44]. Due to the small magnetic moment of the electron spin $\mu_e \approx -9.28 \times 10^{-24}\,\mathrm{J\,T^{-1}}$, its coupling to the environment is weak, and it leads to long spin coherence times [45]. At the same time, this also means that it is hard to measure the electron spin directly. On the other hand, it is possible to electrically control spin states by exploiting the coupling of the electron charge to electric fields, and using spin-to-charge conversion techniques. Indeed, energy-dependent tunneling or the Pauli exclusion principle [46, 47] enable to initialize electrically and readout electron spins, which are projected onto different charge states. Alternatively, a qubit can be defined by two different nuclear states [48], for which coherence times of hours have been demonstrated [49, 50]. We refer the reader to Refs. [51, 45] for quantum information processing encoded in electron holes and nuclear states with high fidelity.

Contrarily to metals, semiconductors can be depleted of conduction electrons at sufficiently low temperatures. It is possible as well to engineer the electron density to confine the electrons in two dimensions (2D) in quantum wells (QWs), or at the interface between two materials [52]. Finally, electrostatic tailoring of the potential landscape can confine electrons to one (1D) or zero (0D) dimensions [54, 53]. In particular, the 0D confinement restricts one or more electrons in quantum dots[1] (QDs), known also as artificial atoms defined in semiconductors [56]. The different semiconductor materials typically used in semiconductor spin qubits include group III–V (e.g. gallium arsenide) or IV (silicon and germanium) of the periodic table, as discussed in Sec. 1.2.

Exchange interaction [57, Chapter 32] is a key ingredient in semiconductor spin qubits. Given two electrons in two distinguishable locations, with overlapping wavefunctions, the exchange coupling J (also known as pseudo-exchange or kinetic exchange [51]) is defined as the energy difference of the spin-singlet state lowered relative to the three spin-triplet states (in the absence of an externally applied magnetic field). The higher energy of the triplets compared to the singlet for spins i and j is given by the Heisenberg exchange Hamiltonian

$$\hat{\mathcal{H}} = J_{ij}\,\hat{\vec{S}}_i \cdot \hat{\vec{S}}_j, \tag{1.1}$$

where $\hat{\vec{S}}_i$ is the operator for the electron spin in site i. (For ease of notation, the $\hat{}$ is dropped to denote operators wherever no ambiguity arises.) The two electrons have an antisymmetric wavefunction because of the Pauli exclusion principle. The electron pair in the singlet spin state

[1] The recent Nobel Prize in Chemistry 2023 has rewarded Moungi G. Bawendi, Louis E. Brus, and Aleksey Yekimov for the discovery and synthesis of quantum dots [55].

(with antisymmetric spin wavefunction) can move to and from the same location. In contrast, in the triplet spin state (with symmetric spin wavefunction), the motion is forbidden. The exchange interaction J_{ij} can be tuned over many orders of magnitude (from a few kHz to tens of GHz) by changing gate voltages [47] and it can be used for both single-qubit [58, 47, 59] and two-qubit gates, depending on the spin qubit encoding [60, 61, 62, 63].

Spins in semiconductors are promising because of their small size of ≈ 100 nm and the expected requirement of at least one million physical qubits for a fully-error corrected quantum computer [64]. The small size would allow the semiconductor industry to produce dense quantum computing architectures [65, 66, 67, 68] based on their decades of experience with classical transistors. However, the nearest neighbor Heisenberg exchange interaction (spatially limited by the wavefunctions overlap) and the small features of spin qubits also come with engineering challenges in terms of design, fabrication, and operation for quantum information processing. Possible solutions for long-range connectivity include physically transporting qubits across the device by surface acoustic waves in piezoelectric materials such as GaAs [69, 70, 71], “bucket brigade" in GaAs [72, 73] and Si [74, 75], conveyor mode single electron and spin shuttling [76, 77], sequence of pairwise SWAPs [44, 47, 78, 79], superexchange by an additional QD-based mediator [80, 81, 35, 82], or microwave photons by cavity quantum electrodynamics (QED) [85, 86, 84, 88, 83, 85, 87, 89, 90]. The previous list is not exhaustive: more details are found in Ref. [51].

Spin qubits are measured at low temperatures in dilution refrigerators on the order of a few tens of mK, a much smaller quantity[2] compared to the typical energy scales for semiconducting quantum dots, on the order of meV. Low-temperature operation also minimizes thermal noise. However, less cooling power is available at such temperatures (about hundreds of μW at about 100 mK), and the thermal budget needed to operate large arrays of qubits may require operation well above the millikelvin regime [65, 92, 91, 93, 95, 94, 96, 97]. Some experiments have been performed above 1 K [93, 95, 94, 96, 98] where at higher temperatures it is more difficult to maintain high state-preparation-and-measurement (SPAM) and gate fidelities compared to millikelvin operation.

In the following section, we introduce two different kinds of spin qubit encodings, followed by the description of two architectures used in this Thesis to explain the difference between “depletion" and “accumulation" mode devices. A reader familiar with semiconductor spin qubits may jump directly to Sec. 1.6, where we provide details on singlet-triplet qubits in GaAs, including standard pulses for spin control and readout, and related introductory experiments. Finally, we introduce feedback and feedforward in quantum devices, with an example of a real-time control loop protocol which lays the premises for the main results of this manuscript.

1.1 Spin qubits encodings

The number of spins used to encode the qubit classifies the spin qubit encoding. In the following, we focus on the Loss-DiVincenzo (one electron) and singlet-triplet (two electrons) encodings. Another type is the exchange-only qubit (three electrons) [29, 51], which requires only exchange interaction to access the entire Bloch sphere, but it is not treated here. We refer to Appendix A for an introduction to the Bloch sphere formalism, single-qubit gates, and decoherence.

Loss-DiVincenzo encoding A single electron encodes quantum information in the single spin Loss-DiVincenzo (LD) qubit. Assuming one electron per dot and tight electronic confinement,

[2] The Boltzmann constant $k_B \approx 86\,\mu\text{eV}\,\text{K}^{-1}$, thus 50 mK ≈ 4.3 μeV.

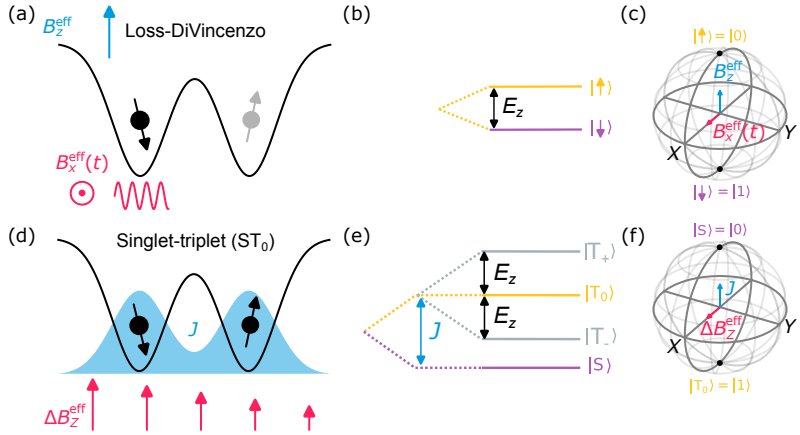

Fig. 1.1: **Loss-DiVincenzo and singlet-triplet encodings. (a)** Loss-DiVincenzo (LD) qubit: a single electron (black circle) is trapped in a potential well, and the externally applied magnetic field B_z^{eff} defines the spin quantization axis. A transverse and weaker AC magnetic field $B_x^{\text{eff}}(t)$ rotates the LD qubit between spin up and spin down. **(b)** Energy levels of the LD qubit with applied magnetic field (assuming $g > 0$) which removes the spin-up $|\uparrow\rangle$ and spin-down $|\downarrow\rangle$ energies degeneracy. **(c)** Bloch sphere of a LD qubit. The state $|\uparrow\rangle$ ($|\downarrow\rangle$) defines the $|0\rangle$ ($|1\rangle$) state. The states are split in energy by B_{eff}^z. The resonant field $B_x^{\text{eff}}(t)$ provides a second, orthogonal rotation axis (e.g. along X). **(d)** Two electrons trapped in a double quantum well encode the singlet-triplet (ST_0) qubit. The qubit Hamiltonian is defined by the exchange coupling interaction J between the two electrons (visualized by the overlap of the electrons wavefunctions), and the difference in the effective magnetic field ΔB_z^{eff} between the two electrons. A globally applied magnetic field B_z (not shown) defines the spin quantization axis. **(e)** Energy level diagram of the four eigenstates of two electrons, one singlet ($|\text{S}\rangle$) and three triplets ($|\text{T}_+\rangle$, $|\text{T}_0\rangle$, $|\text{T}_-\rangle$) (see main text). The $|\text{T}_+\rangle$ and $|\text{T}_-\rangle$ are Zeeman-split in energy by the global field B_z, while $|\text{S}\rangle$ and $|\text{T}_0\rangle$ are split in energy by the exchange coupling J. **(f)** Bloch sphere of the ST_0 qubit, where J (ΔB_z^{eff}) enables rotations around the Z (X) axis.

the Hamiltonian includes the Heisenberg exchange coupling (mentioned previously) and the single-electron Zeeman term:

$$\mathcal{H}(t) = \frac{1}{4}\sum_{\langle i,j\rangle} J_{ij}(t)\boldsymbol{\sigma}_i \cdot \boldsymbol{\sigma}_j + \frac{1}{2}\sum_i g_i \mu_{\text{B}} \mathbf{B}_i \cdot \boldsymbol{\sigma}_i, \tag{1.2}$$

where $\mathbf{B}_i$ and g_i are the effective magnetic field and g–factor at site i, μ_{B} is the Bohr magneton and $\boldsymbol{\sigma}_i = 2\mathbf{S}_i$, with $i = x, y, z$, are the Pauli operators. Single-qubit gates are performed by time-dependent control of $\mathbf{B}_i$ or g_i.

While spin-selective ferromagnetic elements were suggested in Ref. [44], nowadays readout is performed by spin-selective tunneling to a reservoir of electrons, also known as "Elzerman readout" [46]. A sufficiently large static magnetic field is applied compared to the thermal broadening, $gB_z^{\text{eff}} \gg k_B T_e/\mu_{\text{B}}$, where k_B is Boltzmann constant and T_e the electron temperature. The Larmor frequency of the electron spin is then on the order of tens of GHz. For instance, as $\mu_B \approx 58\,\mu\text{eVT}^{-1}$ and $g \approx 2$ in silicon, assuming an electron temperature of 50 mK, it follows $B_z^{\text{eff}} \gg 4.3\,\mu\text{eV}/\left(2\cdot 58\,\mu\text{eVT}^{-1}\right) \approx 40\,\text{mT}$. Thus $B_z^{\text{eff}} \approx 1\,\text{T}$ as an order of magnitude, and the Zee-

man splitting $E_z = g\mu_B B_z^{\text{eff}} \approx 116\,\mu\text{eV} \approx 28\,\text{GHz}$[3]. The chemical potential of the QD is tuned such that only the higher energy spin-state is allowed to tunnel to the Fermi reservoir, whereas tunneling from the lower energy spin-state is energetically forbidden. By charge sensing (see Sec.1.4 later) it is possible to measure the presence or absence of a tunneling event, thus discriminating between the two electron spin states. This measurement is destructive because the measured electron is lost to the reservoir after tunneling out of the QD.

Focusing on one electron in one dot and dropping the subscript i in the notation, see Fig. 1.1(a), the degeneracy between the spin-up $|\uparrow\rangle$ and spin-down $|\downarrow\rangle$ state is lifted by the global magnetic field B_z^{eff} [see (b), with Zeeman splitting E_Z], whereas an AC transverse magnetic field $B_x^{\text{eff}}(t)$ drives the qubit coherently between the two states by electron spin resonance (ESR) [99, 61, 100]. Alternatively, it can be possible to apply electric dipole spin resonance (EDSR) via oscillatory electric fields in a combination of spin-orbit coupling [101, 102], or magnetic field gradients [103, 63, 104]. Figure 1.1(c) depicts the Bloch sphere of the LD qubit. Single-qubit gates X and Y differ by a phase $\pi/2$ of the drive $B_x^{\text{eff}}(t)$.

As mentioned above, gate voltages tune the exchange coupling between single electrons [47] and such interactions allow time-dependent two-qubit control. Silicon spin-qubit devices have achieved high-fidelity single-qubit gates exceeding 99.9% [104] and two-qubit gates [61, 63, 62]. The regime for fault-tolerant operation has been recently reached exceeding 99% [107, 106, 105] in Si, and recently in Ge holes [108].

A main advantage of the LD qubit is that it maps the two possible spin states of an electron in the presence of a magnetic field to a qubit without leakage states (i.e. other spin states outside the computational space). Also, each QD corresponds to one LD qubit. The main disadvantage is that electron spin rotations require tens of GHz frequency range. Moreover, selectivity is challenging and solutions nowadays include using micromagnets or g–factor differences between QDs [51].

Singlet-triplet encoding We have seen how the LD qubit requires a combination of static and oscillating electric or magnetic fields. It is challenging to localize the fields in such devices, and at cryogenic temperatures the available cooling power limits the amount of energy that those fields can dissipate. Also, dephasing due to magnetic noise in materials such as GaAs with spinful nuclei can be detrimental.

These problems can be overcome by encoding a qubit out of two electrons in a double quantum dot (DQD), see Fig. 1.1(d). The singlet-triplet splitting given by the exchange interaction sets the energy splitting of the so-called singlet-triplet (ST_0) qubit [58, 47]. Given a spin quantization axis along z, the qubit basis is defined by the singlet $|S\rangle$ and unpolarized $|T_0\rangle$ states, whereas the polarized triplet states $|T_+\rangle$, $|T_-\rangle$ are the leakage states outside the computational space. The composition of these spin triplet and singlet states is [57, Chapter 32]:

$$\begin{cases} |T_+\rangle = |S=1, M_S=1\rangle = |\uparrow\uparrow\rangle \\ |T_0\rangle = |S=1, M_S=0\rangle = (|\uparrow\downarrow\rangle + |\downarrow\uparrow\rangle)/\sqrt{2} \\ |T_0\rangle = |S=1, M_S=-1\rangle = |\downarrow\downarrow\rangle \end{cases} \tag{1.3}$$
$$|S\rangle = |S=0, M_S=0\rangle = \frac{(|\uparrow\downarrow\rangle - |\downarrow\uparrow\rangle)}{\sqrt{2}},$$

where S is the total spin of the two electrons, M_S is the total spin projection along the given z axis, and e.g. $|\uparrow\uparrow\rangle$ means both electrons are spin-up along z. Notice that in $|S\rangle$ and $|T_0\rangle$ the two electrons

[3] $1\,\mu\text{eV} \approx 242\,\text{MHz}$.

form an entangled pair. By applying a global magnetic field B_z, the $|T_+\rangle$ and $|T_-\rangle$ are split by the Zeeman energy E_z from the $|S\rangle$ and $|T_0\rangle$ [see Fig. 1.1(e)], as both share $M_S = 0$ and their energy does not change by B_z. We reiterate that $|S\rangle =: |0\rangle$ and $|T_0\rangle =: |1\rangle$, whereas the $|T_+\rangle$ and $|T_-\rangle$ are leakage states in this setting detuned by the externally applied magnetic field.

The Hamiltonian of the ST_0 qubit is given by

$$\mathcal{H}_{ST_0} = J_{12}\frac{\sigma_z}{2} + \mu_B\Delta(g^* B_z)\frac{\sigma_x}{2}. \tag{1.4}$$

Again, QD gate voltages can control the exchange coupling J_{12} [47], which enables rotations around the Z axis of the Bloch sphere [see Fig. 1.1(f)]. In the presence of an applied global field along z, $\Delta B_z^{\text{eff}} \equiv \Delta(g^* B_z)$ is the effective difference in the magnetic field between the two QDs along z. This effective magnetic field gradient drives rotations around the X axis. In general, ΔB_z^{eff} is always on, but we can tune the exchange J by electrically tuning the barrier between the two dots, so we can work in the regime where $J \gg |\Delta B_z|$. There is no idle gate in this qubit, except if one works in the resonant mode and in the rotating frame of the qubit [109].

As the total spin projection $M_S = 0$ for the $|S\rangle$ and $|T_0\rangle$ states, the ST_0 qubit is insensitive to fluctuations with respect to global magnetic fields that couple to the spin of the electrons [110]. However, local effective magnetic-field fluctuations cause decoherence because of the $\Delta(g^* B_z)$ appearing in the Hamiltonian defined in Eq. (1.4). The σ_x term can originate from hyperfine fields [111, 112], g-factor variations [114, 113, 115], or micromagnet field gradients [116]. In particular in GaAs, single-qubit gates have been performed by dynamic polarization of the nuclei, also known as “nuclear pumping" [117, 118, 109]. After qubit manipulation, the singlet state is distinguished by the triplet states by Pauli spin blockade (PSB), with a fast and high-fidelity measurement with a nearby quantum dot used as a charge sensor [47, 119]. Upon the measurement, the singlet and triplets are mapped to different spatial configurations of the two electrons in the DQD. Unlike Elzerman readout, the measurement is non-destructive, in the sense that no electrons are exchanged with the reservoir for readout. Moreover, it is faster as its speed is not limited by the tunneling rate of the QD with the reservoir, enabling fast (typically a few µs long) single-shot readout by radio-frequency reflectometry techniques [120]. Moreover, the readout window of PSB is given by the singlet-triplet orbital splitting. The latter has energy scales on the order of 1 meV, which is convenient for high-temperature (≈ 1 K) operation [65].

In the following section we will see why most spin qubit experiments were first performed in GaAs, and then reproduced in Si. Recently, Ge electron holes (often called holes) have entered the race as promising semiconductor spin-qubit platform. Germanium holes have several benefits, including natural strong spin-orbit coupling, which enables full electrical control, Fermi-level pinning of the valence band, and no valley degeneracies. We refer the interested reader to Refs. [121, 122].

1.2 Gallium arsenide and silicon

To illustrate the main differences between GaAs and Si for spin qubit applications, we start by plotting in Fig. 1.2(a) the first Brillouin zone (BZ) of a face-centered-cubic structure (FCC) in direct space. The Γ point is at the origin of $\mathbf{k}$-space, where $\mathbf{k}$ is the crystal momentum. We plot the band structure of bulk GaAs and Si in (b) and (c); they are different as the band structure depends on the crystalline potential of each material [57, 123]. GaAs is a direct gap semiconductor (at $\Gamma = 0_v$) with gap of ≈ 0.4 eV at room temperature (RT). Silicon instead has indirect gap of ≈ 1.1 eV at RT.

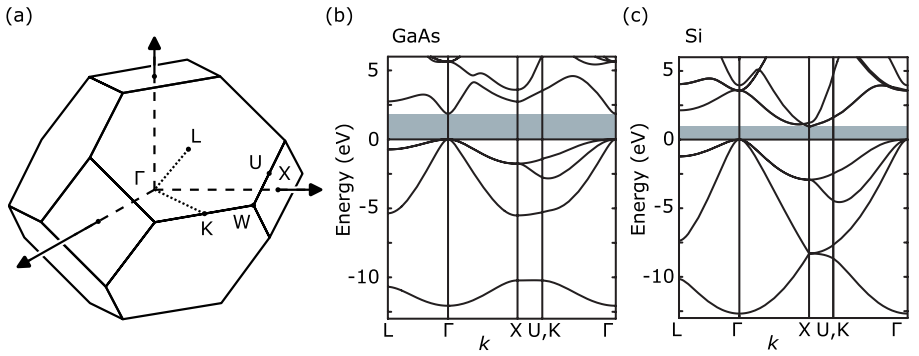

Fig. 1.2: **Bandstructure of bulk GaAs and Si. (a)** Bulk first Brillouin zone of a face-centered-cubic lattice (FCC) with labeled symmetry points. **(b)** Bandstructure of bulk GaAs as a function of the crystal momentum k, along symmetric directions labeled in (a). The band gap (gray) is direct as the nondegenerate conduction band minimum is centered at the Γ point ($k = 0$). **(c)** Bandstructure of bulk Si as a function of the crystal momentum k, along symmetric directions labeled in (a). The band gap (gray) is indirect, and six equivalent conduction band minima are in the 1st BZ [cf. (a)] along the X directions. Figure adapted from [123].

To better understand the properties of electrons in QDs, one can describe the electrons close to the conduction band minima by the effective mass approximation (EMA). The single-particle Hamiltonian is then [124]:

$$\mathcal{H}_{\text{EMA}} = \sum_{i=x,y,z} \frac{-\hbar^2}{2m_i} \frac{\partial^2}{\partial (r_i)^2} + U(\mathbf{r}) + \mu_{\text{B}} \vec{S} \cdot \hat{g} \cdot \vec{B}, \tag{1.5}$$

where m_i are the effective masses, $\mathbf{r} = (r_x, r_y, r_z) = (x, y, z)$ is the position vector, $U(\mathbf{r})$ is a spatially slowly varying potential (compared to the lattice period). Such potential considers the electrostatic potential shaped by the QD gate's voltages. The Zeeman term with an effective g-tensor $\hat{g}$ arises from spin-orbit interaction [125]. In bulk GaAs free electrons fill the isotropic Γ ($\mathbf{k} = 0_v$) conduction band minimum [Fig. 1.2](b) and in the EMA their effective mass $m^* \approx 0.067\, m_0$, where m_0 is the bare electron mass. On the other hand, bulk silicon [Fig. 1.2(c)] has six-fold degenerate conduction band minima at **X**. Each valley has an anisotropic effective mass of about $0.92\, m_0$ and $0.19\, m_0$ along the longitudinal and transverse directions, respectively. The heterostructure and electrostatic confinement break the six-fold valley degeneracy in Si devices, inducing valley splitting [126]. However, in many cases, the atomic disorder can reduce the energy splitting between the lowest valley states, until it becomes comparable to the thermal energy, hindering qubit operation.

Because of its free electrons' relatively small effective mass, the first spin qubit devices were realized in GaAs in 2005 [47]. Small effective mass means QDs can be bigger, thus relaxing fabrication constraints. Also, GaAs has advantageous electronic properties including single conduction band valley, stable dopants, and decades of improvements in the growth of III–V heterostructures by molecular beam epitaxy, yielding high-quality substrates [127]. Though, group III–V have nuclear isotopes that cause poor dephasing times of tens of nanoseconds by hyperfine interaction. Therefore research has focused more on group IV semiconductors such as Si (and Ge), which have smaller percentages of spinful nuclei isotopes and can be isotopically purified, leading to longer

coherence times [45]. However, devices in Si and Ge are more challenging to fabricate because of their larger effective mass than GaAs; thus, they require smaller (and multi-layer) gates to better control the electrons. The more complex fabrication process explains why the first singlet-triplet qubit in Si was demonstrated seven years later than GaAs, in 2012 [112].

The trend to move to Si, and more recently Ge, is promising, but so far it is not scientifically established that group IV is better overall. While a recurrent claimed advantage of Si is its compatibility with complementary metal-oxide-semiconductor (CMOS) foundry fabrication, Si spin qubits require small feature sizes and different layouts compared to classical transistors [127]. Different layouts cause large development costs for the industry. GaAs-based devices remain a leading platform for proof-of-concept quantum information processing and solid-state experiments [29].

1.3 Bandstructure engineering and spin-qubit devices

In heterostructures, single electrons are confined in the growth (out-of-plane) direction by the conduction band offsets at the semiconductor interfaces [123]. In this Thesis measurements from two devices are reported: one device is a depletion-mode GaAs/AlGaAs device fabricated in an academic cleanroom, and the other is an accumulation mode n-type Si metal-oxide-semiconductor (SiMOS). The SiMOS is foundry-fabricated in a 300 mm process, using CMOS-compatible process steps by IMEC [129, 130, 131].

GaAs/AlGaAs depletion mode A two-dimensional electron gas (2DEG) can be hosted in devices defined by Schottky-gated GaAs/AlGaAs heterostructures. Indeed, a 2DEG is formed in the GaAs layer interface with AlGaAs because of the lower conduction band edge of the GaAs layer, see Fig. 1.3(a). The confinement potential is triangular to a good approximation [123]. In general Si atoms are used to dope the AlGaAs layer next to the GaAs one [132]. In the so-called “remote doping" technique the implantation is performed in the AlGaAs layer, whereas the 2DEG is accumulated in the GaAs layer, which has not been implanted. This technique provides fewer defects in the GaAs layer and, thus, higher mobility. A 2DEG can also be formed by sandwiching a thin GaAs layer between two AlGaAs ones, and in general, the 2DEG occupies the whole 2D interface. Ohmic contacts are required to make electrical contact with the 2DEG. The ohmics are contacts where by definition the $I-V$ curve is linear. In (a), below $O_{L(R)}$, the ohmic contacts are depicted by the spikes of Ge, Au, and Pt extending through the AlGaAs, after annealing at high temperature ($\approx 450°$). Without any voltages applied to the gates, if one were to set a voltage bias V between O_L and O_R, the measured current I across the two terminals would be linear and symmetric around zero applied voltage. Once the 2DEG is present, it is then possible to form QDs by applying voltages to the metal gate electrodes on top of the heterostructure [see Fig. 1.3(a)].

In GaAs the gates are in general obtained by depositing metals on the heterostructure surface. The Schottky barrier, which forms at the interface between the semiconductor surface and the metal, can deplete the electrons below, by applying negative voltages. On the other hand, applying a positive voltage to the gates to accumulate electrons beneath may cause leakage current from the donor layer to the gates [133, 134]. Charge carriers tunneling from the donor layer would then cause charge noise and make device tuning more time-consuming. A solution proposed by Refs. [133, 134] to stabilize the device is to apply a positive bias (up to ≈ 200 mV) during the cool-down, also knows as “bias cooling".

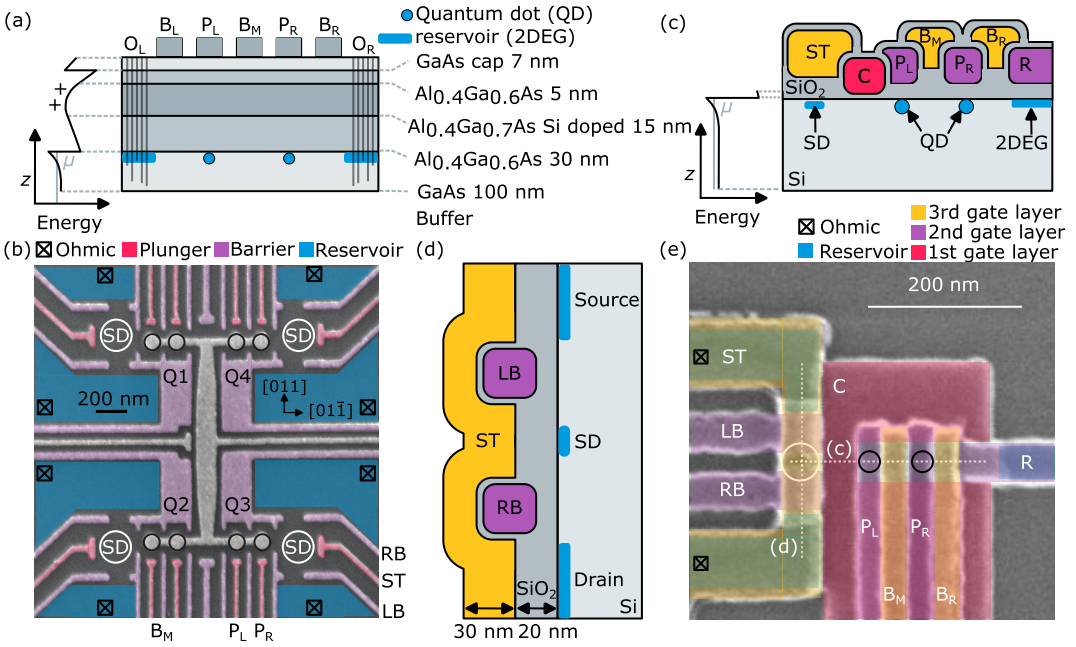

Fig. 1.3: **Depletion mode GaAs/AlGaAs and accumulation mode SiMOS. (a)** Depletion mode device GaAs/AlGaAs heterostructure, whose two-dimensional electron gas (2DEG) resides at the interface of the GaAs bulk with the AlGaAs layer. On the left, $E(z)$ describes the vertical confinement and μ the chemical potential. Ohmics $O_{L/R}$ make electrical connections from the surface to the 2DEG. Gates control the potential landscape and the lateral confinement in the xy-plane: plunger gates $P_{L/R}$ control the chemical potentials of the dots underneath, barrier gates control either the coupling to the reservoir ($B_{L/R}$) or the interdot tunnel coupling (B_M). **(b)** SEM image of FF1B device from [36]. The 2DEG is localized 57 nm below the surface and the GaAs cap is covered with 10 nm of HfO_2. See main text for description. One gate layer is present. Each of the four DQD (black circles) encodes a singlet-triplet qubit with a sensor dot (SD, white circles) next to it for charge sensing. **(c-d-e)** SEM image of foundry-fabricated SiMOS device with overlapping gate architectures, and relative cross sections along the double-quantum dot (c) and the single-electron transistor (or sensor dot) (d). Three gate layers in total. Ohmic contacts to the reservoir implantation region are not shown. SEM from Ref. [128] © [2023] IEEE.

The voltages applied to the gates shape the electrostatic potential $U(\vec{r})$ in Eq. (1.5), and confinement along both in-plane directions can form QDs with single-electron occupancy at the potential minima. In (a), two electrons are below the so-called "plunger gates" P_L and P_R. The plunger gates tune the QDs electrochemical potentials and the shape of the confining potential. The voltage applied to the barrier gate B_M controls the barrier height between the two electrons of the DQD depicted in (a), and therefore the tunnel coupling t_c between the two QDs, or equivalently the energy split between the bonding and antibonding orbitals formed by the DQD. The barrier gates B_L and B_R control the coupling of the electron(s) in the QDs to the reservoir nearby. In theory, plunger gates should control only the electrochemical potential of the QD underneath, and the barriers only the tunneling rates. In real systems, there are cross-capacitance terms [54] that can be compensated for by "virtualizing" the gates [135], which amounts to using properly defined linear combinations of gate voltages.

Device In Fig. 1.3(b), it is shown a top view scanning electron micrograph (SEM) image of the GaAs device FF1B [36], fabricated at the Niels Bohr Institute. There are in total four DQDs in the device, where a black circle represents each QD. A DQD defines a singlet-triplet qubit, which was briefly introduced before. The white circles represent the sensor dots used to charge sense the nearby qubit (see later Sec. 1.4 for charge sensing readout). The light blue area indicates where the 2DEG approximately lies in the GaAs layer when the qubits are tuned. In purple, the barrier gates confine the quantum dots from the reservoirs, whose chemical potential is set by the overall eight ohmics [4]. In red, each plunger gate controls the chemical potential of the dot underneath. The elongated dot at the center controls a multi-electron dot designed initially to couple the qubits among each other. Instructions on how to tune the device are contained in Ref. [136].

In FF1B the surface of the heterostructure has been covered by a 10 nm layer of HfO_2 [not shown in panel (a)] before the metallic gates deposition. The oxide layer is expected to provide quiet and stable devices without requiring the bias cooling mentioned above [137]. The advantage of the oxide layer is that we can apply both positive (on the order of ≈ 100 mV) and negative voltages to the gates without worrying about leakage current. Then, we can both deplete or accumulate electrons underneath the gates. The quantum dots are below a shared accumulation gate that spans all four DQD, and in FF1B we usually set it to about 50 mV.

In terms of design choices, it is known the heterostructure has a density of electrons $\approx 2.4 \cdot 10^{15}\text{m}^{-2}$. Thus one electron corresponds to the area of a circular dot with a radius of 10 nm. The gates are designed to surround the area of a circle of about 100 nm diameter. Secondly, the 2DEG should be closed enough to the metallic gates such that the electrostatic gating dominates $U(\mathbf{r})$ [Eq. 1.5] over the random and intrinsic potential variations, related to inhomogeneities ("disorder") of the heterostructure. At the same time, the 2DEG should not be too close to the gates, to avoid charge noise from the donor layer and to have higher mobility for better device tunability. As a rule of thumb, the 2DEG depth should not exceed 100 nm given a QD diameter of 50 nm. These devices typically show mobilities of $2\text{–}2.5 \cdot 10^6 \text{cm}^2\,\text{V}^{-1}\,\text{s}^{-1}$.

SiMOS accumulation mode At IMEC the SiMOS spin qubit devices are linear qubit arrays with multi-level gate stack. The set of gates consists of alternating plunger and barrier finger gates. The 2DEG is formed at the Si/SiO_2 interface, on the Si side, and the devices strongly resemble classical

[4] While checking whether one ohmic works, it is possible to float the others. But while tuning, all ohmics should always have a well-defined potential to confine the 2DEG.

transistors from the CMOS (complementary MOS) industry, see cross-sections in Fig. 1.3(c-d). Again, the electrons are confined in an approximately triangular potential as a result of the gate-induced electric fields across the oxide. As the used oxides have a large band gap, such out-of-plane electric fields can be high. It is important to notice for the SiMOS device in (c) how, differently from a depletion mode device such as GaAs, at zero voltage applied to the gates, no charge is accumulated at the interface (therefore the "accumulation mode" name). Instead of applying negative voltages to the gate electrodes, to form QDs positive voltages are applied to P_L and P_R. The SEM image of the n-type SiMOS device is shown in (e). The horizontal cross-section, panel (c), shows the three gate layers designed to control a double quantum dot. In the first layer there is the confinement (or screening) gate C, whose purpose is to screen the plunger gates $P_{L(R)}$ and the barrier gates $B_{M(R)}$, such that the quantum dots are confined under an area comparable with the gates length. The target length of the sensor gates, and of the LB-RB space, is usually around 50 nm [130] to satisfy the condition $k_B T \ll E_C$, where E_C is the charging energy (described in next section) for seeing Coulomb oscillations. Comparing the 200 nm scale bars in (a) and (e), the gates are much finer in Si because of its higher effective mass. Thus Si requires tighter confinement, as mentioned previously. The reservoir gate R accumulates electrons close to the right QD, with a tunneling rate set by B_R. As in the GaAs device, B_M sets the interdot tunnel coupling t_c between the two QDs. The sensor dot under ST [see panel (d)] is used to discriminate the charge occupancy in the nearby DQD by charge sensing. The sensor dot is capacitively coupled to the DQD, but in general not tunnel coupled (depending on the voltage applied to C, typically grounded at the beginning of the tuning). In panel (d), the cross-section along the single-electron transistor (SET) or sensor dot (SD) is depicted, where the ST gate accumulates the charge coming from the heavily n-doped source (S) and drain (D) region far from the device [not visible in panel (c)]. The barrier gates LB and RB set the tunnel coupling to the reservoirs.

The first batch of received devices had atomic layer deposited (ALD) TiN gates and ALD silicon oxides. The motivation for choosing TiN is to have fewer strain-induced defects in the devices compared to Al and Pd [130]. Regarding the oxide, high-k materials might have more defective effects than silicon oxide. At a later stage, the TiN gates have been replaced by polysilicon gates, as charge sensors have shown lower disorder and lower required biases to tune to their operation regime [138].

Tuning heuristics To tune a single dot under P_L, after having tuned the SET, the fast way is to set the voltages $V_R = V_{BR} = V_{PR} = [2,3]$ V, with $V_C = 0$ V (grounded). [We use the convention V_X is the voltage applied to the gate X.] Then P_L is swept in the range $[0.5,1]$ V, while its interdot barrier voltage $V_{BM} = [0,0.5]$ V. It is even faster to tune the SET while the other gates are set to the values above. If one were to tune the device from scratch, standard values are again $V_R = V_{BR} = V_{PR} = [2,3]$ V. This time, V_{PL} is set to a value such that there are electrons below. The value can be guessed starting from the SET barrier threshold (after the SET is tuned). The value for V_{PL} should be slightly higher because of the confinement gate C nearby. Then one may sweep V_C and V_{BM}. The confinement gate V_C can be swept within a narrow range (e.g. $[-100,100]$ mV), as it is in the 1st layer. The interdot barrier B_M can have a larger range. However, if its applied voltage is too low, there would be no tunneling from the reservoir. If V_{BM} is set too high, the broadening would not allow the formation of a single dot.

To tune a DQD beneath P_L and P_R, the fast way is to set $V_R = [2,3]$ V, $V_{BM} = 1$ V and $V_{BR} = 2$ V. Then, one sweeps V_{PL} and V_{PR} around 1 V. The alternative way is to tune a single dot under V_{PL},

and then tune a second dot by sweeping V_{PR} and V_{BM}. These tuning procedures are guidelines, a device may require different settings because of design or local disorder variability.

1.4 Spin-to-charge conversion

At the beginning of this Chapter, it has been highlighted that spin qubits have long coherence times because in principle they directly couple to magnetic fluctuations instead of electrical ones. On the other hand, measuring the spin of a single electron is harder than measuring its charge. One can correlate spin and charge degrees of freedom to solve this issue using spin-to-charge conversion protocols. Then we can map different charge configurations in a DQD to different spin states, e.g. $(1,1) \rightarrow |\mathrm{T}\rangle$ and $(0,2) \rightarrow |\mathrm{S}\rangle$. Here $(1,1)$ means one electron is in each QD, whereas $(0,2)$ means both electrons are in the right QD.

The previous sections presented how band structure and electrostatic confinements make it possible to trap single electrons in QDs. However, electron-electron Coulomb interaction is important as electrons are added to the system. The charging energy $E_C = e^2/C$, where C is the total dot capacitance. The charging energy models the classical repulsion energy of the electrons in the QD, that electrostatically repulse any other electron that could be added to the dot. Coulomb blockade is a consequence of this Coulomb repulsion: in Coulomb blockade, the electron occupation is fixed, and no current can flow across the QD [53, 139]. As E_C is in the order of a $\approx 1\,\mathrm{meV}$, Coulomb blockade can be measured only if the thermal excitation in the system $k_B T \approx 86\,\mu\mathrm{eV K}^{-1} \ll E_C$, thus around 10–100 mK of operation, reachable in cryogenic dilution refrigerators (Chapter 2). Another condition to observe Coulomb blockade is that the tunneling resistance should be greater than $h/e^2 \approx 25.8\,\mathrm{k\Omega}$ [123], derived from Heisenberg's uncertainty principle.

Because of quantum confinement, the total energy required to add an electron is different from the charging energy E_C, and it is called the addition energy E_{add}, which is related to the orbital energy E_{orb}. The orbital energy is the change in single-particle energy when another electron must occupy a new orbital level due to the Pauli exclusion principle, which prohibits two electrons from being in the same single energy level (neglecting spin at the moment). Within the constant interaction model [54], the addition energy is then given by $E_{add} = E_C + E_{orb}$.

In the next paragraph, we consider only the charge degree of freedom. At a later stage, we consider the spin degree of freedom and the presence of externally applied magnetic fields.

Charge degree of freedom

We consider a double well potential illustrated in Fig. 1.4(a). Each well represents a dot with a chemical potential $\mu_{L(R)}$. Electrons come from nearby reservoirs (not shown), which have chemical potential μ_F. The applied plunger gates voltages $V_{PL(PR)}$ control the chemical potentials $\mu_{L(R)}$. The difference in the chemical potentials defines the electrical detuning $\varepsilon = \mu_L - \mu_R$ of the double quantum dot. The tunnel coupling t_c sets the hopping rate between the two charge configurations, and it is controlled by the interdot barrier gate V_{BM}. Figure 1.4(b) shows a DQD charge stability diagram as a function of ε and the mean energy $E = (\mu_L + \mu_R)/2$ [123], where each ground state charge configuration is labeled as (N_1, N_2). Here N_i is the number of electrons in the i-th QD. The vertical lines represent interdot transitions where one electron is exchanged from one dot to the other. The diagonal lines represent electron exchanges with the left and right reservoirs. Focusing on $N_1 + N_2 = 1$, namely a DQD with one electron, the charge configurations (1,0) and (0,1) can

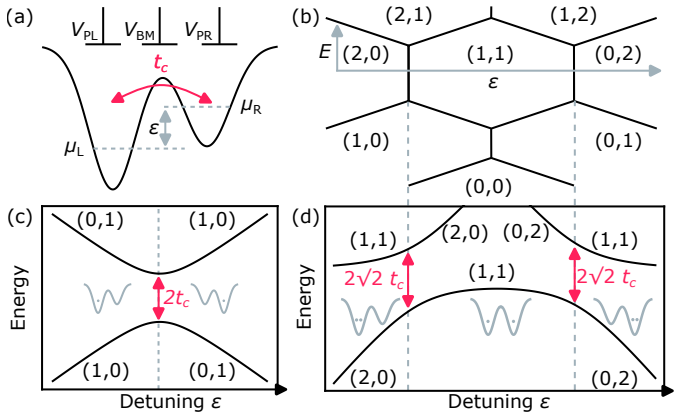

Fig. 1.4: **Charge stability map and energy levels of a double quantum dot. (a)** Sketch of a double well potential defining a DQD. The left (right) dot chemical potential μ_L (μ_R) is controlled by the plunger gate voltage V_{PL} (V_{PR}). The interdot barrier gate V_{BM} controls the tunnel coupling t_c between the two dots. The electrical detuning $\varepsilon \equiv \mu_L - \mu_R$. **(b)** Charge stability map as a function of the electrical detuning ε and the mean energy E. While the detuning ε defines the tilt in the potential between the two dots, E sets the total number of charges. **(c)** Energy levels of one electron in a DQD as a function of ε across the $(1,0)-(0,1)$ charge transition. At low detuning, the diabatic $(1,0)$ state is the system's ground state. After anticrossing with the $(0,1)$ state at higher detuning, the latter becomes the ground state and the $(1,0)$ is the excited state. The splitting at the anticrossing is given by $2t_c$. **(d)** Energy level diagram of two electrons state across the $(2,0)-(1,1)-(0,2)$ transition. The total number of electrons does not change; what changes is the polarization of the DQD with either two electrons in the same dot or on separate dots. The energy splitting between the $(1,1)$ and $(0,2)$ or $(2,0)$ energy levels is proportional to t_c.

approximate the DQD as a two-level system, whose Hamiltonian is:

$$\mathcal{H}_c = \begin{pmatrix} \varepsilon/2 & t_c \\ t_c & -\varepsilon/2 \end{pmatrix}. \tag{1.6}$$

Here the tunnel coupling t_c is in principle an exponential function of the interdot barrier height (controlled by V_{BM}), whereas ε is controlled by a linear combination of the plunger voltages $V_{PL(PR)}$. Figure 1.4(c) shows how the ground state changes between (1,0) and (0,1) depending on ε. Close to $\varepsilon = 0$, antibonding and bonding combinations of the (diabatic) charge states hybridize. The hybridization strength is set by the tunnel coupling t_c.

We focus now on the case where $N_1 + N_2 = 2$, i.e. a two-electron DQD, the (2,0), (1,1), and (0,2) charge states are allowed. Due to Coulomb repulsion, the (2,0) or (0,2) charge states are the ground state only if ε is highly biased ($|\varepsilon| \gg t_c$), see Fig. 1.4(d). Also in this case t_c provides the energy splitting at the anticrossings by a factor $2\sqrt{2}t_c$ [54]. The (2,0) or (0,2) charge states are relevant for spin qubit control, in particular for the initialization of the singlet state $|S\rangle$.

Kinetic exchange in the Fermi-Hubbard hopping model

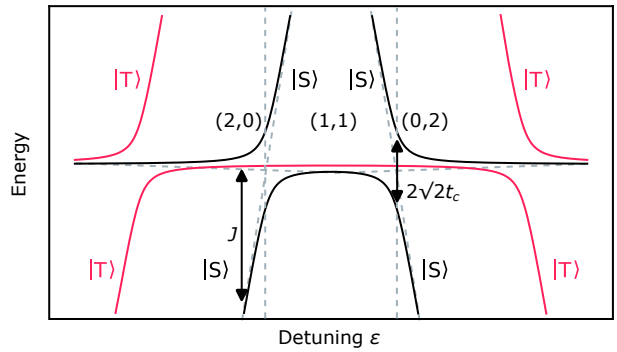

Fig. 1.5: **Energy level diagram of two-electron singlet and triplet states in a DQD.** Energy level diagram of a DQD [cf. Fig. 1.4(d)] including the singlet (black) and triplet (red) states, in the absence of an externally applied magnetic field. When two electrons are in the same dot, the singlet $|\mathrm{S}\rangle$ is the ground state, while the triplet states $|\mathrm{T}\rangle$ are high in energy. In the $(1,1)$ regime, $|\mathrm{S}\rangle$ is still the ground state but with a relatively smaller separation from $|\mathrm{T}\rangle$, as electrons reside in different dots. The tunnel coupling t_c leads to level anticrossing between the singlet states where the on-site Coulomb energy U equals $|\varepsilon|$ (vertical dashed lines).

In this section we use the Fermi-Hubbard model to describe the kinetic exchange J, fundamental for spin qubit operation (see Appendix B for details on the derivation of J). The first assumption is that electrons are tightly bound to their single-electron ground state orbitals $\phi_j(\vec{r})$ in dot j, with $j = 1, 2$. The QD-to-QD Coulomb and direct exchange interactions are assumed to be negligible. What remains is the on-site Coulomb interaction with strength U. A constant tunnel coupling t_c describes the antidiagonal elements of the kinetic energy transition matrix T_{jk} such that $t_c = T_{12}$ for sites 1 and 2 (t_c is assumed to be real). The diagonal elements ($j = k$) correspond to the chemical potential μ_j on each dot j, and they can be controlled by voltages applied to the plunger gates. Focusing on two electrons populating the two sites $j = 1, 2$, in the absence of magnetic field, it is obtained [51]:

$$\mathcal{H}_{\mathrm{FH}} = \sum_{\sigma=\uparrow,\downarrow} \Big[\sum_{j=1,2} \mu_j c^\dagger_{j\sigma} c_{j\sigma} + t_c (c^\dagger_{1\sigma} c_{2\sigma} + c^\dagger_{2\sigma} c_{1\sigma}) \Big] + \sum_{j=1,2} U c^\dagger_{j\uparrow} c_{j\uparrow} c^\dagger_{j\downarrow} c_{j\downarrow}. \tag{1.7}$$

Here we have defined the anticommuting annihilation (creation) operator $c_{j\sigma}$ ($c^\dagger_{j\sigma}$) which annihilates (adds) an electron in the orbital state $\phi_j(\vec{r})$ and spin state σ. It is convenient to write down the states defined by charge and spin configurations to introduce the charge-to-spin protocol later. We rewrite the Hamiltonian in Eq. (1.7). Because of the exclusion principle, the $(2,0)$ and $(0,2)$ states allow only one spin up and one spin down electron (singlet state). (The triplet states are high in energy and neglected). Instead, the $(1,1)$ state allows four possible states, one spin-singlet state, and three spin-triplet states. The detuning $\varepsilon \equiv \mu_{\mathrm{L}} - \mu_{\mathrm{R}}$ and the zero-energy is defined as $\mu_{\mathrm{L}} + \mu_{\mathrm{R}} \equiv 0$. The rewritten Hamiltonian is then:

$$H = (U-\varepsilon)\,|\mathrm{S}(0,2)\rangle\langle\mathrm{S}(0,2)| + (U+\varepsilon)\,|\mathrm{S}(2,0)\rangle\langle\mathrm{S}(2,0)| \\ + \sqrt{2}t_c\,(|\mathrm{S}(2,0)\rangle\langle\mathrm{S}(1,1)| + |\mathrm{S}(0,2)\rangle\langle\mathrm{S}(1,1)| + \mathrm{h.c.})\,, \tag{1.8}$$

where all triplet states are at zero energy and S labels singlet states. Solving the Hamiltonian yields, for $|t_c| \ll U \pm \varepsilon$ and $|\varepsilon| < U$, the eigenstate

$$|S\rangle \simeq |\mathrm{S}(1,1)\rangle - \frac{\sqrt{2}t_c}{U-\varepsilon}|\mathrm{S}(0,2)\rangle - \frac{\sqrt{2}t_c}{U+\varepsilon}|\mathrm{S}(2,0)\rangle, \tag{1.9}$$

with error terms given by $t_c^2/(U\pm\varepsilon)^2$, and kinetic exchange energy (or exchange coupling) $-J$ given by

$$J = \frac{4Ut_c^2}{U^2-\varepsilon^2} + O\left(\frac{t_c^3}{(U\pm\varepsilon)^3}\right). \tag{1.10}$$

The kinetic exchange interaction is indeed due to the virtual hopping between the two sites. The hopping lowers the energy of the lowest singlet state by J, relative to the triplet state energy. Higher energy states that are singlets exist, but are about $U \pm \varepsilon$ away. Similarly, we know that excited (2,0) and (0,2) triplets also have higher energies. Restricting ourselves to the low-energy states, the Hamiltonian of the $(1,1)$ charge configuration is given by

$$\mathcal{H} = -J|S\rangle\langle S| = \frac{J}{2}\left(S^2-2\right) = J\vec{S}_i\cdot\vec{S}_j + \text{const.}, \tag{1.11}$$

as the total spin of sites i and j is $\vec{S} = \vec{S}_i + \vec{S}_j$, yielding the Heisenberg exchange formula, minus an offset in energy.

The result of this section is visually summarized in Fig. 1.5, where the energy spectrum of a double quantum dot as a function of detuning is plotted considering the spin states (without applied magnetic field). Considering the singlet states $|\mathrm{S}\rangle$, the (2,0) [(0,2)] charge configuration is the ground state for $\varepsilon < -U$ [$\varepsilon > U$]. In between, the (1,1) is the ground state, close in energy with the triplet states as the electrons reside in different QDs. The triplet states of (0,2) and (2,0), missing in the previous Hamiltonian, are here plotted and they hybridize with the triplet state of (1,1). The triplet states (0,2) and (2,0) limit the available readout window in ε of PSB.

Charge sensing and Pauli spin blockade readout

In the previous sections, charge states have been related to spin states. In what follows, charge sensing techniques are described to measure the number of electrons in a DQD and for single-shot readout by Pauli spin blockade (PSB).

If next to a DQD another QD is placed, the latter can be used to charge sense the number of electrons in the DQD [140]. The QD used for sensing is often referred to as “sensor dot" (SD) or “single-electron transistor" (SET). To explain how charge sensing works, as an example it is shown in Fig. 1.6(a) a schematic of the SiMOS device already presented in Fig. 1.3. As described before, the DQD is formed by applying positive voltages to the gates $\mathrm{P_L}$ and $\mathrm{P_R}$, while C is grounded, $\mathrm{B_M}$ controls the interdot barrier, $\mathrm{B_R}$ tunes the coupling between the DQD and its electron reservoir on the right. The electron reservoir is indeed provided by a positive voltage applied to gate R, which accumulates electrons from a third ohmic (not shown). To measure the number of electrons under

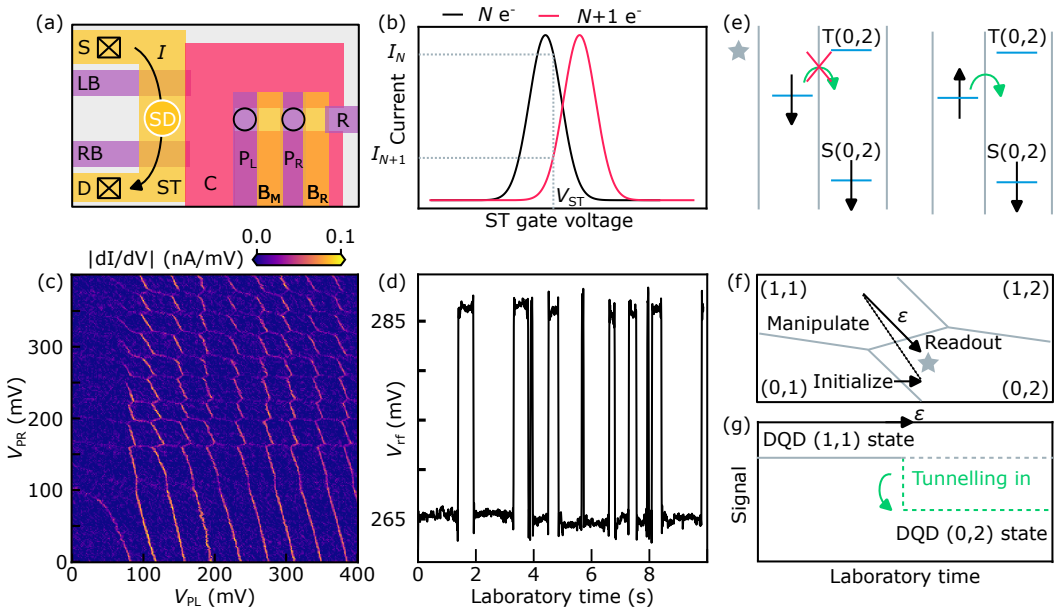

Fig. 1.6: **Charge sensing and spin-to-charge conversion by Pauli spin blockade.** **(a)** Schematic of the SiMOS device shown in Fig. 1.3(e). Black circles are the QDs charge-sensed by the sensor dot (white circle). **(b)** Sketch of measured current by sweeping the plunger gate voltage V_{ST} of the sensor dot, with different numbers of electrons in the dot P_L. **(c)** Charge stability map of the SiMOS device as a function of the double quantum dot voltages V_{PL} and V_{PR} applied to the respective gates. **(d)** Homodyne voltage from radio-frequency reflectometry signal showing an electron jumping in and out of the quantum dot defined under P_L. **(e)** Schematic of spin readout by Pauli spin blockade (PSB) near the $(1,1)-(0,2)$ charge transition [star in panel (f)]. From the (1,1) charge configuration (one electron in each dot), a triplet state remains stuck in the $(1,1)$ charge state because the $T(0,2)$ level is high in energy (and tunneling is assumed to be spin preserving). Instead, the $S(0,2)$ is lower in energy, allowing the electron to tunnel. **(f)** Sketch of a charge stability diagram close to the $(1,1)$–$(0,2)$ interdot transition. The singlet state in $(0,2)$ is initialized by electron exchange with the reservoir going from $(0,1)$ to $(0,2)$. Deep in the $(1,1)$ charge region, qubit manipulation occurs, and it is measured in $(0,2)$. **(g)** Sketch as a function of laboratory time how the signal changes while sweeping the detuning ε, from the $(1,1)$ to $(0,2)$ charge configuration. If the two electrons are in the triplet state, the sensor dot charge senses the $(1,1)$ state (gray dashed line) until relaxation. Otherwise a singlet state results in the electron tunneling from $(1,1)$ to $(0,2)$ (green dashed line).

P_L and P_R, the SD is placed on the left of the DQD, to which it is capacitively coupled. The SD is formed by applying a positive voltage to the top gate ST, and by tuning the tunnel coupling to the reservoirs, by the barrier gates LB and RB. The charge carriers are provided by ohmic contacts (source and drain) represented by the black squares.

Between the two ohmic contacts, a current I flows upon applied bias between the source and drain. In Fig. 1.6(b), it is illustrated a sketch of the measured current across the sensor dot, as a function of the applied sensor dot plunger gate ST voltage. The current shows a Coulomb peak when N electrons reside under the left dot P_L. If no electrons were to tunnel under the left dot while sweeping the gate, the curve would look similar to the black one. Due to a cross-capacitance effect, at a specific voltage of V_{ST}, an electron jumps into the left dot, which is capacitively coupled to the sensor dot. The capacitive coupling causes a shift in the Coulomb peak position (red curve), because the sensor dot chemical potential is affected by the nearby electrostatic potential modulated by both the gates and the electrons occupying the nearby dots. By tuning the sensor at a particular gate voltage V_{ST}, a current signal I_N (I_{N+1}) would correspond to N ($N+1$) electrons under the left dot[5].

The charge stability map of the DQD as a function of the plunger gates P_L and P_R is shown in panel (c). The IMEC device's identifier is AL00126614 D21 D1SD5 2 5. The signal is the norm of the gradient of the measured current with respect to the applied voltages to the gates, and the characteristic honeycomb pattern [54] appears in the top right corner. The almost diagonal lines represent the interdot transitions where one electron is exchanged from one dot to the other. Towards higher voltages, the horizontal (vertical) [to some extent] lines represent electrons accumulated into the QD defined by P_R (P_L) from the nearby reservoirs (presumably P_L receives electrons from the SD, to which it is sufficiently tunnel coupled). In the few-electron regime (bottom left corner), unintentional or not-well-defined dots manifest by charging lines with different slopes than the ones in the top right corner.

One can tune the device at one of the transitions between the right dot and the reservoir to investigate the dynamics of one electron tunneling in and out of the QD. Then it is possible to measure as a function of laboratory time, tunneling events of an electron from the dot to the reservoir and vice versa, as shown in Fig. 1.6(d). A high (low) signal corresponds to $N+1$ (N) electrons under the right dot. The frequency of the jumps depends on the tunneling rate between the right dot and its reservoir, as well as how far the DQD is tuned away from the transition with the reservoir.

We now overview Pauli spin blockade (PSB), a fundamental tool to readout many types of spin qubits and which has been observed in planar GaAs DQDs for the first time in Ref. [141]. An electron singlet pair can be initialized in the same QD in the charge configuration (0,2) [or (2,0)] by electron tunneling between the same QD and the nearby reservoir [47, 142]. Upon initialization, the two electrons can be separated in two different QDs by, e.g. decreasing the electrical detuning ε starting from (0,2) [cf. Fig. 1.5], before being manipulated in the (1,1) charge configuration.

The PSB measurement is performed by stepping ε to, e.g., a high value for readout in (0,2) [cf. Fig. 1.5], namely $|\varepsilon| \gg U$. Figure 1.6(e) shows the spin-to-charge PSB readout technique. Within the readout window, the T(0,2) energy levels are much higher than the singlet state. Therefore after qubit manipulation in (1,1), a triplet state T(1,1) is not energetically allowed to tunnel into the T(0,2) state once ε is stepped. Also, T(1,1) is not allowed to tunnel into the S(0,2) charge configuration as

[5] Notice if one were to sit at the crossing between the red and black curve, the sensor dot would be insensitive to the $N \leftrightarrow N+1$ transition.

electron tunneling prevents spin flips (in the absence of spin-orbit interaction). Whereas, a singlet S(1,1) is allowed to tunnel in S(0,2). The measured signal (see Fig. 1.6(g)) would then be (1,1) for an initial triplet state, and (0,2) for a singlet state. The different charges configuration (1,1)–(0,2) are readout by the nearby SD, and high-fidelity readout has been pioneered by using radio-frequency (RF) reflectometry techniques [143, 144, 119, 120]. Such techniques will be presented in the next Chapter 2.

1.5 Singlet-triplet qubits in GaAs

An electron in a semiconductor couples to the nuclei by hyperfine interaction. The main disadvantage of singlet-triplet qubits in GaA is that fluctuating hyperfine fields limit the dephasing time to $T_2^* \approx 10\,\text{ns}$ [47]. In the following, we summarize the main results of Ref. [111] to obtain the Hamiltonian of a singlet-triplet qubit in GaAs and to explain how we manipulate it.

Electron spin Hamiltonian for a single quantum dot The Fermi contact interaction Hamiltonian between an electron with spin operator $\vec{S}$, interacting with the lattice nuclei of species β in unit cells j carrying spin $\hat{\vec{I}}^{\beta,j}$, is given by

$$\mathcal{H}_{\text{FC}} = \hbar\gamma_e \sum_{\beta,j} b_\beta \alpha_{j,\beta} \hat{\vec{S}} \cdot \hat{\vec{I}}^{\beta,j}, \tag{1.12}$$

where the gyromagnetic ratio for the electron spin $\hat{\vec{S}}$ is $\gamma_e = g^* \mu_B/\hbar$, the sums are over nuclear species β and unit cells j. The effective hyperfine field due to species β is described by b_β, with $b_{^{75}\text{As}} = -1.84$ T, $b_{^{69}\text{Ga}} = -1.52$ T, and $b_{^{71}\text{Ga}} = -1.95$ T [145]. The probability of the electron being at unit cell j is $\alpha_{j,\beta} = v_0 |\psi(\vec{r}_{j,\beta})|^2$, where v_0 is the volume of the unit cell (containing two nuclei) and $\psi(\vec{r})$ is the envelope wavefunction of the localized electron.

After adding an external magnetic field, which contributes to the Hamiltonian by a Zeeman term $\hbar\gamma_e \vec{B}_{\text{ext}} \cdot \hat{\vec{S}}$, the total Hamiltonian can be rewritten as an electron spin that interacts with an external magnetic field $\vec{B}_{\text{ext}}$ and a field $\hat{\vec{B}}_{\text{nuc}}$ such that

$$\mathcal{H}_{\text{eff}} = \hbar\gamma_e (\vec{B}_{\text{ext}} + \hat{\vec{B}}_{\text{nuc}}) \cdot \hat{\vec{S}}\,. \tag{1.13}$$

The nuclear field value is maximum when all spins are fully polarized with value $I = 3/2$. This corresponds to $h_0 = \sum_\beta b_\beta x_\beta I^\beta \sum_k \alpha_k$, where the relative contributions of nuclear species have been separated: $x_{^{75}As} = 1$, $x_{^{69}Ga} = 0.6$, and $x_{^{71}Ga} = 0.4$ for GaAs (removing the β dependence from the $\alpha_{k,\beta}$). It results in $b_0 \approx 5.3\,\text{T}$. Under the assumption that the N nuclear spins are described by a density matrix $\rho = \hat{1}/(2I+1)^N$ in the infinite temperature limit, the nuclear field has a root-mean-square (r.m.s.) strength

$$B_{\text{nuc}} = \sqrt{\langle |\hat{\vec{B}}_{\text{nuc}}|^2 \rangle / 3} = \sqrt{\sum_{\beta,k} b_\beta^2 \alpha_{k,\beta}^2 \langle |\hat{\vec{I}}^{\beta,k}|^2 \rangle / 3} \tag{1.14a}$$

$$= \sqrt{\left(\sum_\beta x_\beta b_\beta^2\right) I(I+1)\, v_0/3 \int d^3r\, |\psi(r)|^4} \tag{1.14b}$$

$$= h_1/\sqrt{N}, \tag{1.14c}$$

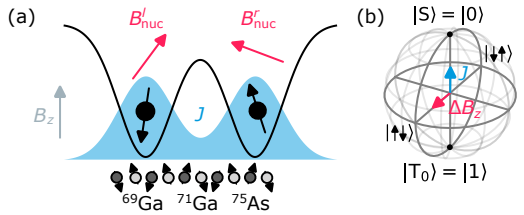

Fig. 1.7: **Singlet-triplet qubit in GaAs. (a)** Schematic of a DQD in the (1,1) configuration in GaAs, with externally applied magnetic field B_z. The exchange interaction J is given by the overlap of the two electrons' wavefunctions. The electrons interact with the spinful nuclei of the GaAs/AlGaAs heterostructure by hyperfine interaction. Thus, in the far-detuned regime in (1,1), the left (right) dot feels an effective field $B^{l(r)}_{\text{nuc}}$, on top of the applied magnetic field. **(b)** The $|S\rangle$ and $|T_0\rangle$ states define the ST_0 qubit. Exchange J drives qubit rotations around the Z axis of the Bloch sphere, whereas the Overhauser gradient $\Delta B_z = B^l_{\text{nuc},z} - B^r_{\text{nuc},z}$ drives rotations around the X axis.

where $\sum_j v_0$ has been replaced by $\int d^3r$. The strength factor h_1 for GaAs is

$$h_1 = \sqrt{2I(I+1)/3 \sum_\beta x_\beta b_\beta^2} = 4.0\,\text{T}, \tag{1.15}$$

as $N = 2/\left[\int d^3r\, |\psi(r)|^4 v_0\right]$ is the number of nuclei which largely overlap with the electron spin. The total interaction between the nuclei and the electrons also includes dipole-dipole interaction terms. Those terms are negligible for electrons in Si and GaAs compared to the Fermi contact one, but they are critical to determining how the nuclear spin path evolves in time [51]. As one one electron in a QD overlaps with many nuclear spins, the nuclei exert an effect "Overhauser" magnetic field on the electron. Because of nuclear dynamics, the Overhauser field fluctuates over time, causing spin qubit dephasing. It has been experimentally demonstrated that spin-orbit terms in the interaction dominate relaxation and dephasing on time scales of milliseconds [111]. In this work we focus on the nanoseconds to hundreds of nanoseconds scale, and we do not address spin-orbit terms.

The quasi-static approximation for nuclear spins

To describe the electron spin dynamics in the large N limit of the number of nuclei, in Eq. (1.13), the operator $\hat{\vec{B}}_{\text{nuc}}$ can be replaced by a random, classical vector $\vec{B}_{\text{nuc}}$. Therefore, it is possible to calculate the observables from the distribution of classical values. In the large N limit, the distribution becomes:

$$P(\vec{B}) = \frac{1}{(2\pi B^2_{\text{nuc}})^{3/2}} \exp\left(-(\vec{B}\cdot\vec{B})/2B^2_{\text{nuc}}\right), \tag{1.16}$$

which stems from the quasi-static approximation (QSA) [111]. At large external magnetic field along z, $\hat{S}_z$ is conserved, but the transverse spin components, e.g. $\hat{S}_y$, decay following

$$\langle \hat{S}_y \rangle_{\text{nuc}} = \frac{\hat{S}_y}{2}(1 + e^{-\frac{1}{2}(\gamma_e B_{\text{nuc}} t)^2}). \tag{1.17}$$

Thus, given an electron in a single QD i at a large magnetic field, the time-ensemble-averaged dephasing is given by

$$T_{2,i}^{*} = \frac{1}{\Omega_{\mathrm{nuc},i}} = \frac{1}{\gamma_e B_{\mathrm{nuc},i}}. \tag{1.18}$$

The QSA is a good approximation at low magnetic fields up to the single electron spin-nuclear spin interaction time $[O(\hbar N/A)]$, typically a few microseconds [111]. By the rotating wave approximation, terms that do not commute with the Zeeman term in the Hamiltonian can be eliminated, resulting in the effective Hamiltonian (here, the external magnetic field is along z):

$$\mathcal{H}_{\mathrm{eff}} = \hbar\gamma_e(B_{\mathrm{ext}} + B_{\mathrm{nuc}}^{z})\hat{S}_z\,. \tag{1.19}$$

In Fig. 1.7(a) we sketch the two electrons trapped in DQD, with a different local nuclear field for each dot, in the presence of an externally applied magnetic field B_z. In the following sections, we extend the results summarized so far to a DQD, which is the case of interest in our work.

Hyperfine interactions in a double quantum dot

To describe the hyperfine interaction in a DQD, we consider the case of two electrons in one of the two QDs, and one electron in each QD. As mentioned before in 1.4, the ground state of a doubly-occupied QD is a singlet $|(0,2)\mathrm{S}\rangle$, separated by its triplet state $|(0,2)\mathrm{T}\rangle$ by a large energy gap. The ground state of the system can be changed to separated electrons in the two QDs of the DQD by electrically controlling the detuning, where $\varepsilon = 0$ at the avoided crossing between (1,1) and (0,2) [dashed gray line on the right in Fig. 1.5]. Following Eq. (1.8), considering only charge coupling and restricting to the diabatic states $|(0,2)\mathrm{S}\rangle$ and $|\mathrm{S}\rangle$ in (1,1) that provides the zero energy reference, the Hamiltonian becomes:

$$\mathcal{H}_{11-02} = \begin{pmatrix} -\varepsilon & t_c \\ t_c & 0 \end{pmatrix}, \tag{1.20}$$

apart from a common shift in energy for the singlet states, and t_c is the (real) tunneling coefficient of the DQD.

In the case of a time-independent Hamiltonian, the eigenstates are

$$\left|\tilde{\mathrm{S}}\right\rangle = \cos\theta\,|\mathrm{S}\rangle + \sin\theta\,|(0,2)\mathrm{S}\rangle \tag{1.21a}$$

$$\left|\tilde{\mathrm{G}}\right\rangle = -\sin\theta\,|\mathrm{S}\rangle + \cos\theta\,|(0,2)\mathrm{S}\rangle\,. \tag{1.21b}$$

Here we follow the convention the tilde $\left|\tilde{X}\right\rangle$ describes an adiabatic state. For instance $\left|\tilde{\mathrm{S}}\right\rangle$ is the lower energy state, with adiabatic angle $\theta = \arctan\left(\frac{2t_c}{\varepsilon - \sqrt{4|t_c|^2+\varepsilon^2}}\right)$. The energies of the two states are

$$E_{\tilde{\mathrm{S}}} = -\frac{t_c}{2}\tan(\theta), \tag{1.22a}$$

$$E_{\tilde{\mathrm{G}}} = \frac{t_c}{2}\tan(\pi/2-\theta). \tag{1.22b}$$

For instance, the eigenstates of the system become $\left|\tilde{\mathrm{S}}\right\rangle \to |1,1)S\rangle$, $\left|\tilde{\mathrm{G}}\right\rangle \to |(0,2)\mathrm{S}\rangle$ if $\varepsilon \ll -|t_c|$, $\theta \to 0$. For $\varepsilon \gg |t_c|$, $\theta \to \pi/2$, and the eigenstates are switched, with $\left|\tilde{\mathrm{S}}\right\rangle \to |(0,2)\mathrm{S}\rangle$ and $\left|\tilde{\mathrm{G}}\right\rangle \to |1,1)S\rangle$.

Now we can add both spin couplings, the Zeeman interactions, and the hyperfine contact coupling, to the DQD mode. Two effective Hamiltonians are obtained for the case where $\varepsilon \ll -|t_c|$ and $\varepsilon \approx 0$, again following [111]. In the basis of the triplet and singlet states $|\mathrm{T}_m\rangle, |\tilde{\mathrm{S}}\rangle$, we can write the interactions of the spins in the far-detuned regime $\varepsilon \ll -|t_c|$ as

$$\mathcal{H}_{\mathrm{hf,tot}} = \mathcal{H}^l_{\mathrm{hf,eff}} + \mathcal{H}^r_{\mathrm{hf,eff}} - J(\varepsilon)\,|\mathrm{S}\rangle\langle S|\,, \tag{1.23}$$

being l and r the left and right QD, the nuclear fields are given by the single dot Hamiltonians (cf. Eq.1.19) and $J(\varepsilon) = -E_{\tilde{\mathrm{S}}}(\varepsilon)$. Substituting, one gets

$$\mathcal{H}_{\mathrm{hf,\,tot}} = \hbar\gamma_e[\vec{B}\cdot(\hat{\vec{S}}^l + \hat{\vec{S}}^r) + \Delta\vec{B}\cdot(\hat{\vec{S}}^l - \hat{\vec{S}}^r)] - J(\varepsilon)\,|\mathrm{S}\rangle\langle S|\,, \tag{1.24}$$

given the average field $\vec{B} = \vec{B}_{\mathrm{ext}} + \left(\vec{B}_{\mathrm{nuc,l}} + \vec{B}_{\mathrm{nuc,r}}\right)/2$ and difference field $\Delta\vec{B} = (\vec{B}_{\mathrm{nuc,l}} - \vec{B}_{\mathrm{nuc,r}})/2$. Then it is possible to write in matrix form Eq. (1.24) in the basis $\{|\mathrm{T}_+\rangle, |\mathrm{T}_0\rangle, |\mathrm{T}_-\rangle, |\mathrm{S}\rangle\}$

$$H = \hbar\gamma_e \begin{pmatrix} B_z & 0 & 0 & \frac{\Delta B_x - i\Delta B_y}{\sqrt{2}} \\ 0 & 0 & 0 & -\Delta B_z \\ 0 & 0 & -B_z & \frac{-\Delta B_x - i\Delta B_y}{\sqrt{2}} \\ \frac{\Delta B_x + i\Delta B_y}{\sqrt{2}} & -\Delta B_z & \frac{-\Delta B_x + i\Delta B_y}{\sqrt{2}} & -J(\varepsilon)/\gamma_e \end{pmatrix}. \tag{1.25}$$

The associated level structure is plotted in Fig. 1.8(a) [negleticing the $|\mathrm{S}\rangle$– $|\mathrm{T}_+\rangle$ anticrossing]. It is interesting to note that because of the negative electron g-factor = -0.44, in GaAs the $|\mathrm{T}_+\rangle$ lies lower in energy than the $|\mathrm{T}_-\rangle$ state. To write Eq. (1.25), we assume the QSA, and spin-up and -down axes are defined along the sum $\vec{B}$ of the external magnetic field and average nuclear field. If there were no external magnetic field, all states would couple to the singlet. Nevertheless, at a finite external magnetic field, a sufficiently large Zeeman splitting for which $B_z \gg B_{\mathrm{nuc}}$ makes the system separable. In other words, in the far-detuned regime the transition occurs only between the $M_S = 0$ states, and in this basis $\{|\mathrm{T}_0\rangle, |\mathrm{S}\rangle\}$ then Eq. (1.25) becomes:

$$\mathcal{H}_{M_S=0} = \hbar\gamma_e \begin{pmatrix} 0 & -\Delta B_z \\ -\Delta B_z & -J(\varepsilon)/\gamma_e \end{pmatrix}. \tag{1.26}$$

The previous Hamiltonian describes the dynamics of the singlet-triplet qubit of this Thesis. The result is summarized in the Bloch sphere in Fig. 1.7(b), where J (ΔB_z) provides Z (X) rotations. Next, we show how we operate the qubit.

1.6 Quantum control of two-electron spin states

In this section it is shown how the singlet-triplet qubit is operated by time-dependent control of the electrical detuning ε. The two main techniques are called rapid adiabatic passage (RAP) and slow adiabatic passage (SAP) [111]. Rapid adiabatic passage involves initializing a separated, two-spin entangled state $|\mathrm{S}\rangle$ in the far-detuned regime, followed by a projective measurement. The measurement distinguishes the triplet states $|T_m\rangle$ from the singlet state $|\mathrm{S}\rangle$. Instead, SAP prepares and measures eigenstates of the nuclear field $|s,-s\rangle$. Here $s = \pm 1/2$ is the eigenvalue of the spin projection on the field of the left dot. These techniques are the fundamental ingredients for the experiments shown later in Fig. 1.9.

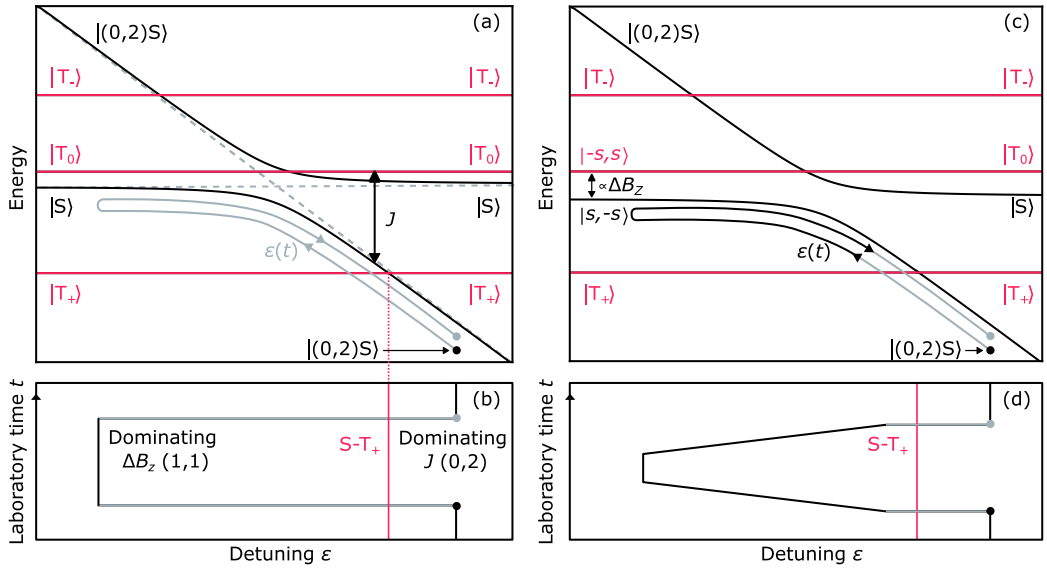

Fig. 1.8: **Rapid- and slow-adiabatic passage. (a)** Energy level diagram of a singlet-triplet qubit in GaAs as a function of detuning ε across the (1,1)-(0,2) transition, upon applied in-plane magnetic field B_z. The leakage states $|T_+\rangle$ and $|T_-\rangle$ are Zeeman split from the $|T_0\rangle$. Rapid-adiabatic passage: starting from the state $|(0,2)S\rangle$, the detuning $\varepsilon(t)$ is swept from $\varepsilon \gg t_c$ to $\varepsilon \ll -t_c$, fast compared to the nuclear energy scale ΔB_z. Here t is the laboratory time. The reversed pulse transfers $|S\rangle$ (RAP) to $|(0,2)S\rangle$ while the other states remain stuck in the (1,1) charge configuration by PSB. **(b)** Pulse sequence corresponding to (a) as a function of laboratory time t. By sweeping fast from the (0,2) charge configuration to (1,1), the spin state remains a singlet and it precesses around X because of ΔB_z-driven rotations. The qubit state is readout in (0,2) by Pauli spin blockade (PSB). **(c)** Slow adiabatic passage: similar to (a), but as the system is past the $S-T_+$ crossing (gray curve), the change of $\varepsilon(t)$ is made slow (black curve) compared to the nuclear energy scale. Then the ground state of ΔB_z ($|\uparrow\downarrow\rangle$ or $|\downarrow\uparrow\rangle$, depending on the sign, see text) is initialized. The reversed pulse transfers the ground state of ΔB_z (SAP) to $|(0,2)S\rangle$ while the other states remain in the (1,1) charge configuration by PSB. **(d)** Pulse sequence of (c) as a function of laboratory time t. Starting from the (0,2), the (0,2)S-T_+ transition (red line) is crossed diabatically. A forward adiabatic ramp prepares the state into the ground state of ΔB_z, e.g. $|\uparrow\downarrow\rangle$. After qubit manipulation, the time-reversed sequence is performed for readout.

Spin-to-charge conversion for preparation and measurement

Rapid adiabatic passage Adiabatic transition from $\varepsilon \ll -t_c$ to $\varepsilon \gg t_c$ maps the far-detuned regime states $|\mathrm{S}\rangle, |T_m\rangle$ to $|(0,2)\mathrm{S}\rangle, |T_m\rangle$ [past the (1,1) -(0,2) charge transition]. The singlet state $|(0,2)\mathrm{S}\rangle$ is distinguished from the $|T_m\rangle$ by the charge measurement. As the adiabatic transfer of states is fast with respect to the nuclear spin-induced mixing, it is called "rapid adiabatic passage" (RAP) [111]. It is important to notice that the change in detuning ε is adiabatic compared to the tunnel coupling t_c (to avoid ending up in the excited state $|\tilde{\mathrm{G}}\rangle$ after the charge transition), but much faster than the Overhauser field gradient ΔB_z from Eq. (1.26). For sufficiently fast sweeps, the adiabatic passage does not depend on the nuclear dynamics. As an example, if one initializes the state $|(0,2)\mathrm{S}\rangle$ ($\approx |\tilde{\mathrm{S}}\rangle$) and $\varepsilon \gg t_c$, using RAP then initial state remains $|\mathrm{S}\rangle$. The latter is an entangled spin state of two electron located in separate dots. The protocol is shown in Fig. 1.8(a), where the $|(0,2)\mathrm{S}\rangle$ state initialization is represented by the black circle. We show the associated control sequence as a function of detuning and laboratory time in panel (b). A readout can be performed by following the procedure in the opposite direction, which converts the singlet state to the charge (0,2), while the triplet state remains in (1,1). A charge sensor next to the DQD distinguishes between the two results.

Slow adiabatic passage If the change of ε is slow compared to ΔB_z, then the adiabatic passage follows the eigenstates of ΔB_z instead of $|\tilde{\mathrm{S}}\rangle$. For now, we assume that RAP is adopted between the charge transition after the S–T_+ [cf. Fig. 1.8(c)], so the transfer between the $|\mathrm{S}\rangle$ and the $|\mathrm{T}_+\rangle$ states can be neglected. (An external magnetic field $|B_{\mathrm{ext}}| \gg B_{\mathrm{nuc}}$ is applied.) Starting then from this $\varepsilon < -t_c$ point to the far-detuned regime deep in (1,1), ε is changed slowly compared to $\hbar\gamma_e B_{\mathrm{nuc}}$. Then, adiabatic passage maps into eigenstates of the nuclear field, $|s,-s\rangle$, as shown in Fig. 1.8(c). The states $|s,-s\rangle$ are product states, with one spin up and the other spin down with respect to the external magnetic field direction. The SAP pulse sequence is shown in panel (d). Notice the RAP across the S–T_+ to avoid leakage to the $|\mathrm{T}_+\rangle$ state, followed by the SAP.

To summarize, RAP maps $|(0,2)\mathrm{S}\rangle \leftrightarrow |\mathrm{S}\rangle\, e^{i\phi}$, where ϕ is the accumulated adiabatic phase, and $|T_m\rangle \leftrightarrow |T_m\rangle$, leaving the triplet states unaffected. Whereas for SAP, the mapping is:

$$\begin{cases} |(0,2)\mathrm{S}\rangle & \leftrightarrow & e^{i\phi}\,|s,-s\rangle \\ |\mathrm{T}_0\rangle & \leftrightarrow & e^{i\phi'}\,|-s,s\rangle\,. \\ |T_{\pm1}\rangle & \leftrightarrow & |T_{\pm1}\rangle \end{cases} \tag{1.27}$$

It is worth mentioning that $|(0,2)\mathrm{S}\rangle$ maps to the current ground state of the nuclear field, whose ground state is different depending on the sign of ΔB_z. Here s is chosen such that $E_{s,-s} < E_{-s,s}$, with $E_{s,-s} = s\gamma_e(B^l_{\mathrm{nuc},z} - B^r_{\mathrm{nuc},z})$ (at large external magnetic field). The adiabatic passage duration is typically about 1 µs, which gives an error probability of a few percent [111] for the adiabatic preparation of the Overhauser gradient ground state. Longer timescales may favor relaxation from $|s,-s\rangle$ to $|T_{+1}\rangle$.

Probing the $|\tilde{\mathrm{S}}\rangle$–$|\mathrm{T}_+\rangle$ resonance, or "spin funnel"

Close to the (1,1)-(0,2) [or (2,0)] charge transition the $|\mathrm{T}_+\rangle$ and $|\tilde{\mathrm{S}}\rangle$ states can be coupled. This coupling corresponds to the adiabatic singlet state $|\tilde{\mathrm{S}}\rangle$ having an exchange energy $J(\varepsilon)$ close to the Zeeman energy $E_z = \hbar\gamma_e B_z$ of the $|\mathrm{T}_+\rangle$ state. It is recalled that $|\mathrm{T}_+\rangle$ is the groundstate instead

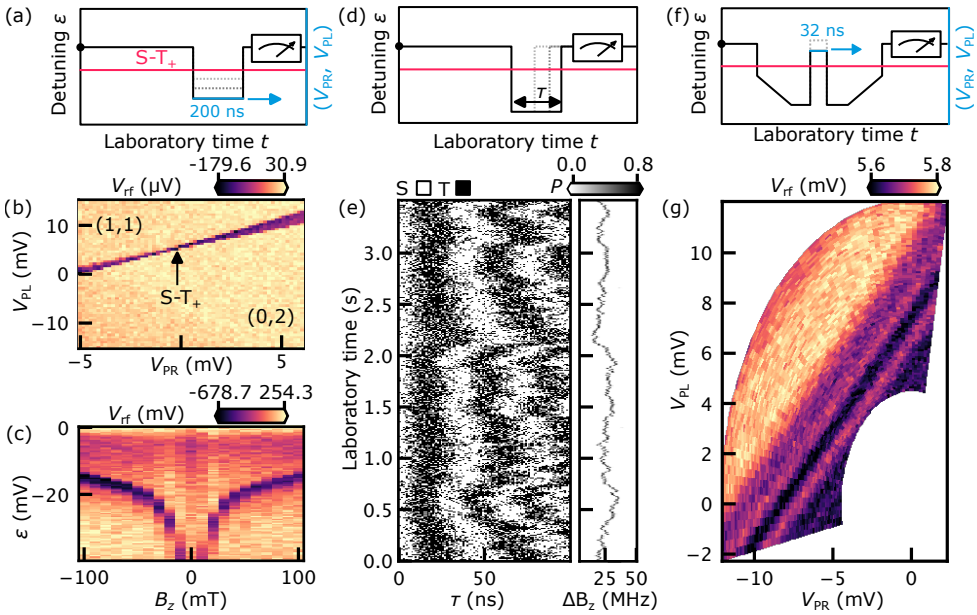

Fig. 1.9: **Spin funnel, Overhauser field driven qubit rotations, exchange oscillations. (a-b-c)** The "spin funnel" (a) Schematic of the pulse sequence to map the (0,2)S-T$_+$ transition. The singlet states $|S(0,2)\rangle$ is diabatically pulsed around the measurement point in a 2D sequence as a function of the plunger gates V_{PL} and V_{PR} of the GaAs DQD (recall Fig. 1.3(b)). At the end, the qubit is readout. (b) Averaged measurement from (a), the stripe corresponds to the (0,2)S-T$_+$ crossing (see main text). In-plane field set to $B_z = 200\,\mathrm{mT}$. (c) Averaged measurement as a function of the externally applied magnetic field. The crossing maps the exchange J profile. **(d-e)** Overhauser gradient-driven free induction decay (FID) (d) Schematic of pulse sequence ε versus laboratory time, used to probe the singlet return probability function by RAP for measurement. After singlet initialization, the qubit evolves deep in the (1,1) region for a stepped time τ and it is measured after evolution. (e) Single-shot measurement where for each row a white (black) pixel corresponds to a singlet (triplet) outcome, at a given FID time τ. On the right, extracted frequency of ΔB_z in real time on the commercial quantum controller (see Chapter 3). **(f-g)** Exchange-based FID. (f) Sketch of SAP pulse sequence for the exchange-gate sequence to probe the exchange interaction J between the two electrons. After singlet initialization, the state is pulsed diabatically across the S-T$_+$ transition, adiabatically ramped ($\approx 1\,\mu\mathrm{s}$) to initialize the ΔB_z groundstate (e.g. $|\uparrow\downarrow\rangle$) for 48 ns, diabatically pulsed closed to (0,2)-(1,1). The same sequence is performed backward before measurement. Here $\tau = 32\,\mathrm{ns}$. The detuning ε is swept as a function of both plungers. (g) Averaged measurement of (f) where the exchange FID time is set to 32 ns, yielding exchange oscillations fringes.

of $|T_-\rangle$ because of the negative electron g-factor in GaAs of ≈ -0.4 . In the basis $\{|T_+\rangle, |\tilde{S}\rangle\}$, the Hamiltonian becomes

$$\mathcal{H}_{\text{flip-flop}} = \hbar\gamma_e \begin{pmatrix} B_z & \frac{\Delta B_x - i\Delta B_y}{\sqrt{2}}\cos\theta \\ \frac{\Delta B_x + i\Delta B_y}{\sqrt{2}}\cos\theta & -J(\varepsilon)/\gamma_e \end{pmatrix}, \tag{1.28}$$

where θ is the adiabatic angle defined before. Here "flip-flop" describes the flips between $|\tilde{S}\rangle$ and $|T_+\rangle$, causing the flipping of a nuclear spin. This can understood by defining $\Delta B_+ = \Delta B_x + i\Delta B_y = \left(\hat{B}_{\text{nuc,l,+}} - \hat{B}_{\text{nuc,r,+}}\right)/2$.

In Figure 1.9(a) a pulse sequence is sketched to map in 2D voltage space the singlet and polarized triplet transition. At the beginning of the sequence a (0,2) singlet is initialized, and then it is quickly ramped in a 2D map close to the interdot (1,1)-(0,2) transition. The blue segment corresponds to a pair of pulses amplitude (V_{PR}, V_{PL}) that are swept with the waveform generator (see Chapter 2). The evolution time deep in (1,1) is fixed to 200 ns to allow for mixing of the two states via the transverse Overhauser field. The result of the pulse sequence is shown in panel (b), where the dark feature on the bright background corresponds to the crossing. The increase of the linewidth corresponds to a broadening caused by a larger pulse amplitude sent to the cryogenic bias-tee in the cryostat. The measurement has been taken at in-plane field 200 mT. To check whether it is the spin funnel, we seep the magnetic field. We use the same pulse sequence with detuning ε stepped between the measurement point and about -40 mV deep in the (1,1) region. Sweeping the magnetic field, the spin funnel maps out the exchange profile (in the absence of nuclear spin polarization [117]).

Free induction decay: probing the nuclear field

In this section it is explained how to probe the nuclear field, dephasing, and the exchange interaction. This technique allows us to probe coherent ST_0 rotations. The separated electrons experience in general a different local nuclear environment corresponding to different local magnetic fields. Thus, the electrons precess at different rates, which coherently mixes singlet and triplet states. Many measurements are taken to evaluate the fraction of the state remaining a singlet. By averaging the time-ensemble, one finds the dephasing of the singlet T_2^* [47].

To understand the effect of the nuclei on the electron spins, it is useful to analyze the singlet probability return function $P_S(t) = |\langle S(t)|S(0)\rangle|^2$ in the far-detuned regime, as evaluated in Ref. [111].

The evolution operator is $U(t)$ and in the Schrödinger picture $|S(t)\rangle = U(t)|S\rangle$. In the limit of $J \to 0$, the two electrons become uncoupled, which simplifies the expression of their dynamics. The equation of motion is solved analytically for any spin state in the (1,1) subspace. More specifically, the Hamiltonian of Eq. (1.23) is written in the form of two effective magnetic fields, each acting separately on one spin. Then $U(t) = \exp(-iHt/\hbar)$ can be factorized as $U(t) = U_l(t) \otimes U_r(t)$, based on

$$U_i(t) = \exp\left(-i\gamma_e t[\vec{B} + \vec{B}_{\text{nuc},i}]\cdot\vec{S}_i\right). \tag{1.29}$$

Here $U_i(t)$ is a rotation of spin i around an axis $\vec{n}_i = (x_i, y_i, z_i) \propto \vec{B} + \vec{B}_{\text{nuc},i}$ of angle $t\omega_i$, having defined $\omega_i = \gamma_e|\vec{B} + \vec{B}_{\text{nuc},i}|/2$.

We assume the electrons are prepared in the state $|S(t=0)\rangle = (|\uparrow\downarrow\rangle - |\downarrow\uparrow\rangle)/\sqrt{2}$, and measured using RAP to discriminate between singlet and triplet states. Initializing a singlet state at $t = 0$,

the probability $P_S(t,B)$ of staying a singlet after a time t is given by (adding the magnetic field dependence)

$$\begin{aligned} P_S(t,B) &= |\langle S(t)|S(t=0)\rangle|^2 \\ &= |\cos(\omega_l t)\cos(\omega_r t) + \vec{n}_l \cdot \vec{n}_r \sin(\omega_l t)\sin(\omega_r t)|^2. \end{aligned} \tag{1.30}$$

In reality, any experiment has to be repeated multiple times, which implicitly averages the result over random fluctuations of the nuclear field. Due to its slow dynamics, we use the quasi-static approximation (QSA), in which B_{nuc} is constant on any particular run of the experiment, but possibly varies between consecutive runs.

When the external field is much larger than the effective nuclear fields ($|\vec{B}| \gg B_{\text{nuc},i}$), the spin-flip terms are highly suppressed and the system can be well approximated by the singlet-triplet two-level system $|\text{S}\rangle$ and $|\text{T}_0\rangle = (|\uparrow\downarrow\rangle + |\downarrow\uparrow\rangle)/\sqrt{2}$. Then $P_S(t,B)$ becomes [111]:

$$P_S(t, B \gg B_{\text{nuc}}) \approx \frac{1}{2}\left[1 + e^{-\left(t/T^*_{2,\text{eff}}\right)^2}\right], \tag{1.31}$$

where $T^*_{2,\text{eff}} = 1/\sqrt{\frac{1}{2}[(T^*_{2,l})^{-2} + (T^*_{2,r})^{-2}]}$ (in the QSA). This result shows how the singlet return probability $P_{S,B}$ has a Gaussian decay because of the nuclear field, with a timescale $T^*_{2,\text{eff}}$.

In Fig. 1.9(d) we show the pulse sequence to probe the nuclear field. Rotations around the X axis are performed by ΔB_z when the initialized singlet is detuned deep in (1,1). At such detuning, for one repetition, the evolution time τ is stepped between zero and ≈ 100 ns. A typical measurement is shown in panel (e), where each row is one repetition, whose white (black) pixels correspond to a singlet (triplet) measurement outcomes. Also, for each row, the frequency of the oscillations is estimated in real-time by Bayesian estimation (presented in Chapter 3). Since ΔB_z changes randomly according to the nuclei spin diffusion, this leads to short dephasing times of the order of tens of ns characteristic of III-V semiconductors. In Chapter 3 we will show how to extend the quality of coherent qubit rotations in real time by the real-time Bayesian estimation of the nuclear field.

Exchange-based free induction decay: probing the exchange interaction

Now we show how the SAP at large external magnetic field allows us to measure the exchange interaction. As mentioned earlier, SAP allows to prepare and measure the spin eigenstate $|s,-s\rangle$ and $|-s,s\rangle$. The rotation angle between the two states is given by the product of the exchange interaction energy during the gate, $J(\varepsilon)$, and the gate time τ during which exchange is non-zero. After the gate, reversing SAP maps the lower energy eigenstate of the nuclear field $|s,-s\rangle \rightarrow |(0,2)\text{S}\rangle$ and the higher energy state $|-s,s\rangle \rightarrow |\text{T}_0\rangle$, which corresponds to the (1,1) charge state. The final measurement evaluates if the final state is the same as the initial state [measurement outcome is (0,2)], or if it has changed to the state with two spins swapped due to the exchange gate [measurement outcome is (1,1)]. Therefore, preparing the state $|s,-s\rangle$ and measuring it in the same basis discriminates the possible measurement outcomes of the exchange-based rotation of the two electron spins. For instance, when the probability of measuring (1,1) approaches 100%, a complete SWAP of the two spins has occurred. If 50%, it corresponds to an exchange $Z(\pi/2)$ pulse which generates the entangling square root for the SWAP gates, i.e. $\sqrt{\text{SWAP}}$. Formally, the effect of exchange can be computed [51] by writing Eq. (1.2) as the projection operator on the spin-singlet state, $H = -J\,|\,\text{S}\rangle\langle\text{S}|$.

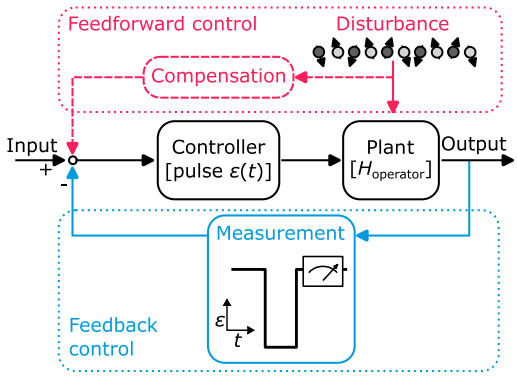

Fig. 1.10: **Fundamental building blocks in a qubit system with feedback and feedforward control.** The plant is the system to be controlled. The input is changed by the controller to affect the plant. The output of the plant contains what is to be controlled, and it is provided to the feedback control. The controller is the control pulse sequence (electrical detuning), which controls the plant (the Hamiltonian). The measurement (output of the free-induction decay) is fed back to the input to estimate the disturbance (fluctuating nuclear field gradient). Compensation is absent in our setup. Adapted from [3].

The corresponding unitary is $U(\phi) = \exp\left(-i\phi|\mathrm{S}\rangle\langle\mathrm{S}|\right) = \mathbb{1} + (e^{i\phi} - 1)|\mathrm{S}\rangle\langle\mathrm{S}|$. Given $\phi = J\tau/\hbar\pi$, we have $U(\pi) = 1 - 2|\mathrm{S}\rangle\langle\mathrm{S}| = \mathrm{SWAP}$ whereas for $\phi = \pi/2$ we get $U(\pi/2) = (1+i)\mathbb{1}/2 + (1-i)\mathrm{SWAP}/2 = \sqrt{\mathrm{SWAP}}$. Similarly to before, we consider the probability of measuring the lower energy eigenstate. This time though the state is $|s,-s\rangle$, upon which the exchange of angle $\theta_\mathrm{E} = J\tau/\hbar$ is performed where τ is the time spent by the state with exchange energy J. This rotation is applied to the state $|s,-s\rangle$, whose survival probability function becomes

$$P_{s,-s}(t) = ||s,-s(t)\rangle\langle s,-s||^2 = \cos^2(\theta_\mathrm{E}/2). \tag{1.32}$$

The exchange interaction depends on the overlap of the orbital wavefunctions of the two electrons, and we can tune such interaction by voltage signals. In Fig. 1.9(g) we plot a sketch of the sequence used to let the initialized ground state of the Overhauser gradient (e.g. spin state $|\uparrow\downarrow\rangle$) evolve around the Z axis. The sequence is also known as exchange-based free induction decay (FID). The voltage is spanned in a 2D map, yielding the averaged result in panel (g), where fringes from exchange oscillations are closer to the (1,1)-(0,2) transition in the bottom right corner, and fade out in the top left corner. The annulus sector is due to the programming of the exchange pulse amplitude and angle in polar coordinates on the quantum controller.

In this section we have seen how to probe the nuclear field and the exchange interaction of a DQD. In the next section, we provide a brief introduction to quantum control and a warm-up example with the device used in this work.

1.7 Real-time feedback and feedforward

Control of quantum processing units (QPUs) in the presence of noise, imperfect devices, and imperfect control systems is a critical problem for developing a useful quantum computer. As

	Linear optics	Superconducting circuits	**Semiconductor spin qubits**
System energy-scale	1 THz	1-10 GHz	10 MHz - 10 GHz
Feedback bandwidth	1 MHz	10 MHz	10 MHz
Decoherence rate	1 MHz	10 - 100 kHz	1 - 100 kHz
Measurement rate	photon flux	100 kHz	100 kHz
Feedback delay	0.1-10 µs	200 ns	200 ns
Working Temperature	300 K	30 mK	30 mK - 1 K

Table 1.1: Characteristic parameters for feedback in various physical settings, first three columns adapted from [3]. See the main text for the semiconductor spin qubit values.

mentioned in the previous Chapter, noise severely limits the performance of today's NISQ devices. In this Thesis, we show how closed-loop control methods can help mitigate the effects of such noise. Additionally, we demonstrate how these methods can be used to perform noise-driven coherent qubit rotations.

In the context of control theory [3], it is possible to break down the control system into three components [see Fig, 1.10]

- The "plant" is the system we want to control, e.g. the Hamiltonian $\mathcal{H}_{\text{operator}}$ of the QPU. It has inputs and outputs.
- The input(s) to the plant (or "control") is what we can change to affect the system, e.g. control pulses of the QPU.
- The output(s) of the plant (or "yield") contains any variables that can be measured to gain information about the plant.

In feedback control, one can think about the interaction between the control system and the plant as a causal structure, according to which the control system obtains information from a measurement that provides the input to the plant. The interaction may not be explicit in the Hamiltonian description [3]. In general, a control steers one or more outputs to an intended action in the presence of noise or disturbance. As illustrated in Fig. 1.10, a *feedforward* controller can be used at the input to cancel the effects of known or measurable disturbances. Differently, if the disturbance is unknown, the role of a *feedback* controller is to change the input according to the output of the predetermined measurements imposed on the plant.

In this Thesis, the plant is a Hamiltonian parameter $x(t)$ we want the quantum controller to estimate. The measurement of the free-induction decay carries information about $x(t)$. The quantum controller estimates $x(t)$ and updates the control pulses accordingly. A feedforward protocol would require a sensor that measures $x(t)$ in real time.

Feedback has been implemented in a great variety of physical systems [3], including superconducting qubits, semiconductor spin qubits, atom optics, cavity QED, and opto-mechanics. In Tab. 1.1, different parameters are summarized from recent state-of-the-art experiments on feedback control in three selected platforms. We add typical semiconductor spin qubits parameters to values found in Ref. [3]. The feedback bandwidth is the fastest rate at which the controller changes the system. This rate sets the lower limit to the timescale of the whole feedback protocol. The measurement strength of a continuous measurement has units of inverse time and the inverse square of the observable to be measured. It can be seen as the rate at which the inverse variance of the observable is increased. The measurement rate units depend on the system of interest.

In linear optics, the system to be measured is generally a continuous-wave laser beam, so the photon flux is the measurement rate. Instead, if one is interested in the position of a harmonic oscillator, the unit of position is the uncertainty in the position for the oscillator ground state. The previously mentioned feedback bandwidth and the time delay of the feedback loops are critical for measurement-based feedback.

Regarding the semiconductor spin qubits values, the system energy scale depends on the qubit encoding, with up to 1 GHz bandwidth for qubits that require baseband control pulses (e.g. singlet-triplet, exchange only encodings), up to microwave control in the tens of GHz range for single-electron spin Loss-DiVincenzo qubits. The feedback bandwidth is chosen based on the quality factor of surface-mounted tank circuits used in spin qubits for radio-frequency reflectometry readout (see Ch. 2), which provides the maximum readout bandwidth. The measurement rate stems from typical qubit cycle periods of around 10 µs (PSB requires a few µs for readout, Elzerman instead tens of µs). The feedback delay is on the order of 200 ns for both commercial and in-house solutions [146, 147]. At the beginning of this chapter, we have mentioned that semiconductor spin qubits have been operated at temperatures above 1 K.

Before illustrating an example of a feedback protocol, one last distinction is crucial. In measurement-based feedback, a series of measurements are performed on the system, and the Hamiltonian is modified after each measurement based on the measurement results [3]. On the other hand, *coherent* feedback is when a classical model cannot describe the joint dynamics of the system and controller. Two disadvantages of measurement-based feedback are that performing measurements on quantum systems requires signal amplification, and some finite time (on the order of hundreds of ns) is required to obtain and process the measurement results. Nevertheless, the advantage of measurement-based feedback is that the information processing is basically noise-free. On the contrary, in coherent feedback the controller can be subjected to noise from its environment.

In this Thesis, we focus on measurement-based feedback: we apply classical feedback to a quantum system, but there is no back-action. We program a quantum controller to probe a fluctuating qubit Hamiltonian parameter and adjust the control pulses accordingly.

A control loop example In this section we present an example of real-time measurement feedback, inspired by a superconducting qubit experiment [148], here applied to a singlet-triplet qubit. Exchange-based free induction decays (FIDs) (see Sec. 1.6) are means of studying charge noise. Charge noise is presumably caused by an ensemble of two-level fluctuators in the heterostructure, on top of $1/f$ noise from the experimental apparatus [149]. Figure 1.11(a) shows the schematics of a PI loop (D=0)[6], where the given input is the averaged signal from exchange-based FID at fixed $\tau = 20$ ns to correct by $\Delta\varepsilon$ fluctuations in the electrical detuning ε. First, an averaged exchange-based FID at the same duration is taken to calibrate the PI loop by sweeping ε. A linear fit approximates the signal on the flank of an oscillation, near -6 mV [see panel (b)].

The top panel of Fig. 1.11(c) shows the measurement outcome without feedback, interleaved with the bottom panel with feedback. It is interleaved in the sense that from each repetition (column) of the top panel, the signal V_{rf} is extracted at $\tau = 20$ ns. The signal is compared to the bias point from the offline model [shown in (b)], and the detuning is corrected accordingly by the PI loop (a). This feedback manages to correct some of the abrupt changes in the qubit frequency [marked

[6] A proportional-integral-derivative controller (PID controller) is a control feedback loop protocol widely used in control systems. A PID system calculates an error $e(t)$, which is the difference between the desired setpoint and the measured observable. The correction is applied based on the proportional, integral, and derivative terms computed from $e(t)$.

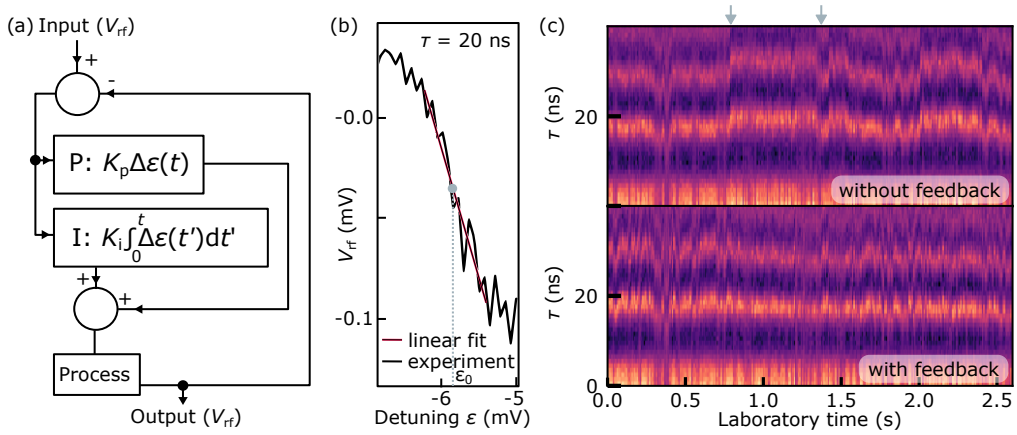

Fig. 1.11: **PI loop to stabilize exchange-based FID in a GaAs singlet-triplet qubit. (a)** Schematic of feedback loop where the input is the RF reflectometry signal V_{rf}, the output is the updated detuning ε. The aim is to stabilize the exchange-based FID fringes. P stands for the proportional part of the feedback, and I for the integral one. **(b)** Feedback calibration. The pulse sequence sketched in Fig. 1.9(f) is performed, this time sweeping the electrical detuning ε at fixed exchange-based evolution time $\tau = 20$ ns. The (1,000 times) averaged RF reflectometry signal V_{rf} is fitted on the flank of the oscillation by the line $V_{rf} = -0.135\varepsilon - 0.830$ mV, centered at $\varepsilon_0 = -5.84$ mV (gray dot). **(c)** Top (bottom) panel shows averaged measurement without (with) feedback. Each column of the top panel is used to measure V_{rf}, whose variation from the setpoint computes the $\Delta\varepsilon$ required to correct for low-frequency fluctuations. Then, a column of the bottom panel takes into account the correction $\Delta\varepsilon$ as schematized in panel (a). Some frequency jumps pointed by the gray arrows are corrected for (see main text).

by the gray arrows in (c)], but not slowly varying fluctuations. A better approach is shown in Chapter 3, where instead of a single data point per repetition, the whole sequence of measurements is considered with a Bayesian protocol.

Bayesian parameter estimation

Mathematical models often describe experimental data by its parametrization. In general the first attempt is to minimize the squared error (classical regression), which assumes there exists a single optimal point in the parameter space [150]. Bayesian parameter estimation (BPE) [151] does not require this assumption, as it is based on a probability distribution in the space of the parameters of the model. On the other hand, machine learning methods (e.g. neural networks) can be used as well to get insights from data when classical regression fails. Nevertheless, there are no reliable methods to interpret and assign errors to these methods [150]. By numerical simulation and BPE it is possible not to use a black box to extract useful information from the data.

As mentioned above, in classical regression the typical approach is to optimize the parameters to minimize a cost function, e.g. the sum of squared errors, between what the model predicts and the "best fit" of set parameters. The minimum value of the cost function is used as a metric to evaluate the goodness of the fit. Possibly, it can hint at effects not included in the model if the cost

function is not “low enough". Also the landscape of the fit around the found optimal-fit point can provide some insights on confidence intervals. Bayesian parameter estimation instead produces a probability distribution given the model parameters. In the Bayesian approach, *each* combination of parameter values gets assigned a strength of belief in being the correct one to describe the data, provided by the probability distribution. The BPE is based on Bayes' theorem, which follows

$$\underbrace{P(H \mid E)}_{\text{posterior}} = \frac{\overbrace{P(E \mid H)}^{\text{likelihood}}\overbrace{P(H)}^{\text{prior}}}{\underbrace{P(E)}_{\text{evidence}}}, \tag{1.33}$$

where E is some evidence, e.g. the observed data, and H is the hypothesis, i.e. a point in the parameter space. The likelihood $P(E \mid H)$ is the probability of observing some evidence given the hypothesis is true. Given the observed evidence, the posterior $P(E \mid H)$ is the probability of our hypothesis being true. In summary, Bayes' theorem converts a likelihood to a posterior, where the likelihood function acts in the observation space containing the evidence E. In contrast, the posterior exists in the parameter space where the hypotheses H are.

In the context of feedback, for example, we can perform a series of “single-shot” measurements with a discrete set of outcomes (the evidence E), and perform a unitary action on the system after selecting the best hypothesis H provided by the BPE. The unitary action is the “feedback" phase of the protocol, after the unknown disturbance has been estimated [cf. Fig. 1.10]. The estimation phase can be considered as “adaptive" if we change the parameters of the probing phase while we perform the estimation. We will further discuss these concepts in Chapters 3, 4, and 5.

1.8 Conclusions

In this Chapter, we have introduced the singlet-triplet (ST_0) spin qubit encoding, and some of the main differences between GaAs and Si for gate-defined quantum dots. We have described two examples of depletion mode GaAs/AlGas device and accumulation mode Silicon metal-oxide semiconductor (SiMOS) devices, as well as spin-to-charge initialization and readout by Pauli spin blockade (PSB). We have presented how to operate a singlet-triplet qubit in GaAs. At last, we have introduced the distinction between feedback and feedforward, Bayesian inference, and a warm-up example of closed-loop control in a singlet-triplet qubit. In the next Chapter 2, we present the experimental setup and radio-frequency reflectometry readout.

2

Experimental Setup

2.1 Triton 4 Dilution Refrigerator

The Triton 4 setup[1] owes its name to the installed Triton^{200} Cryofree® Dilution Refrigerator, by Oxford Instruments. The cryogen-free ^{3}He – ^{4}He dilution refrigerator [152] is equipped with a superconducting magnet (90 mm bore) and a single pulse tube [153], with measured experimental temperatures of about 20 mK and magnetic fields up to 6 T. The refrigerator has been upgraded to the so-called "large" sample puck (74 mm diameter, 16 cm high), which can host up to 28 RF and 96 DC lines.

The interior of the cryostat is shown in Fig. 2.1, with the magnet being temporarily removed to access the plates. As the sample puck during an experiment is docked to the coldfinger, the latter has been changed as well. The superconducting vector magnet (see Fig. 2.2) is thermally anchored to the 4 K plate. It reaches 6 T along the main axis of the refrigerator, here along the z direction, and nominally 1 T along x or y.

Low-frequency electrical lines (DC - 50 kHz)

The cryostat hosts four DC looms (shown in Fig. 2.1), resulting in overall 96 low-frequency electrical lines at the end of the coldfinger, as drawn in Fig. 2.3. While a summary of the wiring is described in Tab. 2.1, more details are presented in the Appendix C.

The DC lines are divided into four looms: each loom carries 12 twisted pairs of constantan wire, which offers low thermal conductivity and small temperature dependence of the electrical resistivity [152]. The looms are accessible on top of the cryostat by hermetic Fischer connectors and they are thermalized at different stages by anchoring them to the plates. As these low-frequency channels require a particularly low-noise environment for current measurements, they are filtered at the mixing chamber (MC) stage by QDevil QFilters. In each QFilter the first "RC " stage filters the electronic noise from 65 kHz up to a few GHz, thermalising the electrons. It is followed by a second "RF" filter bank with LC low pass stages, for filtering out from 225 MHz to the THz regime. In the MC stage also a homemade RC-RF filter realized at Harvard has been installed.

[1] The experimentalist should be familiar with the most updated setup documentation on the QDev Wiki. This Chapter is intended as a general introduction to a typical spin-qubit setup.

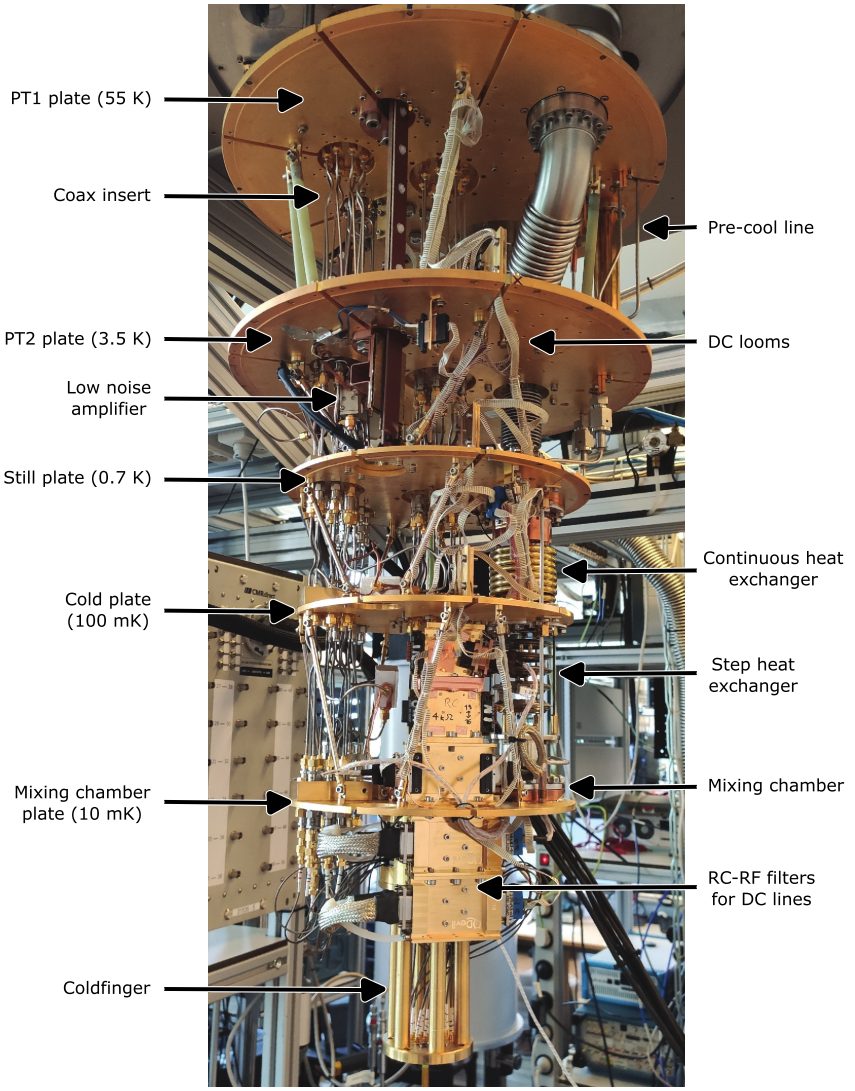

Fig. 2.1: **Triton 4 dilution refrigerator**. Interior of the Oxford Triton dilution refrigerator and its cooling stages from about 55 K down to a few tens of mK. Also, some of the components carrying the DC and RF signals to the coldfinger are labeled.

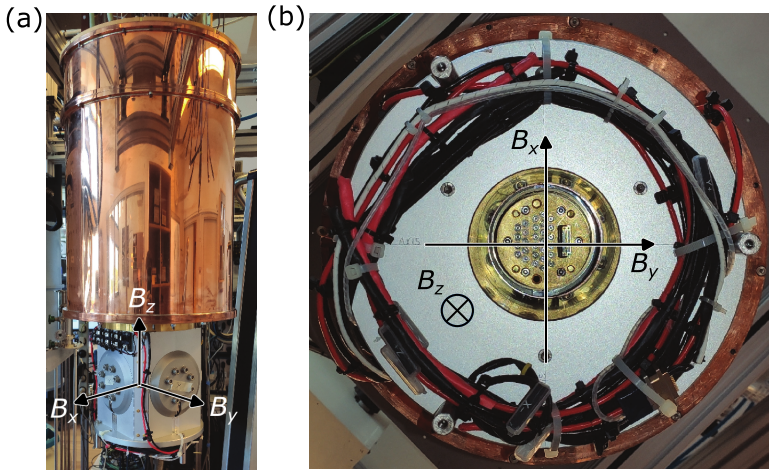

Fig. 2.2: **Vector magnet. (a)** Superconducting magnet thermally anchored to the 4 K plate. The B_z component of the magnetic field is parallel to the main axis of the cryostat. **(b)** Bottom view of the installed magnet, showing its orientation with respect to the coldfinger.

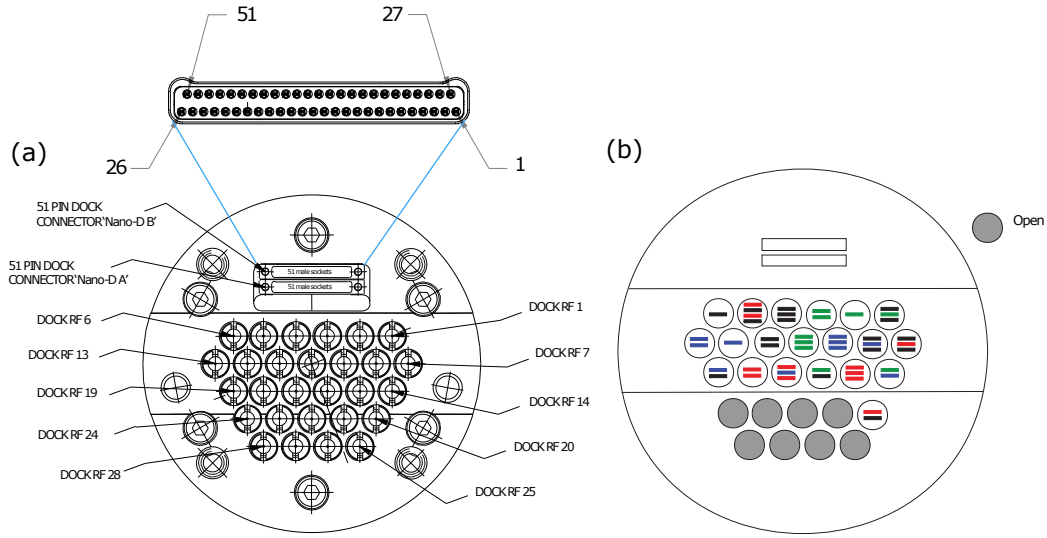

Fig. 2.3: **Pin-out of the coldfinger as seen from the bottom of the refrigerator**. **(a)** Two Nano-D connectors, A and B, deliver the overall 96 DC lines, whereas the 28 RF docks are for the high-frequency signals up to the GHz range. **(b)** The colors refer to the labeling with permanent markers of 20 SMA - SMP coaxial cables delivering the high-frequency electrical signal from the MC to the bottom of the coldfinger. Out of 28 RF docks, 8 have been left open.

nano-D A	1	2	...	24	25	26	27	28	...	50	51
Breakout Box A (QBox)	1	2	...	24	N/C	N/C	25	26	...	48	N/C
Constantan looms R	≈214 Ω						≈214 Ω				
RC/RF Filter	QFilter CM10017-0123						QFilter CM10017-0114				
Total measured R	≈1.92 kΩ						≈1.92 kΩ				
nano-D B	1	2	...	24	25	26	27	28	...	50	51
Breakout Box B	1	2	...	24	N/C	N/C	27	28	...	50	N/C
Constantan loom R	≈127 Ω						≈129 Ω				
RC/RF Filter	bypassed. R ≈ 4.0 kΩ, C ≈ 10 nF						QFilter CM10017-0003				
Total measured R	≈127 Ω						≈1.83 kΩ				

Table 2.1: **Coldfinger DC pin-out**. Summary of DC pin-out from the two nano-D connectors at the bottom of the coldfinger - where the sample puck engages - to the two breakout boxes. Each breakout box has 48 DC ports, resulting in overall 96 DC lines into the cryostat. The measurements are taken with an Agilent U1272A multi-meter. Three DC looms out of four are filtered by QDevil QFilters, while one line is left unfiltered to compare the electron temperature with and without QFilter.

High-frequency electrical lines (100 Hz - 20 GHz)

Voltage signals in the few GHz range are transmitted by coaxial cables, as shown in Fig. 2.1. A summarizing schematic is presented in Fig. 2.4, while coaxes materials and details of the electrical components are found in Fig. C.3. Mainly three stages are distinguished from room temperature (RT) to the MC. Silver-plated[2] stainless steel (SSS-SS) cables run from RT to the 4 K stage and NbTi ones from 4 K down to the MC plate - except for the KF40 Line of Sight (LOS) coaxes, see Fig. 2.4, where NbTi lines are used also between PT2 and the still plate. Both materials have low passive load and NbTi, which is much more expensive, turns superconducting below 10 K, inhibiting Joule heating at the lower stages [154] and yielding excellent signal transmission properties (NbTi also has a rather low thermal conductivity, outperforming SS below 80 mK [152]). Ultimately, flexible silver-plated copper links (Rosenberger L70-180-400-V1) connect the coaxes from the MC to the RF docks of the coldfinger (Fig. 2.3).

Cryogenic attenuators are placed along the lines at different stages to thermalize the incoming photons from RT, with overall nominal attenuation ranging from 23 dB to 28 dB. Further details about the trade-off between the number of photons and required cooling power on the different plates are found in [154]. One line is heavily attenuated (about 65 dB) to be far below the single-photon level for cavity quantum electrodynamics experiments. Measured transmission and reflection of the coax lines are shown in Fig. C.4. Two sets of reflectometry lines are available,

[2]The silver plating of the steel inner conductor significantly improves signal transmission by reducing skin-effect losses associated with the inner conductor. Still, this is at the expense of a higher thermal conductance because of Wiedemann-Franz law (the quality of the silver plating can be quite high, but its RRR value is typically not specified, making it difficult to estimate actual heat loads). Nominally, the different cooling stages should be thermally isolated as much as possible. However, the outer conductor is more responsible for the heat load, due to its larger diameter.

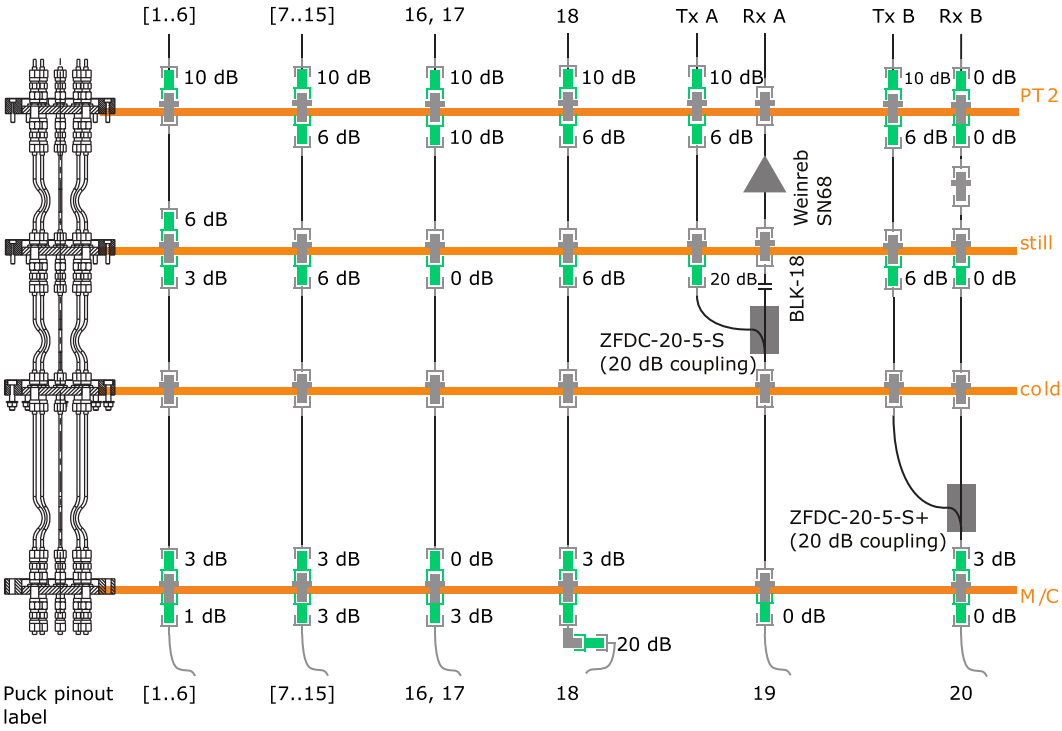

Fig. 2.4: **Coax lines summary**. Coax lines schematic showing the cryogenic attenuators between PT2 (4 K) and MC, Weinreb SN68 amplifier, Minicircuits directional couplers and one DC block for the amplifier. A more detailed schematic is shown in Fig. C.3.

Tx-Rx, A and B. The former contains a cryogenic and low-noise Weinreb SN68 amplifier, whose transmission tests at RT are shown in Appendix C, Fig. C.5. Delay times are described in Tab. C.5.

2.2 Motherboard and daughterboard, and sample-puck

So far we have described the cryostat setup from the RT wiring, down to the coldfinger, which is thermalized by the MC at 20 mK. Now we describe the sample puck, which is docked to the coldfinger after loading. Before loading into the cryostat, the chip bond pads (connected to the device ports) are bonded to the daughterboard with the semi-automatic bonder Bondtech 5630. Figure 2.5(a) shows an example of the QBoard I [155] used throughout this work (by QBoard we mean the combination of the daughterboard, interposer, and motherboard). The daughterboard is grounded during bonding and its cavity (about 10 mm × 10 mm large) hosts the device. The daughterboard may host surface-mounted devices (SMD) for radio-frequency (RF) reflectometry multiplexed readout. The daughterboard is mounted on its motherboard, with electrical connections made by an interposer with fuzz buttons. The advantage of the portable daughterboard is that the motherboard does not have to be disconnected from the sample puck [Fig. 2.5(b)] whenever a new device is to be loaded. The main disadvantage is the cutoff frequency of the fuzz

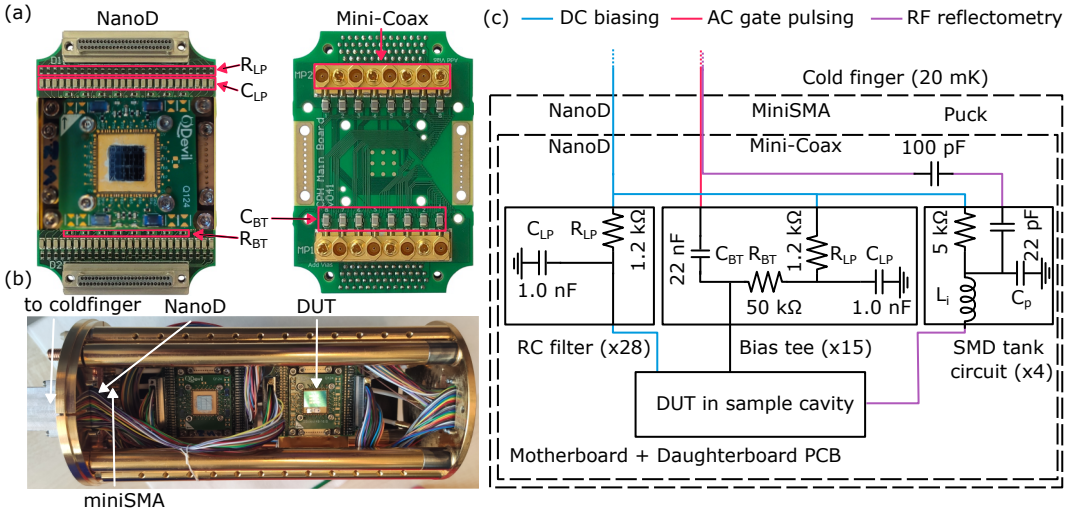

Fig. 2.5: **Board and sample puck.** **(a)** Front (rear) view of the QBoard I on the left (right). The device chip is wire-bonded to the daughterboard. R_{LP} and C_{LP} are the RC elements of the LP filters on the motherboard. The HF electrical lines from the coldfinger are connected to the Mini-Coax ports on the rear of the QBoard (up to 16). The motherboard hosts R_{BT} and C_{BT} components for the bias tees, which provide both a LF and HF signal to the ports of the DUT. **(b)** Triton sample puck that can host two motherboards, mounted in either parallel or perpendicular configuration with respect to the cryostat longitudinal axis. **(c)** Simplified circuit schematic of the QBoard I. The NanoD connectors from the coldfinger deliver the LF electrical signals. Some of the LF signals are connected to the DUT after going through the LP RC filters (R_{LP} and C_{LP}) on the motherboard. Some of them go through the bias-tee on the motherboard that hosts both the low-pass RC filters and the high-frequency lines, connected by R_{BT} and C_{BT}. The high-frequency signals are delivered from the miniSMA connectors in the puck to the Mini-Coax in (a). When the surface-mounted devices (SMDs) for RF reflectometry are mounted, the LF signals supply bias to the inductors, which are wire-bonded to the DUT. C_p is the parasitic capacitance to ground, each of the four tank circuits has an SMD inductor L_i connected by a 22 pF capacitor to another capacitor 100 pF for frequency-multiplexing. The DUT is mounted on the cavity of the daughterboard.

buttons around ≈ 1 GHz [155]. The motherboard has first-order RC low-pass filters consisting of $R_{LP} \approx 1.2\,k\Omega$ and $C_{LP} \approx 1.0\,nF$ to filter the 48 low-frequency signals coming from the NanoD of the sample puck, to the nanoD of the motherboard. The fast lines are delivered from the coldfinger to the sample puck by miniSMA connectors [Fig. 2.5(b)], which then connect to the Mini-Coaxes through flexible Cu coaxes with silver plating (Rosenberger RTK 047). A bias tee with $R_{BT} \approx 50\,k\Omega$ and $C_{BT} \approx 22\,nF$ supplies both the LF and HF signals to the bond pads, which are wire-bonded to the device under test (DUT). The bias-tee RC filters are the same as before ($R_{LP} \approx 1.2\,k\Omega$, $C_{LP} \approx 1.0\,nF$) for the LF lines.

In Fig. 2.5(b) we show a puck with two motherboards to host two experiments at the same time, after the cryostat upgrade. Both motherboards have nanoD cables that connect in parallel to both ends of the sample puck. One end is in general grounded while the user is handling the puck, to protect the device from electrostatic discharge damage. The grounding is maintained until the end of the loading into the cryostat, when the sample puck is engaged to the coldfinger which then provides the grounding from the RT breakout box.

In Fig. 2.5(c) a circuit schematic summarizes all the components used in the printed circuit board (PCB), including the 48 RC filters, of which 16 can be used to supply a low-frequency signal to the device through the bias-tee alongside the HF signals. The daughterboard shown in Fig. 2.5(a) has also SMD components for RF reflectometry multiplexed readout. In particular, it has four tank circuits, each equipped with an inductor L_i that is bonded in series to one of the device's ports [either an ohmic or gate for dispersive readout (see section 2.3)]. Also, an LF line is connected to L_i to provide the DC bias. The parasitic capacitance, typically $C_p \approx 0.8\,pF$, is not known in advance, it depends on the wire bond, and the specific PCB [155]. The coupling capacitors of ≈ 22 pF are all connected on the PCB to one end of a 100 pF capacitor that, if present, allows frequency multiplexing and it connects to the one of Mini-Coax ports on the rear of the motherboard (see Fig.2.5(a), right picture [155]).

2.3 Radio-frequency reflectometry

The idea behind radio-frequency (RF) reflectometry readout is to send a high-frequency sine wave between tens and hundreds of MHz (recall 240 MHz ≈ 1 μeV). The frequency should be sufficiently high to suppress $1/f$ noise, but not too high because of losses in the printed circuit board hosting the device, high-frequency noise and unwanted excitation of higher energy states. We refer the reader to Ref. [120] for more details on RF reflectometry for readout of quantum devices.

Here we describe a particular kind of RF reflectometry, called homodyne detection. In Fig. 2.6(a), the local oscillator (LO) generates a sinusoidal wave of the form $v_{in}(t) = V_{in} \cdot \cos(\omega_{LO} t + \phi_0)$, where V_{in} is the amplitude and ϕ_0 is the phase. The signal goes through a phase shifter that can change the phase of $v_{in}(t)$. For now, we assume the phase shift $\phi = 0$. The signal is attenuated by a factor α because of the attenuation in the coax line and the directional coupler, and it reaches the sample.

In the reflection configuration, the reflected signal is now $v_r(t) = |\Gamma|\alpha V_{in} \cdot \cos(\omega_{LO} t + \phi_0 + \delta_\phi)$, where Γ is the (in general complex) reflection coefficient given by

$$\Gamma = \frac{Z_L - Z_0}{Z_L + Z_0}, \tag{2.1}$$

where $Z_0 = 50\,\Omega$ is the characteristic impedance of the coaxial line. The reflected signal $v_r(t)$ has a different amplitude and phase δ_ϕ compared to the incoming signal, depending on the modulus of

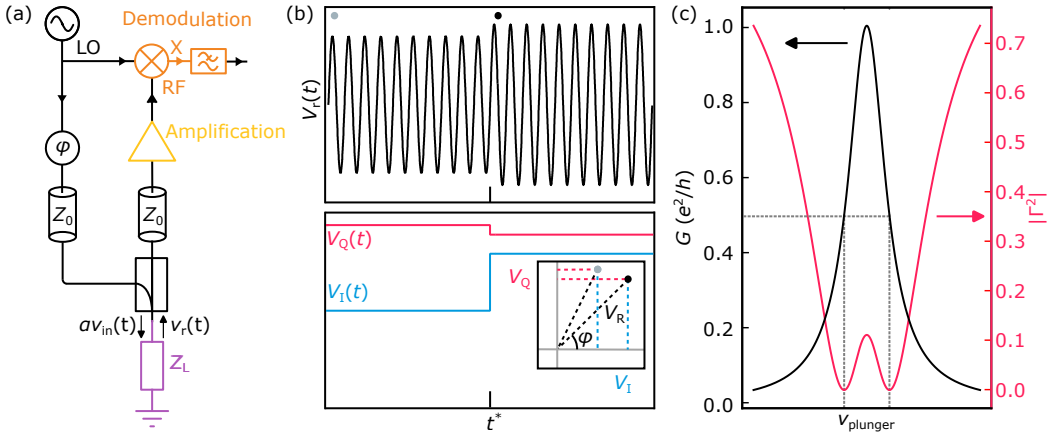

Fig. 2.6: **Radio-frequency reflectometry building blocks. (a)** Radio-frequency (RF) reflectometry setup. An RF carrier is sent from the LO source, travels through a phase shifter, a transmission line and is sent to the device (Z_L) through a directional coupler. The signal is reflected and after being amplified, it is demodulated by a mixer. The homodyne low-frequency voltage is obtained after a low-pass filter is applied to the demodulated voltage. **(b)** Cartoon of change in amplitude and phase of the reflected sine wave when at time t the load Z_L changes. In the bottom panel, we see changes in amplitude and phase of the sine wave are mapped into changes of the demodulated in-phase $[V_I(t)]$ and out-of-phase $[V_Q(t)]$ quadrature voltages. The gray (black) dot corresponds to $v_r(t)$, before (after) time t^*. **(c)** Cartoon to show in general how current measurements are not linearly mapped to the RF signal. The black curve mimics the conductance measurement of a Coulomb peak (normalized to the conductance quantum $e^2/h \approx 3.87 \times 10^{-5}$ S) as the plunger gate voltage is swept. The red curve, right axis, is the fraction of reflected signal assuming the circuit is designed to be matched at $Z_{\text{match}} = 2h/e^2 \approx 51.6\,\text{k}\Omega$, and the dashed gray lines indicate where the matching occurs (reflection coefficient $\Gamma = 0$). Panels (a) and (b) are adapted from Ref. [120].

Γ and its phase $\angle\Gamma$, respectively. After being reflected, assuming negligible insertion loss in the directional coupler and the transmission line, the signal is amplified by a (cryogenic) amplifier by a gain factor G [yellow triangle in Fig. 2.6(a)]. In the demodulation part [orange in (a)], the mixer then multiplies the reflected signal (RF port) by the reference provided by the local oscillator (LO port), and it outputs the demodulated voltage $v_d(t)$ at the X port:

$$v_d(t) = G \cdot v_{in}(t) \cdot v_r(t) = G \cdot V_{in} \cdot \cos\left(\omega_{LO} t + \phi_0\right) \cdot \Gamma \alpha V_{in} \cdot \cos\left(\omega_{LO} t + \phi_0 + \delta_\phi\right) = \tag{2.2a}$$

$$= \frac{G|\Gamma|\alpha V_{in}^2}{2} \cdot \left[\cos\left(\delta_\phi\right) + \cos\left(2\omega_{LO} t + 2\phi + \delta_\phi\right)\right], \tag{2.2b}$$

where the identity $\cos(a) \cdot \cos(b) = [\cos(a-b) + \cos(a+b)]/2$ has been used. This means that at the output X there is a DC component [proportional to $\cos(\delta_\phi)$] superimposed on an AC signal at twice the frequency of the LO. By applying a LP filter to filter out the AC component, we are left with what we define as the in-phase quadrature of the signal

$$I \equiv \frac{G|\Gamma|\alpha V_{in}^2}{2} \cdot \cos\left(\delta_\phi\right). \tag{2.3}$$

The out-of-phase quadrature $Q \equiv G|\Gamma|\alpha V_{\text{in}}^2 \cdot \sin\left(\delta_\phi\right)/2$ can be similarly obtained by multiplying the reflected signal by the reference shifted by $\pi/2$, adding for instance a splitter and a $\pi/2$ phase shifter to the circuit in Fig. 2.6(a). With the phase shifter, it is possible to change the phase $\phi_0 \to \phi_0 + \phi$, recalling ϕ was set to zero at the beginning of the discussion. In theory, the phase shifter could also be placed right before the mixer, but this is not recommended as the optimal power for the input of the phase shifter is much lower than what is required by the mixer's LO port. When only I (or Q) is available, sometimes the component is referred to simply as homodyne voltage V_{H}.

Figure 2.6(b) is a sketch of the change in amplitude and phase of the sine wave $v_{\text{r}}(t)$ being reflected by the load, as Z_{L} changes at a given time. We assume the change is slow compared to the bandwidth of the low-pass filters used to obtain I and Q. The voltage change identifies two different points in the complex plane spanned by I and Q, using the equivalent phasor notation

$$v_{\text{r}}(t) = \text{Re}\left\{\sqrt{I^2(t) + Q^2(t)}\, e^{\,\text{i}\,\text{atan}\left(\frac{Q(t)}{I(t)}\right)}\right\}. \tag{2.4}$$

In an experiment the features measured by RF reflectometry may be different from the ones measured by DC current. To explain why, in Figure 2.6(c) we sketch a DC conductance measurement of a Coulomb peak, which is modeled as a Lorentzian curve, as a function of the plunger gate voltage of a sensor dot. Assuming the load (the sensor dot) has been matched (discussed below) to $Z_0 = 2h/e^2 \approx 51.6\,\text{k}\Omega$ (typical range for sensor dots), we can see that the reflected power (proportional to $|\Gamma^2|$) is not proportional the Lorentzian shape. This means that RF reflectometry's measured quadrature may not linearly map to the conductance measured by DC transport.

Radio-frequency measurement of the SET (and QD)

In the previous section a typical homodyne detection setup has been briefly introduced, showing also with a cartoon model that the homodyne voltage V_{H} does not necessarily map linearly to the current signal. Transmission lines have a characteristic impedance in the range of tens of Ω, with the most common nominal value $Z_0 = 50\,\Omega$. If one were to connect a sensor dot with characteristic impedance in the tens of kΩ, the signal would always be reflected because of $|\Gamma| \approx 1$. It is possible to match the sensor dot by connecting it to a tank circuit with a capacitor and an inductor, realizing an RLC circuit (where the sensor dot is modeled as a variable resistor). Ideally a matched load receives all power from the RF carrier, that otherwise would be reflected. It can be shown in the series RLC approximation [120] that the matching ($Z_{\text{L}} \approx 50\,\Omega$) then occurs when

$$R_{\text{match}} = \frac{L}{C_{\text{p}} Z_0}, \tag{2.5}$$

where R_{match} is the resistance to be matched, and $Z_0 = 50\,\Omega$. Since R_{match} is in general in the tens of kΩ range as mentioned before, Eq. 2.5 gives a constraint in the ratio between the inductor L and the parasitic capacitance C_{p}. The latter is not something that can be properly controlled, as it depends on the printed circuit board, the bonding, and the device capacitance to ground and it is usually in the range of $\approx 1\,\text{pF}$. The second constraint is the wanted resonant frequency

$$f_R = \frac{1}{2\pi\sqrt{LC_{\text{p}}}}. \tag{2.6}$$

Since the wanted resonant frequency is usually in the tens or few hundred MHz range, the inductor L ranges from hundreds of nH up to $\approx 1\,\mu\text{H}$.

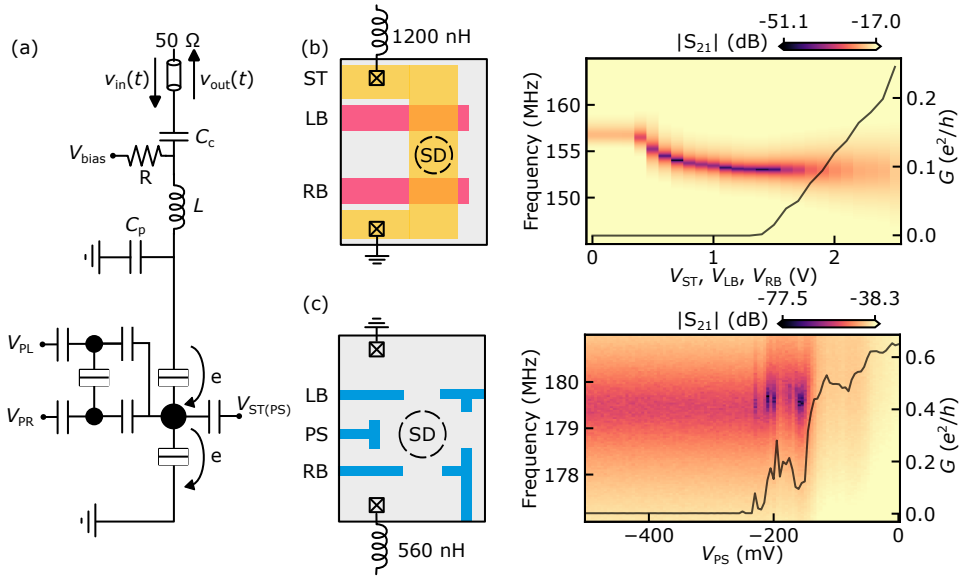

Fig. 2.7: **RF reflectometry response while "turning on" the SETs. (a)** Schematic of a tank circuit wire-bonded to one of the two ohmics of the sensor dot, which is capacitively coupled to two QDs. The sensor dot chemical potential is controlled by a voltage $V_{ST(PS)}$, while the dots are to be charge-sensed by $V_{PL(PR)}$. **(b)** On the right, the RF reflectometry response and turn-on current (black curve) of a SiMOS SET, which is schematized in the left panel. We observe a capacitive shift due to the electron charge accumulating below the ST gate. **(c)** On the right, RF reflectometry response and turn-on current (black curve) of the bottom right GaAs SET of the device 1.3(b), schematized in the left panel. Better matching (dips in |S21|) occurs when Coulomb peaks are measured around −200 mV.

Figure 2.7 (a) is a circuit schematic of RF reflectometry through one ohmic contact of a single-electron transistor, which is capacitively coupled to a DQD. The RF carrier $v_{in}(t) \propto \cos(\omega_{LO} t + \phi_0)$ probes the tank circuit through a coupling capacitor C_c (neglected in Eq. 2.5). The ohmic is biased by V_{bias} through the resistor R connected on the printed circuit board to the inductor. The inductor is wire-bonded to one ohmic of the sensor dot, and the left (LB) and right (RB) gate barriers confine the sensor dot such that the RF excitation provides an AC excitation on top of the DC bias V_{bias}. The excitation makes the electron tunnel in and out of the sensor dot, and the impinging RF signal power is dissipated in the sensor dot, which is resistive. In general dissipation causes a change in amplitude in the frequency response of the tank circuit. The sensor dot is capacitively coupled to both dots in the array to be charge sensed, but there is no electron exchange between the sensor dot and the dots array represented by capacitors in the schematic. The inner dots are tunnel coupled to each other, and their chemical potential is controlled by their respective plunger voltages $V_{PL(PR)}$. In the schematic, cross-capacitance effects between the gates and the dots are neglected, as well as the presence of the barriers.

In Fig. 2.7(b) an example of the RF signal response while turning on the SET of a SiMOS device depicted on the left, measured with a Rohde & Schwarz ZNB20 vector network analyzer

(VNA) with port 1 connected to TxA and port 2 connected to RxA (see Fig. 2.4) using SMA cables HUBER+SUHNER ST18. The IMEC device's identifier is IMEC AL809789 D18 D3SD4 QBB16 3 6. Before the turn-on of the SET, a notable decrease in the resonant frequency is measured, presumably due to the 2DEG accumulating below the ST gate. The signal $|\mathrm{S21}(f)|$ at frequency f is the amplitude ratio of sine wave ($V_{\mathrm{out}}(f)$ using the phasor notation) from RxA [cf. Fig. 2.4] over the sine wave sent to TxA ($V_{\mathrm{in}}(f)$), which in dB reads:

$$|\mathrm{S21}(f)|_{\mathrm{dB}} \equiv 20\log\left(\frac{|V_{\mathrm{out}}(f)|}{|V_{\mathrm{in}}(f)|}\right) = 20\log\big(\alpha(f)G(f)|\Gamma(f)|\big), \tag{2.7}$$

where α denotes the losses, G the gain of the cryogenic amplifier, and Γ the reflection coefficient introduced in the Sec. 2.3, this time adding the frequency dependence f.

Figure 2.7(c) reports a similar measurement, performed this time in T7, for the bottom right sensor dot of Fig. 1.3(c), schematized on the left. From the measurement on the right, at sufficiently negative voltages the 2DEG is pinched off (no current goes through the SET), but as the plunger gate is increased, Coulomb peaks appear corresponding to a decrease in $|\mathrm{S21}(f)|$ close to 180 MHz. In general it is easier to achieve matching in GaAs because of the low resistance of the channel compared to the SiMOS device (which is an accumulation type device), as well as the reduced capacitance of the gates (which are much larger in Si devices than GaAs).

Dispersive readout [120] is an alternative technique to ohmic-based reflectometry. It can be applied to measurement-based feedback protocols without an additional quantum dot acting as a sensor dot. An example of dispersive charge sensing without reservoirs is presented in Appendix D.

2.4 Low- and high-frequency lines in-situ calibration

Cutoff frequencies and correction

To measure the transfer function of the lines, with and without the bias-tee, we use a SiMOS device similar to the one shown in Fig. 1.3(d). Figure 2.8(a) shows an RF reflectometry measurement of the sensor dot Coulomb peaks as a function of the left plunger V_{PL} of the DQD (the qubit dot plunger is capacitively coupled to the sensor dot).

The cutoff frequency of, e.g. a low-pass filter, is the frequency at which the output power is half (−3 dB) of the input power, given a sinusoidal input signal. In the following we use a square waveform instead of a sine wave, which are not equivalent, but the cutoff frequency is expected to be similar. With a square wave input, in theory one could calculate the power of each harmonic component and then determine at which harmonic the power is reduced by half.

First, the low-frequency input port of the bias-tee is characterized using a Keysight 33600A waveform generator. The waveform generator is programmed to output a square wave $v_{\mathrm{PL}}(t)$ 50% duty cycle, $\approx 20\,\mathrm{mV_{pp}}$ [see Fig. 2.8(b)]. The waveform generator can also offset the DC component V_{PL} of the square wave, and it is connected to the breakout box to V_{PL}. Here V_{PL} refers to the low-frequency signal, whereas $v_{\mathrm{PL}}(t)$ is the high-frequency one.

To measure the cutoff frequency from the DC port of the bias-tee, we use as reference the Coulomb peak around 65 mV of panel (a) (pointed by the arrow). In Fig. 2.8(c) the waveform generator sweeps V_{PL} between ≈ 40 mV and ≈ 90 mV, while on top the square waveform $v_{\mathrm{PL}}(t)$ is applied (still from the BNC port) with variable frequency. The fitted cutoff from (c) is (88 ± 15) Hz, close to the value of about 100 Hz found from LTspice simulations described in Appendix C.

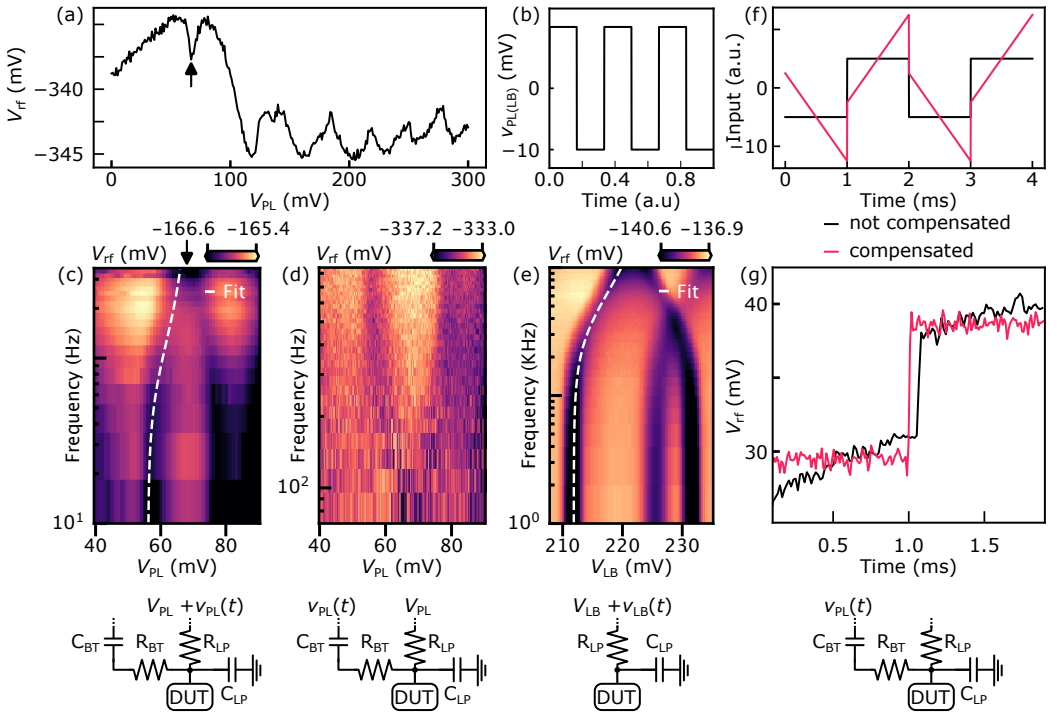

Fig. 2.8: **Bias-tee cutoff frequency and correction**. **(a)** Measured V_{rf} while sweeping the left plunger V_{PL} of a SiMOS device whose schematic is in Fig. 1.6(a), over the Coulomb peaks of the sensor dot under ST to which V_{PL} is capacitively coupled. **(b)** Square waveform with 50% duty cycle applied to the device (with amplitude signal at the device level), to measure the transfer function in situ. **(c)** DUT response while applying the square waveform $v_{PL}(t)$ of (b) with DC offset V_{PL} from the RT BNC breakout box to the low-frequency line of the bias-tee [cf. Fig. 2.5(c)]. The Coulomb peak pointed by the arrow in (a) splits according to the bandwidth of the investigated line. **(d)** DUT response while applying the square waveform $v_{PL}(t)$ of (b) from the RT SMA breakout box to the high-frequency line of the bias-tee, and DC offset V_{PL} to the low-frequency line. **(e)** DUT response while applying the square waveform $v_{LB}(t)$ of (b) with DC offset V_{LB} to a low-frequency line (from the RT BNC breakout box) with only the RC filter. **(f)** The uncompensated (compensated) waveform of period 500 Hz is shown in the black (red) curve. The compensated one takes into account the high-pass filter in the motherboard applied to the high-frequency signal. **(g)** DUT response while applying an uncompensated (compensated) waveform from (f). Due to the high-pass filter, the uncompensated square waveform shows the discharge of the bias-tee.

To characterize the cutoff frequency from the high-frequency port of the bias tee, we repeat a similar measurement, see Fig. 2.8(d). This time we sweep V_{PL} from the BNC port with a QDAC I channel and we apply $v_{\mathrm{PL}}(t)$ with a Tektronix 5014C to the high-frequency line. Note the $v_{\mathrm{PL}}(t)$ amplitude is defined at the device level by taking into account the attenuation in the cryostat lines, as explained in the next section.

Last, we measure the RC time of a low-frequency line (no bias-tee) by using as a feature a similar Coulomb peak, this time sweeping the left barrier LB of the sensor dot as a gate [1.3(d)], capacitively coupled to that feature. Similarly to Fig. 2.8(a), in (e) the Keysight 33600A waveform generator is used to sweep the bias voltage V_{LB} on top the waveform $v_{\mathrm{LB}}(t)$. The fitted cutoff is found to be (47 ± 1) kHz, which does not agree with the value of ≈ 30 kHz found from the LTspice simulations (Appendix C). A sine wave at the input instead of a square wave may help reduce the discrepancy between the measurements and the simulations.

When the high-frequency waveform repetition rate becomes comparable with the bias-tee cutoff frequency (as a rule of thumb, within a factor of 20), the waveform should be compensated for the bias-tee discharge of time constant $\tau = RC$. In Fig. 2.8(f) we plot a square waveform of frequency 500 Hz, and zero-average. The bias V_{PL} is chosen such that the high (low) level of the square pulse corresponds to a Coulomb peak (Coulomb blockade regime) of the sensor dot (again, due to capacitive coupling). By applying a square pulse with the Tektronix 5014C and measuring in the laboratory time domain with the Alazar card digitizer, it can be seen in Fig. 2.8(g) that the high and low levels of the square pulse have a slope because of the bias-tee discharge. The slope is corrected by multiplying the original signal by the inverse of the transverse function of the bias-tee (approximated by a single zero), as offered by the "ripasso" module of the broadbean package [156].

More specifically, the module has two types of filters: an RC-circuit high-pass and an RC-circuit low-pass. We focus on the n-th order high-pass transfer function

$$H_n(f) = \left(\frac{2\pi f \mathrm{i}\tau}{1 + 2\pi f \mathrm{i}\tau} \right)^n, \tag{2.8}$$

where the parameter τ is one over the cutoff frequency. The filter compensation is performed by multiplying with the inverse transfer function in the frequency domain, and transforming back to the time domain, e.g. for a given signal $s(t)$ and a high-pass filter of order n,

$$s_{\mathrm{filtered}}(t) = \mathcal{F}^{-1}[\mathcal{F}[s](f) \cdot H_n(f)](t) \tag{2.9}$$

and

$$s_{\mathrm{compensated}}(t) = \mathcal{F}^{-1}[\mathcal{F}[s](f) \cdot H_{-n}(f)](t). \tag{2.10}$$

We choose $n = 1$, which results in the red curve in Fig. 2.8(f), and we show the corresponding output in panel (g), where the optimal time constant $\tau \approx 1.24$ ms has been optimized by fitting the red curve to a Heavyside function. We measure the black and red traces with a slightly different trigger delay, which explains the time shift of around ≈ 1 ms in the rise of the waveform.

Another point related to the high-pass filtering and pulse design is that in general, one may want the voltage on the gates to be equal to the DC value set by the DAC, whenever the waveform generator outputs zero voltage. The high-pass filter from the bias-tee shifts the average voltage throughout the pulse to zero and causes a heating effect. Often, it is convenient to keep the measurement point where it is set by the DAC, such that all the waveform generator channels are outputting zero at that time. To fix this, an additional pulse segment, in the Spin Qubit group called

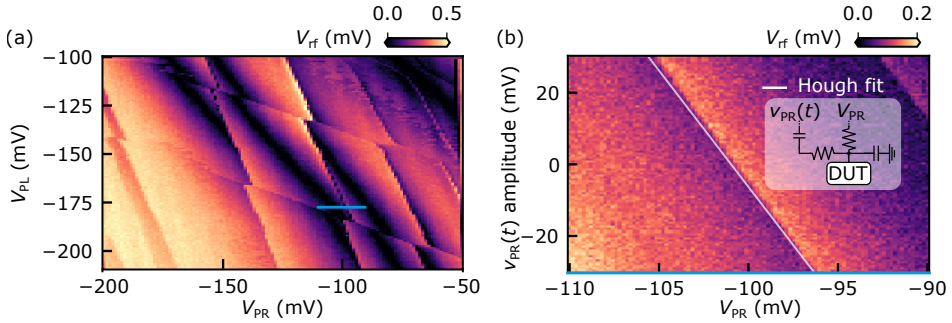

Fig. 2.9: **High-frequency pulse voltage calibration. (a)** Charge stability map as a function of V_{PL} and V_{PR} from the GaAs bottom right DQD shown in Fig. 1.3(b). The charge transition across the blue line is used to extract the divider of the fast line connected to P_R. **(b)** 2D scan is taken in about 3 s by ramping the low-frequency (QDAC-II) and high-frequency (OPX+) channels. The divider is extracted from the slope of the charge transition line, and is fit by a Hough transform (see main text). Inset: applied voltage $v_{PR}(t)$ (V_{PR}) to the AC (DC) side of the bias-tee with the OPX+ (QDAC-II).

"Correction D" or "CorrD" is added to a qubit cycle sequence, such that the average voltage of the qubit cycle pulse is equal to zero. The CorrD pulse can be inserted at the end of the sequence, and it usually lasts a few microseconds, after the measurement and before the initialization, to discharge the bias-tee before the next qubit cycle.

In this section the bias-tee used in this work has been characterized *in situ* with a SiMOS device. Next, we show how to calibrate the output amplitude of the high-frequency waveform generator given the attenuation in the coax lines in the cryostat.

Divider calibration

In a device, the gates have much higher impedance $|Z_L|$ than the cryostat lines and the filters resistance at LF, so in general the potential drop along the cryostat lines is negligible. The situation is different for the high-frequency lines (Fig. 2.4) which are attenuated at different stages of the dilution refrigerator, to reduce the number of thermal photons emitted from RT. This means that whenever a gate is wire-bonded to the output of a bias-tee, the high-frequency waveform generator signal must be amplified by a so-called divider D factor, to have the desired amplitude at the device. The relationship between the line nominal attenuation $\alpha^{(\mathrm{dB})}$ and D is:

$$D = \frac{1}{2} 10^{\alpha^{(\mathrm{dB})}/20}, \tag{2.11}$$

where the factor of 1/2 comes from the gates impedance $|Z_L| \gg 50\,\Omega$. For instance, if a coax has nominal attenuation $\alpha^{(\mathrm{dB})} = 25\,\mathrm{dB}$, then $D \approx 8.9$. This means that if we want a square pulse at the device levels of $\pm 10\,\mathrm{mV}$, then we need to set the output of the waveform generator to $\pm 10\,\mathrm{mV} \times D \approx \pm 89\,\mathrm{mV}$.

In reality, D will differ from the nominal value because of losses, also depending on the frequency (see later Fig. C.4). One way to calibrate it is, for instance, by measuring a charge stability map as the one in Fig. 2.9(a), as a function of $V_{PL(R)}$ in the bottom right DQD in Fig. 1.3. The 2D map is measured by ramping the QDAC-II [157] channels with $\approx 3\,\mathrm{ms}$ per pixel, and (only) at the

beginning of the 2D scan the QDAC-II triggers the OPX for readout by outputting an RF burst of $\approx 3\,\text{ms}$ per pixel, with a total measurement time of $120 \cdot 120 \cdot 3\,\text{ms} \approx 43.2\,\text{s}$. The whole program, including pulling the data from the server and storing it in the database, takes almost 46 s. To extract the divider of the gate P_R, a feature as a function of that gate is needed. We set $V_{PL} \approx -175\,\text{mV}$ and we program V_{PR} to sweep between about $-110\,\text{mV}$ and $-90\,\text{mV}$ [blue line in (a)]. The calibration requires a guess of the divider D_{guess}, which can be set equal to Eq. 2.11 (the expected theoretical one based on the nominal attenuation of the high-frequency line). For Fig. 2.9(b), $D_{\text{guess}} = 6.33$ (from a previous measurement) and the OPX channel associated with P_R is programmed to output a staircase waveform of maximum amplitudes (in absolute value) $\pm 30\,\text{mV} \cdot D_{\text{guess}} \approx \pm 189.9\,\text{mV}$ (assuming high-impedance load). At a given value of V_{PR} on the x-axis of Fig.2.9(b), the OPX channel is stepped from $-189.9\,\text{mV}$ to $189.9\,\text{mV}$ in 100 steps, each step about $1\,\mu\text{s}$ long, as long as the RF readout burst. Notice the OPX average output signal per column is zero. Thus one does not need to worry about the DC component being removed by the capacitor in the bias tee in series with the high-frequency signal. This is repeated 300 times for each column in (b), so each pixel corresponds to an integration time of $300 \cdot 1\,\mu\text{s} = 300\,\mu\text{s}$. At the end of each column, the OPX triggers the QDAC-II which steps to the next P_R value, which is also stepped 100 times between $-110\,\text{mV}$ and $-90\,\text{mV}$. Overall, the measurement takes about $300\,\mu\text{s} \cdot 100 \cdot 100 = 3\,\text{s}$, and the whole program including saving data about $\approx 3.3\,\text{s}$. From the slope of the antidiagonal feature in (b), extracted by a Hough fit giving angle $\alpha \approx 24.68°$ (with respect to $-V_{PR}$) after filtering the norm of the gradient of the 2D map, the new divider is found according to:

$$D_{\text{final}} = \frac{D_{\text{guess}}}{\tan\left(\frac{\pi}{2} + \alpha \cdot \frac{\pi}{180°}\right) \cdot \frac{V_{PR}^{(f)} - V_{PR}^{(i)}}{v_{PR}^{(f)} - v_{PR}^{(i)}}}. \tag{2.12}$$

Given the values $V_{PR}^{(f)} = -90\,\text{mV}$, $V_{PR}^{(i)} = -110\,\text{mV}$, $v_{PR}^{(f)} = -v_{PR}^{(i)} = 30\,\text{mV}$, it is extracted $D_{\text{final}} \approx 8.73$, slightly higher than the expected 7.06 from a 23 dB attenuated line. In theory, by repeating several times the same measurement, D_{guess} should converge to D_{final}, where each D_{final} is used for the following D_{guess}. A similar measurement was repeated for P_L, yielding a divider of ≈ 8.60, again slightly higher than the expected nominal value of 7.06.

2.5 Conclusions

In this Chapter we have presented the Triton 4 setup, from the cryostat main components down to the sample puck where the devices are located. After upgrading the cryostat to a larger puck, we tested coax lines and DC looms at RT (see Appendix C). Last, we have reviewed RF reflectometry working principle. We have characterized *in situ* the cutoff frequencies of the PCB, as well as the attenuation in the cryostat lines. In the next three Chapters, we present the core results of this Thesis.

3

Real-time Two-axis Control of a Spin Qubit

Optimal control of qubits requires the ability to adapt continuously to their ever-changing environment. We demonstrate a real-time control protocol for a two-electron singlet-triplet qubit with two fluctuating Hamiltonian parameters[1]. Our approach leverages single-shot readout classification and dynamic waveform generation, allowing full Hamiltonian estimation to dynamically stabilize and optimize the qubit performance. Powered by a field-programmable gate array (FPGA), the quantum control electronics estimates the Overhauser field gradient between the two electrons in real time, enabling controlled Overhauser-driven spin rotations and thus bypassing the need for micromagnets or nuclear polarization protocols. It also estimates the exchange interaction between the two electrons and adjusts their detuning, resulting in extended coherence of Hadamard rotations when correcting for fluctuations of both qubit axes. Our study highlights the role of feedback in enhancing the performance and stability of quantum devices affected by quasistatic noise.

3.1 Introduction

Feedback is essential for stabilizing quantum devices and improving their performance. Real-time monitoring and control of quantum systems allows for precise manipulation of their quantum states [8, 158]. In this way, it can help mitigate the effects of quantum decoherence and extend the lifetime of quantum systems for quantum computing and quantum sensing applications [3], for example in superconducting qubits [159, 160, 161, 162, 148], spins in diamond [163, 164, 166, 165, 167, 168], trapped atoms [169, 170], and other platforms [171, 172, 173, 174, 175, 176].

Among the various quantum-information processing platforms, semiconductor spin qubits [51, 29] are promising for quantum computing because of their long coherence times [45] and foundry compatibility [67]. Focusing on spin qubits hosted in gate-controlled quantum dots (QDs), two-qubit gate fidelities of 99.5% and single-qubit gate fidelities of 99.8% have recently been achieved in silicon [106]. In germanium, a four-qubit quantum processor based on hole spins enabled all-electric qubit logic and the generation of a four-qubit Greenberger-Horne-Zeilinger state [177]. In gallium arsenide, simultaneous coherent exchange rotations and four-qubit measurements in a 2×2 array of singlet-triplets were demonstrated without feedback, revealing site-specific fluctuations of nuclear spin polarizations [36]. In silicon, a six-qubit processor was operated with

[1] This Chapter is published in Fabrizio Berritta et al. "Real-time two-axis control of a spin qubit". In: *Nature Communications* 15 (2024), p. 1676. DOI: 10.1038/s41467-024-45857-0, and reused in accordance with the CC BY license.

high fidelities enabling universal operation, reliable state preparation and measurement [178]. In germanium, in a 2×4 quantum dot array universal control of four singlet-triplet qubits was shown [179].

Achieving precise control of gated qubits can be challenging due to their sensitivity to environmental fluctuations, making feedback necessary to stabilize and optimize their performance. Because feedback-based corrections must be performed within the correlation time of the relevant fluctuations, real-time control is essential. Continuous feedback then allows to calibrate the qubit environment and to tune the qubit in real time to maintain high-fidelity gates and improved coherence, for instance by suppressing low-frequency noise and improving π-flip gate fidelity [180]. An active reset of a silicon spin qubit using feedback control was demonstrated based on quantum non-demolition readout [181]. Real-time operation of a charge sensor in a feedback loop [182] maintained the sensor sensitivity for fast charge sensing in a Si/SiGe double quantum dot, compensating for disturbances due to gate-voltage variation and $1/f$ charge fluctuations. A quantum state with higher confidence than what is achievable through traditional thermal methods was initialized by real-time monitoring and negative-result measurements [183].

This study implements real-time two-axis control of a qubit with two fluctuating Hamiltonian parameters that couple to the qubit along different directions on its Bloch sphere. The protocol involves two key steps: first, rapid estimation of the instantaneous magnitude of one of the fluctuating fields (nuclear field gradient) effectively creates one qubit control axis. This control axis is then exploited to probe in real time the qubit frequency (Heisenberg exchange coupling) across different operating points (detuning voltages). Our procedure allows for counteracting fluctuations along both axes, resulting in an improved quality factor of coherent qubit rotations.

Our protocol integrates a singlet-triplet (ST_0) spin qubit implemented in a gallium arsenide double quantum dot (DQD) [36] with Bayesian Hamiltonian estimation [109, 184, 185, 186, 187]. Specifically, an FPGA-powered quantum controller (OPX [146]) repeatedly separates singlet-correlated electron pairs using voltage pulses and performs single-shot readout classifications to estimate on-the-fly the fluctuating nuclear field gradient within the double dot [31]. Knowledge of the field gradient in turn enables the quantum controller to coherently rotate the qubit between S and T_0 by arbitrary, user-defined target angles. Differently from previous works, we let the gradient freely fluctuate, without pumping the nuclear field [117], and instead program the quantum controller to adjust the baseband control pulses accordingly.

An adaptive second-axis estimation is performed to also probe the exchange interaction between the two electrons. This exchange interaction estimation scheme is not simply an independent repetition of the single-axis estimation protocol [109, 184, 185, 186, 187]: the design of the exchange-based free induction decay (FID) pulse sequence depends on the outcome of the first-axis estimation and needs to be computed on the fly. Finally, fluctuations along both axes are measured and corrected, enabling the stable coherent rotation of the qubit around a symmetric axis, essential for performing the Hadamard gate.

Our work introduces a versatile method for enhancing coherent control and stability of spin qubits by harnessing low-frequency environmental fluctuations coupling to the system. As such, it is not limited to the operation of ST_0 qubits in GaAs. Our implementation of real-time reaction to fluctuating Hamiltonian parameters can find application in other materials and qubit encodings, as it is not necessarily limited to nuclear noise.

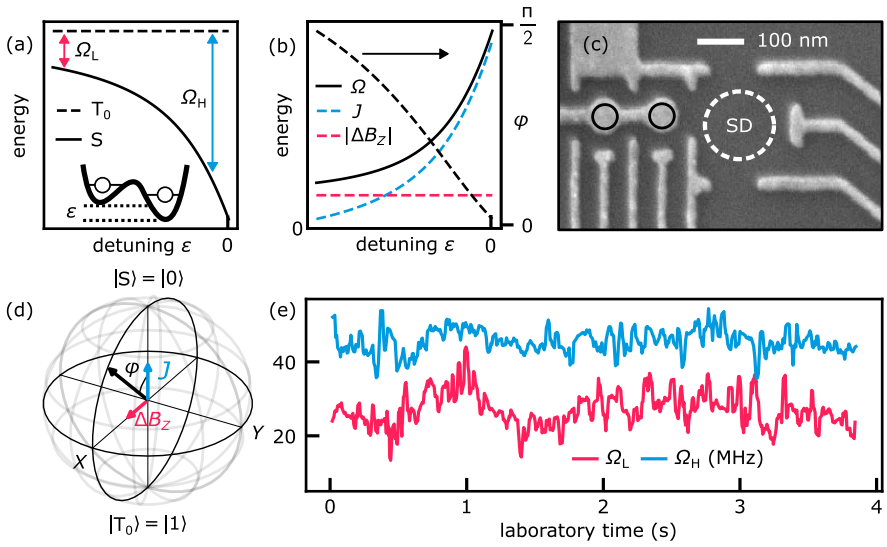

Fig. 3.1: **A singlet-triplet (ST_0) qubit with two fluctuating control axes.** **(a)** The dots' electrical detuning ε tunes from a regime of low qubit frequency, Ω_L, to a regime of high frequency, Ω_H. States outside the computational space are not plotted. **(b)** In the first (second) regime, the Overhauser gradient $|\Delta B_z|$ (the exchange coupling J) dominates the qubit frequency Ω_L (Ω_H) and the polar angle φ of the qubit rotation axis. **(c)** SEM image of the GaAs device [36], implementing a two-electron double quantum dot (black circles) next to its sensor dot (SD) for qubit readout. **(d)** J and ΔB_z drive rotations of the qubit around two orthogonal axes, providing universal qubit control, as depicted in the Bloch sphere. **(e)** Uncontrolled fluctuations of the Larmor frequencies Ω_L and Ω_H, estimated in real time on the quantum controller and plotted with a 30 ms moving average.

3.2 Device and Bayesian estimation

We use a top-gated GaAs DQD array from [36] [Q3 in Fig. 1.3(b)] and tune up one of its ST_0 qubits using the gate electrodes shown in Fig. 3.1(c), at 200 mT in-plane magnetic field in a dilution refrigerator with a mixing-chamber plate below 30 mK. Radio-frequency reflectometry off the sensor dot's ohmic contact distinguishes the relevant charge configurations of the DQD [120].

The qubit operates in the (1,1) and (0,2) charge configuration of the DQD. (Integers indicate the number of electrons in the left and right dot.) The electrical detuning ε quantifies the difference in the electrochemical potentials of the two dots, which in turn sets the qubit's spectrum as shown in Fig. 3.1(a). We do not plot the fully spin-polarized triplet states, which are independent of ε and detuned in energy by the applied magnetic field. We define $\varepsilon = 0$ at the measurement point close to the interdot (1,1)-(0,2) transition, with negative ε in the (1,1) region. In the ST_0 basis, we model the time-dependent Hamiltonian by

$$\mathcal{H}(t) = J(\varepsilon(t))\frac{\sigma_z}{2} + g^*\mu_B\Delta B_z(t)\frac{\sigma_x}{2}, \tag{3.1}$$

which depends on the detuning ε that controls the exchange interaction between the two electrons, $J(\varepsilon(t))$, and the component of the Overhauser gradient parallel to the applied magnetic field

between the two dots, $\Delta B_z(t)$. σ_i are the Pauli operators, g^* is the effective g-factor, and μ_B is the Bohr magneton. In the following, we drop the time dependence of the Hamiltonian parameters for ease of notation. On the Bloch sphere of the qubit [Fig. 3.1(d)], eigenstates of the exchange interaction, $|S\rangle$ and $|T_0\rangle$, are oriented along Z, while ΔB_z enables rotations along X.

The qubit is manipulated by voltage pulses applied to the plunger gates of the DQD, and measured near the interdot (1,1)-(0,2) transition by projecting the unknown spin state of (1,1) onto either the (1,1) charge state ($|T_0\rangle$) or the (0,2) charge state ($|S\rangle$). Each single-shot readout of the DQD charge configuration involves generation, demodulation, and thresholding of a few-microsecond-long radio-frequency burst on the quantum controller (see 3.6 in Sec. 3.9).

The quantum controller allows for real-time calculation of the qubit Larmor frequency $\Omega(\varepsilon) = \sqrt{\Delta B_z^2 + J(\varepsilon)^2}$ at different detunings, based on real-time estimates of ΔB_z and $J(\varepsilon)$.

Inspecting the exchange coupling in a simplified Fermi-Hubbard hopping model [51] and inserting $J(\varepsilon)$ into equation 3.1 suggests two physically distinct regimes [Fig. 3.1(b)]: At low detuning, in the (1,1) charge state configuration, the Overhauser gradient dominates the qubit dynamics. In this regime, the qubit frequency reads $\Omega_L \equiv \sqrt{\Delta B_z^2 + J_{res}^2}$, where we have added a small phenomenological term J_{res} to account for a constant residual exchange between the two electrons at low detuning. Such a term may become relevant when precise knowledge of ΔB_z is required, for example for the Hadamard protocol at the end of this study. At high detuning, close to the (1,1)-(0,2) interdot charge transition, exchange interaction between the two electrons dominates, and the qubit frequency becomes $\Omega_H(\varepsilon) \equiv \sqrt{\Delta B_z^2 + J(\varepsilon)^2}$. As shown in Fig. 3.1(b), the detuning affects both the Larmor frequency Ω and the polar angle φ of the qubit rotation axis $\hat{\boldsymbol{\omega}}$, with φ approaching 0 in the limit $J(\varepsilon) \gg \Delta B_z$ and $\pi/2$ if $J(\varepsilon) \ll \Delta B_z$.

Without the possibility of turning off either J or ΔB_z, the rotation axes of the singlet-triplet qubit are tilted, meaning that pure X- and Z-rotations are unavailable. In their absence, the estimation of the qubit frequency at different operating points is crucial for navigating the whole Bloch sphere of the qubit. Figure 3.1(e) tracks Larmor frequencies Ω_H and Ω_L, both fluctuating over tens of MHz over a period of several seconds, using a real-time protocol as explained later. The presence of low-frequency variations in time traces of Ω_H and Ω_L suggests that qubit coherence can be extended by monitoring these uncontrolled fluctuations in real time and appropriately compensating qubit manipulation pulses on-the-fly.

To estimate the frequency of the fluctuating Hamiltonian parameters on the quantum controller, we employ a Bayesian estimation approach based on a series of free-induction-decay experiments [109]. Using m_i to represent the outcome ($|S\rangle$ or $|T_0\rangle$) of the i-th measurement after an evolution time t_i, the conditional probability $P(m_i|\Omega)$ is defined as the probability of obtaining m_i given a value of Ω:

$$P(m_i|\Omega) = \frac{1}{2}\left[1 + r_i\left(\alpha + \beta\cos(2\pi\Omega t_i)\right)\right], \tag{3.2}$$

where r_i takes a value of 1 (-1) if $m_i = |S\rangle$ ($|T_0\rangle$), and α and β are determined based on the measurement error and axis of rotation on the Bloch sphere.

Applying Bayes' rule to estimate Ω based on the observed measurements $m_N, \ldots m_1$, which are assumed to be independent of each other, yields the posterior probability distribution $P(\Omega\,|m_N, \ldots m_1)$ in terms of a prior uniform distribution $P_0(\Omega)$ and a normalization constant $\mathcal{N}$:

$$P(\Omega\,|m_N, \ldots m_1) = P_0(\Omega)\mathcal{N}\prod_{i=1}^{N}\left[1 + r_i\left(\alpha + \beta\cos(2\pi\Omega t_i)\right)\right]. \tag{3.3}$$

Based on previous works [109, 186, 187], we fix $\alpha = 0.25$ and $\beta = \pm 0.5$, with the latter value positive when estimating Ω_{L} and negative when estimating Ω_{H}. The expectation value $\langle\Omega\rangle$, calculated over the posterior distribution after all N measurements, is then taken as the final estimate of Ω.

3.3 Controlled Overhauser gradient driven rotations

We first implement qubit control using one randomly fluctuating Hamiltonian parameter, through rapid Bayesian estimation of Ω_{L} and demonstration of controlled rotations of a ST_0 qubit driven by the prevailing Overhauser gradient. Notably, this allows coherent control without a micromagnet [116, 188] or nuclear spin pumping [117].

Ω_{L} is estimated from the pulse sequence shown in Fig. 3.2(a): for each repetition a singlet pair is initialized in (0,2) and subsequently detuned deep in the $(1,1)$ region ($\varepsilon_{\mathrm{L}} \approx -40\,\mathrm{mV}$) for $N = 101$ linearly spaced separation times t_i up to 100 ns. After each separation, the qubit state, $|\mathrm{S}\rangle$ or $|\mathrm{T}_0\rangle$, is assigned by thresholding the demodulated reflectometry signal V_{rf} near the (1,1)-(0,2) interdot transition and updating the Bayesian probability distribution of Ω_{L} according to the outcome of the measurement. After measurement m_N, the initially uniform distribution has narrowed [inset of Fig. 3.2(b), with white and black indicating low and high probability], allowing the extraction of $\langle\Omega_{\mathrm{L}}\rangle$ as the estimate for Ω_{L}. For illustrative purposes, we plot in Fig. 3.2(a) the N single-shot measurements m_i for 10,000 repetitions of this protocol, which span a period of about 20 s, and in Fig. 3.2(b) the associated probability distribution $P(\Omega_{\mathrm{L}})$ of each repetition. The quality of the estimation seems to be lower around a laboratory time of 6 seconds, coinciding with a reduced visibility of the oscillations in panel 3.2(a). We attribute this to an enhanced relaxation of the triplet state during readout due to the relatively high $|\Delta B_z|$ gradient during those repetitions [189]. The visibility could be improved by a latched or shelved read-out [190, 191] or energy-selective tunneling-based readout [186].

Even though the rotation speed around $\hat{\boldsymbol{\omega}}_{\mathrm{L}}$ at low detuning is randomly fluctuating in time, knowledge of $\langle\Omega_{\mathrm{L}}\rangle$ allows controlled rotations by user-defined target angles. To show this, we task the quantum controller in Fig. 3.2(d) to adjust the separation times $\tilde{t}_j$ in the pulse sequence to rotate the qubit by $M = 80$ different angles $\theta_j = \tilde{t}_j \langle\Omega_{\mathrm{L}}\rangle$ between 0 and 8π. In our notation, the tilde in a symbol $\tilde{x}$ indicates that the waveform parameter x is computed dynamically on the quantum controller. To reduce the quantum controller memory required for preparing waveforms with nanosecond resolution, we perform controlled rotations only if the expected Ω_{L} is larger than an arbitrarily chosen minimum of 50 MHz. (The associated IF statement and waveform compilation then takes about 40 µs on the quantum controller.) This reduces the number of precomputed waveforms needed for the execution of pulses with nanosecond-scale granularity, for which we use the quantum controller baked waveforms capability. Accordingly, the number of rows in Fig. 3.2(d) (1,450) is smaller than in panel (a), and we only label a few selected rows with their repetition number.

To show the increased rotation-angle coherence of controlled $|\Delta B_z|$-driven rotations, we plot the average of all 1,450 repetitions of Fig. 3.2(d) and compare the associated quality factor[2], $Q \gtrsim 7$, with that of uncontrolled oscillations, $Q \approx 1$. The average of the uncontrolled S-T_0 oscillations in Fig. 3.2(a) can be fit by a decay with Gaussian envelope (solid line), yielding an inhomogeneous dephasing time $T_2^* \approx 30\,\mathrm{ns}$ typical for ST_0 qubits in GaAs [192]. We associate the relatively smaller amplitude of stabilized qubit oscillations with the low-visibility region around 6 seconds

[2] We define the quality factor as the number of oscillations until the amplitude is $1/e$ of its original value.

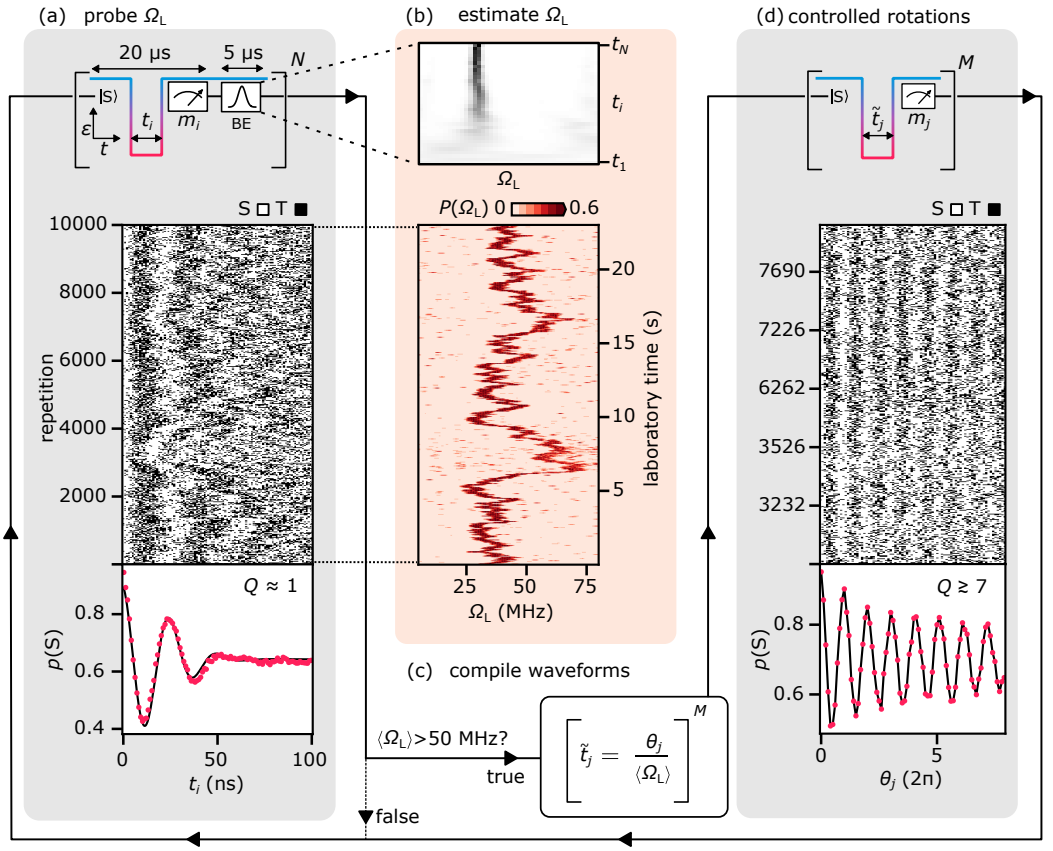

Fig. 3.2: **Controlled Overhauser gradient driven rotations of a ST_0 qubit by real-time Bayesian estimation.** One loop (solid arrows) represents one repetition of the protocol. **(a)** For each repetition, the quantum controller estimates Ω_L by separating a singlet pair for N linearly spaced probe times t_i and updating the Bayesian estimate (BE) distribution after each measurement, as shown in the inset of (b) for one representative repetition. For illustrative purposes, each single-shot measurements m_i is plotted as a white/black pixel, here for $N = 101$ Ω_L probe cycles, and the fraction of singlet outcomes in each column is shown as a red dot. **(b)** Probability distribution $P(\Omega_L)$ after completion of each repetition in a. Extraction of the expected value $\langle\Omega_L\rangle$ from each row completes Ω_L estimation. **(c)** For each repetition, unless $\langle\Omega_L\rangle$ falls below a user-defined minimum (here 50 MHz), the quantum controller adjusts the separation times $\tilde{t}_j$, using its real-time knowledge of $\langle\Omega_L\rangle$, to rotate the qubit by user-defined target angles $\theta_j = \tilde{t}_j \langle\Omega_L\rangle$. **(d)** To illustrate the increased coherence of Overhauser gradient driven rotations, we task the quantum controller to perform $M = 80$ evenly spaced θ_j rotations. Single-shot measurements m_j are plotted as white/black pixels, and the fraction of singlet outcomes in each column is shown as a red dot.

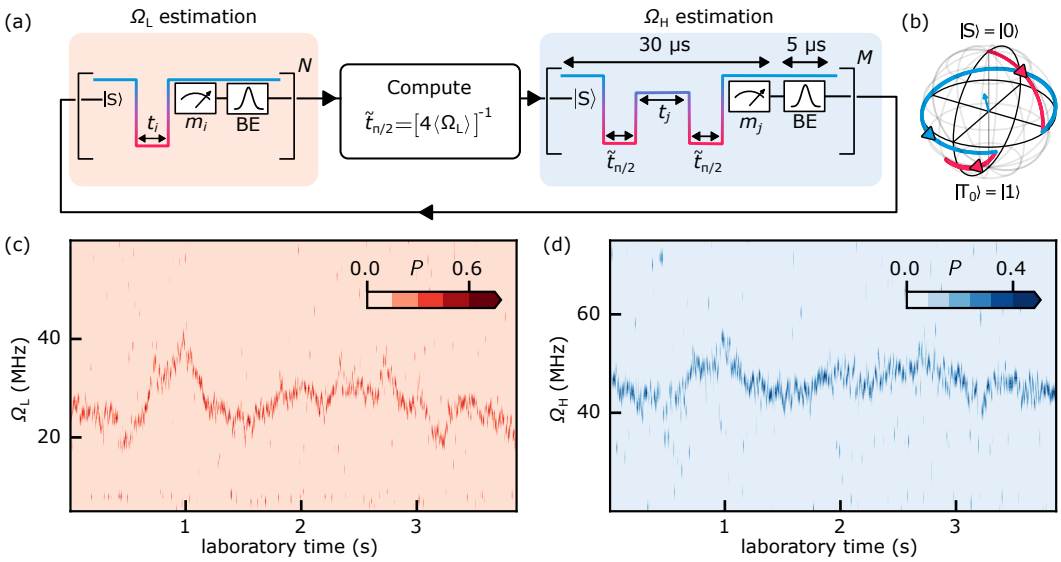

Fig. 3.3: **Real-time Bayesian estimation of two control axes. (a)** One repetition of the two-axis estimation protocol. After estimating Ω_L from $N = 101$ t_i probe cycles [Fig. 3.2(a)], the quantum controller computes on-the-fly the pulse duration $\tilde{t}_{\pi/2}$ required to initialize the qubit near the equator of the Bloch sphere by a diabatic $\Omega_L(\pi/2)$ pulse. After the $\Omega_L(\pi/2)$ pulse, the qubit evolves for time t_j under exchange interaction before another $\Omega_L(\pi/2)$ pulse initiates readout. After each single-shot measurement m_j, the quantum controller updates the BE distribution of Ω_H. Similar to t_i in the Ω_L estimation, t_j is spaced evenly between 0 and 100 ns across $M = 101$ exchange probe cycles. **(b)** Qubit evolution on the Bloch sphere during one exchange probe cycle. **(c)** Each column plots $P(\Omega_L)$ after completion of the Ω_L estimation in each protocol repetition. **(d)** Each column plots $P(\Omega_H)$ after completion of the Ω_H estimation in each protocol repetition.

in Fig. 3.2(d), discussed earlier. Excluding such regions by post selection increases the visibility and quality factor of oscillations (see Fig. 3.10). Overall, the results presented in this section exemplify how adaptive baseband control pulses can operate a qubit reliably, out of slowly fluctuating environments.

3.4 Real-time two-axis estimation

In addition to nuclear spin noise, ST_0 qubits are exposed to electrical noise in their environment, which affects the qubit splitting in particular at higher detunings. It is therefore important to examine and mitigate low-frequency noise at different operating points of the qubit. In the previous section, the qubit frequency Ω_L was estimated entirely at low detuning where the Overhauser field gradient dominates over the exchange interaction. In order to probe and stabilize also the second control axis, namely J-driven rotations corresponding to small φ in Fig. 3.1(d), we probe the qubit frequency Ω_H at higher detunings, using a similar protocol with a modified qubit initialization.

Free evolution of the initial state |S⟩ around $\hat{\boldsymbol{\omega}}_L$ would result in low-visibility exchange-driven

oscillations because of the low value of φ. To circumvent this problem, we precede the Ω_{H} estimation by one repetition of Ω_{L} estimation, as shown in Fig. 3.3(a). This way, real-time knowledge of $\langle\Omega_{\mathrm{L}}\rangle$ allows the initial state $|\mathrm{S}\rangle$ to be rotated to a state near the equator of the Bloch sphere, before it evolves freely for probing Ω_{H}. This rotation is implemented by a diabatic detuning pulse from (0,2) to ε_{L} (diabatic compared to the interdot tunnel coupling) for time $\tilde{t}_{\pi/2}$, corresponding to a rotation of the qubit around $\hat{\boldsymbol{\omega}}_{\mathrm{L}}$ by an angle $\Omega_{\mathrm{L}}\tilde{t}_{\pi/2} = \pi/2$. After evolution for time t_j under finite exchange, another $\pi/2$ rotation around $\hat{\boldsymbol{\omega}}_{\mathrm{L}}$ rotates the qubit to achieve a high readout contrast in the ST_0 basis, as illustrated on the Bloch sphere in Fig. 3.3(b).

As a side note, we mention that in the absence of knowledge of the Overhauser field gradient, the qubit would traditionally be initialized near the equator by adiabatically reducing detuning from (0,2) to the (1,1) charge configuration, and a reverse ramp for readout. Such adiabatic ramps usually last several microseconds each, while our $\tilde{t}_{\pi/2}$ pulses typically take less than 10 ns, thereby significantly shortening each probe cycle.

For the estimate of Ω_{H}, the Bayesian probability distribution of Ω_{H} is updated after each of the $M = 101$ single-shot measurement m_j, each corresponding to a separation time t_j that is evenly stepped from 0 to 100 ns. The Bayesian probability distributions of both Ω_{L} and Ω_{H} are shown in Fig. 3.3(c) and (d), respectively, with the latter being conditioned on $20\,\mathrm{MHz} < \langle\Omega_{\mathrm{L}}\rangle < 40\,\mathrm{MHz}$ to reduce the required quantum controller memory.

This section demonstrated a real-time baseband control protocol that enables manipulation of a spin qubit on the entire Bloch sphere.

3.5 Controlled exchange-driven rotations

Using Bayesian inference to estimate control axes in real-time offers new possibilities for studying and mitigating qubit noise at all detunings. Figure 3.4a describes the real-time controlled exchange-driven rotations protocol aimed at stabilizing frequency fluctuations of the qubit at higher detunings. Following the approach of Fig. 3.3, we first estimate Ω_{L} and Ω_{H} using real-time Bayesian estimation. We then use our knowledge of Ω_{H} to increase the rotation angle coherence of the qubit where the exchange coupling is comparable with the Overhauser field gradient.

As illustrated in Fig. 3.4(a), the qubit control pulses now respond in real time to both qubit frequencies Ω_{L} and Ω_{H}. Similar to the previous section, after determining $\langle\Omega_{\mathrm{L}}\rangle$ and confirming that $30\,\mathrm{MHz} < \langle\Omega_{\mathrm{L}}\rangle < 50\,\mathrm{MHz}$ is fulfilled, the qubit is initialized near the equator of the Bloch sphere by fast diabatic $\Omega_{\mathrm{L}}(\pi/2)$ pulses, followed by an exchange-based FID that probes Ω_{H}. Based on the resulting $\langle\Omega_{\mathrm{H}}\rangle$, the quantum controller adjusts the separation times $\tilde{t}_l$ to rotate the qubit by user-defined target angles $\theta_l = \tilde{t}_l\,\langle\Omega_{\mathrm{H}}\rangle$.

To show the resulting improvement of coherent exchange oscillations, we plot in Fig. 3.4(c) the interleaved $K = 101$ measurements m_l and compare them in Fig. 3.4(b) to the $M = 101$ measurements m_j. Fitting the average of the uncontrolled rotations by an oscillatory fit with Gaussian envelope decay yields $T_{\mathrm{el}}^{*} \approx 60\,\mathrm{ns}$ and $Q \approx 3$, presumably limited by electrical noise [192], while the quality factor of the controlled rotations is enhanced by a factor of two, $Q \approx 6$.

The online control of exchange-driven rotations using Bayesian inference stabilizes fluctuations of the qubit frequency at higher detunings, where fluctuations are more sensitive to detuning noise. Indeed, we attribute the slightly smaller quality factor, relative to Overhauser-driven rotations in Fig. 3.2(d), to an increased sensitivity to charge noise at larger detuning, which, owing to its high-frequency component, is more likely to fluctuate on the estimation timescales [184].

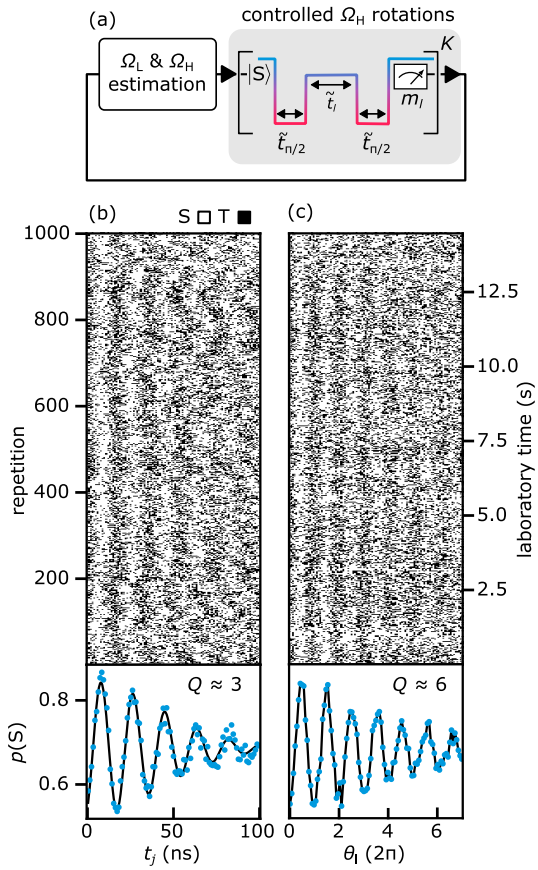

Fig. 3.4: **Real-time-controlled exchange-driven qubit rotations. (a)** One repetition of the exchange rotation protocol. After estimation of Ω_L and Ω_H as in Fig. 3.3, the quantum controller adjusts exchange duration times $\tilde{t}_l$, using real-time knowledge of $\langle\Omega_H\rangle$, to rotate the qubit by user-defined target angles $\theta_l = \tilde{t}_l \langle\Omega_H\rangle$. Pulse durations $\tilde{t}_{\pi/2}$ for qubit initialization and readout use real-time knowledge of $\langle\Omega_L\rangle$. **(b)** Each row plots measurements m_j from one protocol repetition, here $M = 101$ exchange probe outcomes. **(c)** Each row plots measurement m_l from one protocol repetition, here $K = 101$ controlled-exchange-rotation outcomes. To illustrate the increased coherence of controlled exchange rotations, we also plot in (b) and (c) the fraction of singlet outcomes of each column.

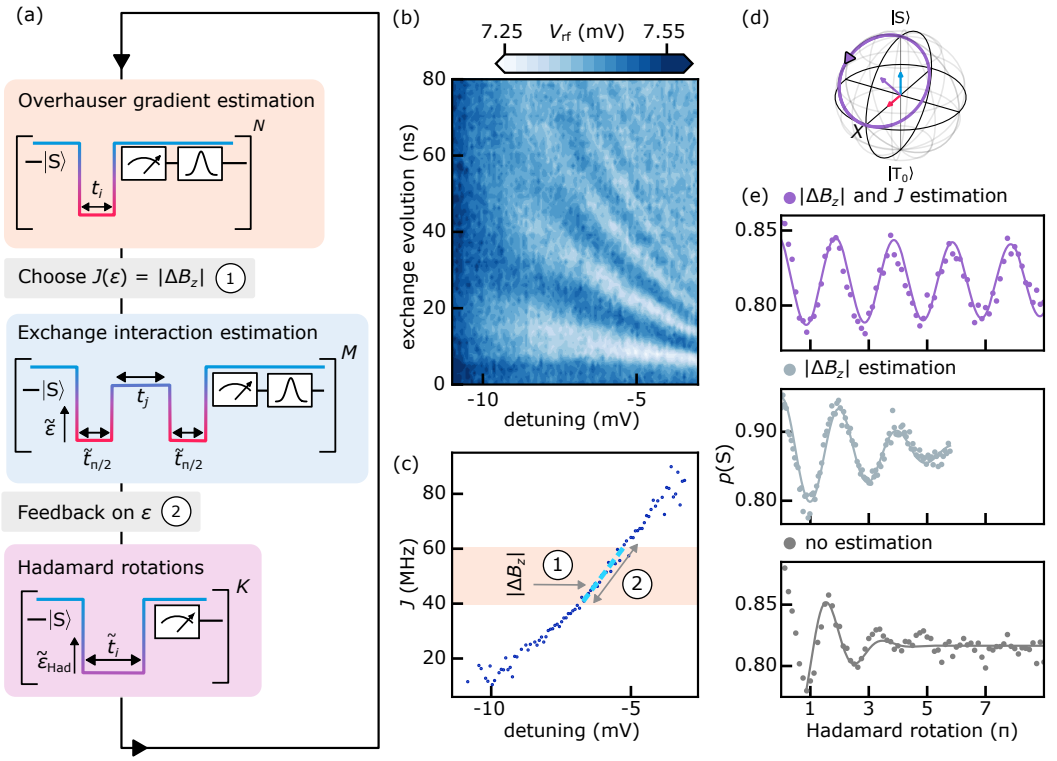

Fig. 3.5: **Real-time universal ST_0 control demonstrated by Hadamard rotations.** **(a)** Hadamard rotation protocol. After estimating Ω_L, ε is chosen in real-time such that $J(\varepsilon) = |\Delta B_z|$, based on a linearized offline model from panel (c). If $40\,\text{MHz} < \langle|\Delta B_z|\rangle < 60\,\text{MHz}$, the detuning is adjusted to account for deviations of the prevailing J from the offline model. Real-time knowledge of $\Omega_{\text{Had}} = \sqrt{2}\,|\Delta B_z|$ then dictates $\tilde{t}_i$ to achieve a user-defined Hadamard rotation angle. **(b)** Averaged exchange driven FID as a function of detuning and evolution time. Here, a diabatic $\Omega_L(\pi/2)$ pulse initializes the qubit near the equator of the Bloch sphere, prior to free exchange evolution, and subsequently prepares it for readout. **(c)** J as a function of ε extracted offline from (b), as well as a linearized model (dashed line) used in the two feedback steps of panel (a). **(d)** Hadamard rotation depicted on the Bloch sphere. **(e)** Measurement of Hadamard rotations with $|\Delta B_z|$ and J estimation (purple, top panel), only $|\Delta B_z|$ estimation (light gray, middle panel), and without the feedback shown in a (dark gray, bottom panel).

This section established for the first time stabilization of two rotation axes of a spin qubit. This advancement should allow for stabilized control over the entire Bloch sphere, which we demonstrate in the next section.

3.6 Hadamard rotations

In this experiment, we demonstrate universal ST_0 control that corrects for fluctuations in all Hamiltonian parameters. We execute controlled Hadamard rotations around $\hat{\boldsymbol{\omega}}_{\mathrm{Had}}$, as depicted by the trajectory on the Bloch sphere of Fig. 3.5(d), by selecting the detuning $\varepsilon_{\mathrm{Had}}$ in real time such that $J(\varepsilon_{\mathrm{Had}}) = |\Delta B_z|$. To achieve this, we do not assume that $\Delta B_z = \Omega_{\mathrm{L}}$ (i.e. we allow contributions of J_{res} to Ω_{L}) or that $J = \Omega_{\mathrm{L}}$ (i.e. we allow contributions of ΔB_z to Ω_{H}). The full protocol is detailed in Sec. 3.9.

Real-time knowledge of both ΔB_z and J would potentially benefit two-qubit gate fidelities [97] and the resonant-driving approach of previous works [109, 186, 187]. In the resonant implementation, constrained to the operating regime $|\Delta B_z| \gg J$, low-frequency fluctuations of J result in transverse noise that causes dephasing and phase shifts of the Rabi rotations [193, 194].

In previous sections, we have shown how to probe the qubit Larmor frequencies Ω_{H} and Ω_{L} at different detunings in real time and correct for their fluctuations. Now, we simultaneously counteract fluctuations in J and $|\Delta B_z|$ on the quantum controller in order to perform the Hadamard gate. As we do not measure the sign of ΔB_z, we identify the polar angle of $\hat{\boldsymbol{\omega}}_{\mathrm{Had}}$ as either $\varphi = \pi/4$ or $-\pi/4$.

In other words, starting from the singlet state, the qubit rotates towards $+X$ on the Bloch sphere for one sign of ΔB_z, and towards $-X$ for the other sign. The sign of the gradient may change over long time scales due to nuclear spin diffusion (on the order of many seconds [31]), but the measurement outcomes of our protocol are expected to be independent of the sign.

The relative sign of Overhauser gradients becomes relevant for multi-qubit experiments [195], and could be determined following [196] by comparing the relaxation time of the ground state (e.g. $|\uparrow\downarrow\rangle$) of ΔB_z with its excited state ($|\downarrow\uparrow\rangle$). Such diagnostic sign-probing cycles on the quantum controller should not require more than a few milliseconds, negligible compared to the expected time between sign reversals.

In preparation for our protocol, we first extract the time-averaged exchange profile by performing exchange oscillations as a function of evolution time [Fig. 3.5(b)]. Removing contributions of ΔB_z to Ω_{H} then yields $J(\varepsilon)$ in Fig. 3.5(c). A linear approximation in the target range $40\,\mathrm{MHz} < \langle J \rangle < 60\,\mathrm{MHz}$ (dashed blue line) is needed later on the quantum controller to allow initial detuning guesses when tuning up $J(\varepsilon) = |\Delta B_z|$. We also provide the quantum controller with a value for the residual exchange at low detuning, $J_{\mathrm{res}} \approx 20\,\mathrm{MHz}$, determined offline as described in Fig. 3.11.

As illustrated in Fig. 3.5(a), the Hadamard rotation protocol starts by estimating $|\Delta B_z|$ from Ω_{L}, taking into account a constant residual exchange by solving $\Delta B_z^2 = \Omega_{\mathrm{L}}^2 - J_{\mathrm{res}}^2$.

Next, an initial value of $\varepsilon_{\mathrm{Had}}$ is chosen based on the linear offline model to fulfill $J(\varepsilon_{\mathrm{Had}}) = |\Delta B_z|$ [feedback ① in panel (a,c)]. To detect any deviations of the prevailing J from the offline model, an exchange-driven FID is performed at $\varepsilon_{\mathrm{Had}}$ to estimate J from Ω_{H}, using $J^2 = \Omega_{\mathrm{H}}^2 - \Delta B_z^2$.

Any deviation of $\langle J \rangle$ from the target value $|\Delta B_z|$ is subsequently corrected for by updating $\varepsilon_{\mathrm{Had}}$ based on the linearized $J(\varepsilon)$ model [feedback ② in panels (a,c)]. Matching J to $|\Delta B_z|$ in the two detuning feedback steps each takes about 400 ns on the quantum controller. Finally, real-time knowledge of $\Omega_{\mathrm{Had}} \equiv \sqrt{2}|\Delta B_z|$ is used to generate the free evolution times $\tilde{t}_i$, spent at the updated value $\tilde{\varepsilon}_{\mathrm{Had}}$, in order to perform Hadamard rotations by K user defined target angles.

The resulting Hadamard oscillations are shown in Fig. 3.5(e) (top panel) and fitted with an exponentially decaying sinusoid, indicating a quality factor $Q > 5$. (According to this naive fit, the amplitude drops to 1/e over approximately 40 rotations, although we have not experimentally ex-

plored rotation angles beyond 9π.) In comparison to exchange-controlled rotations from Fig. 3.4(c), the Hadamard rotations are more stable, which we attribute to the additional feedback on detuning that fixes the oscillation axis and decreases sensitivity to charge noise.

To illustrate the crucial role of real-time estimation for this experiment, we also performed rotation experiments that do not involve any real-time estimation and feedback cycles (dark gray data, bottom panel), as follows. Within minutes after performing the controlled Hadamard rotations (purple data), we executed Hadamard rotations assuming a fixed value of $|\Delta B_z| = \overline{|\Delta B_z|}$, i.e. by pulsing to a fixed detuning value corresponding to $J(\varepsilon_{\mathrm{H}}) = \overline{|\Delta B_z|}$ according to the offline model. Here, $\overline{|\Delta B_z|} \approx 40$ MHz is the average Overhauser gradient that we observed just before executing the Hadamard protocol. Not surprisingly, the quality factor of the resulting Hadamard-like oscillations is low and the rotation angle deviates from the intended target angle, likely due to the Overhauser gradient having drifted in time. As a side note, we mention that the purple data in Fig. 3.5(e) constitutes an average over 5,000 repetitions, corresponding to a total acquisition time of 2 minutes including Overhauser and exchange estimation cycles. In contrast, the dark gray data also constitutes an average over 5,000 repetitions, but only required 15 seconds because of the omission of all estimation and feedback cycles.

To verify that the enhancement in Q is not solely due to the more accurate knowledge of $|\Delta B_z|$, we also performed Hadamard rotations only using the estimation of $|\Delta B_z|$. The quantum controller was programmed to perform a measurement where the initialized singlet is pulsed to a fixed detuning $J(\varepsilon_{\mathrm{H}}) \approx 20\,\mathrm{MHz}$ to perform a Hadamard rotation, only if the estimated $|\Delta B_z|$ on the quantum controller satisfies $17\,\mathrm{MHz} < \langle|\Delta B_z|\rangle < 23\,\mathrm{MHz}$. We then post select the repetitions where $19.5\,\mathrm{MHz} < \langle|\Delta B_z|\rangle < 20.5\,\mathrm{MHz}$. Fitting this by an oscillatory fit with Gaussian envelope decay yields $T_{\mathrm{el}}^{*} \approx 70\,\mathrm{ns}$, $Q \approx 2.0$ and frequency $\approx 29\,\mathrm{MHz}$.

In Figure 3.5(e) we compare these data (light gray, middle panel) with the cases where the quantum controller estimated both $|\Delta B_z|$ and J (purple, top panel) and where the microprocessor does not perform any estimation but simply pulses to $J(\varepsilon_{\mathrm{H}})$ to perform the rotations (dark gray, bottom panel). (In the middle panel the horizontal axis was rescaled to the Hadamard evolution time using the fitted frequency $\approx 29\,\mathrm{MHz}$.) We see that (i) a reduction of the uncertainty in $|\Delta B_z|$ from $\approx 30\,\mathrm{MHz}$ (r.m.s.) to $\approx 2\,\mathrm{MHz}$ (dark gray to light gray) does not yield a proportional gain in Q and (ii) the improvement in Q when including estimation of J (light gray to purple) is much larger than can be justified solely by the slight further reduction of the uncertainty in $|\Delta B_z|$ (roughly from $\approx 2\,\mathrm{MHz}$ to $\approx 1\,\mathrm{MHz}$). This demonstrates the crucial contribution of the estimations along both axes in the improvement of our Hadamard gate quality factor.

Further evidence for the fluctuating nature of non-stabilized Hadamard rotations is discussed in Fig. 3.12.

The stabilized Hadamard rotations demonstrate real-time feedback control based on Bayesian estimation of J and $|\Delta B_z|$, and suggest a significant improvement in coherence for ST_0 qubit rotations around a tilted control axis. Despite the presence of fluctuations in all Hamiltonian parameters, we report effectively constant amplitude of Hadamard oscillations, with a reduced visibility that we tentatively attribute to estimation and readout errors.

3.7 Discussion

Our experiments demonstrate the effectiveness of feedback control in stabilizing and improving the performance of a singlet-triplet spin qubit. The protocols presented showcase two-axis control

of a qubit with two fluctuating Hamiltonian parameters, made possible by implementing online Bayesian estimation and feedback on a low-latency FPGA-powered qubit control system. Real-time estimation allows control pulses to counteract fluctuations in the Overhauser gradient, enabling controlled Overhauser-driven rotations without the need for micromagnets or nuclear polarization protocols. Notably, even in the absence of a deterministic component of the Hamiltonian purely noise-driven coherent rotations of a two-level quantum system were demonstrated.

The approach is extended to the real-time estimation of the second rotation axis, dominated by exchange interaction, which we then combine with an adaptive feedback loop to generate and stabilize Hadamard rotations. In particular, executing the Hadamard gate involves (i) sequentially executing two distinct estimation cycles, where the design of the second cycle relies on the outcomes of the first, (ii) correlating the detected frequencies to distinguish independent fluctuations of the two control axes, and (iii) utilizing this correlated information to dynamically construct and execute a Hadamard gate. These steps demand real-time adaptive estimations and signal generations throughout the protocol, which has not been demonstrated before. A constant Overhauser field gradient, whether stemming from nuclear spin pumping or a micromagnet, is expected to further improve the feedback control. From this perspective, our work represents a worst-case scenario, demonstrating the effectiveness of our experimental technique.

Our protocols assume that ΔB_z does not depend on the precise dot detuning in the (1,1) configuration and remains constant on the time scale of one estimation. Similarly, stabilization of exchange rotations is only effective for electrical fluctuations that are slow compared to one estimation. Therefore, we expect potential for further improvements by more efficient estimation methods, for example through adaptive schemes [197] for Bayesian estimation from fewer samples, or by taking into account the statistical properties of a time-varying signal described by a Wiener process [198] or a nuclear spin bath [199]. Machine learning could be used to predict the qubit dynamics [200, 201, 202], possibly via long short-term memory artificial neural networks as reported for superconducting qubits [203]. While our current qubit cycle time (approximately 30 µs) is dominated by readout and qubit initialization, it can potentially be reduced to a few microseconds through faster qubit state classification, such as enhanced latched readout [191], and faster reset, such as fast exchange of one electron with the reservoir [142]. Our protocol could be modified for real-time non-local noise correlations [204] or in-situ qubit tomography using fast Bayesian tomography [205] to study the underlying physics of the noisy environment, thereby providing qualitatively new insights into processes affecting qubit coherence and multi-qubit error correction.

Beyond ST_0 qubits, our protocols uncover new perspectives on coherent control of quantum systems manipulated by baseband pulses. This work represents a significant advancement in quantum control by implementing an FPGA-powered technique to stabilize in real time the qubit frequency at different manipulation points.

3.8 Methods

Experimental setup

We use an Oxford Instruments Triton 200 cryofree dilution refrigerator with base temperature below 30 mK. The experimental setup employs a Quantum Machines OPX+ for radio-frequency (RF) reflectometry and gate control pulses. The RF carrier frequency is ≈ 158 MHz and the gate control pulses sent to the left and right plunger gates of the DQD are filtered with low-pass filters (≈ 220 MHz) at room temperature, before being attenuated at different stages of the refrigerator.

Low-frequency tuning voltages (high-frequency baseband waveforms) are applied by a QDAC [157] (OPX) via a QBoard high-bandwidth sample holder [155].

Measurement details

Before qubit manipulation, an additional reflectometry measurement is taken as a reference to counteract slow drifts in the sensor dot signal. At the end of each qubit cycle, a $\approx 1\,\mu s$ long pulse is applied to discharge the bias tee. As the qubit cycle period (tens of µs) is much shorter than the bias tee cutoff ($\approx 300\,Hz$), we do not correct the pulses for the transfer function of the bias tee.

3.9 Supplementary

Experimental setup

Figure 3.6 displays the experimental setup used in this study, which comprises a Triton 200 cryofree dilution refrigerator from Oxford Instruments capable of reaching a base temperature below 30 mK. A superconducting vector magnet is thermally anchored to the 4 K plate and can generate 6 T along the main axis z of the refrigerator and 1 T along x or y. It is used to apply an in-plane magnetic field of $B \approx 200\,mT$, along the double quantum dot (DQD) axis (see device schematic in Fig. 3.6). An upper bound of the electron temperature is 100 mK, determined by attributing the observed broadening of the interdot (1,1)-(0,2) charge transition to thermal broadening.

The Quantum Machines OPX+ includes real-time classical processing at the core of quantum control with fast analog feedback. It enables on-the-fly pulse manipulation, which is critical for this experiment [146]. The RF carrier frequency, approximately 158 MHz, is attenuated at room temperature by a programmable step attenuator. The RF carrier power incident onto the PCB sample holder corresponds to between −70 and −80 dBm. Before entering the cryostat, the signal is filtered with low-pass and high-pass filters, and a DC block reduces heating in the coaxial lines caused by the DC component of the RF signal. The RF carrier is reflected by the surface-mounted tank circuit wirebonded to one ohmic of the sensor dot and is amplified by a cryogenic amplifier at 4 K. The RF carrier is then amplified again at room temperature, filtered to avoid aliasing, and digitized at 1 GS/s. As the signal is AC coupled and does not have a $50\,\Omega$ resistance to ground, a bias tee is used to bias the input amplifier of the OPX+.

The QDAC-II [157] can trigger the OPX+, for example while tuning the device in video-mode using the RF reflectometry measurements taken by the OPX+. All the ohmics of the device are grounded at the QDevil QBox, a breakout box where low-pass filters are installed for all the DC lines for the gate voltages. To reduce noise and interference in the signal chain, a QDevil QFilter-II [206] is installed in the cryostat for the DC lines. Additionally, the setup includes a QDevil QBoard sample holder [155], which is a printed circuit board with surface-mounted tank circuits used for multiplexed RF reflectometry. The bias tees have a measured cut-off frequency of $\approx 300\,Hz$, whereas the RC filters have a cut-off frequency $> 30\,kHz$.

Relation between the quality factor and the Bayesian estimation procedure

In this section we show that most of the oscillation decay, i.e., the finite quality factor of coherent rotations in Fig. 3.2, can be explained by the estimation errors. For each estimation procedure we represent the probability distribution of Ω on a regular grid, and update the weights based on

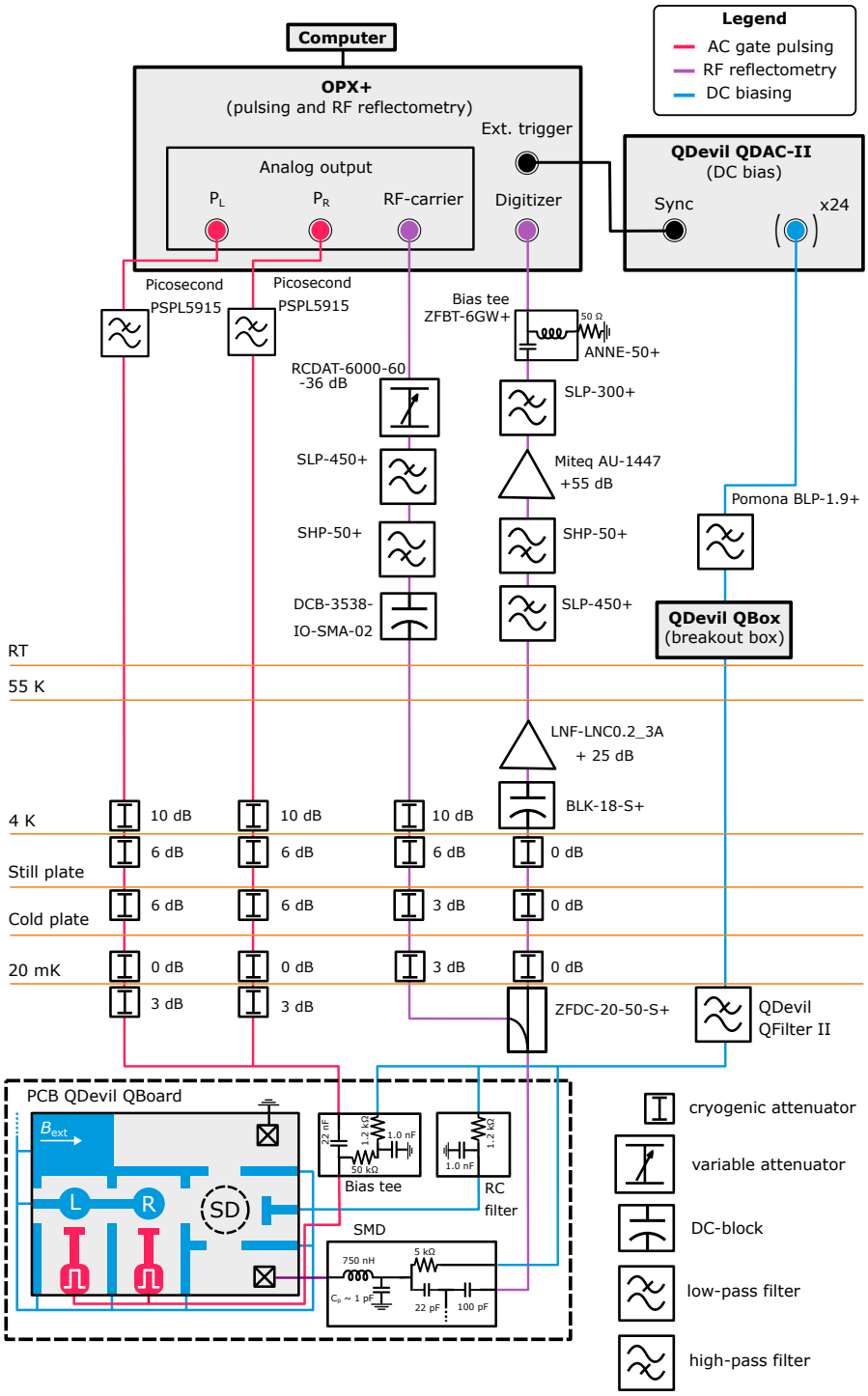

Fig. 3.6: See next page for caption.

Fig. 3.7: **Experimental setup T7 (previous page).** The cryostat is a Triton 200 dilution refrigerator by Oxford Instruments with a base temperature lower than 30 mK. A Quantum Machines OPX+ is used for RF reflectometry and fast gate control pulses with a bandwidth of less than 1 GHz. The RF carrier frequency used is approximately 158 MHz. Additionally, the setup includes a QDevil QDAC-II for generating low-frequency analog signals. A QDevil QFilter-II is used to suppress noise and interference in the signal chain. Finally, the setup incorporates a QDevil QBoard PCB sample holder with surface-mount tank circuits for multiplexed RF reflectometry. Only one of the four qubits of the chip is activated for this experiment.

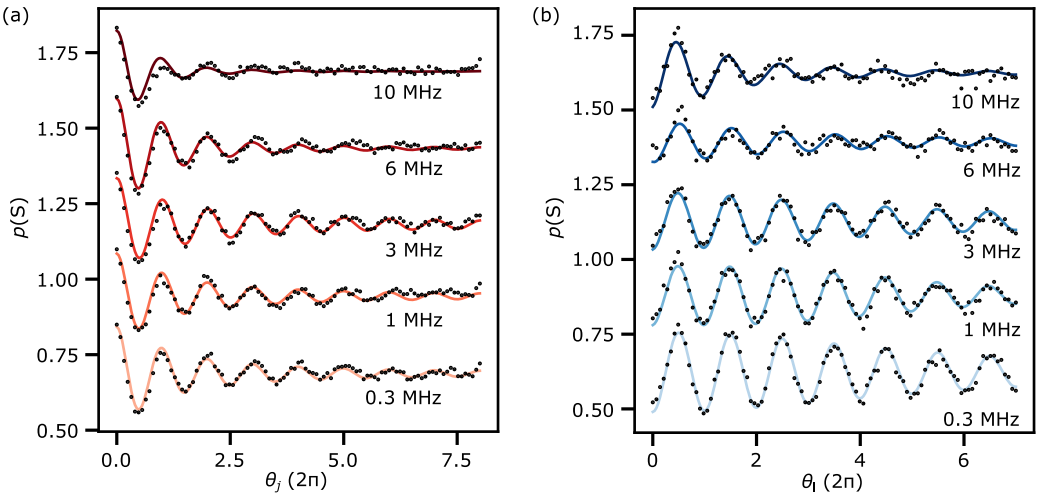

Fig. 3.8: **Frequency resolution of Bayesian estimation. (a)** Each trace shows averaged Overhauser-driven controlled rotations as Fig. 3.2(d). For each trace we used a different frequency resolution for the probability distribution when estimating Ω_{L}, as indicated. The y-axis of each curve is offset for clarity. **(b)** Each trace shows exchange-driven controlled rotations as shown in Fig. 3.4(c). For each trace we used a different frequency resolution for the probability distribution when estimating Ω_{H}, keeping fixed the frequency resolution of Ω_{L} at 1 MHz. The y-axis of each curve is offset for clarity.

the measurement outcome. To convert the final probability distribution to an estimation of the frequency we use the average:

$$\langle \Omega \rangle = \sum_n p(\Omega[n])\Omega[n], \tag{3.4}$$

where $\Omega[n]$ is the frequency and $p(\Omega[n])$ is the corresponding probability. When the estimated frequency is used to adjust the time for coherent rotations $t = \phi/(2\pi\langle\Omega\rangle)$ [in the previous section the qubit rotation angle $\theta \equiv \phi/(2\pi)$], any estimation error $\delta\Omega$ will result in a random phase evolution $\delta\phi = 2\pi\delta\Omega\, t$ that contributes to a decrease in a quality factor.

Finite frequency resolution

The first source of errors can be associated with the finite resolution of the probability distribution. While too high a resolution would significantly slow down an on-the-fly estimation scheme, too

low a resolution would introduce an estimation error, the scale of which can be related to a step size $\delta\Omega \approx (\Omega[n+1] - \Omega[n])/2$.

To optimize the frequency resolution used in the Bayesian estimation, we perform different measurements for both Ω_L and Ω_H. Figure 3.8(a) shows the averaged traces after performing controlled Overhauser-driven rotations whenever $\langle\Omega_L\rangle > 30\,\text{MHz}$, as described in Fig. 3.2. Increasing the frequency resolution from 10 MHz to 0.3 MHz (with frequency span from 10 MHz to 70 MHz) results in an increased number of visible oscillations. However, considering the required computational time by the quantum controller and no appreciable improvements above 0.5 MHz, we choose a resolution of 0.5 MHz throughout this work, resulting in $\approx 5\,\mu\text{s}$ per qubit cycle to update the estimate on the quantum controller.
We also test the frequency resolution of Ω_H in a similar way by performing exchange-driven controlled rotations, as shown in Fig. 3.4, and estimating Ω_H between 40 MHz and 90 MHz. In this case, we also set the resolution to 0.5 MHz to keep the estimation cycle on the few µs scale.

We support the above by a simple model of uncertainty, in which for each realization of the experiment we draw a random error $\delta\Omega \approx \mathcal{N}(0, \sigma^2_{\delta\Omega})$. For simplicity we assume the initialization and measurement axis are perpendicular to the rotation axis, such that the probability of measuring the initial state reads:

$$P_S(\tau) = \frac{1}{2} + \frac{1}{2}\left\langle \cos(2\pi[\Omega + \delta\Omega]\tau)\right\rangle_{\delta\Omega} = \frac{1}{2} + \frac{\cos(2\pi\,\Omega\tau)}{2} W(\tau), \tag{3.5}$$

where $W(\tau)$ is the attenuating function related to classical averaging over repetitions of $\delta\Omega$, which we denoted as $\langle\ldots\rangle_{\delta\Omega}$. For simplicity we assume the errors are normally distributed with characteristic width $\sigma_{\delta\Omega}$, for which $W(\tau) = \exp\left(-2\pi^2\sigma^2_{\delta\Omega}\tau^2\right)$. For the relevant case of stabilized rotations, which are obtained by adjusting evolution time $\tau = 2\pi\Omega/\phi$, we have

$$P_S(\phi) = \frac{1}{2} + \frac{1}{2}\cos(\phi)\exp\left\{-\frac{1}{2}\left(\frac{\sigma_{\delta\Omega}}{\Omega}\right)^2\phi^2\right\} \equiv \frac{1}{2} + \frac{1}{2}\cos(\phi)\exp\left\{-\left(\frac{\phi}{\phi^*_2}\right)^2\right\}, \tag{3.6}$$

where in analogy to dephasing time T_2^* we defined dephasing angle ϕ^*_2, which measures the angle of rotation at which the amplitude falls as 1/e. For a constant estimation error it depends on the estimated frequency, since:

$$\phi^*_2 = \sqrt{2}\,\frac{\Omega}{\sigma_{\delta\Omega}}, \tag{3.7}$$

and can be related to a Q-factor via the equation:

$$Q = \frac{\phi^*_2}{2\pi} = \frac{\Omega}{\sqrt{2}\pi\sigma_{\delta\Omega}}. \tag{3.8}$$

Using the above, we estimate that an resolution-related error of $\sigma_{\delta\Omega} \approx 0.5\,\text{MHz}$ at $\Omega = 20\,\text{MHz}$ (the smallest estimated frequency) should allow for at least $Q \geq 9$. As this number is larger than any measured Q, we conclude the finite resolution of the estimation is not the main factor responsible for observed amplitude decay.

Low quality estimates

Having confirmed sufficiently high resolution (0.5 MHz), another source of errors is associated with low-quality estimates resulting from multi-modal or not sufficiently narrow probability distributions. As a measure of estimation quality we take the variance of the final distribution, defined

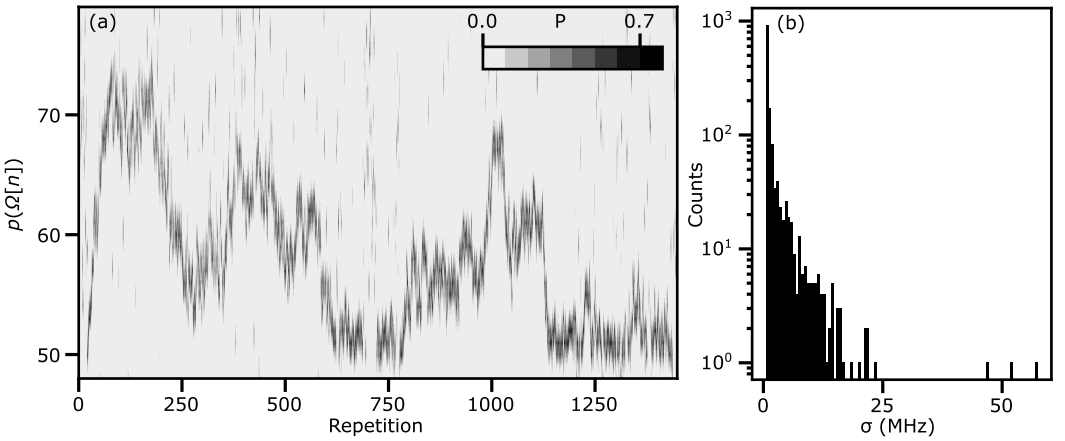

Fig. 3.9: **Standard deviation of Bayesian estimations. (a)** Probability distributions used to estimate frequencies $\langle \Omega_L \rangle > 50\,\text{MHz}$. **(b)** Histogram of corresponding variances σ_{est} of the probability distributions $p(\Omega[n])$.

as:

$$\sigma^2_{\text{est}} = \text{Var}(\Omega) \equiv \sum_n \big(\Omega[n] - \langle \Omega \rangle\big)^2 p(\Omega[n]). \tag{3.9}$$

To show that low-quality estimates play an important role in the loss of oscillation amplitude we post-process the measured data based on σ_{est}. We reject the repetitions with a probability distribution with calculated variance of $\sigma_{\text{est}} > \sigma_{\text{est,max}}$, and we average over the remaining traces. We highlight that in principle, such or an even more sophisticated procedure of quality assessment could also be performed on-the-fly, for instance as a part of the same feedback loop and without the need of measuring the low-quality oscillations.

We test this approach on the experimental data used to generate Fig. 3.2(d). In Fig. 3.9(a), we plot the obtained probability distributions with $\langle \Omega_L \rangle \geq 50\,\text{MHz}$. For each distribution we compute its variance, whose histogram over all the distribution is plotted in Fig. 3.9(b). By imposing an upper bound for the variance $\sigma_{\text{est,max}}$, we can now compute an average such as shown in the bottom panel of Fig. 3.2(d), but now using only a selection of the best estimates.

In Fig. 3.10(b) we plot the ratio of used data $\tilde{N}$ versus total repetition $N = 1450$, as a function of $\sigma_{\text{est,max}}$. For each value of $\sigma_{\text{est,max}}$ we plot in Fig. 3.10(a) the change in the averaged singlet probability $P_S(\theta_j)$ of stabilized oscillations, as compared to the trace shown in Fig. 3.2. In particular, we focus on two different bounds of tolerated variance $\sigma_{\text{est,max}} = 0.8\,\text{MHz}$ and $2.7\,\text{MHz}$, that correspond to rejecting 80% and 50% of the worst estimations, respectively. We mark those values of $\sigma_{\text{est,max}}$ using dashed lines in both panels. Finally, in Fig 3.10c we compare the coherent oscillations obtained using the 20% (green) and 50% (yellow) best estimates against the unfiltered result from Fig. 2(d) (black). We see a significant improvement in the oscillation amplitude, which suggests that the observed decay may be associated with poor performance of the estimation scheme.

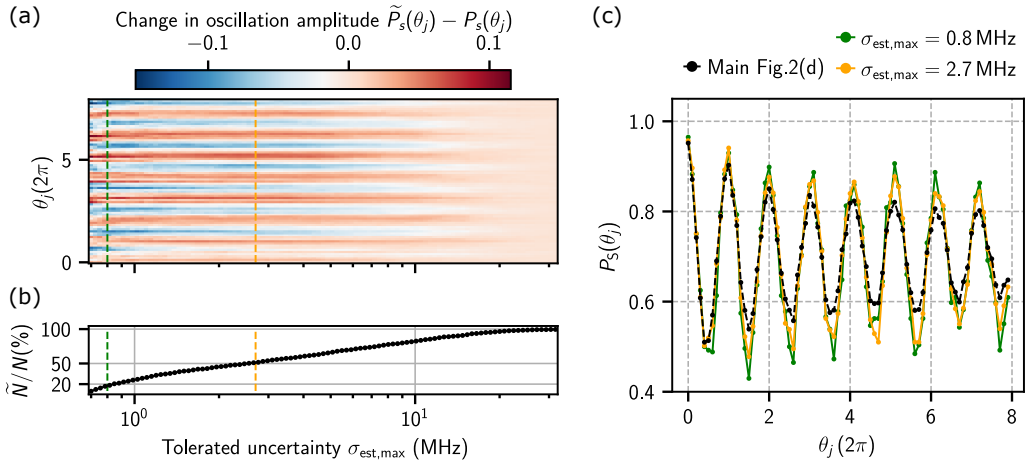

Fig. 3.10: **Improvement of the visibility of coherent oscillations by rejecting low-quality estimates.** **(a)** Change in oscillation amplitude after averaging only the best $\tilde{N}$ estimates out of $N = 1450$ as a function of bound estimation uncertainty $\sigma_{\text{est,max}}$. **(b)** The fraction of used estimations $\tilde{N}/N$ as a function of bound estimation uncertainty $\sigma_{\text{est,max}}$. By dashed lines we mark $\sigma_{\text{est,max}} = 0.7$ MHz (green), and 2.7 MHz (yellow), that correspond to rejecting 80% and 50% of repetitions respectively. **(c)** The resulting averaged oscillations in comparison to unfiltered data (black) from Fig. 3.2(d).

Extracting exchange energy and Overhauser field gradient from Larmor frequencies

In this section, we seek to extract time-dependent knowledge about the exchange energy, $J(t)$, and the Overhauser field gradient, $\Delta B_z(t)$, from the $\Omega_{\text{L}}(t)$ data and $\Omega_{\text{H}}(t)$ data shown in Fig. 3(c,d). To achieve this, we assume $\Omega_{\text{L}}(t) \equiv \sqrt{\Delta B_z^2(t) + J_{\text{res}}^2(t)}$ and $\Omega_{\text{H}}(t) \equiv \sqrt{\Delta B_z^2(t) + J^2(\varepsilon_{\text{H}}, t)}$, and combine this with statistical methods as the problem is not analytically solvable: at each time t, we have two known quantities [$\Omega_{\text{L}}(t)$ and $\Omega_{\text{H}}(t)$] and three unknown ones [$\Delta B_z^2(t)$, $J_{\text{res}}^2(t)$, and $J^2(\varepsilon_{\text{H}}, t)$].

As $\Omega_{\text{H}}(t)$ is probed only when 20 MHz $< \langle\Omega_{\text{L}}(t)\rangle <$ 40 MHz, we downsample $\langle\Omega_{\text{L}}(t)\rangle$ to the same number of points as we have for $\langle\Omega_{\text{H}}(t)\rangle$, by choosing for each value of $\langle\Omega_{\text{H}}(t)\rangle$ the one of $\langle\Omega_{\text{L}}(t)\rangle$ that is closest in time. We then remove any outliers in the data by considering a window of size $w = 15$ around each data point and reject any data point that is more than the standard deviation of its 14 neighboring data points away from the average of those points. In such a case, we replace the rejected data point with that average. We then finally apply a running average with a window size of $w = 5$ to smoothen the data and remove high-frequency noise. In Fig. 3.11a we show the resulting $\langle\Omega_{\text{L,H}}(t)\rangle$, cf. Fig. 3.3(c,d).

We assume the fluctuations of $|\Delta B_z|$ to dominate on this time scale, and thus we square Ω_{L} and Ω_{H} and determine the shift κ_{opt}^2 that results in the best overlap of $\langle\Omega_{\text{L}}(t)\rangle$ and $\sqrt{\langle\Omega_{\text{H}}(t)\rangle^2 - \kappa^2}$, using a least squares method. The result is plotted in Fig. 3.11(b), with $\kappa_{\text{opt}} \approx 36$ MHz, suggesting that on average $J(\varepsilon_{\text{H}})^2 \approx J_{\text{res}}^2 + \kappa_{\text{opt}}^2$. The clear correlation between the two traces confirms the assumption that the fluctuations of $|\Delta B_z|$ dominate over the fluctuations of J. The slightly worse overlap seen in some regions, for instance at about 1 s, are possibly due to fluctuations of J_{res} and $J(\varepsilon_{\text{H}})$.

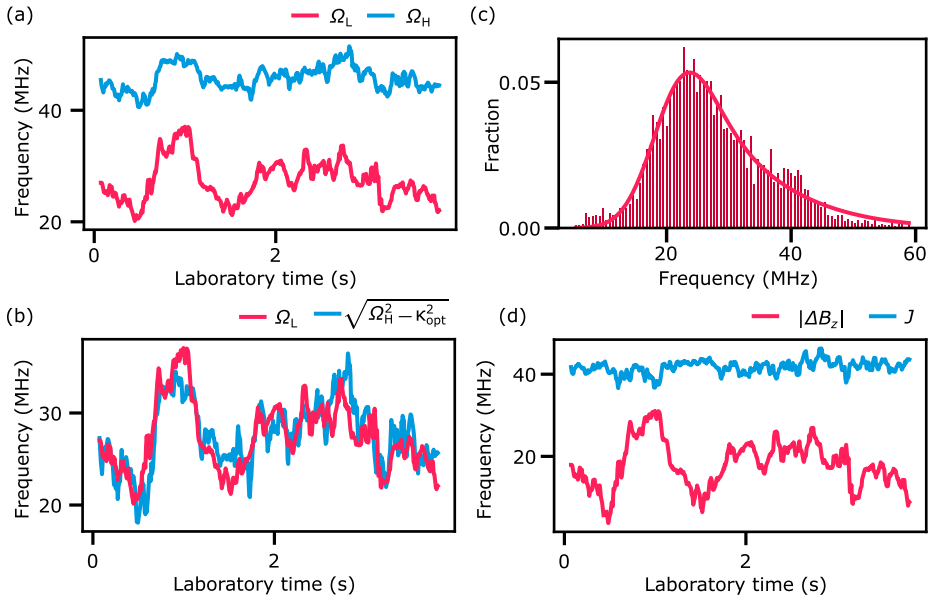

Fig. 3.11: **Extracting fluctuations of the exchange energy and Overhauser field gradient from two different estimated Larmor frequencies. (a)** Fluctuations of the Larmor frequencies Ω_L and Ω_H after removal of estimation outliers (see text). **(b)** The estimated Larmor frequency $\langle\Omega_L(t)\rangle$ and the shifted frequency $\sqrt{\langle\Omega_H(t)\rangle^2-\kappa_{opt}^2}$, based on the same data as shown in Fig. 3.3, where κ_{opt} provides the best overlap using a least-squares error. **(c)** Histogram of a ≈ 36 s long measurement of $\langle\Omega_L\rangle$. From a fit to equation (3.10) (red solid line) the average $J_{res}\approx 20.2$ MHz is found. **(d)** $|\Delta B_z(t)|$ and $J(\varepsilon_H,t)$ extracted from the Larmor frequencies $\Omega_L(t)$ and $\Omega_H(t)$ of main Fig. 3, assuming constant $J_{res}=20.2$ MHz.

Nevertheless, in order to extract direct knowledge about $\Delta B_z(t)$ we still need to determine $J_{res}(t)$ [or $J(\varepsilon_H,t)$] independently. To obtain an average value of $J_{res}(t)$, we combine together longer measurements of $\langle\Omega_L(t)\rangle$ and $\langle\Omega_H(t)\rangle$ taken at different times at the same tuning and cooldown over ≈ 36 s and ≈ 6 s, respectively. We then consider histograms of the measured frequencies without filtering [we show in Fig. 3.11(c) the one obtained for $\langle\Omega_L\rangle$], which we fit to the distribution function

$$\mathcal{P}(\Omega)=\int_{-\Omega}^{\Omega}dJ\frac{1}{\pi\sigma_J\sigma_B}\frac{\Omega}{\sqrt{\Omega^2-J^2}}\exp\left[-\frac{(J-\mu_J)^2}{2\sigma_J^2}\right]\exp\left[-\frac{\Omega^2-J^2}{2\sigma_B^2}\right], \tag{3.10}$$

that gives the probability density for $\Omega=\sqrt{J^2+B^2}$ when J and B are normally distributed variables with means μ_J and zero and variances σ_J^2 and σ_B^2, respectively. The red solid line in Fig. 3.11(c) shows the least-square fit of the data, yielding $\sigma_J\approx 4.63$ MHz, $\sigma_B\approx 22.0$ MHz, $\mu_J\approx 20.2$ MHz for the ≈ 36 s long trace of $\langle\Omega_L(t)\rangle$.

The results of this fit confirm that $\sigma_B>\sigma_J$, i.e., that the fluctuations in the Overhauser gradient dominate those in J_{res}. Indeed, first-order detuning fluctuations of the residual exchange interaction are expected to be zero, as the qubit is tuned close to the symmetry point in the $(1,1)$ charge

state when measuring Ω_{L} [192, 207]. To get a rough picture of the time dependence of $|\Delta B_z(t)|$ we thus replace the residual exchange term $J_{\mathrm{res}}(t)$ by its constant average value μ_J as extracted from the fit and we extract $|\Delta B_z(t)| = \sqrt{\Omega_{\mathrm{L}}^2(t) - \mu_J^2}$ and $J(\varepsilon_{\mathrm{H}}, t) = \sqrt{\Omega_{\mathrm{H}}^2(t) - \Delta B_z^2(t)}$. The result is plotted in Fig. 3.11(d).

Controlled Hadamard rotations

Protocol The aim of this protocol is to perform an adaptive Hadamard gate in a singlet-triplet qubit in GaAs by Bayesian estimation of two Larmor frequencies at different detunings. We define the following quantities:

- $\Omega(\varepsilon) \equiv \sqrt{\Delta B_z^2 + J(\varepsilon)^2}$ is the Larmor frequency at a given detuning ε
- J_{res} is the residual exchange deep in (1,1) ($\varepsilon \approx -40$ mV)
- $\Omega_{\mathrm{L}} \equiv \sqrt{\Delta B_z^2 + J_{\mathrm{res}}^2}$ is the Larmor frequency deep in the (1,1) charge state.
- At the detuning where $J \approx |\Delta B_z|$ (with $|\Delta B_z| \approx [40, 60]$ MHz), we approximate $J(\varepsilon) \approx J(\varepsilon_0) + \alpha\,\Delta\varepsilon$, where α is ≈ 10 MHz/mV and $\varepsilon_0 \approx -16$ mV
- $\Omega_{\mathrm{H}} \equiv \sqrt{\Delta B_z^2 + J(\varepsilon_0)^2}$ is the Larmor frequency at the detuning point defined above
- $\varepsilon_{\mathrm{Had}}$ is the detuning at which $J = |\Delta B_z|$, and in general $\varepsilon_{\mathrm{Had}} \neq \varepsilon_0$ because J fluctuates.

This protocol assumes we have prior knowledge of the residual exchange (assumed constant), an offline model of $J(\varepsilon)$, and $|\Delta B_z|$ does not depend on detuning ε and it fluctuates sufficiently slowly to be considered constant throughout the protocol. Typical values for $J_{\mathrm{res}} \approx [10, 20]$ MHz.

1. Estimate Ω_{L}.
2. Calculate $\Delta B_z^2 = \Omega_{\mathrm{L}}^2 - J_{\mathrm{res}}^2$. If 40 MHz $< |\Delta B_z| <$ 60 MHz, go to the next point. Otherwise repeat 1.
3. Adjust detuning such that $J = |\Delta B_z|$, based on the offline knowledge of $J(\varepsilon) = J(\varepsilon_0) + \alpha\,\Delta\varepsilon$.
4. To learn the prevailing J, perform exchange-based FID around the field found at 3, i.e. where $J = \Delta B_z$, interleaved with $\Omega_{\mathrm{L}}(\pi/2)$ pulses for initialization and readout, from which we estimate Ω_{H} as in Fig. 3.3.
5. Estimate $J^2 = \Omega_{\mathrm{H}}^2 - \Delta B_z^2$ and adjust detuning again such that $J = |\Delta B_z|$ to account for fluctuations of J from the offline model.
6. Perform Hadamard with rotation angle calculated based on $|\Delta B_z|$ by directly jumping to $\varepsilon_{\mathrm{Had}}$.
7. Back to 1.

Details

1. Estimate Ω_{L} by 101 single shots linearly spaced between 0 ns and 100 ns.

2. Calculate $\Delta B_z^2 = \Omega_{\mathrm{L}}^2 - J_{\mathrm{res}}^2 = (\Omega_{\mathrm{L}} + J_{\mathrm{res}})(\Omega_{\mathrm{L}} - J_{\mathrm{res}})$.

3. Adjust detuning such that $J = |\Delta B_z|$. In practice this condition is equivalent to $\Omega_{\mathrm{H}}^2 = 2(\Omega_{\mathrm{L}}^2 - J_{\mathrm{res}}^2)$. Since
$$\Omega_{\mathrm{H}}^2(\varepsilon) \approx (J(\varepsilon_0) + \alpha\Delta\varepsilon)^2 + \Omega_{\mathrm{L}}^2 - J_{\mathrm{res}}^2, \tag{3.11}$$
by solving we get the required detuning shift $\Delta\varepsilon^* = (\Delta B_z - J(\varepsilon_0))/\alpha$.

4. Perform FID with interleaved $\Omega_{\mathrm{L}}(\pi/2)$ pulses, from which we measure $\Omega_{\mathrm{H,meas}}$.

5. Adjust detuning again such that $J = |\Delta B_z|$. We have
$$\Omega_{\mathrm{H,meas}}^2(\varepsilon) \approx (J(\varepsilon_0) + \alpha\Delta\varepsilon_{\mathrm{meas}})^2 + \Omega_{\mathrm{L}}^2 - J_{\mathrm{res}}^2, \tag{3.12}$$
where we have assumed Ω_{L}^2, J_{res}^2 and $J(\varepsilon_0)$ have not changed. We look for the fluctuation in detuning by looking at $\Omega_{\mathrm{H,meas}}^2 - \Omega_{\mathrm{H}}^2$ and find
$$\Delta\varepsilon_{\mathrm{meas}} \approx \frac{\Omega_{\mathrm{H,meas}}^2 - \Omega_{\mathrm{H}}^2}{2J(\varepsilon_0)\alpha} + \Delta\varepsilon^*, \tag{3.13}$$
having neglected second order terms in $\Delta\varepsilon$. So we shift the detuning of the qubit by the amount $\Delta\varepsilon^* - \Delta\varepsilon_{\mathrm{meas}}$.

6. Perform Hadamard with rotation angle calculated based on $\Omega_{\mathrm{Had}} = \sqrt{2}|\Delta B_z|$ by directly jumping to $\varepsilon_{\mathrm{Had}} = \varepsilon_0 + \Delta\varepsilon^* - \Delta\varepsilon_{\mathrm{meas}}$.

7. Back to 1.

Examples of Hadamard rotations without feedback

In Fig. 3.12 we compare the quality of Hadamard rotations with feedback [reproduced from Fig. 3.5(e)] with naive Hadamard rotations without feedback, as explained in Sec. 3.6. In the absence of feedback, the resulting oscillation curves fluctuate randomly in time, even though the cycles of qubit control pulses were nominally identical for panels (b, c, d). This is likely due to the Overhauser gradient drifting over time. (All panels were taken within minutes of each other.) For example, data in panel (b) and (d) suggests a slight under- and over-rotation relative to the target rotation angles, while in c we have picked a data set that happens to show approximately the correct rotation angles. For all nominally identical uncontrolled Hadamard experiments that we acquired, we observe a quality factor that is much lower compared to the stabilized oscillations in panel (a).

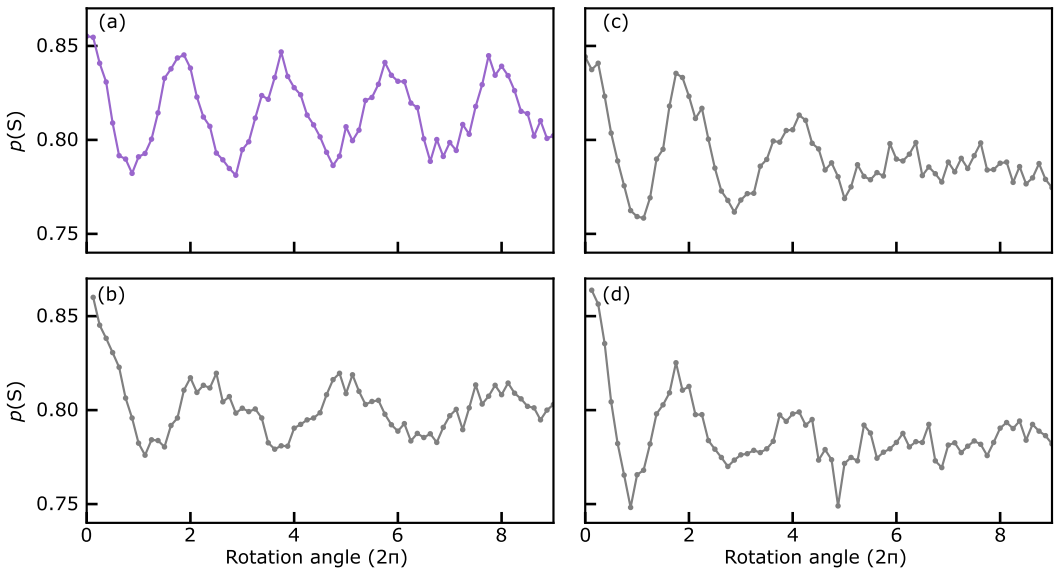

Fig. 3.12: **Comparing Hadamard rotations with and without real-time stabilization. (a)** Measurement of Hadamard rotations with feedback, same data as shown in Fig. 3.5(e). **(b-c-d)** Additional measurements of Hadamard rotations without feedback, not shown in Sec. 3.6.

Simultaneous controlled qubits rotations by uncontrolled frequencies

In this section we also tune the top right singlet-triplet qubit, Q4 [cf. 1.3(b)] to simultaneously perform controlled rotations in both Q3 and Q4. Differently from before, whenever the previously estimated value of $\Omega_{\mathrm{H(L)}}$ is available, we set a window prior distribution of span $\approx 2\,\mathrm{MHz}$, with a mean equal to the previously estimated value to reduce estimation errors. In the next Chapter 4, the window prior will be replaced by a physics-informed model.

Ω_{L} is estimated as in Fig. 3.2(b): for each repetition a singlet pair is initialized in (0,2) and subsequently detuned deep in the (1,1) region ($\varepsilon_{\mathrm{L}} \approx -100\,\mathrm{mV}$ in Q4) for $N = 101$ linearly spaced separation times t_i up to 100 ns. The result is shown in the top panel Fig. 1.3(a), which shows the probability distribution $P(\Omega_{\mathrm{L}})$ of each repetition for Q3(4) in the left (right) panel.
Again, knowledge of $\langle\Omega_{\mathrm{L}}\rangle$ allows controlled rotations by user-defined target angles as in Fig. 3.2(d), this time for both qubits. To show this, we task the quantum controller to adjust the separation times $\tilde{t}_j$ in the pulse sequence to rotate each qubit by $M = 41$ different angles $\theta_j = \tilde{t}_j \langle\Omega_{\mathrm{L}}\rangle$ between 0 and 5π, see Fig. 3.13(b), bottom panel. The controlled rotations are performed only if both estimated frequencies of the qubits lie in the window [30, 70] MHz.

Again, real-time knowledge of $\langle\Omega_{\mathrm{L}}\rangle$ [similarly to 3.13(a)] allows the initial state $|\mathrm{S}\rangle$ to be rotated to a state near the equator of the Bloch sphere, before it evolves freely for probing Ω_{H}, this time in both qubits. This rotation is implemented by a diabatic detuning pulse from (0,2) to ε_{L} (diabatic compared to the interdot tunnel coupling) for a time $\tilde{t}_{\pi/2}$, corresponding to a rotation of the qubit around $\hat{\boldsymbol{\omega}}_{\mathrm{L}}$ by an angle $\Omega_{\mathrm{L}}\tilde{t}_{\pi/2} = \pi/2$. After evolution for time t_j under finite exchange, another

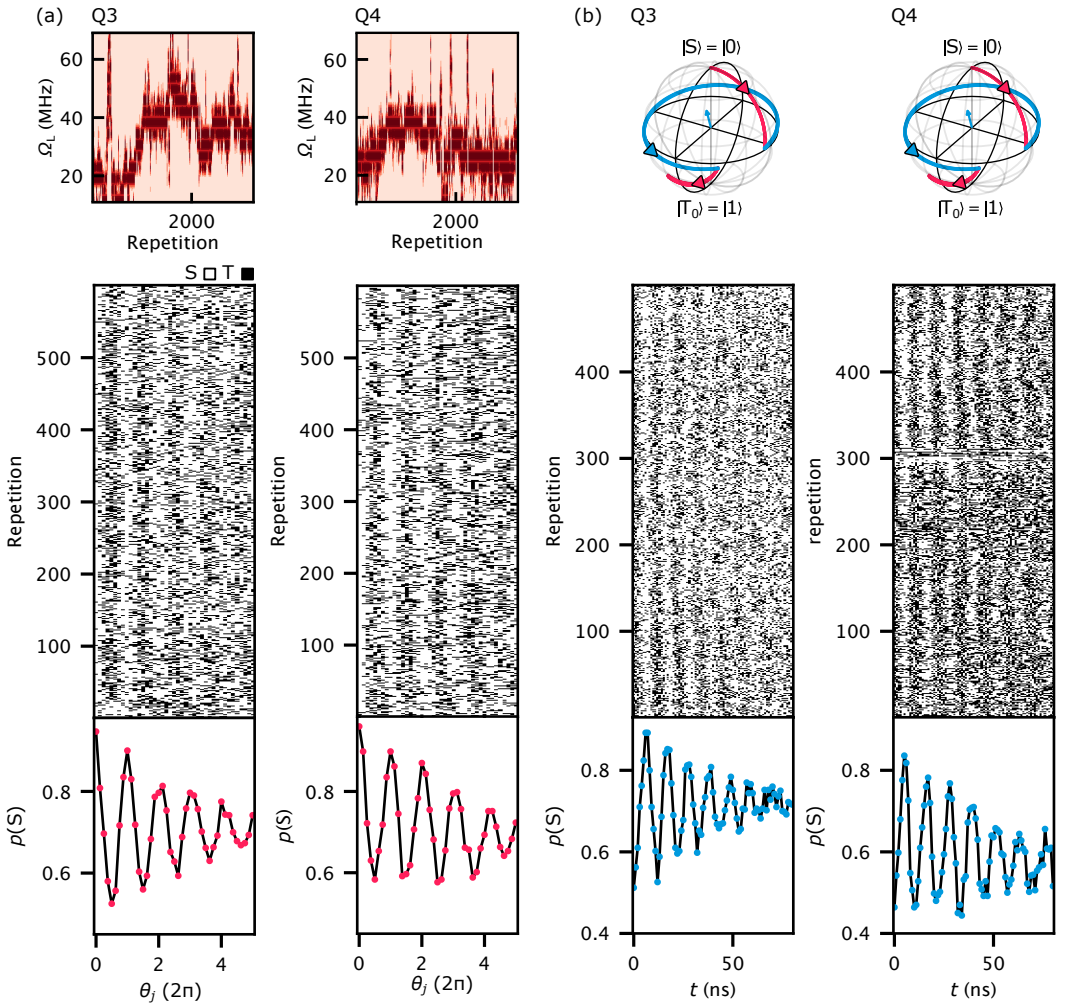

Fig. 3.13: **Simultaneous controlled qubits rotations by uncontrolled frequencies. (a)** (top panels) Probability distribution $P(\Omega_L)$. Extraction of the expected value $\langle\Omega_L\rangle$ from each row completes Ω_L estimation. (bottom panels) To illustrate the increased coherence of Overhauser gradient-driven rotations, we task the quantum controller to perform $M = 80$ evenly spaced θ_j rotations. Single-shot measurements m_j are plotted as white/black pixels, and the fraction of singlet outcomes in each column is shown as a red dot. **(b)** (top panels) One repetition of the exchange rotation protocol. The quantum controller estimates $\Delta B_{z,i}$ of qubits $i = 1,2$, then lets the qubits evolve under an exchange-based FID simultaneously. Pulses duration $\tilde{t}_{\pi/2,i}$ for qubit initialization and readout use real-time knowledge of $\Delta B_{z,i}$. (bottom panels) Each row plots single-shot measurements outcomes singlet or triplet for both qubits as a function of the exchange-based FID time t, and the fraction of singlet outcomes $p(\mathrm{S})$ in each column is shown as a dot.

$\pi/2$ rotation around $\hat{\boldsymbol{\omega}}_{\mathrm{L}}$ rotates the qubit to achieve a high readout contrast in the ST_0 basis, as illustrated on the Bloch spheres in the top panel of Fig. 3.13(b).

We set a window prior distribution of span $\approx 3\,\mathrm{MHz}$ centered around the previously estimated value, with $N = 101$ measurements per repetition. Also, the quantum controller performs exchange-based FIDs if $25\,\mathrm{MHz} < \langle \Omega_{\mathrm{L,\,Q3}} \rangle < 40\,\mathrm{MHz}$ and $30\,\mathrm{MHz} < \langle \Omega_{\mathrm{L,\,Q4}} \rangle < 45\,\mathrm{MHz}$.

We plot in Figure 3.13(b) [bottom panel] the single-shot measurements for 500 repetitions of this protocol, and the fraction of singlet outcomes as a function of the time t where both qubits performed exchange-based FID at the same time. The rotation is executed through a diabatic detuning pulse from ε_{L} to $\varepsilon_{\mathrm{H}} = -12\,\mathrm{mV}$ ($-50\,\mathrm{mV}$) (diabatic compared to the interdot tunnel coupling) for $\mathrm{Q_3}$ ($\mathrm{Q_4}$).

In summary, this section presents a protocol where information obtained from tracking estimation enables synchronized angle rotations in both qubits simultaneously, even though the control frequencies randomly fluctuate in both qubits.

Acknowledgments

This work received funding from the European Union's Horizon 2020 research and innovation programme under grant agreements 101017733 (QuantERA II) and 951852 (QLSI), from the Novo Nordisk Foundation under Challenge Programme NNF20OC0060019 (SolidQ), from the Inge Lehmann Programme of the Independent Research Fund Denmark, from the Research Council of Norway (RCN) under INTFELLES-Project No 333990, as well as from the Dutch National Growth Fund (NGF) as part of the Quantum Delta NL programme.

Author contributions

F.B. led the measurements and data analysis, and wrote the manuscript with input from all authors. F.B., T.R., J.v.d.H., A.C. and F.K. performed the experiment with theoretical contributions from J.A.K., J.D. and E.v.N. F.F. fabricated the device. S.F., G.C.G. and M.J.M. supplied the heterostructures. A.C. and F.K. supervised the project.

4

Physics-informed Tracking of Qubit Fluctuations

Environmental fluctuations degrade the performance of solid-state qubits but can in principle be mitigated by real-time Hamiltonian estimation down to time scales set by the estimation efficiency. We implement a physics-informed and an adaptive Bayesian estimation strategy and apply them in real time to a semiconductor spin qubit[1]. The physics-informed strategy propagates a probability distribution inside the quantum controller according to the Fokker–Planck equation, appropriate for describing the effects of nuclear spin diffusion in gallium-arsenide. Evaluating and narrowing the anticipated distribution by a predetermined qubit probe sequence enables improved dynamical tracking of the uncontrolled magnetic field gradient within the singlet-triplet qubit. The adaptive strategy replaces the probe sequence by a small number of qubit probe cycles, with each probe time conditioned on the previous measurement outcomes, thereby further increasing the estimation efficiency. The combined real-time estimation strategy efficiently tracks low-frequency nuclear spin fluctuations in solid-state qubits, and can be applied to other qubit platforms by tailoring the appropriate update equation to capture their distinct noise sources.

4.1 Introduction

Low-frequency environmental fluctuations cause decoherence in solid-state qubits [149, 208, 209]. Quantum error correction strategies [2] can detect and correct errors but demand an increased number of physical qubits. Conventional noise reduction techniques, such as dynamical decoupling [210, 211] and active suppression of environmental fluctuations [117, 212, 213], are not universally effective and may not align with specific experimental goals.

Hamiltonian learning emerges as a promising solution for compensating for uncontrolled environmental effects and enhancing the qubit quality factor [109, 180, 186, 148, 187, 42, 214]. This approach leverages modern hardware capabilities to provide real-time feedback, but comes at the cost of dedicating time to estimate the fluctuating Hamiltonian parameters. Although several theoretical estimation schemes [197, 215, 151, 198, 199, 216, 217, 218] have been proposed to boost the estimation efficiency, no experiment has yet demonstrated a *physics-informed* scheme within any qubit platform, where understanding of the physical processes driving the fluctuations is utilized to improve the estimations. Even the experimental adoption of real-time *adaptive* Bayesian strategies [164, 219], where measurement parameters are chosen based on the previous

[1]This Chapter is published in Fabrizio Berritta et al. *Physics-informed tracking of qubit fluctuations.* 2024. DOI: 10.48550/arXiv.2404.09212, and reused in accordance with the CC BY license.

measurements, is still missing in gate-defined spin qubits. This work reports the first real-time physics-informed and adaptive Bayesian estimation of a qubit.

To demonstrate an adaptive and physics-informed estimation protocol, we employ a singlet-triplet (ST_0) qubit in GaAs. In nitrogen-vacancy centers in diamond [220] and semiconductor spin qubits [51], low-frequency noise from spinful nuclear isotopes decreases qubit performance through hyperfine interactions. Isotopic purification techniques [221, 222] mitigate this issue in group IV semiconductors such as silicon and germanium, though it comes with significant effort and does not remove low-frequency noise originating from other sources. For our demonstration we choose GaAs as its nuclear noise spectrum is well understood [111, 31]. Our technique involves programming a commercial quantum controller, powered by an integrated field-programmable gate array (FPGA), to propagate the probability distribution of the effective nuclear fields on the dots in real time, using the Fokker–Planck (FP) equation [217, 218]. This enables the dynamic tracking of the fluctuating nuclear field gradient across the qubit, which is the main source of decoherence in ST_0 qubits in GaAs [111, 31].

The propagation of probability distributions on the quantum controller, here according to the FP equation, can be replaced by other update equations, e.g., a transition matrix for Markov processes [223], or machine-learning-based methods for signal prediction [201], the details of which depend on the specific nature of the qubit system.

Real-time capabilities of quantum controllers can also be used advantageously to choose optimal measurement parameters within an *adaptive* estimation sequence (in our case updating free-induction-decay times on the fly, based on previous measurement outcomes), which we will analyze separately below.

Our scheme can accomplish Hamiltonian learning for intermittent calibration of circuit parameters, making it ideal for the recurrent and reliable execution of quantum circuits against the impact of drift. Since the interleaved estimation and qubit operation take place in the same qubit, there is an intricate interplay between the correlation time of the fluctuations being estimated, the efficiency of the estimation procedure, and the required time for coherent operations between estimations. Optimizing and managing these time scales will be essential when going from single-qubit devices to multi-qubit devices, making it even more valuable to estimate qubit and noise correlations times quickly and efficiently.

4.2 Device and Bayesian estimation

We employ the top-gated GaAs double quantum dot (DQD) Q3 and experimental setup described in Chapter 3. The qubit operates in the $(1,1)$ and $(0,2)$ charge configuration, where the integers stand for the number of electrons in the left and right dot of the DQD. In the two-electron ST_0 basis, the Hamiltonian can be approximated in the regime of interest as

$$\mathcal{H}(t) = \frac{J(\varepsilon)}{2}\sigma_z + \frac{g^*\mu_B\Delta B(t)}{2}\sigma_x, \tag{4.1}$$

where σ_i represent the Pauli operators, g^* is the effective g-factor, and μ_B is the Bohr magneton. The energy $J(\varepsilon)$ characterizes the exchange interaction between the two electrons, which is tunable via the relative electrical detuning of the dots. By defining $\varepsilon = 0$ at the (1,1)–(0,2) charge-state degeneracy, the detuning is proportional to the difference in the effective on-site potentials on the two dots of the singlet-triplet qubit, where negative ε corresponds to the (1,1) ground-state region.

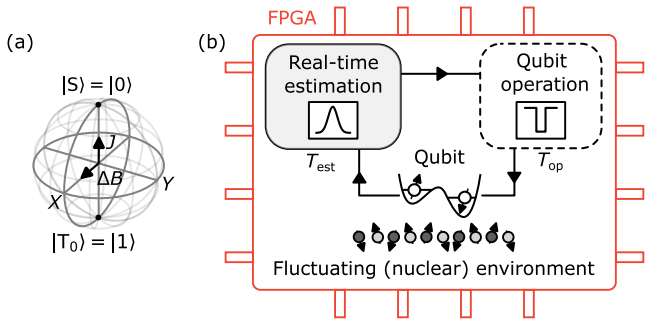

Fig. 4.1: **Qubit implementation and estimation schedule**. **(a)** Exchange coupling $J(\varepsilon)$ and Overhauser gradient $\Delta B \propto h f_B(t)$ drive rotations of the qubit around two orthogonal axes of the Bloch sphere, providing universal qubit control if the prevailing Overhauser frequency f_B can be estimated sufficiently efficiently. **(b)** Qubit schedule, alternating between periods T_{op} of quantum information processing (dashed box), and short periods T_{est} for efficiently learning the fluctuating environment (gray box).

The field $\Delta B(t)$ denotes the z-component of the Overhauser gradient, which is the difference in effective magnetic fields on the two dots due to the hyperfine interaction of the electrons with approximately 10^5–10^6 of spinful nuclei on each dot [111]. This gradient fluctuates slowly, and our goal is to efficiently estimate the corresponding Overhauser frequency $f_B(t) \equiv g^* \mu_B \Delta B(t)/h$ in real time on the quantum controller, using a physics-informed model with and without adaptive probe times.

A Bloch-sphere representation of the two contributions to $\mathcal{H}$ is sketched in Fig. 4.1(a). The qubit undergoes manipulation through voltage pulses applied to the plunger gates of the DQD, which effectively control the magnitude of $J(\varepsilon)$. Deep in the (1,1) regime, where $J(\varepsilon) \ll |h f_B|$, the qubit is almost purely driven by the Overhauser gradient, whereas close to $\varepsilon = 0$ typically $J(\varepsilon) \gtrsim |h f_B|$.

After manipulation, the qubit is measured by projecting the unknown final spin state onto either the (1,1) charge state ($|\mathrm{T}_0\rangle$) or the (0,2) charge state ($|\mathrm{S}\rangle$), by tuning to positive ε. Each single-shot readout of the DQD charge configuration involves the generation, demodulation, and thresholding of a few-microsecond-long radio-frequency burst on the quantum controller [42].

The fluctuating frequency f_B is assessed on the quantum controller using a Bayesian estimation approach based on a series of N free-induction-decay experiments with evolution times t_i where $i = 1, 2, \ldots, N$ [109, 180, 186, 187, 42, 214]. Employing m_i to represent the outcome ($|\mathrm{S}\rangle$ or $|\mathrm{T}_0\rangle$) of the i-th measurement, the likelihood function $P(m_i|f_B)$ is defined as the probability of obtaining m_i given a value of f_B,

$$P\left(m_i|f_B\right) = \frac{1}{2}\left[1 + m_i\left(\alpha + \beta\cos\left(2\pi f_B t_i\right)\right)\right], \tag{4.2}$$

where m_i takes a value of 1 (-1) if $m_i = |\mathrm{S}\rangle$ ($|\mathrm{T}_0\rangle$), and α and β are parameters accounting for the measurement error and axis of rotation on the Bloch sphere during a free-induction decay experiment [109]. In this work we use $\alpha = 0.28$ and $\beta = 0.45$ extracted from a series of separate free-induction decay (FID) experiments. Applying Bayes' rule to estimate f_B based on the series of measurements $m_N, \ldots m_1$, which are assumed to be independent of each other, yields the final

probability distribution $P_{\text{final}}(f_B) \equiv P(f_B \,|m_N, \ldots m_1)$ given by

$$P_{\text{final}}(f_B) \propto P_0(f_B) \prod_{i=1}^{N} \left[1 + m_i\left(\alpha + \beta \cos\left(2\pi f_B t_i\right)\right)\right], \tag{4.3}$$

where $P_0(f_B)$ is the initial probability distribution assumed for f_B before the estimation starts. Equivalently, the measurement outcome m_i updates the Bayesian probability distribution according to $P_i(f_B) \propto P_{i-1}(f_B)P(m_i|f_B)$, up to a normalization factor, where the likelihood function $P(m_i|f_B)$ is given by Eq. (4.2). The final estimate of f_B is taken to be the expectation value $\langle f_B \rangle$, calculated over the final distribution $P_{\text{final}}(f_B)$ after all N measurements have been performed. The estimation protocol can be repeated at user-defined times when the qubit is not in use for other operations.

Estimating low-frequency fluctuations is useful as outlined in the following example, depicted in Figure 4.1(b): one starts by estimating the instantaneous magnitude of the slowly fluctuating field (the Overhauser frequency in our case), resulting in a strongly reduced uncertainty in this field. Subsequently, that knowledge is used to compensate for the random value of the field during coherent qubit operation, resulting in an increased qubit quality factor [42]. However, while operating the qubit for a period T_{op}, the field will again slowly drift, which can be captured by letting its distribution function evolve over time according to a known noise model [31]. For the Overhauser gradient, this amounts to a diffusion of its mean towards zero mean field and an increase of the uncertainty towards a maximum value that depends on the number and coupling strengths of the involved nuclear spins. Before such a stationary state is reached, the known dynamics of the probability distribution can be used to improve the feedback or make the next estimation more efficient. After a user-defined period T_{op}, qubit operations are momentarily halted and a new real-time estimation is initiated on the quantum controller. Its duration, approximately $T_{\text{est}} \propto N$, depends on the desired estimation accuracy as discussed below. A series of estimation sequences, each resulting in an accurate distribution $P_{\text{final}}(f_B)$, is what we refer to as qubit tracking.

4.3 Physics-informed tracking of the qubit frequency

This section describes how such "stroboscopic" physics-informed tracking of an Overhauser field is implemented on the quantum controller and to what extent it produces higher-quality estimates than obtainable via more commonly used estimation sequences [109, 42]. The protocol is physics-informed in the sense that the assumed evolution of the distribution function in between two estimations is based on a physical model describing the nuclear spin dynamics in GaAs-based quantum dots.

The FPGA-based estimation of the Overhauser frequency f_B is illustrated in Fig. 4.2(a): One estimation sequence consists of N repetitions of a free-induction decay (FID) probe cycle. In each probe cycle, a singlet pair is initialized in (0,2) and then detuned deeply into the (1,1) region. At $\varepsilon \approx -40\,\text{mV}$, the quantum controller lets the qubit evolve for a probe time $t_i = i\,t_0$, before thresholding the resulting qubit state and updating the probability distribution $[P_i(f_B) \propto P_{i-1}(f_B)P(m_i|f_B)]$. In this sequence, the probe times t_i are predetermined and linearly distributed by the probe time spacing $t_0 = 1\,\text{ns}$. We assume that N is sufficiently small such that the Overhauser gradient remains constant during the sequence.

We model the dynamics of the Overhauser gradient as an Ornstein–Uhlenbeck (or drift–diffusion) process [31], driven by randomly occurring nuclear spin flips. The time dependence of

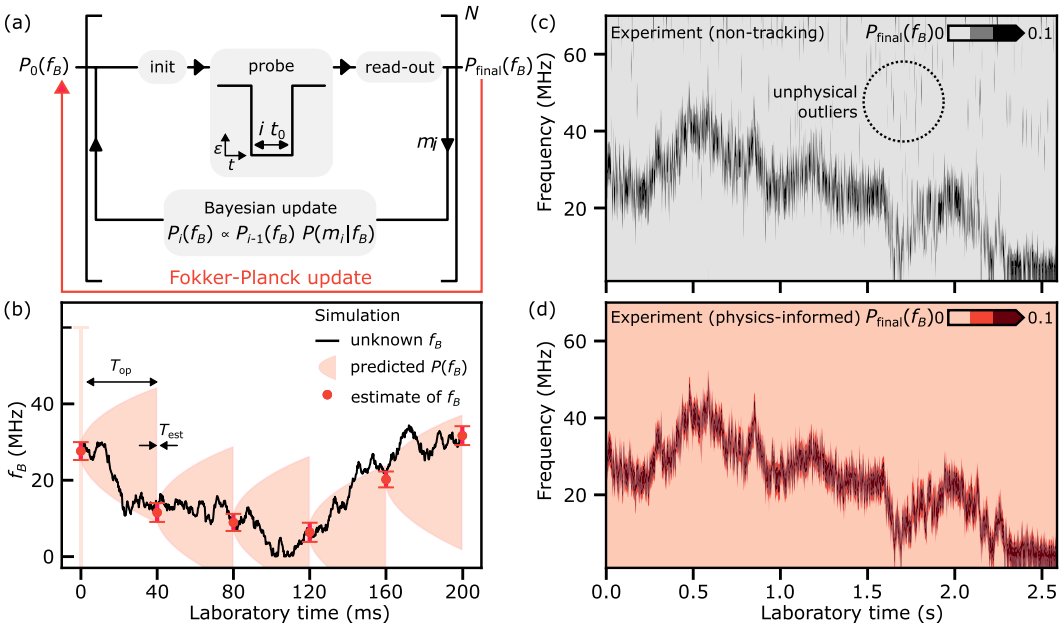

Fig. 4.2: **Tracking of the Overhauser frequency by anticipating nuclear spin diffusion on the quantum controller. (a)** The physics-informed estimation sequence for f_B initializes the prior distribution $P_0(f_B)$ by evolving an older final distribution $P_{\text{final}}(f_B)$ (Fokker-Planck update). For each of the N probe cycles, labeled i, the quantum controller initializes the qubit to the singlet state, performs a FID for time $t_i = i\,t_0$, then updates the probability distribution $P_i(f_B)$ based on the measurement outcome m_i. After N probe cycles, the final distribution $P_{\text{final}}(f_B)$ is saved. **(b)** Simulation of the unknown fluctuating Overhauser gradient (black) and five physics-informed estimation sequences, illustrating the tracking protocol. Every 40 ms, a sequence of FID probe cycles results in a final distribution with expected value $f_B^f = \langle f_B \rangle$ and error bar $2\sigma_f$ (red markers). The simulation assumes a uniform prior distribution $P_0(f_B)$ at $t = 0$, whereas subsequent priors $P_0(f_B)$ are based on the mean $\mu(t)$ and standard deviation $\sigma(t)$ propagated by the Fokker-Planck equation over period T_{op} (shaded in light red). **(c)** Experimental results for the non-tracking reference protocol, using $P_0(f_B) \equiv P_{\text{uniform}}(f_B)$ for each estimation sequence. **(d)** Experimental results for the physics-informed tracking protocol, obtained simultaneously with non-tracking estimates in panel (c). The initial prior $P_0(f_B)$ for each column is $P_{\text{final}}(f_B)$ from the previous column, propagated in time according to Equation (4.5). Note the absence of multi-peaked distributions $P_{\text{final}}(f_B)$.

the distribution function $P(f_B, t)$ resulting from such a process is governed by a Fokker–Planck (FP) equation [224, 217, 218], allowing the prediction of $P(f_B)$ in periods when the qubit is used for other operations (T_{op}). Assuming that each final distribution $P_{\text{final}}(f_B)$ is sufficiently characterized by its mean and variance, we instruct the quantum controller to approximate it by a Gaussian distribution [2]. Denoting the mean and variance immediately after estimation (time $t = 0$) as f_B^f and σ_f^2, respectively, the FP equation yields as solution for $t > 0$

$$P(f_B, t) = \frac{1}{\sqrt{2\pi\sigma(t)^2}} \exp\left\{-\frac{[f_B - \mu(t)]^2}{2\sigma(t)^2}\right\}, \tag{4.4}$$

where

$$\mu(t) = f_B^f e^{-\Gamma t}, \tag{4.5a}$$

$$\sigma(t)^2 = \sigma_K^2 + \left[\sigma_f^2 - \sigma_K^2\right] e^{-2\Gamma t}. \tag{4.5b}$$

Here, σ_K is the steady-state root mean square value of the Overhauser field frequency (typically around $30 - 50$ MHz [31]), while Γ reflects the slow relaxation rate of nuclear spin polarization (measured to be $\Gamma \approx 1.1$ Hz from autocorrelation). Notably, the inverse of Γ, denoted as $T_c = \Gamma^{-1} \approx 0.91$ s, defines the timescale for the correlation of fluctuations in f_B; this establishes the time window within which an estimate of f_B is expected to remain useful.

In Figure 4.2(b) we numerically simulate a fluctuating Overhauser gradient with $T_c = 1$ s and $\sigma_K = 30$ MHz. The associated unknown frequency f_B (black trace) is assumed to be estimated every $T_{\text{op}} = 40$ ms (red markers). The physics-informed evolution of probability distributions (shaded red areas, adapted from Ref. [218]) captures two properties expected for nuclear spin diffusion, namely the inclination of the average of the Overhauser gradient to drift back towards zero [Eq. (4.5a)], and a progressive expansion of the uncertainty in the gradient towards σ_K [Eq. (4.5b)]. Both processes take place on a timescale of T_c.

Initially, no knowledge of f_B is available, reflected by a uniform prior distribution $P_{\text{uniform}}(f_B)$ at $t = 0$ represented by the semi-transparent error bar spanning the entire frequency range of the simulation (60 MHz) [3]. A number of FID cycles are performed until the updated probability distribution has a fitted $\sigma < 2$ MHz. This estimation sequence is assumed to take only a few hundred microseconds, i.e. much shorter than T_{op} and T_c, and we only plot the mean f_B^f and 95% confidence interval of the final distribution $P_{\text{final}}(f_B)$ (first red marker).

After the first estimation sequence, the Overhauser fields are left to evolve freely for T_{op}. During this time, the distribution function is assumed to be Gaussian; the time dependence of its mean and variance is given by Eq. (4.5). The evolution of the 95% confidence interval is indicated by the red shaded area in Fig. 4.2(b). At the end of T_{op} ($t = 40$ ms) the associated Gaussian distribution is characterized by $\mu(T_{\text{op}})$ and $\sigma(T_{\text{op}})$, and serves as the initial prior distribution for the next estimation sequence. Similarly, estimations at $t = 80$, 120, 160 and 200 ms use as prior the most recent Gaussian.

If T_{op} is smaller than T_c, the physics-informed $P_0(f_B)$ will remain somewhat constrained, providing a better prior compared to a uniform distribution and potentially requiring fewer FID

[2] Since we only work with positive frequencies f_B, one should be aware that this becomes inaccurate for distributions that have significant weight close to $f_B = 0$, i.e., that have a variance larger than the square of the mean.

[3] We choose our prior distribution to be non-zero for positive frequencies only, resulting in a unimodal final distribution. As the sign of the Overhauser gradient is unknown, the true final distribution would always be symmetric around zero.

experiments for a more accurate estimate of f_B. If T_{op} becomes comparable to or larger than T_c, prior knowledge about f_B becomes irrelevant and is not expected to improve the next estimation.

To experimentally test the benefits of physic-informed priors, we define a non-tracking estimation scheme that always sets the initial distribution $P_0(f_B)$ to a uniform distribution $P_{\text{uniform}}(f_B)$ between 1 MHz and 70 MHz with 1 MHz resolution. Thus, as in previous works [109, 42], each estimation sequence does not retain any memory of previous estimations. In parallel to this non-tracking estimation, we instruct the quantum controller to also generate estimates based on the physics-informed initialization of $P_0(f_B)$, thereby improving the estimation accuracy as quantified below.

Figure 4.2(c) plots 1,000 final probability distributions of the non-tracking scheme, acquired over a span of 2.6 s using an $N = 31$ schedule with $T_{est} = 0.6$ ms and $T_{op} = 2$ ms. Specifically, each FID probe cycle lasts 20 µs, of which 5 µs is dedicated to qubit readout, 2.6 µs to initialize the qubit and discharge the bias tee with a zero-averaging pulse, and the remaining time is used to update the non-tracking and physics-informed distributions $P_i(f_B)$ on the FPGA. Several estimation sequences result in a multi-peaked probability distribution, with secondary peaks that randomly jump from one column to another. In simulations, such "outliers" also appear in the absence of measurement errors and appear to be a shortcoming of the algorithm, not an artifact of the device or the quantum controller. The known correlation time of the Overhauser field dynamics makes it improbable that the sudden jumps of the outliers represent the actual Overhauser field gradient, and similar jumps in previous work were associated with compromised qubit quality factors (cf. discussion of Fig. 3.9(b) of Ch. 3).

Figure 4.2(d) shows the physics-informed estimates $P_{\text{final}}(f_B)$, acquired concurrently with the non-tracking estimates in panel (c). Strikingly, multi-peaked probability distributions are absent, suggesting that the physics-informed model on the quantum controller suppresses unphysical jumps of the estimated Overhauser gradient (here with $T_c = 0.91$ s and $\sigma_K = 50$ MHz). By extracting the standard deviation from each column in Figure 4.2(d), we find that its average is reduced relative to the average standard deviation extracted from panel 4.2(c), suggesting an improved estimation accuracy.

Figure 4.3 compares the performance of the non-tracking and physics-informed estimation sequences as a function of the number of FID probe cycles, for different choices of T_{op}. Each data point corresponds to an independent experiment comprising 10,000 repetitions of an estimation sequence. The plotted uncertainty is defined as the average standard deviation of the final probability distribution $P_{\text{final}}(f_B)$ of each of the 10,000 estimations. The shaded areas indicate the standard deviation of the associated 10,000 standard deviations. In our experiment, the true value of the real field, and thus the actual error in the estimation, is unknown, and therefore we rely on the uncertainty measure plotted as a reasonable metric. Indeed, low uncertainties at the end of T_{est} correlate with increased quality factors of controlled Overhauser rotations during T_{op} (see Sec. 4.6).

The uncertainty of the non-tracking estimates in Fig. 4.3(a) does not depend on T_{op}. This is expected, as the prior distributions $P_0(f_B)$ in the non-tracking scheme are always the uniform distribution $P_{\text{uniform}}(f_B)$, with no memory of the previous estimates. In contrast, the uncertainty of the physics-informed estimates decreases with decreasing T_{op}, for fixed number of measurements in the estimation sequence. This suggests that a narrower prior yields a more accurate estimate.

Remarkably, with as few as 10 probes the physic-informed estimates for $T_{op} = 1$ ms are more accurate than non-tracking estimates based on 100 probes (in Fig. 4.3(a) the uncertainties are approximately 3 MHz and 5 MHz, respectively). With increasing number of probe cycles, the uncer-

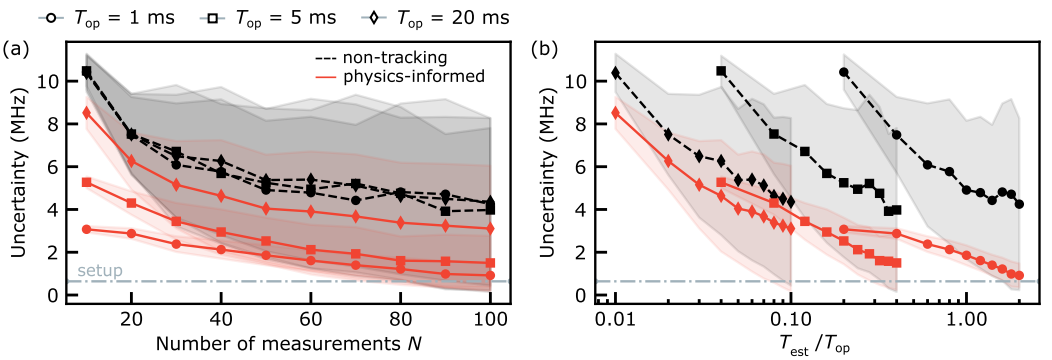

Fig. 4.3: **Efficiency of the non-tracking and physics-informed protocols. (a)** Estimation uncertainty as a function of the number of FID probes in the estimation sequence, for the non-tracking (black) and physics-informed (red) protocols. Symbols denote the average standard deviation of 10,000 $\langle f_B \rangle$ values, whereas shaded regions show their standard deviation, for different choices of operation time. **(b)** Uncertainty from (a) plotted as a function of the ratio $T_{\text{est}}/T_{\text{op}}$, where the estimation time is $T_{\text{est}} = N \cdot 20\,\mu\text{s}$. The dash-dotted gray line indicates the resolution limit imposed by our setup, see main text.

tainty of non-tracking estimates saturates near 5 MHz, whereas the physics-informed estimation uncertainty approaches the limitation imposed by our choice of frequency binning (0.8 MHz [4]).

The trade-off between "qubit duty cycle" ($T_{\text{op}}/T_{\text{est}}$) and estimation accuracy is evident in Fig. 4.3(b). Here, we replot the uncertainties from (a) as a function of the estimation time $T_{\text{est}} = N \cdot 20\,\mu\text{s}$, where N is the number of qubit probes and 20 µs is the probe cycle duration. Depending on the desired Hamiltonian uncertainty, a maximum operation limit T_{op} and a significant qubit downtime (high $T_{\text{est}}/T_{\text{op}}$ ratio) for estimation must be tolerated. The optimum choice of N depends on details of the noise spectrum and the estimation efficiency [218].

One may be tempted to pursue the lowest possible uncertainty while estimating the environmental fluctuations, but the operational benefits will depend on details such as the tolerable estimation uncertainty for a certain application and how long it is expected to survive given a specific environment. Because achieving lower uncertainties in general requires more qubit down time for estimation, quantum information processing applications may need to define a tolerated "error budget", which translates into a useful operation time T_{op} depending on the correlation time of the fluctuations T_{c} and a minimized estimation time T_{op} depending on the efficiency of the protocol.

So far, we demonstrated an improved Hamiltonian learning protocol that tracks a slowly fluctuating environmental parameter, by instructing a quantum controller to generate in real time physics-informed priors. Next, we instruct the controller to adaptively choose the probe times, thereby reducing the length of the estimation sequences.

[4] We programmed the frequency resolution on the quantum controller to be 1 MHz. The associated minimum standard deviation of $P_{\text{final}}(f_B)$ calculated on the FPGA is approximately 0.8 MHz.

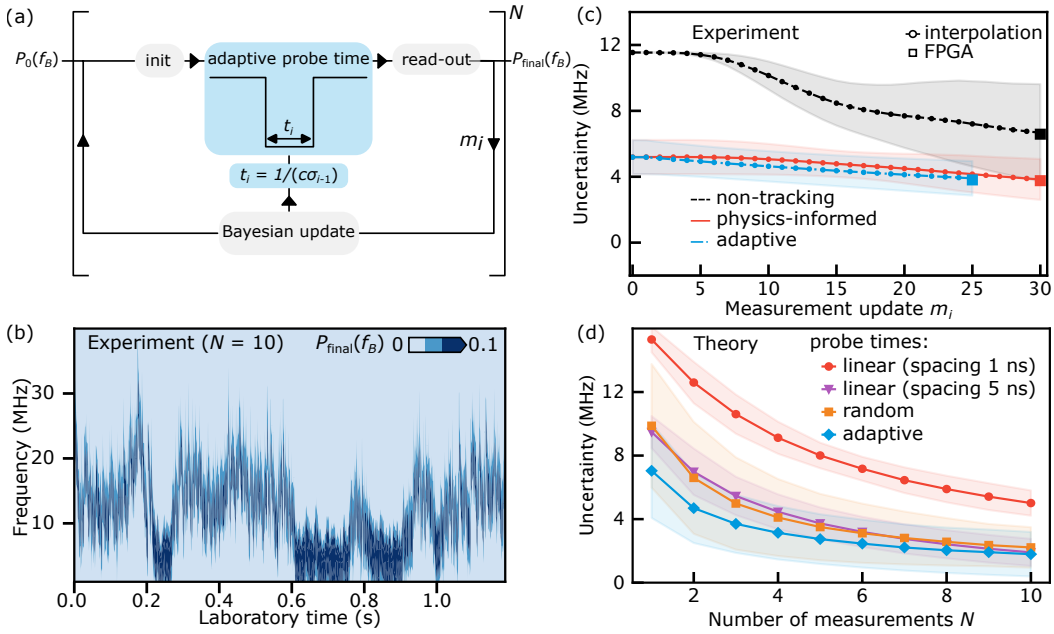

Fig. 4.4: **Adaptive Bayesian tracking by real-time choice of qubit probe times. (a)** In this adaptive Bayesian estimation sequence, probe times t_i are chosen based on the standard deviation σ_{i-1} of the previous Bayesian distribution. $P_0(f_B)$ is initialized based on the FP equation. **(b)** Adaptive tracking obtained from short estimation sequences ($N = 10$) for $T_{op} = 1\,\mu s$. **(c)** Reconstructed uncertainty in the distribution function within an estimation sequence (defined in the text) as a function of the measurement update m_i. Squares at the end of the curves correspond to the experimental posterior distributions computed on the quantum controller. **(d)** Simulated uncertainty expected at the end of a short estimation sequence ($N \leq 10$) for different probe time protocols, including evenly distributed t_i (probe time spacing of 1 or 5 ns), adaptive probe times, and random probe times (see main text). The initial prior distributions are assumed to be determined from the FP equation.

4.4 Adaptive Bayesian tracking of the qubit frequency

For the purpose of only monitoring fluctuating Hamiltonian parameters without interspersed qubit operation, non-adaptive Bayesian estimation is straightforward to execute because it does not require real-time feedback and could even be carried out a posteriori. However, numerical studies [197, 215, 198, 199, 217, 218] suggest the beneficial use of adaptive estimation sequences in which the probe times t_i are chosen based on previous measurement outcomes, as experimentally realized in nitrogen-vacancy centers [164, 219].

Previous experiments with gate-defined spin qubits employed non-tracking and non-adaptive FID-based Bayesian estimation to probe the qubit frequency [109, 42]. In this section, we supplement the generation of physics-informed time-evolved priors by the generation of adaptive probe times in real time, thereby reducing the number of required probes and showing a path towards

much shorter estimation sequences.

Figure 4.4(a) illustrates the key difference of the adaptive estimation sequence, relative to that in Fig. 4.2(a): the free-evolution time t_i for the i-th FID probe now depends on the previous Bayesian update as

$$t_i = \frac{1}{c\sigma_{i-1}}, \tag{4.6}$$

where σ_{i-1} is the standard deviation of the Gaussian-approximated probability distribution $P_{i-1}(f_B)$, except σ_0, which is the standard deviation of prior $P_0(f_B)$ based on the FP equation. The optimal numerical prefactor c is expected to depend on the experimental setup [199]. Intuitively, this choice for the free evolution times can be motivated by our desire that two oscillations with frequencies that differ by Δf develop a phase shift of π after time $t = 1/(2\Delta f)$. In other words, Eq. (4.6) maps a frequency range of width $c\sigma_{i-1}/2$ to a large phase contrast in the likelihood function.

Implementation of the estimation protocol of Fig. 4.4(a) on the quantum controller yields reliable estimates for f_B from only 10 probes per sequence, as shown in Fig. 4.4(b) for $T_{\mathrm{op}} = 1\,\mathrm{ms}$ and $c \approx 13$ [5]. This example demonstrates the estimation of a slowly fluctuating qubit frequency within 200 microseconds, which is one order of magnitude shorter and with better accuracy than previously reported [42]. Here, $c \approx 13$ was chosen empirically, and further improvements may be possible by better choices informed from numerical simulations, see Sec. 4.6.

Outliers appear to be absent both for the physics-informed [Fig. 4.2(c)] and adaptive tracking [Fig. 4.4(b)], likely for similar reasons, motivating a quantitative comparison based on experimental data and theoretical insights.

Figure 4.4(c) compares average uncertainties, inferred from experimental data in Fig. 4.6 of Sec. 4.6 We choose $T_{\mathrm{op}} = 5\,\mathrm{ms}$ and perform 10,000 repetitions of three protocols, focusing on $N \leq 30$ to test whether short sequences benefit from adaptive probe cycles. The three squares at the end of the curves show the uncertainties σ (defined as in Fig. 4.3 and computed on the quantum controller from the posterior distributions P_{final}) for non-tracking (black), physics-informed (red), and adaptive (blue) estimation sequences. For $N = 30$, the non-tracking scheme yields an average $\sigma \approx 7.3\,\mathrm{MHz}$, while the physics-informed scheme yields $\sigma \approx 3.5\,\mathrm{MHz}$. The uncertainty of the adaptive scheme is similar, though obtained with fewer probes ($N = 25$).

To investigate how each probe cycle contributes information gain, we analyze how uncertainties evolve within a sequence (additional details can be found in Fig. 4.6 of Sec. 4.6). Specifically, we reconstruct the Bayesian probability updates $P_i(f_B)$ from our record of raw single-shot measurement outcomes m_i [6]. For each i, we plot the standard deviation of $P_i(f_B)$ (reconstruction), averaged over all 10,000 repetitions, as well as their standard deviation (shaded areas).

The non-tracking method is clearly outperformed by the physics-informed and adaptive schemes. This is expected, as both the physics-informed and adaptive protocols use physics-informed prior distributions. Furthermore, the adaptive scheme has consistently lower uncertainty than the physics-informed scheme, though only marginally. Finally, we note that the uncertainties for the non-tracking and physics-informed schemes barely decrease during the first few measurements ($i \lesssim 5$), as shown by the nearly flat curves in this range. In contrast, the adaptive scheme shows a negative slope already for the first measurement outcomes, indicating information gain and a narrowing of the probability distribution.

[5] Due to the numerical precision of the quantum controller and the discreteness of the t_i that can be implemented, the actual ratio between $1/\sigma_{i-1}$ and t_i varies slightly between FID probe cycles.

[6] To increase the estimation bandwidth within the FPGA memory constraints, the quantum controller overwrites Bayesian updates $P_i(f_B)$ and only records $P_{\mathrm{final}}(f_B)$ at the end of each sequence, as well as all N measurement outcomes.

To explore the ultimate estimation efficiencies that can be expected for our spin-qubit system, unconstrained by coarse frequency binning and limited memory on the FPGA-powered controller, we now turn towards simulated Overhauser fluctuations, assumed to follow an Ornstein–Uhlenbeck process with $T_c = 1\,\mathrm{s}$ and $\sigma_K = 40\,\mathrm{MHz}$, and simulate estimation sequences on a much finer and larger frequency grid (0 to 150 MHz with 0.25 MHz bin size) than currently possible in our experimental setup.

Figure 4.4(d) shows the resulting uncertainties and their standard deviations, assuming $T_{\mathrm{op}} = 5\,\mathrm{ms}$, for different distributions of probe times (see Figs. 4.7,4.8 of Sec. 4.6 for further details): In the sequences with "linear" probe times, $t_i = i\,t_0$, we observe that the choice of the probe time spacing t_0 (shown 1 and 5 ns) has a drastic influence on the resulting accuracy. In the sequences with "random" probe times, t_i is randomly chosen from a uniform distribution between 1 ns and 50 ns. In the sequences with "adaptive" probe times, $t_i = 1/(c\sigma_{i-1})$, now with $c = 6$ and without rounding t_i to the temporal granularity of the quantum controller (see Sec. 4.6).

The adaptive-probe-time sequence outperforms the linear sampling approach with $t_0 = 1\,\mathrm{ns}$, yielding uncertainties that are on average smaller by a factor of ≈ 2.7, and is also superior to $t_0 = 5\,\mathrm{ns}$ and random probe times, resulting in approximately 30% smaller uncertainties for short estimation sequences ($N \lesssim 5$). We therefore believe that adaptive estimation sequences will become crucial in applications that only permit a small number of probe cycles.

In summary, the results shown in Fig. 4.4 present the first adaptive Bayesian estimation scheme implemented in a semiconductor-defined spin qubit.

The real-time capabilities of the quantum controller enable probe times t_i to be updated based on previous measurement outcomes $m_{i-1}, m_{i-2}, \ldots, m_1$, resulting in a small but measurable improvement compared to linearly spaced probe times. Our approach is substantiated by numerical simulations, indicating that high-quality estimates of the qubit frequency achieving only a few percent error (approximately 3 MHz uncertainty with a simulated dynamic range of $\approx 150\,\mathrm{MHz}$) should be possible with fewer than five qubit probe cycles.

4.5 Outlook

We have implemented physics-informed and adaptive estimation sequences that allowed the efficient tracking of low-frequency fluctuations in a solid-state qubit. A quantum controller estimates in real time the uncontrolled magnetic field fluctuations in a gallium-arsenide singlet-triplet spin qubit, yielding improved accuracy by temporally evolving a sufficiently recent probability distribution according to the Fokker-Planck equation. In addition, the adaptive choice of qubit probe times, based on the standard deviation of the updated probability distribution, allows for significantly shorter estimation sequences yielding similar or reduced uncertainties. Compared to the previous experiments [42] in Chapter 3, this work extends the estimation bandwidth from a few hundred Hz to $\approx 2.5\,\mathrm{kHz}$, due a tenfold reduction of the estimation time and a reduced uncertainty.

While our work marks the first real-time adaptive tracking of a semiconductor spin qubit, determining optimal protocols compatible with constraints of the control hardware and application requirements remains an open question. We anticipate further progress by research that combines theoretical and hardware aspects.

Possibly useful modifications of the protocol could relax the assumption of single-shot readout [225] or mitigate state preparation and measurement errors by duplication of probe cycles [197, 151]. Probe times can further be optimized by also taking into account the estimated qubit fre-

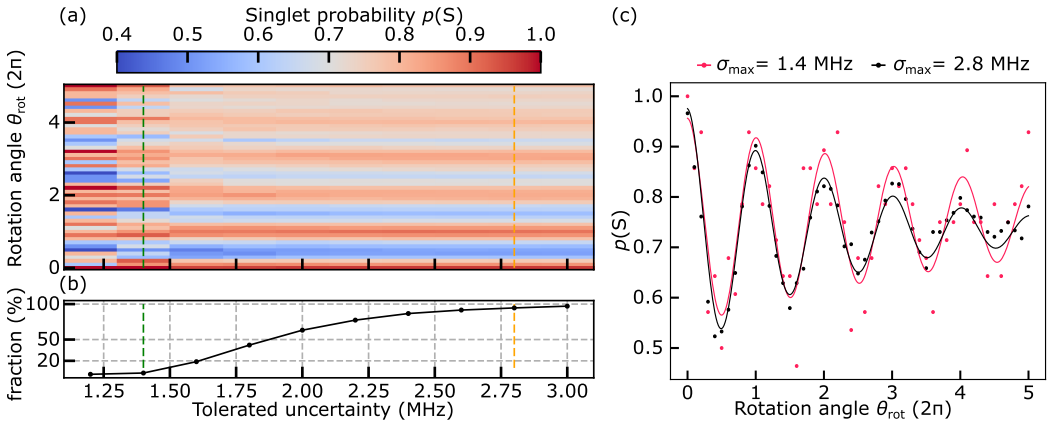

Fig. 4.5: **Improved qubit quality factor from lower estimation uncertainties. (a)** Average measured singlet–triplet oscillations resulting from averaging over only the best estimates, as a function of rotation angle and cutoff uncertainty $\sigma_{\text{est,max}}$. **(b)** The fraction of used estimations as a function of $\sigma_{\text{est,max}}$. **(c)** Dots: the averaged oscillations at $\sigma_{\text{est,max}} = 1.4\,\text{MHz}$ (red, corresponding to rejecting 97% of the repetitions), and 2.8 MHz (black, rejecting 3%), corresponding to the green and orange vertical dashed lines in (a,b), respectively. Solid lines: Fitted exponentially decaying sinusoidal oscillations.

quency, not just its uncertainty, and possibly it is advantageous to terminate an estimation sequence when reaching an accuracy target, rather than a predetermined length.

Fault-tolerant quantum computing based on quantum error correction will likely require qubits that are affected by limited amounts of Markovian noise. Therefore, real-time frequency tracking protocols may become important tools, as they suppress non-Markovian noise [214].

By properly modifying the tracking equation relevant to the specific noise source, this work offers an efficient, physics-informed, and adaptive Hamiltonian learning protocol for real-time estimation of low-frequency noise in solid-state qubits.

4.6 Supplementary

Variance of the distribution as a measure of estimation error

The true frequency of the Overhauser field gradient is not known, so to benchmark the different estimation protocols we choose as a figure of merit the standard deviation σ_{est} of the final probability distributions resulting from the estimations. Formally, this standard deviation follows from

$$\sigma_{\text{est}}^2 = \text{Var}(f_B) \equiv \sum_n \big(f_B[n] - \langle f_B \rangle\big)^2 P_{\text{final}}(f_B[n]), \tag{4.7}$$

where the index n labels the bins of the (discrete) probability distribution stored on the quantum controller. In this section we demonstrate that lower σ_{est} indeed correlates with a better estimation of $f_B(t)$, by performing Overhauser-driven controlled rotations of the qubit based on the information provided by the final probability distributions [42].

We thus perform a series of $N = 3,668$ estimations of the Overhauser gradient, spanning a few seconds of laboratory time. The experiment ends whenever the number of repetitions with Overhauser-controlled rotations (explained later) reaches 1,000. Due to finite FPGA program memory, the controlled rotations are executed whenever $20\,\text{MHz} \leq \langle f_B \rangle \leq 45\,\text{MHz}$. The repetitions of controlled rotations happen to be executed 1,000 times out of the $N = 3,668$ repetitions of estimations because of the chosen frequency range. For each estimation repetition, the quantum controller initializes the qubit in the singlet state, pulses deep into the (1,1) region, where the qubit undergoes rotations along σ_x with the instantaneous frequency $f_B(t)$, and after time τ_{rot} the quantum controller pulses back into the (0,2) region for qubit readout. The quantum controller repeats this experiment 3,668 times with τ_{rot} linearly increasing by 1 ns from $\tau_{\text{rot}} = 1\,\text{ns}$ to $\tau_{\text{rot}} = 50\,\text{ns}$. From the 50 single-shot outcomes of each estimation repetition, $\langle f_B \rangle$ is estimated.

After each estimation repetition, if $20\,\text{MHz} \leq \langle f_B \rangle \leq 45\,\text{MHz}$, the quantum controller performs Overhauser-driven controlled rotations of the qubit by an user-defined unit less target angle $\theta_{\text{rot}} = 2\pi \langle f_B \rangle \tilde{\tau}_{\text{rot}}$, where $\langle f_B \rangle$ is the expectation value for f_B resulting from the estimation performed just before the cycle of rotation experiments, which is different for each trace, θ_{rot} is linearly spaced between 0 and 5 in 51 points and $\tilde{\tau}_{\text{rot}}$ is computed on-the-fly on the quantum controller. The controlled rotations consist of the following steps: the quantum controller initializes the qubit in the singlet state, pulses deep into the (1,1) region, where the qubit undergoes rotations along σ_x with the instantaneous frequency $f_B(t)$, and after time $\tilde{\tau}_{\text{rot}}$ to rotate the qubit by the wanted angle θ_{rot}, the quantum controller pulses back into the (0,2) region for qubit readout. The time $\tilde{\tau}_{\text{rot}}$ thus corresponds exactly to the required time to rotate the qubit by the user-defined angle of rotation θ_{rot}, if the frequency was indeed exactly $\langle f_B \rangle$. We then study the average of the 1,000 traces based on their respective estimation uncertainty σ; the quality factor of the averaged oscillations is the result of the qubit decoherence time and the average accuracy of the knowledge about f_B. We assume the qubit decoherence time does not change across repetitions and the quality factor is mostly dependent on the uncertainty on f_B.

To show that low-quality estimates play an important role in the loss of oscillation amplitude we post-process the measured data based on the σ_{est} of all repetitions: We introduce the variable $\sigma_{\text{est,max}}$, and for given $\sigma_{\text{est,max}}$ we reject all repetitions with a probability distribution with a calculated variance of $\sigma^2_{\text{est}} > \sigma^2_{\text{est,max}}$, and we average over the remaining traces. We consider the controlled rotations of the qubit taken whenever the $20\,\text{MHz} \leq \langle f_B \rangle \leq 45\,\text{MHz}$ (the chosen interval is limited by the quantum controller program memory). In Fig. 4.5(a,b) we show the result for 10 choices of $\sigma_{\text{est,max}}$, ranging from 1.2 MHz to 3.0 MHz. Fig. 4.5(a) shows the singlet probability $P(S)$ of the averaged oscillations as a function of τ and $\sigma_{\text{est,max}}$, and in Fig. 4.5(b) we plot the corresponding fraction of used data for each $\sigma_{\text{est,max}}$. In Fig. 4.5(c) we focus on two specific choices for $\sigma_{\text{est,max}}$ [1.4 MHz (red) and 2.8 MHz (black)], that correspond to rejecting 97% and 3% of the estimations, respectively [see the vertical dashed lines in Fig. 4.5(a,b)]. The dots represent the averaged oscillations, as shown in Fig. 4.5(a), and the solid curves fitted sinusoidal oscillations with an exponentially decaying envelope. We thus see a significant improvement in the quality factor of the oscillations, which suggests that an important part of the observed decay may be associated with the performance of the estimation scheme. In that sense, σ_{est} thus seems to be a valid metric to benchmark the different protocols when the real field is not known.

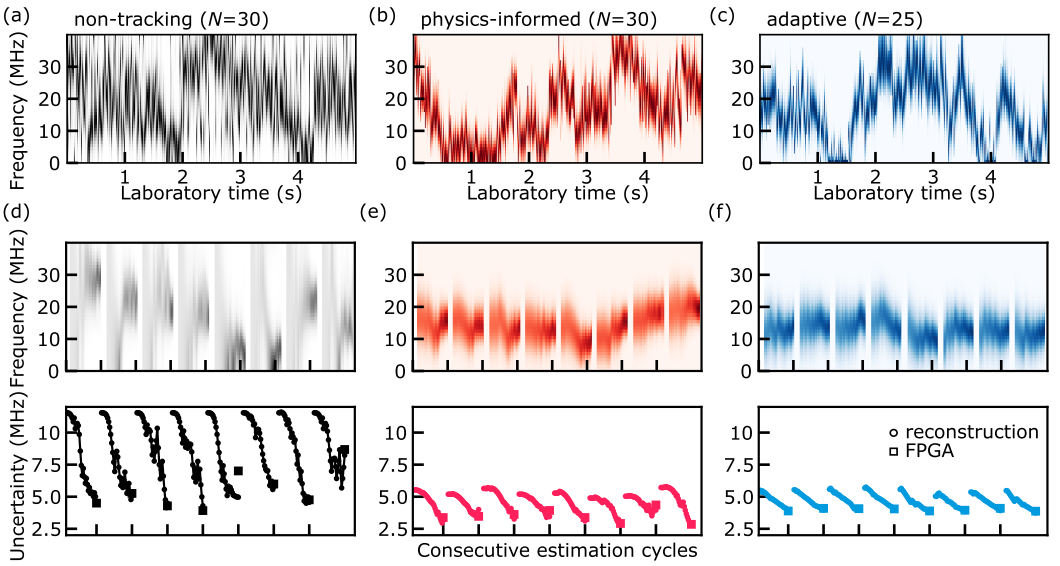

Fig. 4.6: **Reconstruction of probability distributions. (a–c)** Final probability distribution on the quantum controller of 1,000 repetitions, using the non-tracking (a), tracking (b), and adaptive scheme (c). **(d–f)** Reconstructed evolution of the distribution during the estimation, for 8 consecutive repetitions (top panels) and corresponding reconstructed uncertainty σ during estimation (bottom panels).

Reconstructing the distribution during estimation [Fig. 4.4(c) of Sec. 4.4]

In Fig. 4.6 we present more detailed data underlying Fig. 4.4(c) in Sec. 4.4. Figure 4.6(a–c) presents the first 1,000 out of 10,000 repetitions of experimental final posterior distributions $P_{\text{final}}(f_B)$ computed on the quantum controller with $\sigma_K = 40\,\text{MHz}$ for the estimation methods tracking (a), tracking (b) (both with a total number of measurements $N = 30$), and adaptive (c) (with $N = 25$). These repetitions serve as the benchmark for comparing the different methods in Fig. 4.4(c) of Sec. 4.4 and the following. To compare the methods fairly in Fig. 4.4(c) of Sec. 4.4 we exclude estimation runs where the estimated frequency $\langle f_B \rangle$ is smaller than the minimum measurable value of $\approx 2.5\,\text{MHz}$ resulting from discretization in the quantum controller program (such small $\langle f_B \rangle$ cause problems in the adaptive-time scheme, as explained in more detail in Fig. 4.8 below). In the top row of Fig. 4.6(d–f) we display the reconstructed evolution of the probability distributions during the estimation procedure for 8 consecutive repetitions, where the ticks at the horizontal axis mark the end of each estimation. The bottom row shows the corresponding evolution of the uncertainty σ during the estimations. While the distributions shown in (a–c) have been computed on the quantum controller, (d–f) show results that were reconstructed from the recorded measurement outcomes m_i (see description below). As in Sec. 4.4, squares represent uncertainties computed from the distribution in (a), demonstrating good agreement with the reconstructions most of the time, with a few exceptions. These occasional deviations are likely attributed to variations in numerical accuracy between the quantum controller and the desktop computer. A detailed discussion of setup limitations is provided in the next section.

Method of reconstructing from the measurement outcomes

The reconstruction process involves the analysis of raw data, obtained from experimental measurements by the quantum controller in conjunction with the evolution times t_i used, where $i = 1,2\ldots N$ labels measurement updates (shots). Differently from the previous sections, here we label the repetitions of estimation cycles by n. It follows the evolution times $t_{n,i}$ are loaded from the quantum controller. On top of this, we use the corresponding thresholded reflectometry measurement. As a result, the matrix representing single-shot measurements $m_{n,i} = \pm 1$ is generated.

Subsequently, the elements of the arrays $t_{n,i}$ and $m_{n,i}$ are employed to update the probability distribution based on a Bayesian update rule:

$$P_{n,i}(f_{B,j}) = \mathcal{N}_{n,i} P_{n,i-1}(f_{B,j})[1 + m_{n,i}(\alpha + \beta\cos(2\pi f_{B,j} t_{n,i}))]/2, \tag{4.8}$$

where $\mathcal{N}_{n,i}^{-1} = \sum_j P_{n,i-1}(f_{B,j})[1 + m_{n,i}(\alpha + \beta\cos(2\pi f_{B,j} t_{n,i}))]/2$ and $f_{B,j}$ is defined on a discrete grid.

At each pair of indices n, i, the first two moments are computed:

$$\langle (f_B)^k \rangle_{n,i} = \sum_j P_{n,i}(f_{B,j})(f_{B,j})^k, \tag{4.9}$$

which can be linked to the expectation value ($\mu_{n,i}$) and the standard deviation ($\sigma_{n,i}$) of the field:

$$\mu_{n,i} = \langle f_B \rangle_{n,i}, \quad \sigma_{n,i} = \sqrt{\langle f_B^2 \rangle_{n,i} - \langle f_B \rangle_{n,i}^2}. \tag{4.10}$$

The quantity $\sigma_{n,i}$ serves as a measure of field uncertainty, which is used as a figure of merit in the study. For visual representation, reconstructed values of $\sigma_{n,i}$ are depicted in Fig. 4.6 d-f) as a function of i for eight consecutive realizations $n = 641, 642 \ldots 648$.

In the first repetition ($n = 1$), the initial distribution $P_{1,0}(f_B)$ is flat. In subsequent repetitions ($n > 1$), either a flat distribution (non-adaptive schemes) or a Gaussian distribution with parameters computed from the previous $n-1$ are used (adaptive schemes). For the adaptive prior methods, we use the update equation:

$$P'_{n+1,0}(f_{B,j}) = \exp\left(-\frac{(f_{B,j} - \mu_{n+1,0}[T_{\mathrm{op}}])^2}{2\sigma^2_{n+1,0}[T_{\mathrm{op}}]}\right), \tag{4.11}$$

with the normalization:

$$P_{n+1,0}(f_{B_j}) = P'_{n+1,0}(f_{B,j}) / \sum_{j'} P'_{n+1,0}(f_{B,j'}), \tag{4.12}$$

where the expectation value and uncertainty are propagated from the last measurement of the previous estimation sequence, using Fokker-Planck update:

$$\mu_{n+1,0}[T_{\mathrm{op}}] = \mu_{n,N} e^{-T_{\mathrm{op}}/T_{\mathrm{c}}}, \quad \sigma^2_{n+1,0}[T_{\mathrm{op}}] = \sigma_K^2 + \left(\sigma^2_{n,N} - \sigma_K^2\right) e^{-2T_{\mathrm{op}}/T_{\mathrm{c}}}. \tag{4.13}$$

T_{op} serves as the separation time between two consecutive repetitions n and $n+1$. In the reconstruction we use parameters that mimic experimental setup, i.e. we set $\alpha = 0.28$, $\beta = 0.45$, $\sigma_K = 40\,\mathrm{MHz}$, $T_{\mathrm{c}} \approx 1\,\mathrm{s}$ and use the frequency grid $f_{B,j} = 1, 2 \ldots 40\,\mathrm{MHz}$.

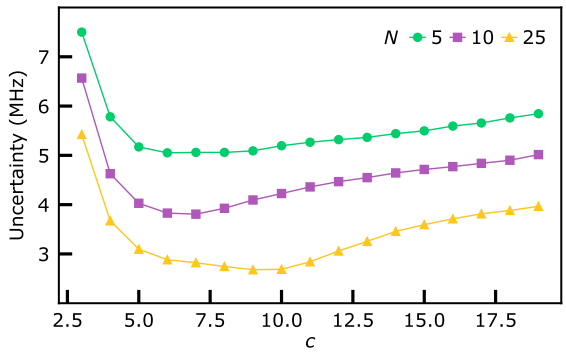

Fig. 4.7: **Optimal choice of c in $t_i = 1/(c\sigma_{i-1})$.** Numerically simulated uncertainty as a function of c and number of measurements $N = 5$ (green), $N = 10$ (blue), $N = 25$ (yellow) for the adaptive estimation method. To reflect experimental scenario we set $\alpha = 0.28$, $\beta = 0.45$, $\sigma_K = 40\,\mathrm{MHz}$, $T_c \approx 1\,\mathrm{s}$ and us the frequency grid $f_j = 1, 2 \ldots 40\,\mathrm{MHz}$. The estimation protocol consists of 1,000 realizations, and is averaged over 100 independent numerical experiments.

Numerical simulation of estimations

We support our results by the numerical study, that aims at simulating relevant features of estimation setup. For each realization of the algorithm we generate a random trajectory of the field $f_B(t)$, modeled as the Ornstein-Uhlenbeck process with $\sigma_K = 40\,\mathrm{Hz}$ and $T_c \approx 1\,\mathrm{s}$. We use quasistatic approximation, i.e. assume that the frequency is constant during single evolution time $f_B^{(r,i)}$ and varies only between the consecutive FID experiments. For each repetition r and each measurement i, we use the value of simulated field to compute probability of measuring singlet $P_{r,i}(f_B^{(r,i)}) = 1 + (\alpha + \beta\cos\left(2\pi f_B^{(r,i)} t\right)]/2$, where the evolution time t is selected based on the method used. With this distribution, we use a random number generator to draw the single-shot outcomes $m_{r,i}$, which we then feed to the algorithm described in the previous section.

Determine optimal adaptive-time parameter c

Firstly, we use the simulation to find the optimal value of parameter $c = 1/(t_i\sigma_{i-1})$, which minimizes estimation uncertainty, given the constraints of the quantum controller. To achieve that, we kept the simulation parameters from experimental and reconstruction protocols, the details of which are described in the previous section. We sweep the value of c in the numerical simulation of the adaptive method that uses $N = 5$, 10, 25 measurements (colors) and find that $c \approx 5 - 10$ typically gives the smallest uncertainties [see Fig. 4.7].

As our simulations do not include other sources of qubit dephasing, this range of c may not be the best choice in the experiment. In principle, as σ_{i-1} decreases, longer sensing times are more efficient in further decreasing the frequency uncertainty. In practice, however, the range of useful sensing times is limited by the qubit decoherence time, on the order of 100 ns in our system. Consequently, for experiments with $N = 25$, we empirically tuned the parameter c to $c \approx 13$, which seems to limit the allowed sensing time to a reasonable range.

Benchmarking the different estimation methods [Fig. 4.4(d) of Sec. 4.4]

In our experimental setup, the estimations encountered limitations stemming from readout quality and quantum controller memory constraints. We envision that advancements in both aspects could significantly enhance the speed and robustness of the adaptive-time scheme (see also next section). To explore the potential, we conduct a benchmark of the estimation schemes outlined in Sec. 4.4, comparing them against two additional schemes incorporating adaptive priors and using distinct evolution time schedules: randomly picked times t_i and linearly spaced t_i but with a larger time step. We thus simulate a series of 4,000 estimations spaced by $T_{\text{op}} = 5\,\text{ms}$, spanning 20 s of "lab" time, using different estimation schemes. In our estimations, the true Overhauser gradient follows an Ornstein–Uhlenbeck process with $\sigma_K = 40\,\text{MHz}$ and $T_{\text{c}} \approx 1\,\text{s}$. We further assume for simplicity ideal conditions, amounting to:

- ideal readout ($\alpha = 0$, $\beta = 1$);
- a broader frequency grid $[0, 150]\,\text{MHz}$ instead of $(0, 40]\,\text{MHz}$ with 0.25 MHz bin size;
- the possibility to use non-integer sensing times ($t_i = i\,t_0$ with $t_0 = 1$ ns).

We compute the average uncertainty at the end of 4,000 estimation cycles, separated by $T_{\text{op}} = 5\,\text{ms}$. For statistical purpose we additionally average this quantity over 100 independent realizations of the field and measurement outcomes. Obtained in this way average uncertainty, as a function of number of measurements in each estimation N, is shown in Fig. 4.4(d).

To shed more light on the performance of different estimation schemes as well as the correlation between uncertainty and the error we concentrate on a single realization of the field. Fig. 4.8(a) shows the resulting final distributions as a function of the lab time for $N = 5$, where all plots are based on the same simulated realization of $f_{B,\text{sim}}(t)$, whose trajectory is shown in Fig. 4.8(b). The statistics of the uncertainties in the final distributions $P_{\text{final}}(f_B)$ (their mean and standard deviation) are plotted in Fig. 4.8(c) as a function of measurement update, where value $i = 0$ corresponds to average initial distribution while $i = 5$ is the average final one. We again used the uncertainties in $P_{\text{final}}(f_B)$ as a measure for the error in the estimate, in order to make comparison to the experimental results fair. However, in the simulations we of course know the true instantaneous value $f_{B,\text{sim}}(t)$ of the frequency, and we can thus also assess the actual error in the estimation, which we define as $|\langle f_B \rangle - f_{B,\text{sim}}|$ and plot its median in Fig. 4.8(d) for the same collection of estimations as used in Fig. 4.8(c).

These findings show first of all that the non-tracking scheme [black in (a)] is relatively ineffective and, among the methods using a physics-informed prior distribution, the adaptive-time scheme performs best. Furthermore, we see that the uncertainties σ plotted in panel (c), which we use in the previous sections as a measure for the estimation error, indeed correlate with the median of actual errors, shown in (d) (as also investigated above). We note that the overall error can be as low as 2.5 MHz, with $N = 5$, which would translate to total estimation time $T_{\text{est}} = 5 \cdot 20\,\mu\text{s} = 100\,\mu\text{s}$, where 20 µs is the typical duration of a single free-induction decay experiment.

Physics-informed adaptive Bayesian tracking: setup limitations

In this section we discuss the limitations of our setup. We show experimental results where the adaptive-time scheme deviates from the expected behavior, affecting the statistics of the performance of the scheme. We explain how we accounted for them when presenting the performance

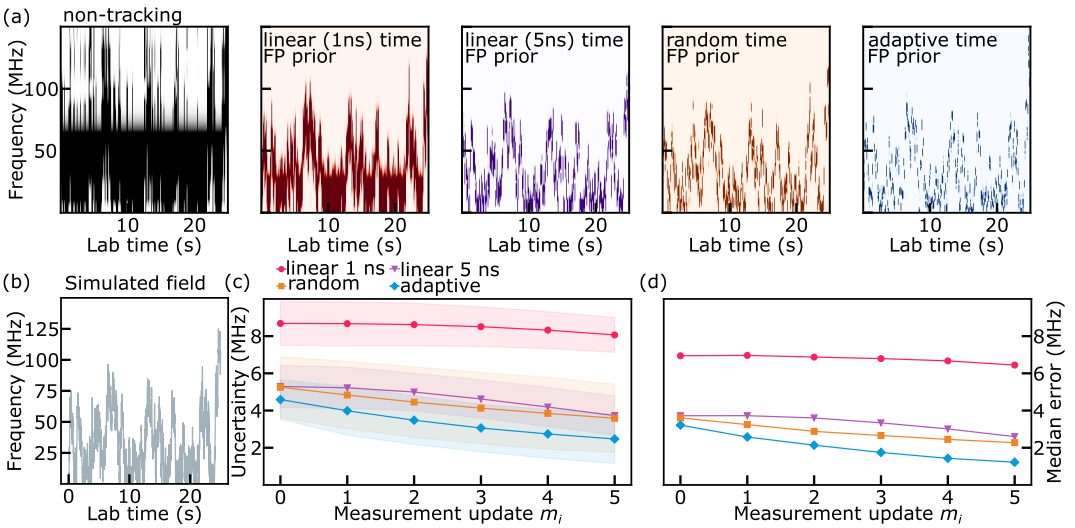

Fig. 4.8: **Numerical simulation of estimation methods.** **(a)** Simulated posterior distributions $P_{\text{final}}(f_B)$ for different estimation methods, given the simulated frequency shown in (b). "FP prior" means that the prior distribution $P_0(f_B)$ at the beginning of each repetition follows from the Fokker–Planck equation, as described in Sec. 4.3. **(b)** Simulated frequency of the Overhauser magnetic field gradient. **(c)** Statistics of the uncertainties in the final distributions of the protocols shown in (a) (except the inefficient non-tracking protocol), as a function of the measurement updates $i = 0,1,2,3,4,5$ in estimation cycle [same plot as Fig. 4.4(c)]. **(d)** Median of the absolute error of the protocols shown in (a) (except non-tracking) as a function of $i = 0,1,2,3,4,5$ [same legend as in panel (c)].

of the scheme in Sec. 4.4, and we also discuss potential underlying causes and propose possible solutions for future work.

Bias towards lower frequencies

Fig. 4.9(a) shows the final distributions of a series of 10,000 adaptive-time estimations (approximately 30 s of lab time) where we used $c = 6$, $N = 40$, and $T_{\text{op}} = 20\,\text{ms}$. We immediately notice that there seems to be an unexpectedly large number of distributions that peak sharply in the first bin (the frequency range 0–1 MHz). We corroborate this observation in Fig. 4.9(b), which shows a two-dimensional histogram of the final mean and standard deviation $\{\langle f_B\rangle, \sigma_f\}$ of all estimations shown in (a). We see that there is indeed a disproportionate number of estimated frequencies taking the lowest value of $\langle f_B\rangle \approx 0.5\,\text{MHz}$, all having an extremely narrow final distribution. We consider these estimations to be anomalies caused by the limitations of our setup, and thus filtered them out before performing the benchmarking presented in Sec 4.4. Since we thus reject a number of estimations with very small associated uncertainty, our comparison of the adaptive-time scheme to other methods in Fig. 4.4(c) can be seen as a worst-case benchmark for the experimentally implemented adaptive-time scheme.

To investigate the cause of this behavior, we zoom in on a range of repetitions with a significant

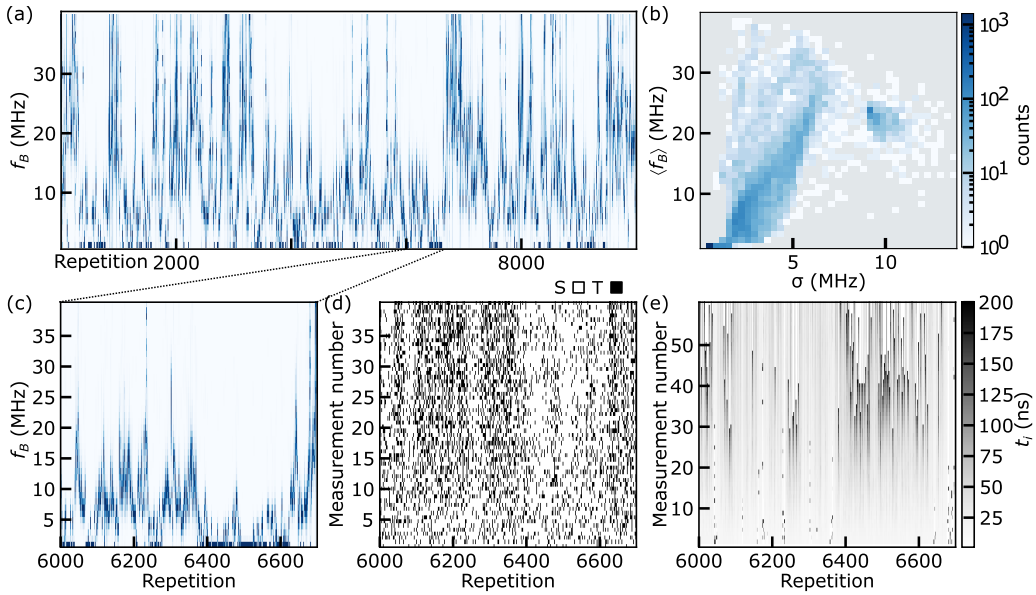

Fig. 4.9: **Bias of the adaptive-time estimation scheme at low frequencies.** **(a)** An example of a complete adaptive-time estimation trace across 10,000 repetitions (≈ 30 s of laboratory time), with $N = 40$ and $T_{\text{op}} = 20$ ms. **(b)** Histogram of the means and standard deviations $\{\langle f_B \rangle, \sigma_f\}$ of all repetitions in (a). **(c)** Zoom in on repetitions 6,000–6,700 from (a). **(d)** Single-shot measurement outcomes used for the estimations during the repetitions shown in (c). **(e)** Sensing times used for all single-shot measurement across the different repetitions.

number of anomalous estimations, shown in Fig. 4.9(c), and we plot the corresponding single-shot measurement outcomes m_i [Fig. 4.9(d)] and sensing times t_i [Fig. 4.9(e)] used during each estimation. This allows us to make two observations: (i) The ranges where the estimated frequency is small correspond to white “stripes" of singlet-biased data in Fig. 4.9(d), see, e.g., the repetitions in the interval [6400,6600]. (ii) Inside these ranges, the sensing times t_i, shown in Fig. 4.9(e), increase much faster than elsewhere; eventually it reaches the maximum sensing time of 200 ns allowed by the quantum controller, after which the time is reset to the user-defined value of 1 ns. Below we will discuss several mechanisms we identified that could play a role in this behavior, and we give an outlook on possible ways to mitigate these issues.

Qubit dephasing. We recall that the sensing time is determined by the posterior distribution variance at each step as $t_i = 1/c\sigma_{i-1}$, where $c \approx 13$ was used in the experiments. This in fact helps the estimation being attracted to small $\langle f_B \rangle$ and σ_f during the estimation cycle in the following way: Small posterior uncertainties σ_i lead to longer separation times, which at some point become comparable with the qubit decoherence time T_2, on the order of ≈ 100 ns. When $t_i \gtrsim T_2$ there is no information left in the measurement outcomes and the probabilities for measuring $m_i = \pm 1$ become independent of t_i. Since the scheme we use does not include a finite dephasing in the likelihood function, the absence of oscillations at larger times is in fact processed as correct information and can be treated as evidence for vanishing f_B (depending on the saturation value of

the singlet probability), yielding (i) an estimate with both very small $\langle f_B \rangle$ and σ_f and (ii) a relatively quick divergence of t_i during the estimation, as indeed seen in Fig. 4.9(e).

A straightforward improvement in the estimation scheme would be to modify Eq. (4.3) by adding a phenomenological dephasing time T_2 as follows

$$P_{\text{final}}(f_B) \propto P_0(f_B) \prod_{i=1}^{N} \left[1 + m_i \left(\alpha + \beta e^{-t_i/T_2} \cos(2\pi f_B t_i)\right)\right]. \tag{4.14}$$

The exponential factor will decrease the weight of the information gained at longer separation times, thus taking into account the decoherence of the qubit.

Residual exchange coupling. The relatively high number of data points in the lowest frequency bin could also be partly attributed to a non-vanishing field along the z-axis of the qubit Bloch sphere at the sensing point deep in the $(1,1)$ region, due to residual exchange coupling. When the magnitude of the Overhauser field gradient becomes comparable to or smaller than the instantaneous exchange splitting, i.e., $hf_B \lesssim J(\varepsilon)$, then the free-induction decay precession on the Bloch sphere will no longer let the qubit evolve approximately along a meridian from the north pole (singlet) to the south pole (triplet) and back, but rather only partly reach the triplet state. This will thus bias the measurement outcomes towards more singlets in this low-Overhauser-field limit. Since the likelihood function we use for the Bayesian update assumes the rotations to be along the x-axis and thus does not account for residual exchange coupling, the bias towards more measured singlets results in a bias towards believing that the qubit does not rotate at all, thus contributing to confidence that the frequency is zero. As the Overhauser field becomes larger this biasing effect becomes less and less pronounced.

The residual exchange may be reduced by reducing the tunnel coupling between the two dots during FID. Alternatively, the estimation protocol could be modified by considering the residual exchange when the qubit frequency is estimated.

Gaussian approximation. The way we convert each final posterior distribution to a Gaussian, as input for the physics-informed evolution of the distribution, can contribute to artificial narrowing of the distribution for small $\langle f_B \rangle$. Indeed, an underlying probability distribution for f_B that has significant weight at both positive and negative frequencies will yield a distribution for $|f_B|$ on the quantum controller that is in fact narrowed, up to a factor 2. The σ_f extracted as input for the FP evolution can thus be smaller than the actual uncertainty in the underlying distribution, and this artificial reduction will contribute to the bias toward small $\{\langle f_B \rangle, \sigma_f\}$ as described above.

For future experiments, one could try to derive an improved version of the FP equation, that takes the indiscernibility of the sign of f_B into account, not producing artificial narrowing of σ for small frequencies. However, one can argue that for any practical purpose (e.g., using the Overhauser gradient as a coherent control axis) the regime of very small f_B should be avoided anyway, and the pragmatic way to mitigate this issue is thus simply to discard estimations that yield an $\langle f_B \rangle$ below some user-defined threshold. We note that this "sign problem" also plays a role in the numerical simulations we performed, in contrast to the qubit dephasing and residual exchange coupling discussed above, which we set to be absent in the simulations.

Numerical errors on the quantum controller hardware

Finally, we note that in some cases σ_i becomes sufficiently small or large to cause errors on the FPGA-powered quantum controller, because of its available numerical accuracy, leading to

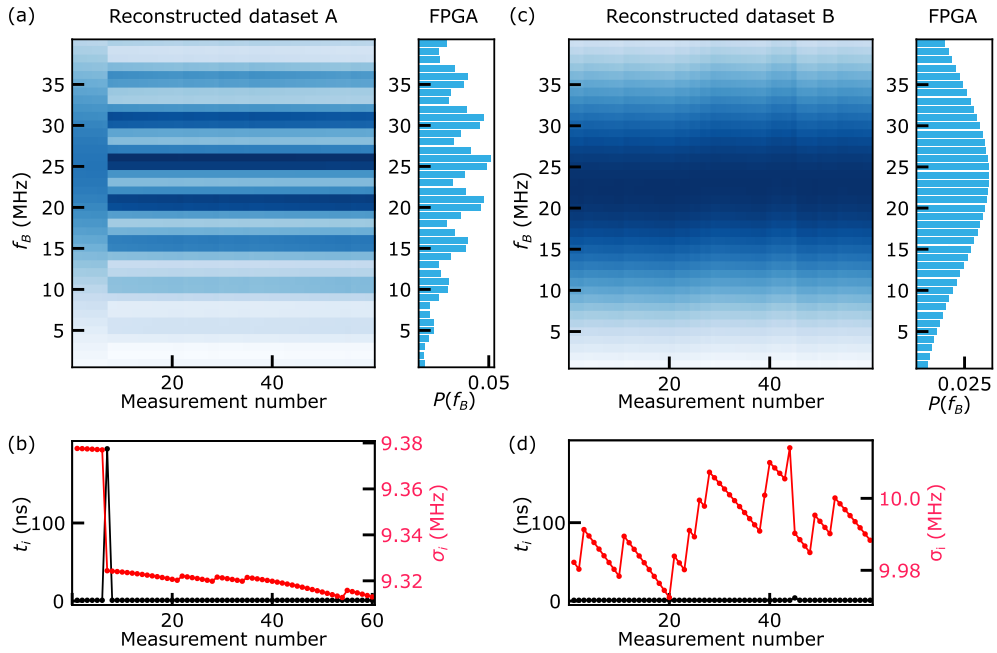

Fig. 4.10: **Examples of potential numerical errors. (a)** (left) Reconstructed (by post processing) Bayesian update of a distribution that becomes multi modal. (right) The corresponding experimental posterior as computed on the quantum controller. **(b)** Sensing time and standard deviation for every single-shot outcome in the estimation run. **(c)** (left) Reconstructed Bayesian update of a distribution that remains almost unchanged during estimation. (right) The corresponding final posterior as computed on the quantum controller. **(d)** sensing time and standard deviation for every single-shot outcome in the estimation run.

presumably incorrect estimations. In Figure 4.10 we show two examples of unexpected behavior during an estimation that we attribute to an error on the quantum controller. In (a,c) we show in the right panel the final distributions of the two estimations as stored on the quantum controller and in the left panel we present the reconstructed evolution of the distribution during the estimation, as explained above. In (b,d) we show the corresponding series of t_i and σ_i during the estimation, resulting from the reconstruction. In dataset A [Fig 4.10(a,b)] we see that the sensing time t_i suddenly jumps to a large value (≈ 200 ns) and then drops back again to a very small value (≈ 1 ns). This results in a posterior that has many peaks, due to the rapid oscillation of the likelihood function $P(m_i|f_B)$ when t_i is large. When waiting 20 ms between estimations, such upward jumps in t_i over 100 ns happen for 30% of estimations. In dataset B [Fig 4.10(c,d)] the sensing time [Fig 4.10(d)] almost does not change at all from 1 ns so that the final posterior distribution is almost equal to the initial prior distribution. This seems to happen much less frequently, with only about 1% of estimations (with 20 ms waiting time between estimations) having values of t_i that are all smaller than 5 ns. We note that in both datasets the final distributions end up having relatively large variances. When the waiting time in between estimations is 1 ms or 5 ms, the only instances where

t_i suddenly jumps up is when the standard deviation is very low, and there are no estimations where t_i are all smaller than 5 ns.

It is only in the $T_{\mathrm{op}} = 20$ ms case where the starting standard deviation at each estimation is above 8.9 MHz, indicating that numerical overflows are the likely cause. Indeed, overflow errors in the quantum controller are expected to happen for variances outside the range of standard deviations $1/(8\sqrt{10})$ MHz ≈ 40 kHz $< \sigma < \sqrt{80}$ MHz ≈ 8.9 MHz. However, the adaptive separation times produced during overflow errors are not retrievable through post-processing, preventing a definitive attribution of these errors to the aforementioned overflow issues. Nevertheless, for the two examples depicted in the figures above, we observe that the reconstructed standard deviations (which are in good agreement with the final posterior standard deviations found by the quantum controller) are greater than the 8.94 MHz threshold capable of causing the quantum controller to overflow.

A possible solution for future works when evaluating the standard deviation on the FPGA is to count the number of zeros in the mantissa of the fixed point number [limited to the range $[-8, 8)$] and choose a different conversion factor accordingly, at the expense of added program complexity.

4.7 Author contributions

F.B. led the measurements and data analysis, and wrote the manuscript with input from all authors. F.B., J.v.d.H., A.C. and F.K. performed the experiment with theoretical contributions from J.A.K., J.B., J.D. and E.v.N. F.F. fabricated the device. S.F., G.C.G. and M.J.M. supplied the heterostructures. A.C. and F.K. supervised the project.

4.8 Acknowledgments

We thank Torbjørn Rasmussen for help with the experimental setup. This work received funding from the European Union's Horizon 2020 research and innovation programme under grant agreements 101017733 (QuantERA II) and 951852 (QLSI), from the Novo Nordisk Foundation under Challenge Programme NNF20OC0060019 (SolidQ), from the Inge Lehmann Programme of the Independent Research Fund Denmark, from the Research Council of Norway (RCN) under INTFELLES-Project No 333990, as well as from the Dutch National Growth Fund (NGF) as part of the Quantum Delta NL programme.

5

Qubit Stabilization by Binary Search Hamiltonian Tracking

Previously we have shown how to efficiently estimate low-frequency noise stemming from nuclear spins and compensate the qubit for it. In this Chapter, we stabilize a flux-tunable transmon qubit from noise in magnetic flux. Different from the nuclear spin noise with characteristic $1/f^2$ spectrum [31], flux noise is mostly $1/f$ [148] and requires higher feedback bandwidth. We task the quantum controller to perform an adaptive frequency binary search by Bayesian estimation in real time. The qubit Hamiltonian tracking improves the coherence time by 49% and the single-qubit error rate is reduced from $(7.6 \pm 0.3) \times 10^{-4}$ to $(6.9 \pm 0.2) \times 10^{-4}$. By gate set tomography, we show that the protocol also reduces the non-Markovian noise in the system. The frequency binary search can be used in any resonantly-driven qubit platform and it provides a useful calibration subroutine during the execution of general quantum circuits.

5.1 Introduction

Flux-tunable transmon qubits are designed to be mostly insensitive to charge noise, and an externally applied magnetic field can tune their frequency. However, the effective magnetic field is sensitive to random flux fluctuations known as flux noise. We refer the reader to Ref. [226] for a review on superconducting qubits. Flux-tunable transmon qubits are typically operated at bias points (sweet spots), which are first-order insensitive to small changes in flux. Real-time frequency estimation and stabilization can enable the operation of these qubits far from the sweet spots, to reduce frequency crowding in large qubit arrays or coupling to a two-level system (TLS). Moreover, online qubit frequency estimation enables compensating for drifts of the qubit frequency even in the presence of a TLS [227].

The frequency binary search presented in this Chapter is an adaption of Ref. [151], where the “optimal" solution of the probing time τ is the one that partitions the prior distribution in an equal left and right part, performing a type of “ binary search". In Ref. [151], the lack of control of the qubit drive frequency means the binary search breaks down at sufficiently small frequency fluctuations x. Instead, in a transmon qubit, we can tune the drive frequency, which allows us to implement the binary search for all values of x in a quantum controller in real time.

5.2 Device and frequency binary search by Bayesian estimation

Similarly to the previous Chapters, the estimation of low-frequency fluctuations is useful as shown in Figure 5.1(a): one starts by estimating the qubit frequency in the quasistatic approximation.

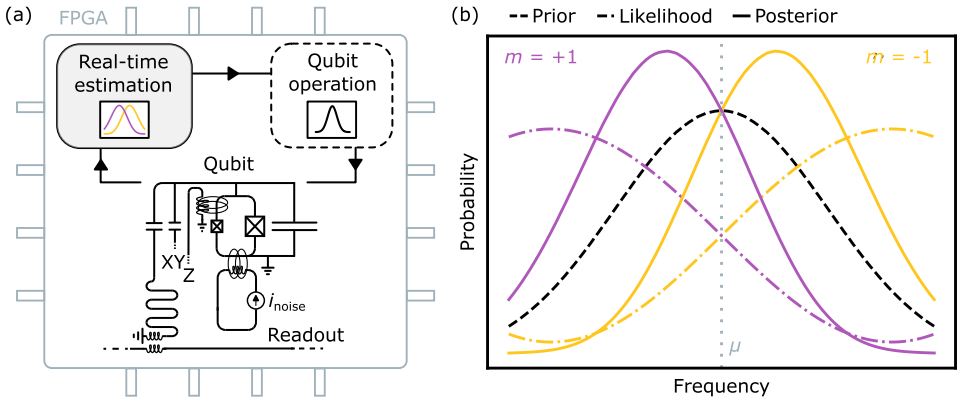

Fig. 5.1: **Qubit implementation and frequency binary search**. **(a)** Qubit schedule, alternating between periods of quantum information processing (dashed box), and periods for efficiently learning the fluctuating environment (gray box). **(b)** Illustration of the frequency binary search algorithm. At each step, the probing time and detuned frequency are chosen so that the distribution moves left or right, while reducing the standard deviation by a fixed fraction.

Afterwards, the qubit frequency is updated accordingly resulting in an increased qubit fidelity [148].

We use a superconducting qubit array from Ref. [228] and tune up one of its flux-tunable transmon qubits in a dilution refrigerator with a mixing-chamber plate below 30 mK. A commercial FPGA-powered quantum controller [146] applies high-frequency waveforms to the lines for qubit control and single-shot readout. A Yokogawa GS200 provides the DC flux bias source through a room temperature bias-tee (see Fig. 5.5 in Sec. 5.7 for details on the experimental setup).

The transmon has an asymmetric superconducting quantum interference device loop, and microwave Z and XY control lines [see (a)] of drive frequency f_d. The qubit is dispersively coupled to a coplanar waveguide resonator for its state readout.

To increase the qubit sensitivity to magnetic flux noise, the transmon is tuned at quarter flux $\Phi_{ext} = \pi\Phi_0/4$, where $\Phi_0 = h/(2e)$ is the superconducting magnetic flux quantum and Φ_{ext} is the applied magnetic flux through the flux line Z. The qubit has a transition frequency $f_q \approx 3.78\,\text{GHz}$ and we model its Hamiltonian in a rotating frame, within the rotating wave approximation by [226]:

$$\mathcal{H}(t) = -\frac{\Delta f}{2}\sigma_z + \frac{u(t)}{2}\sigma_x. \tag{5.1}$$

Here σ_i are the Pauli matrices, and the prefactor $\Delta f = f_d - f_q$ is the detuned frequency between f_q and the chosen rotating frame f_d. The control $u(t)$ is the envelope of a drive pulse with carrier frequency f_d.

For the frequency binary search (FBS), we assume the probability of measuring an outcome $m \in \{-1, 1\}$ corresponding to the states $|0\rangle$ and $|1\rangle$ is given by the following model:

$$P(m|x, \Delta f, \tau) = \frac{1}{2}\left(1 + m[\alpha + \beta e^{-\tau/T}\cos(2\pi(\Delta f + x)\tau)]\right), \tag{5.2}$$

where we can experimentally control the set detuned frequency $\Delta f = f_d - f_q$ and the evolution time of the Ramsey τ. The parameters $\alpha = -0.02$ and $\beta = 0.6$ are coefficients capturing initialization/readout errors, while T describes a coherence time that limits how long measurements remain useful. We set $T \approx 10\,\mu s$ based on the Hahn echo value $T_2^H \approx 12\,\mu s$ fit with exponential envelope.

The qubit fluctuation x is what we want to estimate. In the quasistatic approximation, we want to find the optimal sequence of τ's to estimate x in as few measurements as possible. By using Bayesian estimation we know that:

$$P(x|m_{n+1},\ldots,m_1,\Delta f_{n+1},\tau_{n+1}) = P(x|m_n,...,m_1,\Delta f_n,\tau_n)P(m_{n+1}|x,\Delta f_{n+1},\tau_{n+1}), \tag{5.3}$$

with the assumption that $P(x|m_{n+1},\ldots,m_1,\Delta f_{n+1},\tau_{n+1})$ is always Gaussian. Since this is not exactly the case, one is forced to fit $P(x|m_{n+1},\ldots,m_1,\Delta f_{n+1},\tau_{n+1})$ to a Gaussian, with the idea that a Gaussian should remain quite close to the actual distribution. The "optimal" solution presented by Ref. [151] indicates that the best τ is one that partitions the prior distribution $P(x)$ in an equal left and right part, performing the binary search.

Two steps are needed to implement the binary search in the quantum controller. The first step is to determine optimal experiment parameters τ and Δf based on the prior distribution. Then, one must fit the resulting posterior $P(x|m_{n+1},\ldots,m_1,\Delta f_{n+1},\tau_{n+1})$ when using these parameters to a Gaussian. This can be done using equations implemented on the quantum controller.

The prior distribution, dashed line in Fig. 5.2(b), in the Gaussian approximation is given by

$$P(x) = \frac{1}{\sqrt{2\pi\sigma_n^2}} \exp\left\{-\left(\frac{x-\mu_n}{\sqrt{2\pi}\sigma_n}\right)^2\right\}. \tag{5.4}$$

where μ_n is our guess for what x is with uncertainty σ_n. The probing time is given by:

$$\tau_{n+1} = \frac{\sqrt{16\pi^2\sigma_n^2 + 1/T^2} - 1/T}{8\pi\sigma_n^2}, \tag{5.5}$$

and in order to divide the prior at the center by the likelihood functions, the detuned frequency must satisfy

$$\Delta f_{n+1} = \frac{4}{\tau_{n+1}} - \mu_n. \tag{5.6}$$

After measuring $m = \pm 1$, the posterior distribution is obtained by multiplying the initial prior by the likelihood function related to the measurement outcome [cf. panel (b)]. In the end, the posterior is fit to a Gaussian by calculating its mean and variance:

$$\mu_{n+1} = \mu_n - \frac{2\pi m_{n+1}\beta\sigma_n^2\tau e^{-\tau_{n+1}/T - 2\pi^2\sigma_n^2\tau_{n+1}^2}}{1 + m_{n+1}\alpha}, \tag{5.7}$$

$$\sigma_{n+1}^2 = \sigma_n^2 - \frac{4\pi^2\beta\sigma_n^4\tau^2 e^{-2\tau_{n+1}/T - 4\pi^2\sigma_n^2\tau_{n+1}^2}}{(1 + m_{n+1}\alpha)^2}. \tag{5.8}$$

Based on these equations we get a new prior with updated values μ_{n+1} and σ_{n+1}, and this scheme is repeated N times to obtain a sufficiently narrow distribution. In the following, we optimize the number of single-shot measurements N based on the specific experiment. In the next section we test the FBS by performing Ramsey experiments to verify that it finds the correct qubit frequency.

5.3 Improvement of the qubit coherence

We implement qubit control through rapid FBS of x and demonstrate extended coherence of the flux-tunable transmon qubit.

The qubit quasistatic fluctuation x is estimated from the Ramsey pulse sequence shown in Fig. 5.2(a): for each repetition the Bloch vector is positioned on the equator using an $X_{\pi/2}$-pulse. After precessing for a time τ_i, a virtual $Z(\Delta f_i)$ gate [229] is performed, which corresponds to adding a phase offset $\phi = 2\pi\Delta f_i \tau_i$ to the following $X_{\pi/2}$-pulse. The latter pulse projects the Bloch vector back onto the z-axis, followed by the measurement. After each measurement, the qubit state s_i, ground ($s_i = 0$) or excited ($s_i = 1$), is assigned by thresholding.

The Bayesian probability distribution of x is updated according to the two outcomes s_i and s_{i-1}, as we do not initialize the qubit to the ground state at the beginning of the repetition to reduce the qubit cycle period (thus higher feedback bandwidth). It follows that in Eq. (5.2) $m_i = 2\,\mathrm{XOR}\,(s_i, s_{i-1}) - 1$. For instance, if in the previous measurement the qubit was in the ground state $s_{i-1} = 0$ and now it is in the excited state ($s_i = 1$) then $m_i = +1$. This is a good approximation as the qubit cycle period (a few µs) is short compared to the measured $T_1 \approx 80\,\mu\mathrm{s}$ at quarter flux. The readout length is 1.44 µs and the cooldown time of the resonator is about 2 µs (to deplete the residual photons after the readout pulse), the average Ramsey evolution time is $\approx 2.7\,\mu\mathrm{s}$.

The quantum controller is programmed to start with $\mu_0 = 0$ and $\sigma_0 = 30\,\mathrm{kHz}$. After each measurement, the quantum controller updates the Bayesian probability according to the outcome m_i which narrows the prior distribution. For illustrative purposes, we plot in the bottom panel of Fig. 5.2(a) the evolution of $P(x|m_{n+1},\ldots,m_1,\Delta f_{n+1},\tau_{n+1})$ from Eq. (5.3) as a function of the number of measurements N. Each black dot is the estimated x on the quantum controller and the shaded area shows the 68% credible interval for x. In the middle panel we plot the associated probability distribution $P(x|m_{n+1},\ldots,m_1,\Delta f_{n+1},\tau_{n+1})$ of each repetition after $N = 8$ measurements (downsampled to $\approx 8\,\mathrm{ms}$ for clarity).

After the estimation of x, the quantum controller updates the qubit frequency f_q and it performs a Ramsey sequence of evolution time τ_j and set detuned frequency $\Delta f_j = 1\,\mathrm{MHz}$, see Fig. 5.2(b). Below the pulse sequence, we plot the single-shot measurements p_j of this protocol as white/black pixels, spanning about 24 s.

After the Ramsey sequence with feedback, the quantum controller resets f_q to the offline-calibrated value, and it performs the same pulse sequence by linearly stepping τ_k at set $\Delta f_k = 1\,\mathrm{MHz}$, see Fig. 5.2(c). To show the increased coherence of the qubit, we plot the average of all Ramsey sequences. The decays are fit with Gaussian envelopes (solid line), yielding $T_2^* \approx 3.73\,\mu\mathrm{s}$ without feedback and $T_2^* \approx 5.57\,\mu\mathrm{s}$ with feedback, resulting in a 49% improvement.

Overall, the results presented in this section show how the FBS can efficiently find and stabilize the qubit frequency.

5.4 Improvement of the qubit fidelity

In this section we show improvement of the qubit fidelity by the FBS protocol by single-qubit randomized benchmarking (RB) [230].

The pulse sequence is shown in Fig. 5.3(a): the quantum controller resets the qubit frequency f_q and it performs the FBS with $N = 15$ measurements, starting with $\mu_0 = 0$ and $\sigma_0 = 200\,\mathrm{kHz}$. At the end of the estimation, f_q is updated and an RB sequence of depth L_s is performed. An interleaved

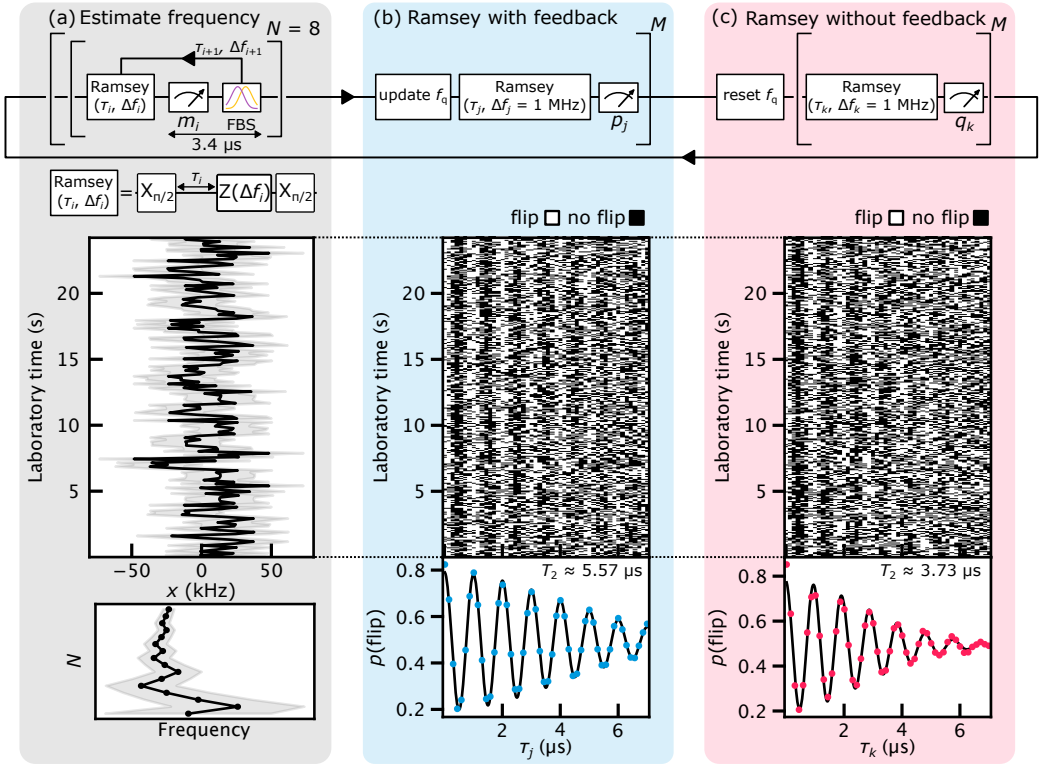

Fig. 5.2: **Suppressed dephasing of a qubit in a feedback-controlled rotating frame**. One loop (solid arrows) represents one repetition of the protocol. **(a)** For each repetition, the quantum controller estimates x by $N = 8$ Ramsey cycles of adaptive probe times t_i and detuned frequency Δf_i computed in real time. The quantum controller updates the frequency binary search (FBS) distribution after each measurement, as shown in the bottom panel for one representative repetition. The shaded area shows the 68% confidence interval computed on the quantum controller. Middle panel: probability distribution $P(x|m_8,\ldots,m_1,\Delta f_8,\tau_8)$ after completion of each repetition. **(b)** For each repetition the quantum controller updates the qubit frequency f_q, using its real-time knowledge of x. To illustrate the increased coherence, we task the quantum controller to perform a Ramsey cycle of set $\Delta f_j = 1\,\mathrm{MHz}$. The FBS estimation and evenly spaced Ramsey cycles are repeated $M = 50$ times. Single-shot measurements p_j are plotted as white/black pixels, and the fraction of flipped outcomes in each column is shown as a blue dot. **(c)** To test the feedback, the quantum controller resets f_q to the offline-calibrated value and performs $M = 50$ evenly spaced Ramsey cycles of set $\Delta f_k = 1\,\mathrm{MHz}$. Single-shot measurements q_k are plotted as white/black pixels, and the fraction of flipped outcomes in each column is shown as a red dot. Comparing (b) to (c), the coherence time improves by ≈ 49% with feedback.

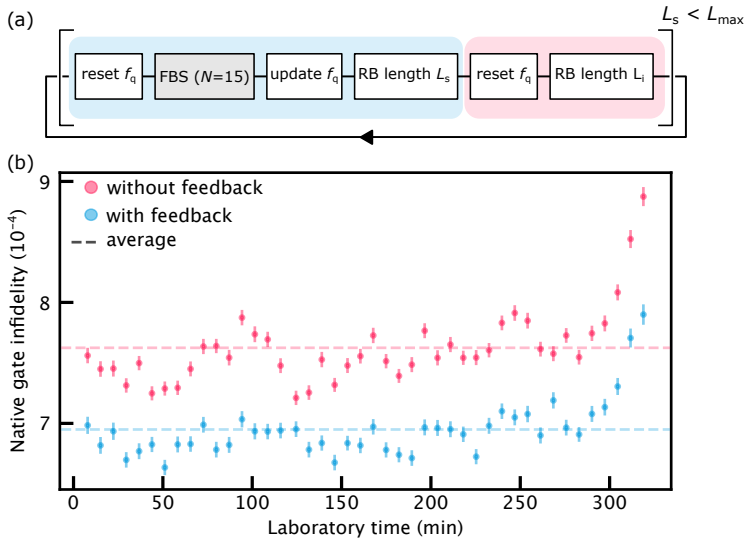

Fig. 5.3: **Randomized benchmarking**. **(a)** A randomized benchmarking sequence of length L_s combined with the FBS feedback (with $N = 15$ probing cycles). **(b)** Randomized benchmarking is repeated 44 times with the feedback (blue dots) and without (red dots). The native gate errors are extracted from the fit to the data, which consists of 10,000 realizations of 30 random Clifford sequences with and without the feedback. The error bars show the 68% confidence interval for the fitted gate error. Dashed lines are the averaged gate infidelities.

RB measurement without feedback follows by resetting the qubit frequency to the offline-calibrated value. The maximum circuit depth $L_{max} = 2,300$ and the measurement is averaged 10,000 times. We implement DRAG (derivative reduction by adiabatic gate) for our 20 ns pulses to suppress leakage errors [226].

Similarly to the previous section, the qubit is not initialized to the ground state at the beginning of the qubit cycle: the quantum controller keeps track of whether the state is different or not compared to the previous measurement.

Every 1,000 times averages, the threshold that classifies the state is updated online in the quantum controller by taking the average of 10,000 single-shot measurements after performing an $X_{\pi/2}$-pulse to the qubit.

The quantum controller performs the RB sequence for 6 hours, yielding a native gate infidelity of $(7.6 \pm 0.3) \times 10^{-4}$ without feedback and $(6.9 \pm 0.2) \times 10^{-4}$ with feedback [dashed lines in Fig. 5.3(b)]. The infidelities are higher than the T_1 limit [231] approximated by $t_{gate}/(3T_1) \approx 8 \times 10^{-5}$, given $t_{gate} \approx 20$ ns and $T_1 \approx 80$ µs at quarter flux. The feedback protocol always performs better than without, and with less spread around the mean value as a result of the stabilization. Some of the drifts of the infidelity remain correlated, and we tentatively attribute it to remaining low-frequency fluctuations not corrected by the FBS or other factors (e.g. changes in T_1).

We highlight the RB has been performed at quarter flux, far from the sweet spot to make the qubit more sensitive to qubit fluctuations. The improved fidelities of single-qubit gates by feedback by interleaved RB are presented in Sec. 5.7, Fig. 5.8.

The implemented feedback scheme demonstrates improvement of the qubit control. In the next section, we further characterize low-frequency drifts by gate set tomography.

5.5 Reduction of non-Markovian noise

Quantum error correction schemes assume Markovian noise [232], thus the effects of non-Markovian noise must be mitigated for fault tolerance.

We implement gate set tomography (GST) [233] using the pyGSTi [234] software package to show the improved stability of the qubit by the FBS, similar to what was implemented in Ref. [214] with a silicon spin qubit. The pulse sequence implemented on the quantum controller is shown in Fig. 5.4(a). The FBS requires $N = 6$ measurements per sequence with feedback, the initial $\mu_0 = 0$ and $\sigma_0 = 30\,\text{kHz}$. Each repetition is repeated 100 times for each of the 616 sequences constructed for GST.

As before, the qubit is not initialized to the ground state at the beginning of the qubit cycle for higher feedback bandwidth.

Gate set tomography assumes a Markovian gate set, or equivalently stationary noises for error prediction. It follows that GST does not fit well measurements in the presence of non-Markovian noise. In principle, the amount of non-Markovian noise is described by the goodness-of-fit [233], for which a sufficiently Markovian noise would satisfy

$$k - \sqrt{2k} < 2\Delta \log L_\text{s} < k + \sqrt{2k}, \tag{5.9}$$

where $\log L_\text{s}$ is the log-likelihood ratio between the predicted and observed value, and k is the number of independent measurement outcomes of a single circuit. If the observed data is well fitted by the model, $2\Delta \log L_\text{s} = 2\log L_\text{max,s} - 2\log L_\text{s}$ is expected to follow the χ^2_k distribution with a mean k and standard deviation $\sqrt{2k}$. The theoretical upper bound of the GST model is provided by $\log L_\text{max,s}$.

Figure 5.4(b) shows a reduction of non-Markovian noise with feedback. The non-Markovian noise shows up as the red squares, which have values $2\Delta \log L_\text{s}$ outside the range of Eq. (5.9) with a confidence level of 95%. To quantify the reduction of non-Markovian noise, the quantum controller repeats the GST experiment 30 times spanning a laboratory time of 40 minutes. In Fig. 5.4(c) we plot as a function of the maximum length the average total amount of $2\Delta \log L = \sum_s 2\Delta \log L_\text{s}$. While for maximum lengths of 1 and 2 there is no clear improvement, the latter is evident for longer sequences.

The GST protocol yields an $X_{\pi/2}$-pulse infidelity of $(2.6 \pm 0.3) \times 10^{-2}$ with and without feedback, and for the $Y_{\pi/2}$-pulse $(1.6 \pm 0.3) \times 10^{-2}$ with and without feedback. These values are two orders of magnitude larger than what is reported by RB. This discrepancy may be explained by GST's ability to identify non-Markovian noise and that non-Markovian effects dominate the Markovian stochastic noise in the system [232].

Drifts in the qubit frequency causes time-varying coherent errors in the gates. Randomized benchmarking is in principle insensitive to coherent errors [235]. Gate set tomography is sensitive to non-Markovian noise, but it misclassifies the slow drift as stochastic noise. It follows that GST overestimates stochastic noise, whereas RB underestimates the total noise.

In summary, even though the goodness-of-fit overestimates the actual degree of non-Markovian noise, the model violations suggest that the feedback protocol is likely to mitigate the effects of non-Markovian processes on the qubit.

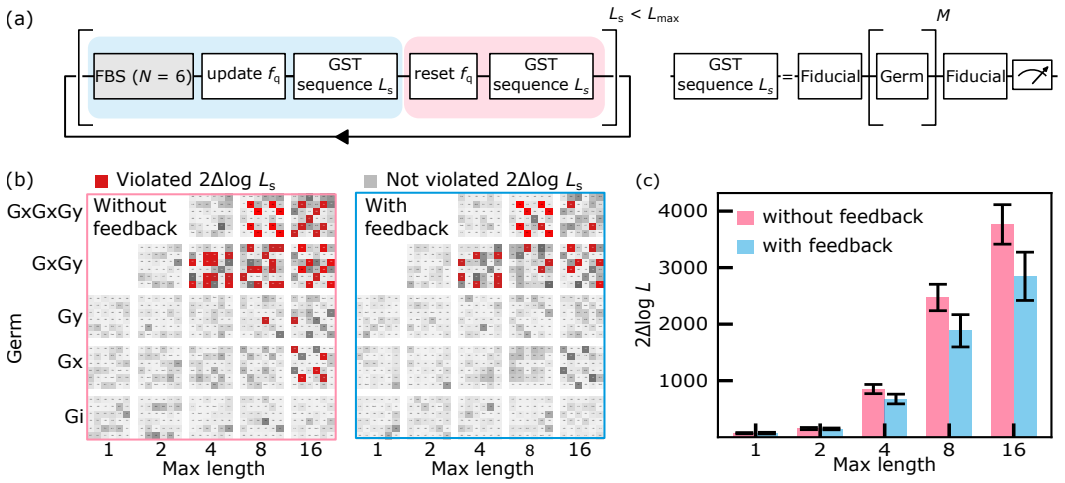

Fig. 5.4: **Gate set tomography and model violation**. **(a)** A gate set tomography (GST) sequence combined with the FBS feedback (with $N = 6$ probing cycles). **(b)** Model violation plot without (left) and with (right) FBS feedback. The red marks reveal detection of model violation at a confidence level of more than 95% and the gray boxes indicate statistical fluctuations. **(c)** The FBS feedback decreases the total amount of the log-likelihood ratios $2\Delta \log L$ (see main text) at maximum lengths of 4, 8, and 16, extracted from 30 GST runs. Error bars show the 68% confidence interval.

5.6 Outlook

We have introduced an adaptive frequency binary search algorithm to track low-frequency fluctuations in a resonantly-driven qubit efficiently. The algorithm has been implemented in a quantum controller to estimate in real time the flux noise in a transmon qubit, by adaptively choosing the frequency of the XY pulses and the duration of the probing evolution times. This work marks the first implementation of a flexible Bayesian approach for real-time frequency tracking in a superconducting qubit. Furthermore, we show by GST that the algorithm reduces the amount of non-Markovian noise in the system. Quantum error correction approaches rely on Markovian noise, but real-time frequency tracking protocols can suppress non-Markovian noise [214] to bring qubits to a fault-tolerant regime.

While the feedback bandwidth is limited by readout and resonator cooldown time, higher bandwidth could be obtained by adding a Purcell filter [226] while protecting the qubit from relaxing into its environment. The use of feedback approaches, as described in this Chapter, may favor using symmetric junctions to increase the frequency range of the qubit, without worrying about increased sensitivity to flux noise.

Possible modification of the protocol may involve the addition of a physics-informed prior [43] that considers $1/f$ noise, which has proven to require higher feedback bandwidth than nuclear spin noise. Also, the online calibration of single-qubit gates is a possible direction with available hardware, for single-qubit corrections in two-qubit gates [236] by actual (not virtual) Z gates.

Beyond superconducting qubits, our protocol efficiently calibrates solid-state qubits manipulated by resonant pulses. This work represents a significant advancement in quantum control by

implementing a Bayesian adaptive technique to stabilize in real time the qubit frequency with a small number of measurements.

5.7 Supplementary

Experimental setup

The measurements are performed in a Bluefors XLD-600 dilution refrigerator with a base temperature of 20 mK and the setup is shown in Fig. 5.5. The Quantum Machines OPX+ and Octave are used for the XY control of the qubit and readout signal. Each drive pulse is 28 ns long, with a cosine rise and fall envelope of 5 ns each. (Except for the randomized benchmarking and gate set tomography experiments, where the pulses are 20 ns long and calibrated by DRAG.)

The OPX+ includes real-time classical processing at the core of quantum control with fast analog feedback programmed in QUA software [146]. The OPX+ and Octave are frequency-locked by a Quantum Machines OPT (not shown). The microwave readout tone, approximately 7.08 GHz, is filtered and attenuated at room temperature by passive components. The readout tone is attenuated in the cryostat to remove excess thermal photons from higher-temperature stages, and low-pass filtered at the mixing chamber. The device is shielded magnetically with a superconducting can. The transmitted signal from the feedline goes through a circulator placed after the sample to remove all reflected noise of the Josephson traveling wave parametric amplifier (JTWPA) and dump it in a 50 Ω terminator (not shown). We preamplify the readout signal at base temperature using a Holzworth HS9000 Synthesizer.

To prevent noise from higher-temperature stages from reaching the JTWPA and the sample, two microwave isolators are placed after the JTWPA. A high-electron mobility transistor amplifier thermally anchored at the 3 K stage further amplifies the readout signal. At room temperature, the readout line is again amplified by an amplifier. A Yokogawa GS200 provides the DC bias flux through a bias-tee terminated by 50 Ω from the AC side, as we perform virtual Z gates in this work.

Qubit stabilization over six hours

We perform the protocol explained in Fig. 5.2 for hours as shown for the interleaved measurements in Fig. 5.7(a). In the left (right) panel the feedback is turned off (on) for over 6 hours. By taking the average (not shown) along laboratory time, we find a dephasing time $T_2^* \approx 4.2\,\mu s$ without feedback and $T_2^* \approx 5.2\,\mu s$ with feedback.

Figure 5.7(b) shows the values of Δf obtained from Ramsey measurements with feedback off (red curve) and on (blue curve). The feedback significantly reduces the fluctuation of Δf.

Interleaved randomized benchmarking

We perform interleaved randomized benchmarking (RB) [237] with and without feedback. The protocol consists of interleaving the gate $\mathcal{C}$ of interest with random gates from the Clifford sequence. A final gate is performed to make the total sequence equal to the identity operation. In Fig. 5.8 we plot the fraction of not-flipped state $p(\text{no flip})$ as a function of the number of Clifford gates in a random sequence, terminated by a Clifford gate that would in principle bring the qubit back to the initial state. For each gate, 30 random sequences are generated and they are averaged 1,000 times. We find a $X_{\pi/2}$-pulse gate infidelity improvement from $(5.75 \pm 0.04) \times 10^{-4}$ to $(5.47 \pm 0.04) \times 10^{-4}$,

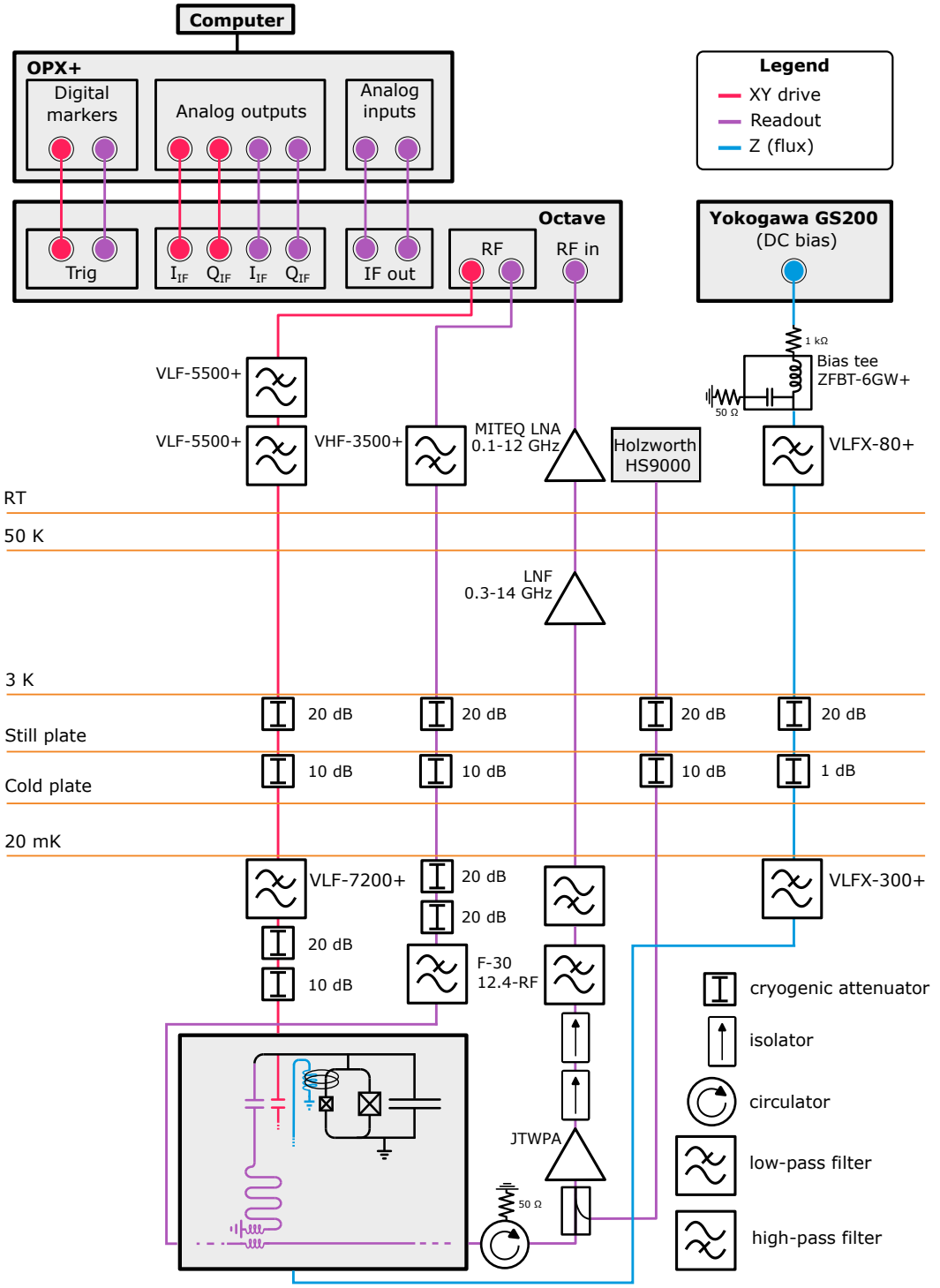

Fig. 5.5: See next page for caption.

Fig. 5.6: **Experimental setup BF2 (previous page).** The cryostat is a Bluefors XLD-600 dilution refrigerator with a base temperature lower than 30 mK. A Quantum Machines OPX+ and Octave are used for the XY drive pulses and readout. The setup includes a Yokogawa GS200 for DC flux biasing.

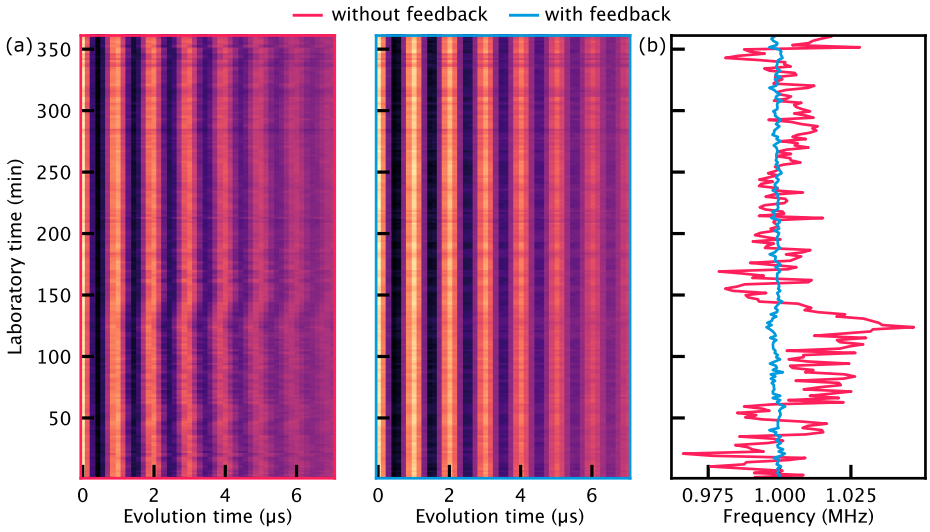

Fig. 5.7: **Qubit frequency stabilization over 6 hours. (a)** Ramsey experiment repeated for 6 hours without (left) and with (right) feedback by the frequency binary search. With the feedback, the qubit frequency is locked during the whole duration of the experiment. **(b)** Time dependence of the measured frequency detuning extracted from Ramsey measurements in (a). The red trace is taken with a fixed drive frequency f_{d}, and the blue trace is taken with a feedback-controlled f_{d}.

and for the $Y_{\pi/2}$-pulse from $(5.26 \pm 0.04) \times 10^{-4}$ to $(5.04 \pm 0.04) \times 10^{-4}$. The interleaved RB infidelities are in the same order of magnitude as the standard RB shown in Fig. 5.3. For each gate, feedback shows a similar improvement.

Acknowledgments

We thank the EQuS group at the Massachusetts Institute of Technology, particularly Lukas Pahl, Melvin Mathews, Jeff Grover and Will Oliver for providing the experimental setup and helping with the measurements. We also thank the ConSpiQuOS team at the Niels Bohr Institute, Norwegian University of Science and Technology, and Leiden University for fruitful discussions, particularly Jacob Benestad and Jan A. Krzywda for developing the frequency binary search algorithm. F.B. received funding from the Danish Agency for Higher Education and Science (Uddannelses- og Forskningsministeriet).

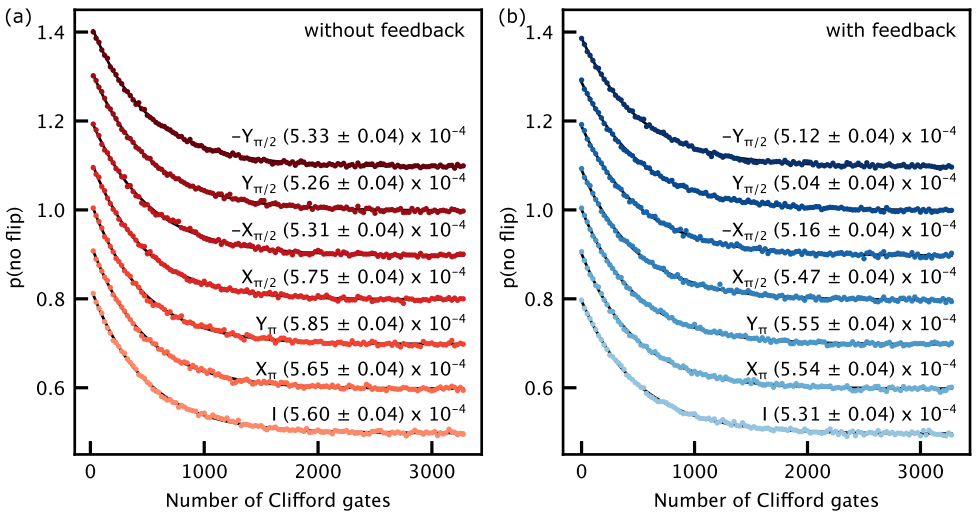

Fig. 5.8: **Interleaved randomized benchmarking with and without frequency binary search. (a)** Sequence infidelities for interleaved randomized benchmarking without frequency estimation by FBS. Traces are offset by 0.1 for clarity. Interleaved sequences are annotated with corresponding single-qubit gates and extracted natural gate infidelities. **(b)** Interleaved with (a) using frequency estimation by FBS. For all gates, the infidelity is slightly lower with feedback by a few 10^{-5}.

6

Conclusion and Outlook

Real-time Hamiltonian learning and feedback control can improve the performance of qubits affected by environmental fluctuations. In the first part of this work, we have presented a protocol for optimizing the control of a solid-state qubit in real time, which has effectively enhanced the qubit performance even in the presence of uncontrollably fluctuating Hamiltonian parameters.

In particular, we have employed an FPGA-powered quantum controller for dynamic, real-time baseband waveform generation and qubit manipulation. Combining this approach with real-time Hamiltonian Bayesian estimation, we have demonstrated the stabilization of a singlet-triplet qubit in GaAs. Our protocol has enabled real-time estimation of the Overhauser field gradient between the two electrons, allowing controlled Overhauser-driven rotations without the need for micromagnets or nuclear polarization protocols. In other words, the protocol has enabled noise-driven coherent rotations. Additionally, by estimating the exchange interaction between the electrons, we have performed a Hadamard gate, and extended its coherence by compensating for fluctuations in both rotation axes of the qubit.

In the second part of this work, we have implemented an online physics-informed estimation strategy. Specifically, we have programmed the quantum controller to propagate a probability distribution according to the Fokker–Planck equation, and adaptively generate qubit probe times that maximized the resulting estimation accuracy. The physics-informed protocol has yielded significantly higher-quality qubit tracking than obtainable via established estimation schemes. Remarkably, we have demonstrated a 10-fold increase in estimation speed *and* increased accuracy compared to previous schemes. The fast and efficient physics-informed Hamiltonian learning protocol readily applies to any spin qubit platforms affected by nuclear spin noise, e.g. gate-defined quantum dots, relaxing the effort in isotopic purification, and nitrogen-vacancy centers in diamonds.

In the last part, we have shown an adaptive frequency binary search algorithm by Bayesian estimation in real time, implemented in a flux-tunable transmon qubit. The qubit Hamiltonian tracking protocol has improved the coherence time by 49%, and the single-qubit error rate has been reduced from $(7.6 \pm 0.3) \times 10^{-4}$ to $(6.9 \pm 0.2) \times 10^{-4}$. By gate set tomography, we have shown that the scheme also reduces the non-Markovian noise in the system. The frequency binary search can be used in any resonantly-driven qubit platform, and it provides a useful calibration subroutine during the execution of general quantum circuits. Also, this experiment has demonstrated for the first time that real time Bayesian techniques can improve the stabilization of a qubit frequency with characteristic $1/f$ noise (here dominated by magnetic flux noise), which requires higher bandwidth than the $1/f^2$ noise spectrum characteristic of nuclear spins.

Still, at the current stage it is unclear what the future FPGA resources and limitations will be for operating a multi-qubit experiment. We speculate that a large overhead on classical computing and classical FPGA-based quantum control is a valid path forward, as these are relatively easy to engineer. Offloading technological developments from scaling of qubit hardware to scaling of classical control hardware is an exciting research direction. In this view, this Thesis provides valuable insights into the synergy between quantum control, quantum computation, and computer science.

A

Bloch Sphere, Single-qubit Gates, Decoherence

Bloch sphere

The *Bloch sphere* is a geometrical representation of the state of a two-dimensional system, e.g., a qubit. We follow the introduction of Ref. [226]. Figure A.1 shows a Bloch sphere with a Bloch vector which represents the state $|\psi\rangle = \alpha|0\rangle + \beta|1\rangle$ (with α and β complex numbers). The Hilbert space of the qubit is mapped to a sphere of unit length, with antipodal points (north-south poles) corresponding to the orthogonal state $|0\rangle$ and $|1\rangle$. Here $|\psi\rangle$ is a pure quantum state: this means $|\alpha|^2 + |\beta|^2 = 1$, or in words the vector connects the center of the sphere to a point on its surface. The longitudinal axis is the Z-axis and it represents the qubit quantization axis for the states $|0\rangle$ and $|1\rangle$, in the qubit eigenbasis. The x-y plane instead is the transverse plane with transverse axes X and Y. The unit Bloch vector $\vec{a} = (\sin\theta\cos\varphi, \sin\theta\sin\varphi, \cos\theta)$ in a Cartesian coordinate system, and it is described using the polar angle $0 \leq \theta \leq \pi$ and the azimuthal angle $0 \leq \varphi < 2\pi$, as shown in Fig. A.1. Therefore, we can equivalently represent the quantum state by the angles θ and φ:

$$|\psi\rangle = \alpha|0\rangle + \beta|1\rangle = \cos\left(\frac{\theta}{2}\right)|0\rangle + e^{i\varphi}\sin\left(\frac{\theta}{2}\right)|1\rangle\,. \tag{A.1}$$

In the laboratory frame, a Bloch vector precesses around the Z-axis at the qubit frequency $|E_1 - E_0|/\hbar$.

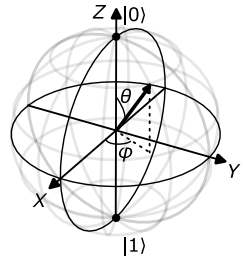

Fig. A.1: **Bloch sphere representation.** Bloch sphere representation of the quantum state $|\psi\rangle = \cos\left(\frac{\theta}{2}\right)|0\rangle + e^{i\varphi}\sin\left(\frac{\theta}{2}\right)|1\rangle$. The qubit quantization axis – the Z axis – corresponds to σ_z terms in the qubit Hamiltonian. The X-Y plane corresponds to σ_x and σ_y terms in the qubit Hamiltonian.

The density matrix $\rho = |\psi\rangle\langle\psi|$ for a pure state $|\psi\rangle$ can be described as

$$\rho = \frac{1}{2}(I + \vec{a}\cdot\vec{\sigma}) = \frac{1}{2}\begin{pmatrix} 1+\cos\theta & e^{-i\varphi}\sin\theta \\ e^{i\varphi}\sin\theta & 1+\sin\theta \end{pmatrix} \tag{A.2a}$$

$$= \begin{pmatrix} \cos^2\frac{\theta}{2} & e^{-i\varphi}\cos\frac{\theta}{2}\sin\frac{\theta}{2} \\ e^{i\varphi}\cos\frac{\theta}{2}\sin\frac{\theta}{2} & \sin^2\frac{\theta}{2} \end{pmatrix} \tag{A.2b}$$

$$= \begin{pmatrix} |\alpha|^2 & \alpha\beta^* \\ \alpha^*\beta & |\beta|^2 \end{pmatrix} \tag{A.2c}$$

given I is the identity matrix, and $\vec{\sigma} = [\sigma_x, \sigma_y, \sigma_z]$ is the vector of Pauli matrices. When $\vec{a}$ is a unit vector, ρ describes a pure state ψ and $\mathrm{Tr}(\rho^2) = 1$. We mention that the Bloch sphere can also represent the so-called mixed states, for which $|\vec{a}| < 1$; in this case, the Bloch vector connects the center of the Bloch sphere to points inside the unit sphere, and $0 \le \mathrm{Tr}(\rho^2) < 1$, where Tr is the trace. To sum up, the surface of the unit sphere describes pure states, whereas its interior describes mixed states [15].

The guidelines for quantum computation, known as the “DiVincenzo criteria" in the literature, can be stated as follows [238, 239]:

1. The elementary units of information, the qubits, must be stored in a scalable quantum register. A qubit is a quantum two-level system with orthogonal basis states $|0\rangle$ and $|1\rangle$.
2. The qubits can be prepared in a known state, e.g. $|00\ldots0\rangle$, where i-th "0" refers to the i-th
3. The quantum system must remain coherent for times longer than the duration of elementary logic gates because decoherence causes computational errors.
4. While keeping coherence, a high-fidelity gate set (single-qubit and two-qubit gates) must be available.
5. It should be possible to readout a sufficiently large part of the quantum register at the end of the computation.

Single-qubit gates

In this manuscript we have used spin-operators $\vec{S}$ that are in general represented as Pauli operators, similarly to Ref. [51]. Here we use the notation of Pauli operators, in terms of the Pauli matrices

$$\sigma_x = \begin{pmatrix} 0 & 1 \\ 1 & 0 \end{pmatrix}, \quad \sigma_y = \begin{pmatrix} 0 & -i \\ i & 0 \end{pmatrix}, \quad \sigma_z = \begin{pmatrix} 1 & 0 \\ 0 & -1 \end{pmatrix},$$

for the qubit states $|0\rangle$ and $|1\rangle$. Single-qubit operations are then generated by the Pauli operators

$$R_{\vec{n}}(\theta) = e^{-i\vec{n}\cdot\boldsymbol{\sigma}\theta/2}. \tag{A.3}$$

For instance the unitary $R_{\vec{n}}(\pi)$, i.e. a π-pulse, applies $-i\vec{n}\cdot\boldsymbol{\sigma}$, which means if $\vec{n}$ is along x, y or z, it is a Pauli operator with an overall phase (we recall a Pauli-operators applies ±1 to the two eigenstates of the qubit in the corresponding basis). Some of the single-qubit gates are summarized in Fig. A.2, including the Hadamard gate that performs a π rotation about an axis diagonal in the X–Z plane.

Gate	Matrix representation	Bloch sphere
I identity-gate: no rotation is performed	$\begin{matrix} \vert 0\rangle & \vert 1\rangle \\ \end{matrix}$ $\begin{pmatrix} 1 & 0 \\ 0 & 1 \end{pmatrix}$	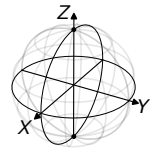
X gate: rotates the qubit state by π radians (180°) about the *X*-axis	$\begin{pmatrix} 0 & 1 \\ 1 & 0 \end{pmatrix}$	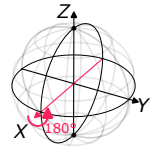
Y gate: rotates the qubit state by π radians (180°) about the *Y*-axis	$\begin{pmatrix} 0 & -i \\ i & 0 \end{pmatrix}$	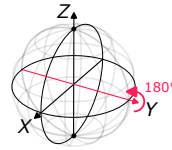
Z gate: rotates the qubit state by π radians (180°) about the Z-axis	$\begin{pmatrix} 1 & 0 \\ 0 & -1 \end{pmatrix}$	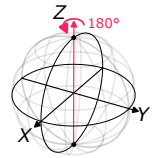
Hadamard gate: rotates the qubit state by π radians (180°) about an axis diagonal in the *X*-*Z* plane	$\frac{1}{\sqrt{2}}\begin{pmatrix} 1 & 1 \\ 1 & -1 \end{pmatrix}$	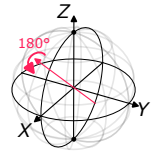

Fig. A.2: **Single-qubit gates.** For each gate, the name, a short description, matrix representation, and Bloch sphere representation are provided. Matrices are defined in the basis spanned by the state vectors $|0\rangle \equiv (1,0)^{\mathrm{T}}$ and $|1\rangle \equiv (0,1)^{\mathrm{T}}$. Adapted from Ref. [226].

Relaxation, decoherence, dephasing

As quantum devices are sensitive to changes in their environment, they can easily lose their intended quantum properties, a phenomenon known as decoherence. Different decoherence sources exist in semiconductor spin qubits [51], with terms borrowed from the NMR and ESR community. A *relaxation* process nondegenerate spin states exchange energy with the environment (e.g. via phonons or photons), with characteristic time T_1. In *pure dephasing*, the phase of the qubits is changed by random elastic (energy-conserving) processes (T_2). In *inhomogeneous dephasing*, the qubit's phase is steady for long periods, however it is not well synchronized with itself in a later time, a clock or another qubit (T_2^*).

B

Exchange Interaction

Exchange interaction is a fundamental physical property of spin qubits, and due to the broad use of this term, this section aims to describe what is meant by exchange in the spin qubit community. In the following the main steps are adapted from Ref. [51]. Exchange origins from Fermi statistics, Coulomb repulsion, and electron tunneling. We introduce the single-particle basis functions $\phi_m(\vec{r})\chi_\sigma$, where m denotes the spatial orbital, $\sigma = \uparrow, \downarrow$ is the electron spin, and $\vec{r}$ the position. For instance, we show in Fig. B.1(a) the real part of the one-electron wavefunctions $\phi_m(\vec{r})\chi_\sigma$ of a single QD [approximated by a parabolic potential $V(x)$], where the first excited state $|e\rangle$ is separated from $|g\rangle$ by the orbital energy E_{orb}, typically on the order of a few meV. Each dashed gray line has two-fold degeneracy $\sigma = \uparrow, \downarrow$, without externally applied magnetic fields. The exchange is described in more detail next to understand what happens if a second electron is added to the same QD.

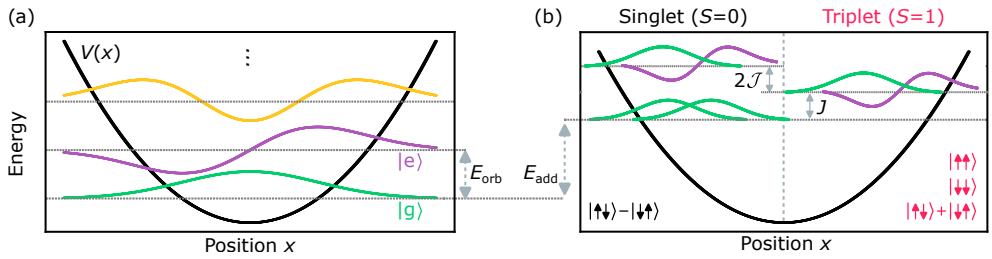

Fig. B.1: **Low-energy spectrum of a one- and two-electron QD with spin degree of freedom (in the absence of an external magnetic field) (a)** Confining potential of a quantum dot approximated by the parabolic potential of a harmonic oscillator as a function of the position x. The different curves are the real part of the wavefunctions solution of the 1D quantum harmonic oscillator problem, plotted at their corresponding eigenenergies. For the following discussion, only the first two orbital levels are considered, the ground state $|g\rangle$ and the excited state $|e\rangle$. Dashed gray lines represent two-fold degenerate spin states. **(b)** For two electrons, considering the spin degree of freedom, but still in the absence of an applied magnetic field, the spin component of the wavefunction can be singlet (with total spin $S = 0$) or triplet ($S = 1$). The singlet state is the ground state, with additional energy E_{add} compared to the single electron case. The second state in energy is the triplet, where also the excited orbital $|e\rangle$ participates in the wavefunction. Its energy is lower than the independent electron approximation because of the exchange interaction $2\mathcal{J}$. The separation in energy J is what is commonly called the (kinetic) exchange energy in the spin-qubit community.

The Pauli exclusion principle states that the multiparticle wavefunction $\Psi_{\sigma_1\sigma_2\ldots}(\vec{r}_1,\vec{r}_2,\ldots)$ must be antisymmetric given the N electrons $1,2,\ldots,N$. We can obtain a basis set for antisymmetrized many-particle states using the Slater determinant. Any fermionic wavefunction can thus be written as a linear combination of Slater determinants. We assume we have N electrons in states $(m_1,\sigma_1)\ldots(m_N,\sigma_N)$. We write the antisymmetrized many-particle wavefunction as

$$\Psi_{m_1\sigma_1,m_2\sigma_2,\ldots m_N\sigma_N}(\vec{r}_1,\vec{r}_2,\ldots,\vec{r}_N)=\frac{1}{\sqrt{N}}\begin{vmatrix}\phi_{m_1}(\vec{r}_1)\chi_{\sigma_1} & \phi_{m_2}(\vec{r}_1)\chi_{\sigma_2} & \cdots & \phi_{m_N}(\vec{r}_1)\chi_{\sigma_N}\\ \phi_{m_1}(\vec{r}_2)\chi_{\sigma_1} & \phi_{m_2}(\vec{r}_2)\chi_{\sigma_2} & \cdots & \phi_{m_N}(\vec{r}_2)\chi_{\sigma_N}\\ \vdots & \vdots & \ddots & \vdots\\ \phi_{m_1}(\vec{r}_N)\chi_{\sigma_1} & \phi_{m_2}(\vec{r}_N)\chi_{\sigma_2} & \cdots & \phi_{m_N}(\vec{r}_N)\chi_{\sigma_N}\end{vmatrix}. \tag{B.1}$$

For instance, focusing on two electrons, their wavefunction is

$$\Psi_{m_1\sigma_1,m_2\sigma_2}(\vec{r}_1,\vec{r}_2)=\frac{\phi_{m_1}(\vec{r}_1)\chi_{\sigma_1}\phi_{m_2}(\vec{r}_2)\chi_{\sigma_2}-\phi_{m_2}(\vec{r}_1)\chi_{\sigma_2}\phi_{m_1}(\vec{r}_2)\chi_{\sigma_1}}{\sqrt{2}}. \tag{B.2}$$

After swapping the two electrons, the wavefunction satisfies $\Psi_{m_1\sigma_1,m_2\sigma_2}(\vec{r}_2,\vec{r}_1)=-\Psi_{m_1\sigma_1,m_2\sigma_2}(\vec{r}_1,\vec{r}_2)$. Within the second quantization formalism, we define the anticommuting annihilation (creation) operator $c_{m\sigma}$ ($c^\dagger_{m\sigma}$) which annihilates (adds) an electron in the orbital state $\phi_m(\vec{r})$ and spin state σ. Then, the same state described by Eq. (B.2) can be represented as

$$\left|\Psi_{m_1\sigma_1,m_2\sigma_2}\right\rangle = c^\dagger_{m_1\sigma_1}c^\dagger_{m_2\sigma_2}\left|\text{vac}\right\rangle, \tag{B.3}$$

where the vacuum state with no electrons is $|\text{vac}\rangle$. Thus, rewriting the EMA Hamiltonian of Eq. (1.5) in this notation yields

$$\mathcal{H}=\sum_\sigma\sum_{mn}T_{mn}c^\dagger_{m\sigma}c_{n\sigma}+\frac{1}{2}\sum_{\sigma_1\sigma_2}\sum_{mn\ell p}V_{mn\ell p}c^\dagger_{m\sigma_1}c^\dagger_{n\sigma_2}c_{p\sigma_2}c_{l\sigma_1}, \tag{B.4}$$

where the single-particle kinetic and electrostatic potential energy integral is

$$T_{mn}=\int d^3\vec{r}\;\phi^*_m(\vec{r})\left[-\frac{\hbar^2}{2}\nabla\cdot(\boldsymbol{\beta}\cdot\nabla)+U(\vec{r})\right]\phi_n(\vec{r}). \tag{B.5}$$

In the previous equation it has been introduced $\boldsymbol{\beta}=(m_x^{-1},m_y^{-1},m_z^{-1})$ to describe the inverse effective masses. The effect of the electrostatic potential, due to the voltages applied to the gates and built-in electric fields, is captured by $U(\vec{r})$. The Coulomb integral is given by

$$V_{mn\ell p}=\int d^3\vec{r}_1d^3\vec{r}_2\phi^*_m(\vec{r}_1)\phi^*_n(\vec{r}_2)\frac{e^2}{4\pi\epsilon_r\epsilon_0|\vec{r}_1-\vec{r}_2|}\phi_\ell(\vec{r}_2)\phi_p(\vec{r}_1), \tag{B.6}$$

having introduced the semiconductor relative permittivity ϵ_r and the vacuum permittivity ϵ_0. For simplicity, image charges from metal gates are neglected. We recall that the *spatial* wavefunction must be symmetric (antisymmetric) under particle exchange, given the spin state is singlet (triplet). It is worth noticing that electrons in the singlet states can occupy the same orbital, whereas in triplets the electrons must reside in different orbitals. Anyway, singlet states are allowed to have electrons in different orbitals, as we discuss below.

To describe direct exchange, one may consider two different orbitals 1 and 2 of the same QD with high spatial overlap. Then the Coulomb integral of Eq. (B.6) can be split into a direct Coulomb

term $\mathcal{K}$, when $m \neq n$, $m = p$, and $n = \ell$, e.g. V_{1221}, and a direct exchange term $\mathcal{J}$ when $m = n$ and $\ell = p$, e.g. V_{1122}. The consequence is that given a pair of two electrons, the energy of the triplet states (spin component symmetric, orbital component antisymmetric) is $\mathcal{K} - \mathcal{J}/2$, whereas for the singlet state (spin component antisymmetric, orbital component symmetric) is $\mathcal{K} + 3\mathcal{J}/2$. Overall, the singlet state energy is higher than the triplet states one by $2\mathcal{J}$ (no magnetic field is considered.)

Here we summarize the result for two electrons in a QD. The higher energy of the singlet state compared to the triplet state, when both electrons have different orbitals in both spin states, is shown in Fig. B.1(b) [notice the three triplet states are degenerate in the absence of magnetic fields]. They are separated by the energy $2\mathcal{J}$. In the spin qubit community, it is defined as (kinetic) exchange[1] the singlet-triplet splitting of the lowest two states $J = E_{\mathrm{T}} - E_{\mathrm{S}}$, where E_{T} is the energy of the triplet state shown in (b), and E_{S} is the energy of the singlet state where both electrons occupy the lowest orbital state. As the triplet has one electron each in its ground and excited orbital state, then the exchange $J > 0$, and for the contribution of the direct Coulomb exchange interaction $2\mathcal{J}$ mentioned above, in a two-electron QD[2] $J < E_{\mathrm{orb}}$. Spin qubits leverage the kinetic exchange interaction, caused by the Pauli exclusion principle on the T_{mn} and $\mathcal{K}$ spin-independent terms.

[1] In atomic physics or chemistry the “exchange energy" is what here has been introduced as the Coulomb exchange integral $\mathcal{J}$, which describes the interaction between singlet and triplet states with the same set of orbitals. In spin qubits the orbital content is disregarded [51].

[2] It can be shown that any two-electron system has a singlet ground state in the absence of magnetic fields [57, Chapter 32].

C

Experimental Setup Characterization

DC Pin-out

Fig. C.1 shows the pin-out convention used in this manuscript. On top of the cryostat two turrets - A and B - are installed for the five DC looms, numbered starting from the top of each turret. The Weinreb amplifier is powered outside the cryostat by a BNC cable that goes to Fischer 4 and 11 of loom 3B. Inside the refrigerator, the amplifier is powered by a voltage-ground twisted pair.
To check for leakage between different DC lines, all the channels on the breakout box have been

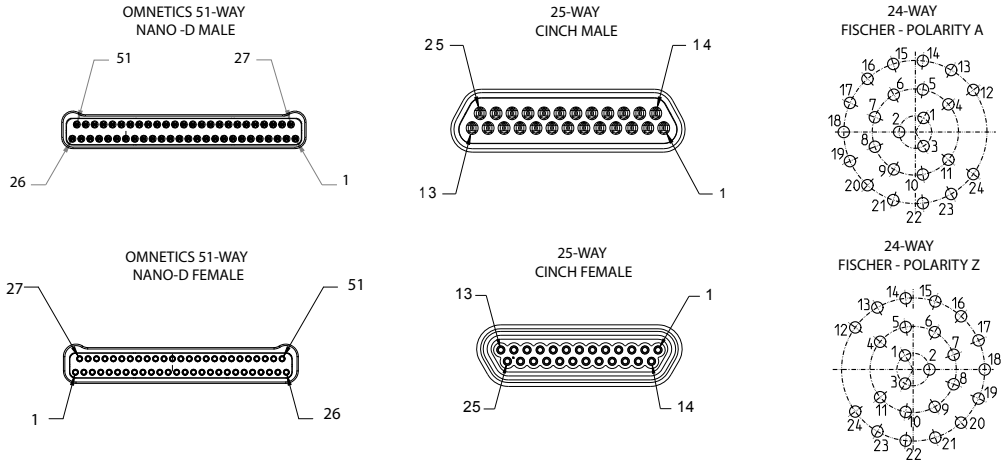

Fig. C.1: **Pin-out numbering convention for Nano-D, cinch and Fischer ports.**

grounded except one connected to the BUS line. Then, the resistance between the BUS line and the ground common to the instrument and the cryostat has been measured with the Keysight 34465A, expecting its overload in the absence of a shortage. Channels 23 and 24 of breakout box B (DC loom 1B) were shorted to each other (we observed a leakage resistance of about 200 Ω), it was fixed by replacing one of the DC looms with a nominally identical one that was characterized as well.

Breakout Box A QBox [1..24]	Fischer 1A 24-way	RT - MC	Cinch 1A	MC - coldfinger	Omnetics Nano-D 51-way
1	1	twin-twisted	1	copper	1
2	2	constantan	14	copper	2
3	3	twin-twisted	2	copper	3
4	4	constantan	15	copper	4
5	5	twin-twisted	3	copper	5
6	6	constantan	16	copper	6
7	7	twin-twisted	4	copper	7
8	8	constantan	17	copper	8
9	9	twin-twisted	5	copper	9
10	10	constantan	18	copper	10
11	11	twin-twisted	6	copper	11
12	12	constantan	19	copper	12
13	13	twin-twisted	7	copper	13
14	14	constantan	20	copper	14
15	15	twin-twisted	8	copper	15
16	16	constantan	21	copper	16
17	17	twin-twisted	9	copper	17
18	18	constantan	22	copper	18
19	19	twin-twisted	10	copper	19
20	20	constantan	23	copper	20
21	21	twin-twisted	11	copper	21
22	22	constantan	24	copper	22
23	23	twin-twisted	12	copper	23
24	24	constantan	25	copper	24
		open	13	open	25, 26

Table C.1: DC pin-out from Nano-D connector A to QDevil QBox (Breakout box A), channels [1..24].

Breakout Box A QBox [25..48]	Fischer 2A 24-way	RT - MC	Cinch 2A	MC - coldfinger	Omnectics Nano-D 51-way
25	1	twin-twisted	1	copper	27
26	2	constantan	14	copper	28
27	3	twin-twisted	2	copper	29
28	4	constantan	15	copper	30
29	5	twin-twisted	3	copper	31
30	6	constantan	16	copper	32
31	7	twin-twisted	4	copper	33
32	8	constantan	17	copper	34
33	9	twin-twisted	5	copper	35
34	10	constantan	18	copper	36
35	11	twin-twisted	6	copper	37
36	12	constantan	19	copper	38
37	13	twin-twisted	7	copper	39
38	14	constantan	20	copper	40
39	15	twin-twisted	8	copper	41
40	16	constantan	21	copper	42
41	17	twin-twisted	9	copper	43
42	18	constantan	22	copper	44
43	19	twin-twisted	10	copper	45
44	20	constantan	23	copper	46
45	21	twin-twisted	11	copper	47
46	22	constantan	24	copper	48
47	23	twin-twisted	12	copper	49
48	24	constantan	25	copper	50
		open	13	open	51

Table C.2: DC pin-out from Nano-D connector A to QDevil QBox (Breakout box A), channels [25..48].

Breakout Box B [1..24]	Fischer 1B 24-way	RT - MC	Cinch 1B	MC - coldfinger	Omnectics Nano-D 51-way
1	1	twin-twisted	1	copper	1
2	2	constantan	14	copper	2
3	3	twin-twisted	2	copper	3
4	4	constantan	15	copper	4
5	5	twin-twisted	3	copper	5
6	6	constantan	16	copper	6
7	7	twin-twisted	4	copper	7
8	8	constantan	17	copper	8
9	9	twin-twisted	5	copper	9
10	10	constantan	18	copper	10
11	11	twin-twisted	6	copper	11
12	12	constantan	19	copper	12
13	13	twin-twisted	7	copper	13
14	14	constantan	20	copper	14
15	15	twin-twisted	8	copper	15
16	16	constantan	21	copper	16
17	17	twin-twisted	9	copper	17
18	18	constantan	22	copper	18
19	19	twin-twisted	10	copper	19
20	20	constantan	23	copper	20
21	21	twin-twisted	11	copper	21
22	22	constantan	24	copper	22
23	23	twin-twisted	12	copper	23
24	24	constantan	25	copper	24
		open	13	open	25, 26

Table C.3: DC pin-out from Nano-D connector B to Breakout box B, channels [1..24].

Breakout Box B [27..50]	Fischer 2B 24-way	RT - MC	Cinch 2B	MC - coldfinger	Omnectics Nano-D 51-way
27	1	twin-twisted	1	copper	27
28	2	constantan	14	copper	28
29	3	twin-twisted	2	copper	29
30	4	constantan	15	copper	30
31	5	twin-twisted	3	copper	31
32	6	constantan	16	copper	32
33	7	twin-twisted	4	copper	33
34	8	constantan	17	copper	34
35	9	twin-twisted	5	copper	35
36	10	constantan	18	copper	36
37	11	twin-twisted	6	copper	37
38	12	constantan	19	copper	38
38	13	twin-twisted	7	copper	39
40	14	constantan	20	copper	40
41	15	twin-twisted	8	copper	41
42	16	constantan	21	copper	42
43	17	twin-twisted	9	copper	43
44	18	constantan	22	copper	44
45	19	twin-twisted	10	copper	45
46	20	constantan	23	copper	46
47	21	twin-twisted	11	copper	47
48	22	constantan	24	copper	48
49	23	twin-twisted	12	copper	49
50	24	constantan	25	copper	50
		open	13	open	51

Table C.4: DC pin-out from Nano-D connector B to Breakout box B, channels [27..50].

Simulated cut-off frequencies of QBoard I

Here we simulate on LTspice V. 17.1.4 the cut-off frequencies of the PCB presented in Chapter 2. In Figure C.2(a), we show the circuit and transfer function from a BNC channel at the breakout box at RT, without bias-tee. The found cut-off frequency is ≈ 30 kHz. In the presence of a bias-tee [panel (b)], the cut-off frequency is ≈ 100 Hz.

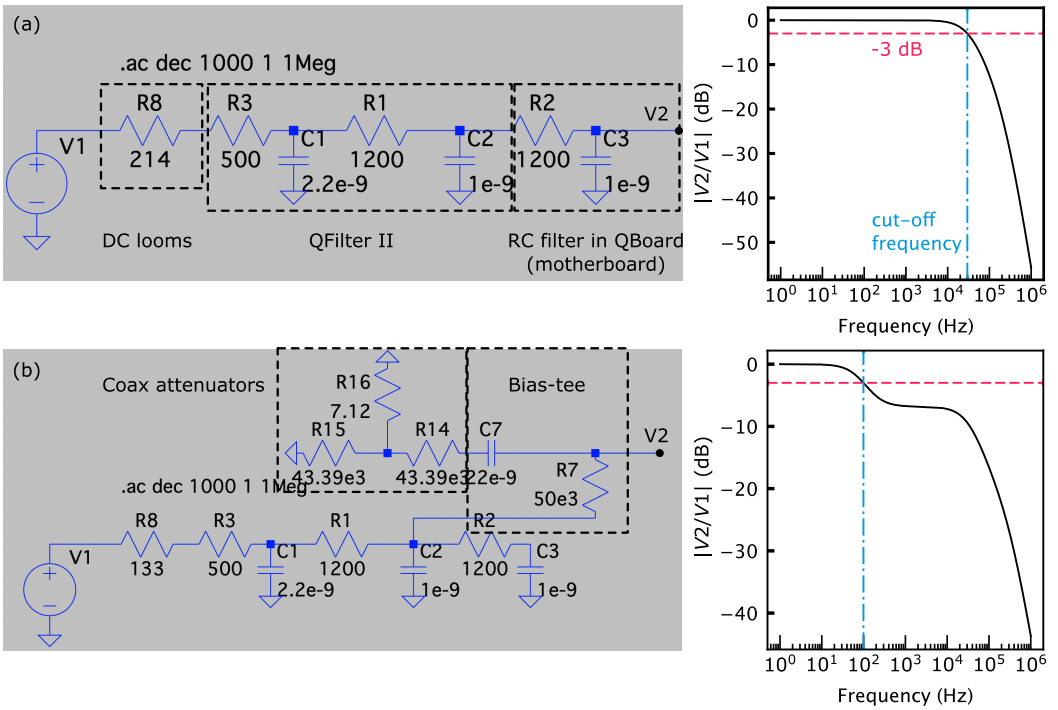

Fig. C.2: **Simulated bias-tee cut-off frequency (a)** Simulated circuit for the cut-off frequency of a low-frequency line (from RT BNC breakout box) with only the RC filter of Fig. 2.5(c). Electrical components of T7. **(b)** Simulated circuit for cut-off frequency of the low-frequency line (from RT BNC breakout box) part of the bias-tee. Electrical components of T7.

RF lines - Detailed schematics

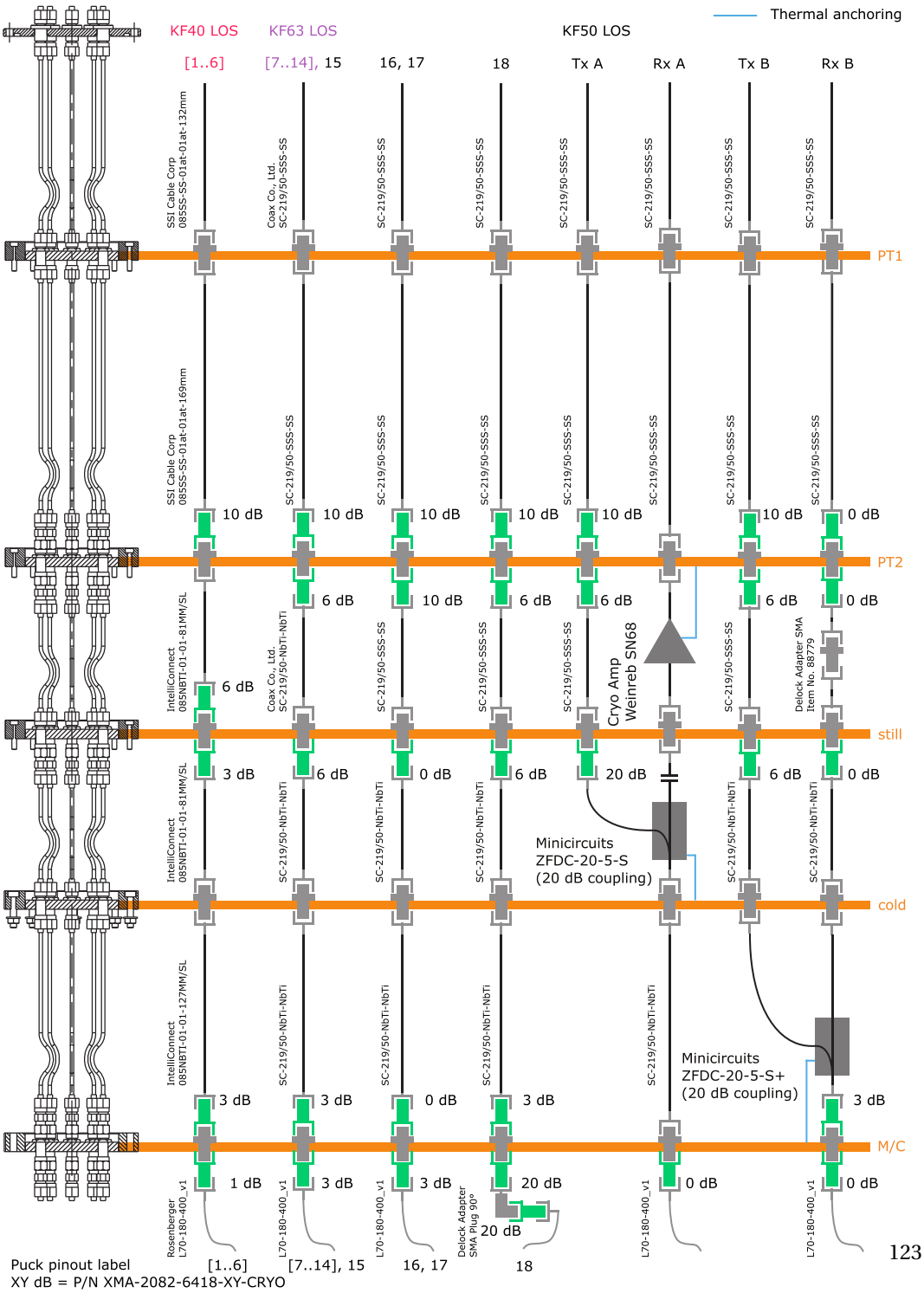

Fig. C.3: **Detailed schematics with part numbers of electrical components.** Coax 15 is SC-219/50-SSS-SS between PT2 and still plate. Thermal anchoring (blue line) is provided by a high-purity copper strand.

RF lines - transmission and reflection at room temperature

The transmission and reflection of each coax have been measured between the input port on top of the cryostat and the associated RF dock at the bottom of the coldfinger. The ZNB 20 Vector Network Analyzer output power was set to -20 dBm, with nominal frequency resolution 20 MHz and 100 averages. For testing the amplifier in Fig. C.5, the power was reduced to -30 dBm and the resolution to about 5 MHz.

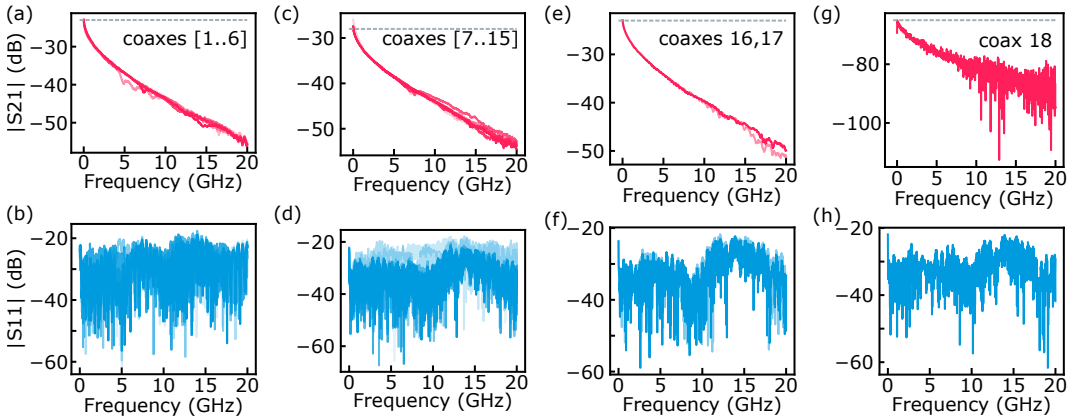

Fig. C.4: **Room temperature characterization of coax lines. (a, c, e, g)** Forward transmission (from port 1 to port 2) of the VNA. **(b, d, f, h)** Input reflection coefficient from port 1 of the VNA.

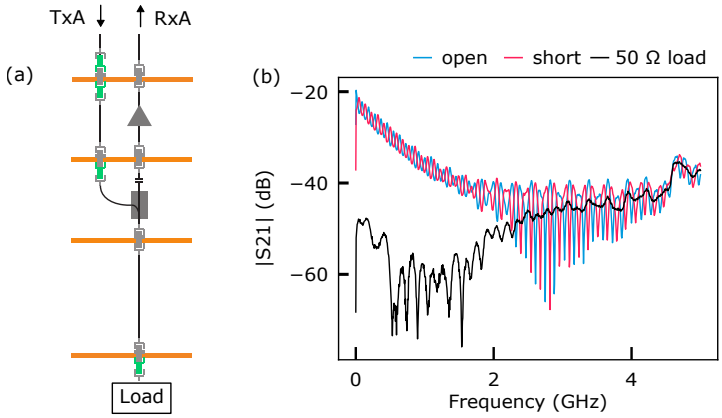

Fig. C.5: **Room temperature characterization of RF reflectometry setup. (a)** Setup: the load is the termination of the coax at the coldfinger. **(b)** Transmission from Tx to Rx (A), with different loads at RF dock 19 of the coldfinger. Notice the opposite phase of the ripples for the opened and shorted termination. From the period of the ripples an electrical length of about 1.1 m is found.

RF lines - delay times

The relative delay between the lines has been measured by generating on two channels a sine wave 1 V peak-to-peak at 120 MHz with a Tektronix 5014C Arbitrary Waveform Generator (AWG), in direct output mode. Sine waves have been chosen as in theory they are not distorted through the lines. While the first channel was connected directly to the oscilloscope MSO S234A, the other channel was connected to the RT input of the coaxes [1..17] and then to another channel of the oscilloscope. Finally, the delay between the two zero-crossings has been measured. Being coax 18 heavily attenuated, the signal from coax 18 was too noisy to be measured on the oscilloscope. In Tab. C.5 the relative delays compared to line 17 are shown.

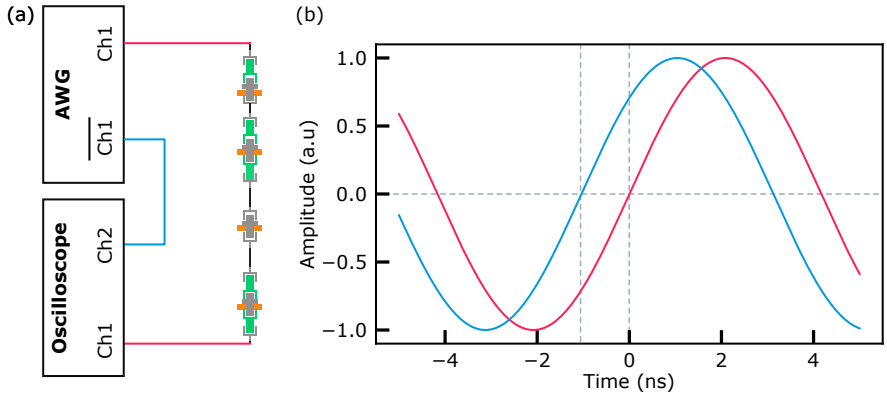

Fig. C.6: **Relative delay among the coax lines. (a)** The AWG sends two nominally identical sinusoidal waves, one directly to one channel of the oscilloscope, the other to one coax. The output of the coax is measured on another channel of the oscilloscope. **(b)** The horizontal distance between the zero-crossings gives an absolute time, to be referenced to the one of a coax.

Fast line:	Delay relative to line 17	Fast line:	Delay relative to line 17
1	(1.12 ± 0.02) ns	9	(-5 ± 32) ps
2	(1.12 ± 0.02) ns	10	(-2 ± 33) ps
3	(1.12 ± 0.02) ns	11	(-4 ± 37) ps
4	(1.12 ± 0.02) ns	12	(-10 ± 40) ps
5	(1.12 ± 0.02) ns	13	(-25 ± 34) ps
6	(1.12 ± 0.03) ns	14	(-40 ± 30) ps
7	(-5 ± 27) ps	15	(-23 ± 21) ps
8	(43 ± 30) ps	16	(-4 ± 21) ps

Table C.5: Relative delays among the coax lines measured with the oscilloscope and the AWG, as described in the main text.

D

Dispersive Charge Sensing without Reservoirs

Dispersive charge sensing without reservoirs

The measurement-based feedback protocol presented in Chapters 3 and 4 uses an independent sensor dot, since the technique relies on fast projective measurement of each qubit. Dispersive readout is an alternative technique to ohmic-based reflectometry to measure the charge occupation in QD arrays, for instance by the single-electron box (SEB) [120]. The SEB is a charged island connected to one lead only, instead of two as in the previously described SETs. The SEB is capacitively coupled to at least one other gate defining a QD. The periodic tunneling of an electron between the island and its reservoir can be modeled as an effective so-called quantum capacitance. The analytical expression of the quantum capacitance for a zero-dimensional density of states is [120]:

$$C_Q = \frac{(e\alpha)^2}{4k_B T} \frac{\gamma_0^2}{\gamma_0^2 + \omega^2} \cosh^{-2}\left(\frac{\epsilon_0}{2k_B T}\right), \tag{D.1}$$

where γ_0 is the tunneling rate between the SEB and the reservoir at the charge degeneracy point, ϵ_0 is the bias point (tuned by the gates voltages) and ω is the RF carrier angular frequency. The island potential shifts when the electron occupation of nearby QD changes, which changes the capacitance that can be proved by the reflectometry measurement. As SEBs require only one lead, they require less space.

When scaling from 2x2 devices to longer 2xN arrays, the source and drain reservoirs will eventually be too distant to support charge sensing within the bulk of the array. We address this challenge by demonstrating that charge sensing is possible without exchanging electrons with the leads [1]. Our technique is based on creating a hybridized double dot within the array (Fig. D.1a), whose quantum capacitance is sensitive to nearby charges Fig. D.1 and can be detected as a dispersive shift in the reflectometry signal [240]. We show this in a 2x2 device [38, 39] by activating two dots as a sensing DQD and the other two dots as qubit dots.

To create the sensing DQD, the top gate (not shown in the SEM) is set to +30 V and QD_4 is populated by 6-7 electrons. In this regime, the interdot transition between QD_4 and QD_1 hybridizes charge states on both dots and gives rise to an enhanced reflectometry signal (black star in Fig. D.1b). Its sensitivity to nearby charges becomes evident by sweeping G_2 vs. G_3, as done in Fig. D.1c. The observed honeycomb pattern in V_H indicates that the sensor DQD not only senses changes to the

[1] This section is published in Fabio Ansaloni et al. "Gate reflectometry in dense quantum dot arrays". In: *New Journal of Physics* 25.3 (2023), p. 033023. DOI: 10.1088/1367-2630/acc126, and reused in accordance with the CC-BY 3.0 license.

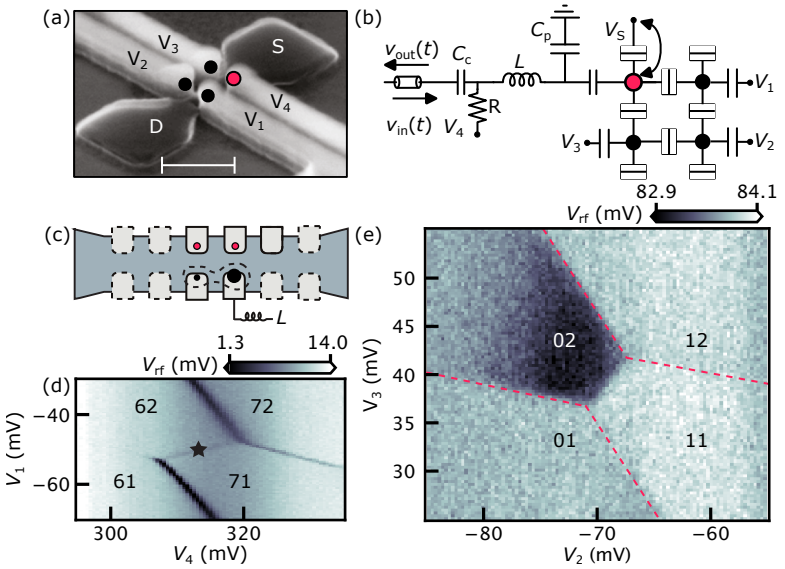

Fig. D.1: **Molecular sensing. (a)** SEM of a 2x2 QD array in a fully depleted silicon-on-insulator (FD-SOI) transistor [38, 39]. The scale bar is 200 nm. **(b)** Circuit schematic showing the LC resonator connected to the SEB charge sensor, which probes the other QDs of the 2x2 array. A bias-tee provides the gate voltage V_4. The arrow represents the electron tunneling between the SEB and the source reservoir. **(c)** A 2xN quantum dot array model where the reflectometry dot and its longitudinal neighbor (black circles) exchange electrons and are cut off from the leads. The so-formed molecule is used for locally sensing the qubit states (red circles). **(d)** An uncompensated stability diagram featuring a DQD formed below G_1 and G_4 acquired at $V_{tg} = 30$ V and having two/zero electrons on QD_3/QD_2. **(e)** Stability diagram for the DQD formed below G_2 and G_3 obtained by fixing V_1 and V_4 at the interdot transition (as shown with a star symbol in (b)). When the charge configuration of QD_2–QD_3 changes from (0,2), the demodulated signal changes from yellow to blue. This enables a new charge technique that relies on charge sensing of quantum dots in a 2xN array with a local, reconfigurable reflectometry molecule sensor that is decoupled from the electron reservoirs.

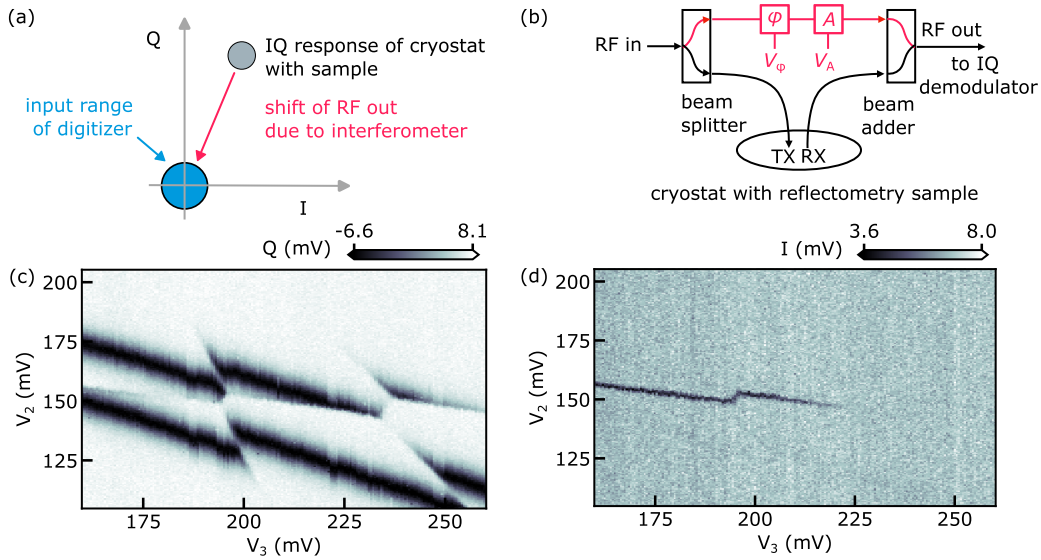

Fig. D.2: **Interferometric reflectometry**. **(a)** The blue circle represents the input range of the digitizer. The gray circle, outside the range, is shifted towards the origin of the IQ plane by an interferometric arm at RT. **(b)** In the interferometric arm, we tune the attenuation A by a programmable attenuator (MiniCircuits RCDAT-6000-60) connected in series to a voltage-controlled continuous one (ZX73-2500M-S+). The phase shifter Pulsar SO-06-411 tunes the phase φ of the arm. **(c-d)** In IQ space different physical processes in a charge stability diagram show up differently. Without the interferometric arm, only (c) would be available.

total charge in the qubit array (note the strong contrast between (02) and (12), for example), but also inter-qubit charge transitions [such as (02) to (11)].

Ultimately, future 2xN devices may benefit from reconfigurable dots, serving as qubit sites at some times and employed for readout or charge sensing at other times. Our gate-based DQD reflectometry technique may simplify such applications, as it does not require proximal reservoirs or dedicated sensor dots.

Translation in IQ space

When performing reflectometry with spin qubits, the reflected carrier from the cryostat may reside within a small region of the IQ plane, far away from the origin of the IQ plane (grey area in Figure D.2, panel (a). By far we mean compared to the input range of a DC-coupled digitizer, e.g. an Alazar card. A standard solution we use is the addition of a phase shifter to shift one quadrature of the IQ response into the (small) input range of one Alazar channel. Effectively, we are then only sensitive to phase changes of the reflected carrier, and do not learn anything about amplitude changes.

To also allow the detection of amplitude changes, we implement an interferometric technique, shown in panel (b). One arm of the interferometer is the cryostat. The other arm contains a voltage-controlled phase shifter and a voltage-controlled continuous attenuator, and produces a reference signal that results in complete deconstructive interference with the cryostat signal. Thereby, the

interferometer effectively relocates the carrier towards the origin of the IQ plane [red arrow in (a)], such that conventional demodulation into I and Q channels of the Alazarcard provides information about phase changes *and* amplitude changes arising from the sample. We show the results of this method in panels (c-d), where different physical processes within a quadruple dot show up differently in IQ space. For instance, the loading of the electron under dot 2, either from the nearby reservoir or from dot 3 shows up in (d) but not in (c). Vice versa, the sensor dot coulomb peaks from (c) do not show up in (d). Without the interferometer, only the Q panel would be available.

Bibliography

[1] John Preskill. *Quantum computing 40 years later*. 2021. DOI: 10.48550/arXiv.2106.10522.

[2] Barbara M. Terhal. "Quantum error correction for quantum memories". In: *Reviews of Modern Physics* 87.2 (2015), pp. 307–346. DOI: 10.1103/revmodphys.87.307.

[3] Jing Zhang et al. "Quantum feedback: Theory, experiments, and applications". In: *Physics Reports* 679 (2017), pp. 1–60. DOI: 10.1016/j.physrep.2017.02.003.

[4] Otto Mayr. *The Origins of Feedback Control*. The MIT Press, 1975, p. 158. ISBN: 9780262630566.

[5] J. C. Maxwell. In: *Proceedings of the Royal Society of London* 16 (1868), pp. 270–283. DOI: 10.1098/rspl.1867.0055.

[6] V. P. Belavkin. "Quantum continual measurements and a posteriori collapse on CCR". In: *Communications in Mathematical Physics* 146.3 (1992), pp. 611–635. DOI: 10.1007/bf02097018.

[7] Viacheslav P Belavkin. "Quantum stochastic calculus and quantum nonlinear filtering". In: *Journal of Multivariate Analysis* 42.2 (1992), pp. 171–201. DOI: 10.1016/0047-259x(92)90042-e.

[8] H. M. Wiseman. "Quantum theory of continuous feedback". In: *Physical Review A* 49.3 (1994), pp. 2133–2150. DOI: 10.1103/physreva.49.2133.

[9] Masahiro Yanagisawa and Hidenori Kimura. "A control problem for Gaussian states". In: *Lecture Notes in Control and Information Sciences*. Springer London, pp. 294–313. ISBN: 9781852330767. DOI: 10.1007/bfb0109736.

[10] A. C. Doherty and K. Jacobs. "Feedback control of quantum systems using continuous state estimation". In: *Physical Review A* 60.4 (1999), pp. 2700–2711. DOI: 10.1103/physreva.60.2700.

[11] P. A. M. Dirac. In: *Proceedings of the Royal Society of London. Series A, Containing Papers of a Mathematical and Physical Character* 123.792 (1929), pp. 714–733. DOI: 10.1098/rspa.1929.0094.

[12] Yuri Manin. "Computable and Uncomputable (in Russian)". In: *Sovetskoye Radio, Moscow* (1980).

[13] Paul Benioff. “The computer as a physical system: A microscopic quantum mechanical Hamiltonian model of computers as represented by Turing machines”. In: *Journal of Statistical Physics* 22.5 (1980), pp. 563–591. DOI: 10.1007/bf01011339.

[14] Paul M. Alsing, Carlo Cafaro, and Stefano Mancini. “Feynman’s "Simulating Physics with Computers"”. In: (2024). DOI: 10.48550/arXiv.2405.03366.

[15] Michael A. Nielsen and Isaac L. Chuang. *Quantum computation and quantum information*. 10th anniversary ed., repr. Cambridge [u.a.]: Cambridge University Press, 2012. 676 pp. ISBN: 9781107002173.

[16] Alexander M. Dalzell et al. *Quantum algorithms: A survey of applications and end-to-end complexities*. 2023. DOI: 10.48550/arXiv.2310.03011.

[17] Jordan S. *The quantum algorithm zoo*. 2024. URL: http://math.nist.gov/quantum/zoo/.

[18] Rolf Landauer. “Information is Physical”. In: *Physics Today* 44.5 (1991), pp. 23–29. DOI: 10.1063/1.881299.

[19] Tsubasa Ichikawa et al. “Current numbers of qubits and their uses”. In: *Nature Reviews Physics* (2024). DOI: 10.1038/s42254-024-00725-0.

[20] John Preskill. “Quantum Computing in the NISQ era and beyond”. In: *Quantum* 2 (2018), p. 79. DOI: 10.22331/q-2018-08-06-79.

[21] Earl Campbell. “A series of fast-paced advances in Quantum Error Correction”. In: *Nature Reviews Physics* 6.3 (2024), pp. 160–161. DOI: 10.1038/s42254-024-00706-3.

[22] C. Ryan-Anderson et al. “Realization of Real-Time Fault-Tolerant Quantum Error Correction”. In: *Physical Review X* 11.4 (2021), p. 041058. DOI: 10.1103/physrevx.11.041058.

[23] C. Ryan-Anderson et al. *Implementing Fault-tolerant Entangling Gates on the Five-qubit Code and the Color Code*. 2022. DOI: 10.48550/arXiv.2208.01863.

[24] Sebastian Krinner et al. “Realizing repeated quantum error correction in a distance-three surface code”. In: *Nature* 605.7911 (2022), pp. 669–674. DOI: 10.1038/s41586-022-04566-8.

[25] Rajeev Acharya et al. “Suppressing quantum errors by scaling a surface code logical qubit”. In: *Nature* 614.7949 (2023), pp. 676–681. DOI: 10.1038/s41586-022-05434-1.

[26] Dolev Bluvstein et al. “Logical quantum processor based on reconfigurable atom arrays”. In: *Nature* 626.7997 (2023), pp. 58–65. DOI: 10.1038/s41586-023-06927-3.

[27] Kenta Takeda et al. “Quantum error correction with silicon spin qubits”. In: *Nature* 608.7924 (2022), pp. 682–686. DOI: 10.1038/s41586-022-04986-6.

[28] A. K. Fedorov et al. *Quantum computing at the quantum advantage threshold: a down-to-business review*. 2022. DOI: 10.48550/arXiv.2203.17181.

[29] Anasua Chatterjee et al. “Semiconductor qubits in practice”. In: *Nature Reviews Physics* 3.3 (2021), pp. 157–177. DOI: 10.1038/s42254-021-00283-9.

[30] Filip K. Malinowski et al. “Notch filtering the nuclear environment of a spin qubit”. In: *Nature Nanotechnology* 12.1 (2016), pp. 16–20. DOI: 10.1038/nnano.2016.170.

[31] Filip K. Malinowski et al. “Spectrum of the Nuclear Environment for GaAs Spin Qubits”. In: *Physical Review Letters* 118.17 (2017), p. 177702. DOI: 10.1103/physrevlett.118.177702.

[32] Frederico Martins et al. “Negative Spin Exchange in a Multielectron Quantum Dot”. In: *Physical Review Letters* 119.22 (2017), p. 227701. DOI: 10.1103/physrevlett.119.227701.

[33] Filip K. Malinowski et al. “Spin of a Multielectron Quantum Dot and Its Interaction with a Neighboring Electron”. In: *Physical Review X* 8.1 (2018), p. 011045. DOI: 10.1103/physrevx.8.011045.

[34] Filip K. Malinowski et al. “Symmetric operation of the resonant exchange qubit”. In: *Physical Review B* 96.4 (2017), p. 045443. DOI: 10.1103/physrevb.96.045443.

[35] Filip K. Malinowski et al. “Fast spin exchange across a multielectron mediator”. In: *Nature Communications* 10 (2019), p. 1196. DOI: 10.1038/s41467-019-09194-x.

[36] Federico Fedele et al. “Simultaneous Operations in a Two-Dimensional Array of Singlet-Triplet Qubits”. In: *PRX Quantum* 2.4 (2021), p. 040306. DOI: 10.1103/prxquantum.2.040306.

[37] Christian Volk et al. “Fast Charge Sensing of Si/SiGe Quantum Dots via a High-Frequency Accumulation Gate”. In: *Nano Letters* 19.8 (2019), pp. 5628–5633. DOI: 10.1021/acs.nanolett.9b02149.

[38] Fabio Ansaloni et al. “Single-electron operations in a foundry-fabricated array of quantum dots”. In: *Nature Communications* 11 (2020), p. 6399. DOI: 10.1038/s41467-020-20280-3.

[39] Fabio Ansaloni et al. “Gate reflectometry in dense quantum dot arrays”. In: *New Journal of Physics* 25.3 (2023), p. 033023. DOI: 10.1088/1367-2630/acc126.

[40] Anasua Chatterjee et al. “Autonomous Estimation of High-Dimensional Coulomb Diamonds from Sparse Measurements”. In: *Physical Review Applied* 18.6 (2022), p. 064040. DOI: 10.1103/physrevapplied.18.064040.

[41] Oswin Krause et al. “Estimation of Convex Polytopes for Automatic Discovery of Charge State Transitions in Quantum Dot Arrays”. In: *Electronics* 11.15 (2022), p. 2327. DOI: 10.3390/electronics11152327.

[42] Fabrizio Berritta et al. “Real-time two-axis control of a spin qubit”. In: *Nature Communications* 15 (2024), p. 1676. DOI: 10.1038/s41467-024-45857-0.

[43] Fabrizio Berritta et al. *Physics-informed tracking of qubit fluctuations*. 2024. DOI: 10.48550/arXiv.2404.09212.

[44] Daniel Loss and David P. DiVincenzo. “Quantum computation with quantum dots”. In: *Physical Review A* 57.1 (1998), pp. 120–126. DOI: 10.1103/physreva.57.120.

[45] Peter Stano and Daniel Loss. “Review of performance metrics of spin qubits in gated semiconducting nanostructures”. In: *Nature Reviews Physics* 4.10 (2022), pp. 672–688. DOI: 10.1038/s42254-022-00484-w.

[46] J. M. Elzerman et al. “Single-shot read-out of an individual electron spin in a quantum dot”. In: *Nature* 430 (2004), p. 431. DOI: 10.1038/nature02693.

[47] J. R. Petta et al. “Coherent manipulation of coupled electron spins in semiconductor quantum dots.” In: *Science* 309 (2005), pp. 2180–2184. DOI: 10.1126/science.1116955.

[48] B. E. Kane. “A silicon-based nuclear spin quantum computer”. In: *Nature* 393 (1998), p. 133. DOI: 10.1038/30156.

[49] Alexei M. Tyryshkin et al. “Electron spin coherence exceeding seconds in high-purity silicon”. In: *Nat. Mater.* 11 (2012), pp. 143–147. DOI: 10.1038/nmat3182.

[50] Kamyar Saeedi et al. “Room-Temperature Quantum Bit Storage Exceeding 39 Minutes Using Ionized Donors in Silicon-28”. In: *Science* 342 (2013), pp. 830–833. DOI: 10.1126/science.1239584.

[51] Guido Burkard et al. “Semiconductor spin qubits”. In: *Reviews of Modern Physics* 95.2 (2 2023), p. 025003. DOI: 10.1103/revmodphys.95.025003.

[52] Tsuneya Ando, Alan B. Fowler, and Frank Stern. “Electronic properties of two-dimensional systems”. In: *Rev. Mod. Phys.* 54 (1982), pp. 437–672. DOI: 10.1103/RevModPhys.54.437.

[53] L.P. Kouwenhoven, D. G. Austing, and S. Tarucha. “Few-electron quantum dots”. In: *Rep. Prog. Phys.* 64 (2001), p. 701. URL: http://stacks.iop.org/0034-4885/64/i=6/a=201.

[54] W. G. van der Wiel et al. “Electron transport through double quantum dots”. In: *Rev. Mod. Phys.* 75 (1 2002), pp. 1–22. DOI: 10.1103/RevModPhys.75.1.

[55] www.nobelprize.org, accessed on 3 April, 2024.

[56] M. A. Kastner. “The single-electron transistor”. In: *Rev. Mod. Phys.* 64 (3 1992), pp. 849–858. DOI: 10.1103/RevModPhys.64.849.

[57] N. Ashcroft and N. Mermin. *Solid State Physics*. Cengage Learning, 1976. ISBN: 9788131500521.

[58] Jeremy Levy. “Universal Quantum Computation with Spin-1/2 Pairs and Heisenberg Exchange”. In: *Phys. Rev. Lett.* 89 (14 2002), p. 147902. DOI: 10.1103/PhysRevLett.89.147902.

[59] Kevin Eng et al. “Isotopically enhanced triple-quantum-dot qubit”. In: *Sci. Adv.* 1 (2015), p. 1500214. DOI: 10.1126/sciadv.1500214.

[60] K. C. Nowack et al. “Single-Shot Correlations and Two-Qubit Gate of Solid-State Spins”. In: *Science* 333 (2011), pp. 1269–1272. DOI: 10.1126/science.1209524.

[61] M. Veldhorst et al. “A two-qubit logic gate in silicon”. In: *Nature* 526 (2015), pp. 410–414.

[62] T. F. Watson et al. “A programmable two-qubit quantum processor in silicon”. In: *Nature* 555 (2018), p. 633. URL: https://doi.org/10.1038/nature25766.

[63] D. M. Zajac et al. “Resonantly driven CNOT gate for electron spins”. In: *Science* 359 (2018), pp. 439–442. DOI: 10.1126/science.aao5965.

[64] Austin G. Fowler et al. “Surface codes: Towards practical large-scale quantum computation”. In: *Phys. Rev. A* 86 (3 2012), p. 032324. DOI: 10.1103/PhysRevA.86.032324.

[65] L M K Vandersypen et al. “Interfacing spin qubits in quantum dots and donors—hot, dense, and coherent”. In: *npj Quantum Inf.* 3 (2017), p. 34. DOI: 10.1038/s41534-017-0038-y.

[66] M. F. Gonzalez-Zalba et al. “Scaling Silicon-Based Quantum Computing Using CMOS Technology”. In: *Nature Electronics* 4.12 (2021), pp. 872–884. DOI: 10.1038/s41928-021-00681-y.

[67] A. M. J. Zwerver et al. “Qubits made by advanced semiconductor manufacturing”. In: *Nature Electronics* 5.3 (2022), pp. 184–190. DOI: 10.1038/s41928-022-00727-9.

[68] Marco De Michielis et al. “Silicon spin qubits from laboratory to industry”. In: *Journal of Physics D: Applied Physics* 56.36 (2023), p. 363001. DOI: 10.1088/1361-6463/acd8c7.

[69] R. P. G. McNeil et al. “On-demand single-electron transfer between distant quantum dots”. In: *Nature* 477 (2011), pp. 439–442.

[70] B. Bertrand et al. “Fast spin information transfer between distant quantum dots using individual electrons”. In: *Nature Nano.* 11 (2016), pp. 672–676.

[71] B. Jadot et al. “Distant spin entanglement via fast and coherent electron shuttling”. In: *Nature Nano.* 16 (2021), p. 570. DOI: 10.1038/s41565-021-00846-y.

[72] T. A. Baart et al. “Single-spin CCD”. In: *Nature Nano.* 11 (2016), p. 330. DOI: 10.1038/nnano.2015.291.

[73] Takafumi Fujita et al. “Coherent shuttle of electron-spin states”. In: *npj Quant. Info.* 3 (2017), p. 22. DOI: 10.1038/s41534-017-0024-4.

[74] A. R. Mills et al. “Shuttling a single charge across a one-dimensional array of silicon quantum dots”. In: *Nat. Commun.* 10 (2019), p. 1063. DOI: 10.1038/s41467-019-08970-z.

[75] Jun Yoneda et al. “Coherent spin qubit transport in silicon”. In: *Nat. Commun.* 12 (2021), pp. 1–9. DOI: 10.1038/s41467-021-24371-7.

[76] Inga Seidler et al. “Conveyor-mode single-electron shuttling in Si/SiGe for a scalable quantum computing architecture”. In: *npj Quantum Information* 8.1 (2022). DOI: 10.1038/s41534-022-00615-2.

[77] Tom Struck et al. “Spin-EPR-pair separation by conveyor-mode single electron shuttling in Si/SiGe”. In: *Nature Communications* 15 (2024), p. 1325. DOI: 10.1038/s41467-024-45583-7.

[78] John M. Nichol et al. “High-fidelity entangling gate for double-quantum-dot spin qubits”. In: *npj Quant. Info.* 3 (2017), p. 3. DOI: 10.1038/s41534-016-0003-1.

[79] A. J. Sigillito et al. “Coherent transfer of quantum information in a silicon double quantum dot using resonant SWAP gates”. In: *npj Quant. Info.* 5 (2019), p. 110. DOI: 10.1038/s41534-019-0225-0.

[80] F. R. Braakman et al. “Long-distance coherent coupling in a quantum dot array”. In: *Nature Nano.* 8 (2013), pp. 432–437.

[81] Timothy Alexander Baart et al. “Coherent spin-exchange via a quantum mediator”. In: *Nature Nano.* 12 (2017), pp. 26–30. DOI: 10.1038/nnano.2016.188.

[82] Kok Wai Chan et al. “Exchange Coupling in a Linear Chain of Three Quantum-Dot Spin Qubits in Silicon”. In: *Nano Lett.* 21 (2021), pp. 1517–1522. DOI: 10.1021/acs.nanolett.0c04771.

[83] K. D. Petersson et al. “Circuit quantum electrodynamics with a spin qubit”. In: *Nature* 490 (2012), p. 380. DOI: 10.1038/nature11559.

[84] A. J. Landig et al. “Coherent spin-photon coupling using a resonant exchange qubit”. In: *Nature* 560 (2018), pp. 179–184. DOI: 10.1038/s41586-018-0365-y.

[85] X. Mi et al. “A coherent spin-photon interface in silicon”. In: *Nature* 555 (2018), p. 599. DOI: https://doi.org/10.1038/nature25769.

[86] N. Samkharadze et al. “Strong spin-photon coupling in silicon”. In: *Science* 359 (2018), pp. 1123–1127. DOI: 10.1126/science.aar4054.

[87] Guoji Zheng et al. “Rapid gate-based spin read-out in silicon using an on-chip resonator”. In: *Nat. Nanotechnol.* 14 (2019), p. 742. DOI: 10.1038/s41565-019-0488-9.

[88] F. Borjans et al. “Resonant microwave-mediated interactions between distant electron spins”. In: *Nature* 577 (2020), pp. 195–198. DOI: 10.1038/s41586-019-1867-y.

[89] F. Borjans, X. Mi, and J.R. Petta. “Spin Digitizer for High-Fidelity Readout of a Cavity-Coupled Silicon Triple Quantum Dot”. In: *Phys. Rev. Applied* 15 (2021), p. 044052. DOI: 10.1103/PhysRevApplied.15.044052.

[90] Jurgen Dijkema et al. “Two-qubit logic between distant spins in silicon”. In: (2023). DOI: 10.48550/arXiv.2310.16805.

[91] Carmen G Almudever et al. “The engineering challenges in quantum computing”. In: *Design, Automation & Test in Europe Conference & Exhibition (DATE), 2017*. IEEE. 2017, pp. 836–845. DOI: 10.23919/DATE.2017.7927104.

[92] Earl T Campbell, Barbara M Terhal, and Christophe Vuillot. “Roads towards fault-tolerant universal quantum computation”. In: *Nature* 549.7671 (2017), pp. 172–179. DOI: 10.1038/nature23460.

[93] L. Petit et al. “Spin lifetime and charge noise in hot silicon quantum dot qubits”. In: *Physical Review Letters* 121.7 (2018), p. 076801. DOI: 10.1103/PhysRevLett.121.076801.

[94] Luca Petit et al. “Universal quantum logic in hot silicon qubits”. In: *Nature* 580.7803 (2020), pp. 355–359. DOI: 10.1038/s41586-020-2170-7.

[95] Chih Heng Yang et al. “Operation of a silicon quantum processor unit cell above one kelvin”. In: *Nature* 580.7803 (2020), pp. 350–354. DOI: 10.1038/s41586-020-2171-6.

[96] Leon C. Camenzind et al. “A hole spin qubit in a fin field-effect transistor above 4 kelvin”. In: *Nature Electronics* 5.3 (2022), pp. 178–183. DOI: 10.1038/s41928-022-00722-0.

[97] Luca Petit et al. “Design and integration of single-qubit rotations and two-qubit gates in silicon above one Kelvin”. In: *Communications Materials* 3.1 (2022), p. 82. DOI: 10.1038/s43246-022-00304-9.

[98] Jonathan Y. Huang et al. “High-fidelity spin qubit operation and algorithmic initialization above 1 K”. In: *Nature* 627.8005 (2024), pp. 772–777. DOI: 10.1038/s41586-024-07160-2.

[99] F. H. L. Koppens et al. “Driven coherent oscillations of a single electron spin in a quantum dot”. In: *Nature* 442 (2006), p. 766. URL: http://dx.doi.org/10.1038/nature05065.

[100] Jarryd J. Pla et al. “A single-atom electron spin qubit in silicon”. In: *Nature* 489 (2012), pp. 541–545.

[101] K. C. Nowack et al. “Coherent Control of a Single Electron Spin with Electric Fields”. In: *Science* 318 (2007), p. 1430. DOI: 10.1126/science.1148092.

[102] S. Nadj-Perge et al. “Spin-orbit qubit in a semiconductor nanowire”. In: *Nature* 468 (2010), pp. 1084–1087.

[103] R. Brunner et al. “Two-Qubit Gate of Combined Single-Spin Rotation and Interdot Spin Exchange in a Double Quantum Dot”. In: *Phys. Rev. Lett.* 107 (14 2011), p. 146801. DOI: 10.1103/PhysRevLett.107.146801.

[104] Jun Yoneda et al. “A quantum-dot spin qubit with coherence limited by charge noise and fidelity higher than 99.9 per cent”. In: *Nat. Nanotechnol.* 13 (2018), pp. 102–106. DOI: 10.1038/s41565-017-0014-x.

[105] Adam R. Mills et al. “Two-qubit silicon quantum processor with operation fidelity exceeding 99%”. In: *Science Advances* 8.14 (2022). DOI: 10.1126/sciadv.abn5130.

[106] Akito Noiri et al. “Fast universal quantum gate above the fault-tolerance threshold in silicon”. In: *Nature* 601.7893 (2022), pp. 338–342. DOI: 10.1038/s41586-021-04182-y.

[107] Xiao Xue et al. “Quantum logic with spin qubits crossing the surface code threshold”. In: *Nature* 601.7893 (2022), pp. 343–347. DOI: 10.1038/s41586-021-04273-w.

[108] Chien-An Wang et al. *Operating semiconductor quantum processors with hopping spins*. 2024. DOI: 10.48550/arXiv.2402.18382.

[109] M. D. Shulman et al. “Suppressing qubit dephasing using real-time Hamiltonian estimation”. In: *Nature Communications* 5 (2014), p. 5156. DOI: 10.1038/ncomms6156.

[110] D. A. Lidar, I. L. Chuang, and K. B. Whaley. “Decoherence-Free Subspaces for Quantum Computation”. In: *Phys. Rev. Lett.* 81 (12 1998), pp. 2594–2597. DOI: 10.1103/PhysRevLett.81.2594.

[111] J. M. Taylor et al. “Relaxation, dephasing, and quantum control of electron spins in double quantum dots”. In: *Physical Review B* 76.3 (2007), p. 035315. DOI: 10.1103/physrevb.76.035315.

[112] B. M. Maune et al. “Coherent singlet-triplet oscillations in a silicon-based double quantum dot”. In: *Nature* 481 (2012), p. 344.

[113] M. A. Fogarty et al. “Integrated silicon qubit platform with single-spin addressability, exchange control and single-shot singlet-triplet readout”. In: *Nat. Commun.* 9 (2018), p. 4370. DOI: 10.1038/s41467-018-06039-x.

[114] Ryan M. Jock et al. “A silicon metal-oxide-semiconductor electron spin-orbit qubit”. In: *Nature Comm.* 9 (2018), p. 1768. DOI: 10.1038/s41467-018-04200-0.

[115] Y.-Y. Liu et al. “Magnetic-Gradient-Free Two-Axis Control of a Valley Spin Qubit in Si_xGe_{1-x}”. In: *Phys. Rev. Applied* 16 (2021), p. 024029. DOI: 10.1103/PhysRevApplied.16.024029.

[116] Xian Wu et al. “Two-axis control of a singlet–triplet qubit with an integrated micromagnet”. In: *Proceedings of the National Academy of Sciences* 111.33 (2014), pp. 11938–11942. DOI: 10.1073/pnas.1412230111.

[117] Sandra Foletti et al. “Universal quantum control of two-electron spin quantum bits using dynamic nuclear polarization”. In: *Nature Physics* 5.12 (2009), pp. 903–908. DOI: 10.1038/nphys1424.

[118] H. Bluhm et al. “Dephasing time of GaAs electron-spin qubits coupled to a nuclear bath exceeding 200 μs”. In: *Nat. Phys.* 7 (2010), pp. 109–113. DOI: 10.1038/nphys1856.

[119] C. Barthel et al. “Fast sensing of double-dot charge arrangement and spin state with a radio-frequency sensor quantum dot”. In: *Phys. Rev. B* 81 (16 2010), p. 161308. DOI: 10.1103/PhysRevB.81.161308.

[120] Florian Vigneau et al. “Probing quantum devices with radio-frequency reflectometry”. In: *Applied Physics Reviews* 10.2 (2023). DOI: 10.1063/5.0088229.

[121] Giordano Scappucci et al. “The germanium quantum information route”. In: *Nature Reviews Materials* 6.10 (2020), pp. 926–943. DOI: 10.1038/s41578-020-00262-z.

[122] Yinan Fang et al. “Recent advances in hole-spin qubits”. In: *Materials for Quantum Technology* 3.1 (2023), p. 012003. DOI: 10.1088/2633-4356/acb87e.

[123] Thomas Ihn. *Semiconductor nanostructures. quantum states and electronic transport*. Oxford University Press, 2010, p. 552. ISBN: 9780199534425.

[124] Peter Y. Yu and Manuel Cardona. *Fundamentals of Semiconductors*. Berlin: Springer, 2010. ISBN: 978-3-642-00710-1. (Visited on 05/16/2015).

[125] Roland Winkler. *Spin-Orbit Coupling Effects in Two-Dimensional Electron and Hole Systems*. Springer Tracts in Modern Physics Ser. v.191. Description based on publisher supplied metadata and other sources. Berlin, Heidelberg: Springer Berlin / Heidelberg, 2003. 1237 pp. ISBN: 9783540366164.

[126] Floris A. Zwanenburg et al. “Silicon quantum electronics”. In: *Reviews of Modern Physics* 85.3 (2013), pp. 961–1019. DOI: 10.1103/revmodphys.85.961.

[127] Arne Laucht et al. “Roadmap on quantum nanotechnologies”. In: *Nanotechnology* 32.16 (2021), p. 162003. DOI: 10.1088/1361-6528/abb333.

[128] Francesco Lorenzelli et al. “Study of Transistor Metrics for Room-Temperature Screening of Single Electron Transistors for Silicon Spin Qubit Applications”. In: *2023 IEEE European Test Symposium (ETS)*. IEEE, 2023. DOI: 10.1109/ets56758.2023.10173954.

[129] R. Li et al. “A flexible 300 mm integrated Si MOS platform for electron- and hole-spin qubits exploration”. In: *2020 IEEE International Electron Devices Meeting (IEDM)*. IEEE, 2020. DOI: 10.1109/iedm13553.2020.9371956.

[130] Nard Dumoulin Stuyck et al. “An Integrated Silicon MOS Single-Electron Transistor Charge Sensor for Spin-Based Quantum Information Processing”. In: *IEEE Electron Device Letters* 41.8 (2020), pp. 1253–1256. DOI: 10.1109/led.2020.3001291.

[131] Francesco Lorenzelli et al. “Wafer-Scale Electrical Characterization of Silicon Quantum Dots from Room to Low Temperatures”. In: *2023 IEEE International Test Conference (ITC)*. IEEE, 2023. DOI: 10.1109/itc51656.2023.00031.

[132] Michael J. Manfra. “Molecular Beam Epitaxy of Ultra-High-Quality AlGaAs/GaAs Heterostructures: Enabling Physics in Low-Dimensional Electronic Systems”. In: *Annu. Rev. Condens. Matter Phys.* 5 (2014), pp. 347–373. DOI: 10.1146/annurev-conmatphys-031113-133905. (Visited on 06/05/2021).

[133] M. Pioro-Ladrière et al. “Origin of switching noise in GaAs/Al_xGa_{1-x} As lateral gated devices”. In: *Physical Review B* 72.11 (2005), p. 115331. DOI: 10.1103/physrevb.72.115331.

[134] Christo Buizert et al. “In Situ Reduction of Charge Noise in GaAs/Al_xGa_{1-x} As Schottky-Gated Devices”. In: *Physical Review Letters* 101.22 (2008), p. 226603. DOI: 10.1103/physrevlett.101.226603.

[135] T. Hensgens et al. “Quantum simulation of a Fermi-Hubbard model using a semiconductor quantum dot array”. In: *Nature* 548 (2017), p. 70. DOI: 10.1038/nature23022.

[136] F. Fedele. “Spin interactions within a two-dimensional array of GaAs double dots”. PhD thesis. University of Copenhagen, 2020.

[137] J. Medford. “Spin Qubits in Double and Triple Quantum Dots”. Available at http://nrs.harvard.edu/urn-3:HUL.InstRepos:11156788. PhD thesis. University of Harvard, 2013.

[138] N. I. Dumoulin Stuyck et al. “Uniform Spin Qubit Devices with Tunable Coupling in an All-Silicon 300 mm Integrated Process”. In: *2021 Symposium on VLSI Circuits*. IEEE, 2021. DOI: 10.23919/vlsicircuits52068.2021.9492427.

[139] R. Hanson et al. “Spins in few-electron quantum dots”. In: *Rev. Mod. Phys.* 79 (4 2007), p. 1217. DOI: 10.1103/RevModPhys.79.1217.

[140] M. Field et al. “Measurements of Coulomb blockade with a noninvasive voltage probe”. In: *Phys. Rev. Lett.* 70 (9 1993), pp. 1311–1314. DOI: 10.1103/PhysRevLett.70.1311.

[141] A. C. Johnson, J. R. Petta, and C. M. Marcus. “Singlet-triplet spin blockade and charge sensing in a few-electron double quantum dot”. In: *Phys. Rev. B* 72 (2005), p. 165308. DOI: 10.1103/PhysRevB.72.165308.

[142] Tim Botzem et al. “Tuning Methods for Semiconductor Spin Qubits”. In: *Physical Review Applied* 10.5 (2018), p. 054026. DOI: 10.1103/physrevapplied.10.054026.

[143] D. J. Reilly et al. “Fast single-charge sensing with a rf quantum point contact”. In: *Appl. Phys. Lett.* 91 (2007), p. 162101. DOI: 10.1063/1.2794995.

[144] C. Barthel et al. “Rapid Single-Shot Measurement of a Singlet-Triplet Qubit”. In: *Phys. Rev. Lett.* 103 (16 2009), p. 160503. DOI: 10.1103/PhysRevLett.103.160503.

[145] D. Paget et al. “Low field electron-nuclear spin coupling in gallium arsenide under optical pumping conditions”. In: *Physical Review B* 15.12 (1977), pp. 5780–5796. DOI: 10.1103/physrevb.15.5780.

[146] Quantum Machines model OPX+, www.quantum-machines.co.

[147] Leandro Stefanazzi et al. *The QICK (Quantum Instrumentation Control Kit): Readout and control for qubits and detectors*. 2021. DOI: 10.48550/arXiv.2110.00557.

[148] Antti Vepsäläinen et al. “Improving qubit coherence using closed-loop feedback”. In: *Nature Communications* 13 (2022), p. 1932. DOI: 10.1038/s41467-022-29287-4.

[149] Luca Chirolli and Guido Burkard. “Decoherence in solid-state qubits”. In: *Advances in Physics* 57.3 (2008), pp. 225–285. DOI: 10.1080/00018730802218067. eprint: https://doi.org/10.1080/00018730802218067.

[150] Rachel C. Kurchin. “Using Bayesian parameter estimation to learn more from data without black boxes”. In: *Nature Reviews Physics* 6.3 (2024), pp. 152–154. DOI: 10.1038/s42254-024-00698-0.

[151] Christopher Ferrie, Christopher E Granade, and D G Cory. “How to best sample a periodic probability distribution, or on the accuracy of Hamiltonian finding strategies”. In: *Quantum Inf. Process.* 12.1 (2013), pp. 611–623.

[152] Frank Pobell. *Matter and Methods at Low Temperatures*. Springer-Verlag GmbH, 2007. 461 pp. ISBN: 9783540463603.

[153] G. Batey et al. "Integration of superconducting magnets with cryogen-free dilution refrigerator systems". In: *Cryogenics* 49.12 (2009), pp. 727–734. DOI: 10.1016/j.cryogenics.2009.09.008.

[154] S. Krinner et al. "Engineering cryogenic setups for 100-qubit scale superconducting circuit systems". In: *EPJ Quantum Technology* 6.1 (2019). DOI: 10.1140/epjqt/s40507-019-0072-0.

[155] QDevil model QBoard-I, www.quantum-machines.co, accessed on 3 April, 2024.

[156] https://github.com/QCoDeS/broadbean, accessed on 27 April, 2024.

[157] QDevil model QDAC-II, www.quantum-machines.co.

[158] Howard M. Wiseman and Gerard J. Milburn. *Quantum Measurement and Control*. Cambridge University Press, 2009. DOI: 10.1017/cbo9780511813948.

[159] R. Vijay et al. "Stabilizing Rabi oscillations in a superconducting qubit using quantum feedback". In: *Nature* 490.7418 (2012), pp. 77–80. DOI: 10.1038/nature11505.

[160] P. Campagne-Ibarcq et al. "Persistent Control of a Superconducting Qubit by Stroboscopic Measurement Feedback". In: *Physical Review X* 3.2 (2013), p. 021008. DOI: 10.1103/physrevx.3.021008.

[161] G. de Lange et al. "Reversing Quantum Trajectories with Analog Feedback". In: *Physical Review Letters* 112.8 (2014), p. 080501. DOI: 10.1103/physrevlett.112.080501.

[162] Y. Masuyama et al. "Information-to-work conversion by Maxwell's demon in a superconducting circuit quantum electrodynamical system". In: *Nature Communications* 9 (2018), p. 1291. DOI: 10.1038/s41467-018-03686-y.

[163] M. S. Blok et al. "Manipulating a qubit through the backaction of sequential partial measurements and real-time feedback". In: *Nature Physics* 10.3 (2014), pp. 189–193. DOI: 10.1038/nphys2881.

[164] C. Bonato et al. "Optimized quantum sensing with a single electron spin using real-time adaptive measurements". In: *Nature Nanotechnology* 11.3 (2015), pp. 247–252. DOI: 10.1038/nnano.2015.261.

[165] J. Cramer et al. "Repeated quantum error correction on a continuously encoded qubit by real-time feedback". In: *Nature Communications* 7 (2016), p. 11526. DOI: 10.1038/ncomms11526.

[166] Masashi Hirose and Paola Cappellaro. "Coherent feedback control of a single qubit in diamond". In: *Nature* 532.7597 (2016), pp. 77–80. DOI: 10.1038/nature17404.

[167] Shu-Hao Wu, Ethan Turner, and Hailin Wang. "Continuous real-time sensing with a nitrogen-vacancy center via coherent population trapping". In: *Physical Review A* 103.4 (2021), p. 042607. DOI: 10.1103/physreva.103.042607.

[168] Ethan Turner et al. "Spin-based continuous Bayesian magnetic-field estimations aided by feedback control". In: *Physical Review A* 106.5 (2022), p. 052603. DOI: 10.1103/physreva.106.052603.

[169] Pavel Bushev et al. “Feedback Cooling of a Single Trapped Ion”. In: *Physical Review Letters* 96.4 (2006), p. 043003. DOI: 10.1103/physrevlett.96.043003.

[170] K. Singh et al. “Mid-circuit correction of correlated phase errors using an array of spectator qubits”. In: *Science* 380.6651 (2023), pp. 1265–1269. DOI: 10.1126/science.ade5337.

[171] Daniel A. Steck et al. “Quantum Feedback Control of Atomic Motion in an Optical Cavity”. In: *Physical Review Letters* 92.22 (2004), p. 223004. DOI: 10.1103/physrevlett.92.223004.

[172] Clément Sayrin et al. “Real-time quantum feedback prepares and stabilizes photon number states”. In: *Nature* 477.7362 (2011), pp. 73–77. DOI: 10.1038/nature10376.

[173] D. J. Wilson et al. “Measurement-based control of a mechanical oscillator at its thermal decoherence rate”. In: *Nature* 524.7565 (2015), pp. 325–329. DOI: 10.1038/nature14672.

[174] Massimiliano Rossi et al. “Measurement-based quantum control of mechanical motion”. In: *Nature* 563.7729 (2018), pp. 53–58. DOI: 10.1038/s41586-018-0643-8.

[175] Lorenzo Magrini et al. “Real-time optimal quantum control of mechanical motion at room temperature”. In: *Nature* 595.7867 (2021), pp. 373–377. DOI: 10.1038/s41586-021-03602-3.

[176] Felix Tebbenjohanns et al. “Quantum control of a nanoparticle optically levitated in cryogenic free space”. In: *Nature* 595.7867 (2021), pp. 378–382. DOI: 10.1038/s41586-021-03617-w.

[177] Nico W. Hendrickx et al. “A four-qubit germanium quantum processor”. In: *Nature* 591.7851 (2021), pp. 580–585. DOI: 10.1038/s41586-021-03332-6.

[178] Stephan G. J. Philips et al. “Universal control of a six-qubit quantum processor in silicon”. In: *Nature* 609.7929 (2022), pp. 919–924. DOI: 10.1038/s41586-022-05117-x.

[179] Xin Zhang et al. *Universal control of four singlet-triplet qubits*. 2023. DOI: 10.48550/arXiv.2312.16101.

[180] Takashi Nakajima et al. “Coherence of a Driven Electron Spin Qubit Actively Decoupled from Quasistatic Noise”. In: *Physical Review X* 10.1 (2020), p. 011060. DOI: 10.1103/physrevx.10.011060.

[181] T. Kobayashi et al. “Feedback-based active reset of a spin qubit in silicon”. In: *npj Quantum Information* 9.1 (2023). DOI: 10.1038/s41534-023-00719-3.

[182] Takashi Nakajima et al. “Real-Time Feedback Control of Charge Sensing for Quantum Dot Qubits”. In: *Phys. Rev. Appl.* 15 (3 2021), p. L031003. DOI: 10.1103/PhysRevApplied.15.L031003.

[183] Mark A. I. Johnson et al. “Beating the Thermal Limit of Qubit Initialization with a Bayesian Maxwell’s Demon”. In: *Phys. Rev. X* 12 (4 2022), p. 041008. DOI: 10.1103/PhysRevX.12.041008.

[184] O. E. Dial et al. “Charge Noise Spectroscopy Using Coherent Exchange Oscillations in a Singlet-Triplet Qubit”. In: *Physical Review Letters* 110.14 (2013), p. 146804. DOI: 10.1103/physrevlett.110.146804.

[185] Pascal Cerfontaine et al. “Closed-loop control of a GaAs-based singlet-triplet spin qubit with 99.5% gate fidelity and low leakage”. In: *Nature Communications* 11 (2020), p. 4144. DOI: 10.1038/s41467-020-17865-3.

[186] Jehyun Kim et al. “Approaching Ideal Visibility in Singlet-Triplet Qubit Operations Using Energy-Selective Tunneling-Based Hamiltonian Estimation”. In: *Physical Review Letters* 129.4 (2022), p. 040501. DOI: 10.1103/physrevlett.129.040501.

[187] Jonginn Yun et al. “Probing two-qubit capacitive interactions beyond bilinear regime using dual Hamiltonian parameter estimations”. In: *npj Quantum Information* 9.1 (2023), p. 30. DOI: 10.1038/s41534-023-00699-4.

[188] Wonjin Jang et al. “Individual two-axis control of three singlet-triplet qubits in a micromagnet integrated quantum dot array”. In: *Applied Physics Letters* 117.23 (2020), p. 234001. DOI: 10.1063/5.0031231.

[189] C. Barthel et al. “Relaxation and readout visibility of a singlet-triplet qubit in an Overhauser field gradient”. In: *Physical Review B* 85.3 (2012), p. 035306. DOI: 10.1103/physrevb.85.035306.

[190] C. H. Yang et al. “Charge state hysteresis in semiconductor quantum dots”. In: *Applied Physics Letters* 105.18 (2014), p. 183505. DOI: 10.1063/1.4901218.

[191] Patrick Harvey-Collard et al. “High-Fidelity Single-Shot Readout for a Spin Qubit via an Enhanced Latching Mechanism”. In: *Phys. Rev. X* 8 (2 2018), p. 021046. DOI: 10.1103/PhysRevX.8.021046.

[192] Frederico Martins et al. “Noise Suppression Using Symmetric Exchange Gates in Spin Qubits”. In: *Phys. Rev. Lett.* 116 (11 2016), p. 116801. DOI: 10.1103/PhysRevLett.116.116801.

[193] F. H. L. Koppens et al. “Universal Phase Shift and Nonexponential Decay of Driven Single-Spin Oscillations”. In: *Physical Review Letters* 99.10 (2007), p. 106803. DOI: 10.1103/physrevlett.99.106803.

[194] Guy Ramon and Łukasz Cywiński. “Qubit decoherence under two-axis coupling to low-frequency noises”. In: *Physical Review B* 105.4 (2022), p. l041303. DOI: 10.1103/physrevb.105.l041303.

[195] Pascal Cerfontaine et al. “High-fidelity gate set for exchange-coupled singlet-triplet qubits”. In: *Physical Review B* 101.15 (2020), p. 155311. DOI: 10.1103/physrevb.101.155311.

[196] Xinxin Cai et al. “Coherent spin-valley oscillations in silicon”. In: *Nature Physics* 19 (2023), pp. 386–393. DOI: 10.1038/s41567-022-01870-y.

[197] Alexandr Sergeevich et al. “Characterization of a qubit Hamiltonian using adaptive measurements in a fixed basis”. In: *Physical Review A* 84.5 (2011), p. 052315. DOI: 10.1103/physreva.84.052315.

[198] Cristian Bonato and Dominic W. Berry. “Adaptive tracking of a time-varying field with a quantum sensor”. In: *Physical Review A* 95.5 (2017), p. 052348. DOI: 10.1103/physreva.95.052348.

[199] Eleanor Scerri, Erik M Gauger, and Cristian Bonato. “Extending qubit coherence by adaptive quantum environment learning”. In: *New Journal of Physics* 22.3 (2020), p. 035002. DOI: 10.1088/1367-2630/ab7bf3.

[200] Sandeep Mavadia et al. “Prediction and real-time compensation of qubit decoherence via machine learning”. In: *Nature Communications* 8 (2017), p. 14106. DOI: 10.1038/ncomms14106.

[201] Riddhi Swaroop Gupta and Michael J. Biercuk. "Machine Learning for Predictive Estimation of Qubit Dynamics Subject to Dephasing". In: *Physical Review Applied* 9.6 (2018), p. 064042. DOI: 10.1103/physrevapplied.9.064042.

[202] Lukas J. Fiderer, Jonas Schuff, and Daniel Braun. "Neural-Network Heuristics for Adaptive Bayesian Quantum Estimation". In: *PRX Quantum* 2.2 (2021), p. 020303. DOI: 10.1103/prxquantum.2.020303.

[203] G. Koolstra et al. "Monitoring Fast Superconducting Qubit Dynamics Using a Neural Network". In: *Phys. Rev. X* 12 (3 2022), p. 031017. DOI: 10.1103/PhysRevX.12.031017.

[204] Piotr Szańkowski, Marek Trippenbach, and Łukasz Cywiński. "Spectroscopy of cross correlations of environmental noises with two qubits". In: *Physical Review A* 94.1 (2016), p. 012109. DOI: 10.1103/physreva.94.012109.

[205] T.J. Evans et al. "Fast Bayesian Tomography of a Two-Qubit Gate Set in Silicon". In: *Phys. Rev. Appl.* 17 (2 2022), p. 024068. DOI: 10.1103/PhysRevApplied.17.024068.

[206] QDevil model QFilter-II, www.quantum-machines.co.

[207] M. D. Reed et al. "Reduced Sensitivity to Charge Noise in Semiconductor Spin Qubits via Symmetric Operation". In: *Phys. Rev. Lett.* 116 (11 2016), p. 110402. DOI: 10.1103/PhysRevLett.116.110402.

[208] J. Bergli, Y. M. Galperin, and B. L. Altshuler. "Decoherence in qubits due to low-frequency noise". In: *New Journal of Physics* 11.2 (2009), p. 025002. DOI: 10.1088/1367-2630/11/2/025002.

[209] Giuseppe Falci, Pertti J. Hakonen, and Elisabetta Paladino. "1/f noise in quantum nanoscience". In: *Encyclopedia of Condensed Matter Physics*. Elsevier, 2024, pp. 1003–1017. ISBN: 9780323914086. DOI: 10.1016/b978-0-323-90800-9.00250-x.

[210] Lorenza Viola, Emanuel Knill, and Seth Lloyd. "Dynamical Decoupling of Open Quantum Systems". In: *Physical Review Letters* 82.12 (1999), pp. 2417–2421. DOI: 10.1103/physrevlett.82.2417.

[211] P. Szańkowski et al. "Environmental noise spectroscopy with qubits subjected to dynamical decoupling". In: *Journal of Physics: Condensed Matter* 29.33 (2017), p. 333001. DOI: 10.1088/1361-648x/aa7648.

[212] P. London et al. "Detecting and Polarizing Nuclear Spins with Double Resonance on a Single Electron Spin". In: *Physical Review Letters* 111.6 (2013), p. 067601. DOI: 10.1103/physrevlett.111.067601.

[213] Jochen Scheuer et al. "Optically induced dynamic nuclear spin polarisation in diamond". In: *New Journal of Physics* 18.1 (2016), p. 013040. DOI: 10.1088/1367-2630/18/1/013040.

[214] Jaemin Park et al. "Passive and active suppression of transduced noise in silicon spin qubits". In: (2024). DOI: 10.48550/arXiv.2403.02666.

[215] Paola Cappellaro. "Spin-bath narrowing with adaptive parameter estimation". In: *Physical Review A* 85.3 (2012), p. 030301. DOI: 10.1103/physreva.85.030301.

[216] Angel Gutierrez-Rubio, Peter Stano, and Daniel Loss. "Optimal frequency estimation and its application to quantum dots". In: (2020). DOI: 10.48550/arXiv.2004.12049.

[217] K Craigie et al. “Resource-efficient adaptive Bayesian tracking of magnetic fields with a quantum sensor”. In: *Journal of Physics: Condensed Matter* 33.19 (2021), p. 195801. DOI: 10.1088/1361-648x/abe34f.

[218] Jacob Benestad et al. “Efficient adaptive Bayesian estimation of a slowly fluctuating Overhauser field gradient”. In: (2023). DOI: 10.48550/arXiv.2309.15014.

[219] Muhammad Junaid Arshad et al. “Real-time adaptive estimation of decoherence timescales for a single qubit”. In: *Physical Review Applied* 21.2 (2024), p. 024026. DOI: 10.1103/physrevapplied.21.024026.

[220] Romana Schirhagl et al. “Nitrogen-Vacancy Centers in Diamond: Nanoscale Sensors for Physics and Biology”. In: *Annual Review of Physical Chemistry* 65.1 (2014), pp. 83–105. DOI: 10.1146/annurev-physchem-040513-103659.

[221] G. Feher et al. “Spontaneous Emission of Radiation from an Electron Spin System”. In: *Physical Review* 109.1 (1958), pp. 221–222. DOI: 10.1103/physrev.109.221.

[222] J. P. Gordon and K. D. Bowers. “Microwave Spin Echoes from Donor Electrons in Silicon”. In: *Physical Review Letters* 1.10 (1958), pp. 368–370. DOI: 10.1103/physrevlett.1.368.

[223] Soeren Asmussen. *Applied Probability and Queues*. 2nd ed. Stochastic Modelling and Applied Probability Ser. v.51. Description based on publisher supplied metadata and other sources. New York, NY: Springer New York, 2003. 1451 pp. ISBN: 9780387215259.

[224] N. G. van Kampen. *Stochastic processes in physics and chemistry*. North-Holland, Amsterdam, 1990.

[225] Hossein T. Dinani et al. “Bayesian estimation for quantum sensing in the absence of single-shot detection”. In: *Physical Review B* 99.12 (2019), p. 125413. DOI: 10.1103/physrevb.99.125413.

[226] P. Krantz et al. “A quantum engineer’s guide to superconducting qubits”. In: *Applied Physics Reviews* 6.2 (2019). DOI: 10.1063/1.5089550.

[227] Bao-Jie Liu et al. *Observation of discrete charge states of a coherent two-level system in a superconducting qubit*. 2024. DOI: 10.48550/arXiv.2401.12183.

[228] Lukas Pahl et al. *Suppressing errors in quantum circuits using real-time, closed-loop feedback*. APS March Meeting 2024. 2024. URL: https://meetings.aps.org/Meeting/MAR24/Session/G47.2.

[229] David C. McKay et al. “Efficient Z gates for quantum computing”. In: *Physical Review A* 96.2 (2017), p. 022330. DOI: 10.1103/physreva.96.022330.

[230] E. Knill et al. “Randomized benchmarking of quantum gates”. In: *Physical Review A* 77.1 (2008), p. 012307. DOI: 10.1103/physreva.77.012307.

[231] P. J. J. O’Malley et al. “Qubit Metrology of Ultralow Phase Noise Using Randomized Benchmarking”. In: *Physical Review Applied* 3.4 (2015), p. 044009. DOI: 10.1103/physrevapplied.3.044009.

[232] Juan P Dehollain et al. “Optimization of a solid-state electron spin qubit using gate set tomography”. In: *New Journal of Physics* 18.10 (2016), p. 103018. DOI: 10.1088/1367-2630/18/10/103018.

[233] Erik Nielsen et al. “Gate Set Tomography”. In: *Quantum* 5 (2021), p. 557. DOI: 10.22331/q-2021-10-05-557.

[234] Erik Nielsen et al. “Probing quantum processor performance with pyGSTi”. In: *Quantum Science and Technology* 5.4 (2020), p. 044002. DOI: 10.1088/2058-9565/ab8aa4.

[235] Yuval R. Sanders, Joel J. Wallman, and Barry C. Sanders. “Bounding quantum gate error rate based on reported average fidelity”. In: *New Journal of Physics* 18.1 (2015), p. 012002. DOI: 10.1088/1367-2630/18/1/012002.

[236] Youngkyu Sung et al. “Realization of High-Fidelity CZ and ZZ -Free iSWAP Gates with a Tunable Coupler”. In: *Physical Review X* 11.2 (2021), p. 021058. DOI: 10.1103/physrevx.11.021058.

[237] Easwar Magesan et al. “Efficient Measurement of Quantum Gate Error by Interleaved Randomized Benchmarking”. In: *Physical Review Letters* 109.8 (2012), p. 080505. DOI: 10.1103/physrevlett.109.080505.

[238] David P. DiVincenzo. “Quantum gates and circuits”. In: *Proceedings of the Royal Society of London. Series A: Mathematical, Physical and Engineering Sciences* 454.1969 (1998), pp. 261–276. DOI: 10.1098/rspa.1998.0159.

[239] David P. DiVincenzo. “The Physical Implementation of Quantum Computation”. In: *Fortschritte der Physik* 48.9–11 (2000), pp. 771–783. DOI: 10.48550/arXiv.quant-ph/0002077.

[240] K. D. Petersson et al. “Charge and Spin State Readout of a Double Quantum Dot Coupled to a Resonator”. In: *Nano Letters* 10.8 (2010), pp. 2789–2793. DOI: 10.1021/nl100663w.